Final Report

Performance Improvement of High Early Strength (HES) Concrete for Pavement Replacement Slabs

FDOT Contract Number: BDV25-977-23

Date: September 2018

Submitted to

Research Center (Research.center@dot.state.fl.us)
The Florida Department of Transportation
Research Center
605 Suwannee Street, MS 30
Tallahassee, FL 32399

c/o Dr. Harvey DeFord
Structural Materials Research Specialist
State Materials Office
5007 NE 39th Avenue
Gainesville, FL 32609
Phone: (352)955-6671
Email: Harvey.deford@dot.state.fl.us

Submitted by

Principal Investigator: Dr. A. Zayed
Department of Civil and Environmental Engineering
University of South Florida
4202 E Fowler Avenue; ENB 118
Tampa, FL 33620-5350
Email: zayed@usf.edu

Disclaimer

The opinions, findings, and conclusions expressed in this publication are those of the authors and not necessarily those of the State of Florida Department of Transportation (FDOT) or the U.S. Department of Transportation (USDOT) or the Federal Highway Administration (FHWA).

Approximate Conversions to SI Units (from FHWA)

Symbol	When You Know	Multiply By	To Find	Symbol
Length				
in	inches	25.4	millimeters	mm
ft	feet	0.305	meters	m
yd	yards	0.914	meters	m
mi	miles	1.61	kilometers	km
Area				
in^2	square inches	645.2	square millimeters	mm^2
ft^2	square feet	0.093	square meters	m^2
yd^2	square yard	0.836	square meters	m^2
mi^2	square miles	2.59	square kilometers	km^2
Volume				
fl oz	fluid ounces	29.57	milliliters	mL
gal	gallons	3.785	liters	L
ft^3	cubic feet	0.028	cubic meters	m^3
yd^3	cubic yards	0.765	cubic meters	m^3
NOTE: volumes greater than 1000 L shall be shown in m^3				
Mass				
oz	ounces	28.35	grams	g
lb	pounds	0.454	kilograms	kg
Temperature (exact degrees)				
°F	Fahrenheit	5 (F-32)/9 or (F-32)/1.8	Celsius	°C
Illumination				
fc	foot-candles	10.76	lux	lx
fl	foot-Lamberts	3.426	candela/m^2	cd/m^2
Force and Pressure or Stress				
lbf	pound-force	4.45	newtons	N
lbf/in^2	pound-force per square inch	6.89	kilopascals	kPa

Technical Report Documentation Page

1. Report No.

2. Government Accession No.

3. Recipient's Catalog No.

4. Title and Subtitle
Performance Improvement of High Early Strength (HES) Concrete for Pavement Replacement Slabs

5. Report Date
November 2018

6. Performing Organization Code

7. Author(s)
A. Zayed, K. Riding, A. Sedaghat, D. Mapa, A. Markandeya, N. Shanahan, F. Nosouhian, and A. Williams

8. Performing Organization Report No.

9. Performing Organization Name and Address
Department of Civil and Environmental Engineering
University of South Florida
4202 E Fowler Avenue; ENB 118
Tampa, FL 33620-5350

10. Work Unit No. (TRAIS)

11. Contract or Grant No.
BDV25-977-23

12. Sponsoring Agency Name and Address
Florida Department of Transportation
605 Suwannee Street, MS 30
Tallahassee, FL 32399

13. Type of Report and Period Covered
Final Report. 11/25/2015-12/1/2018

14. Sponsoring Agency Code

15. Supplementary Notes
None

16. Abstract

The objectives of this study were to identify concrete mixture combinations, slab base-restraint, and placement conditions that can reduce the risk of early-age cracking potential of concrete pavement repair slabs and to provide recommendations for specifications changes. Towards satisfying the objectives, a battery of laboratory tests as well as field slab placements were conducted to assess several mitigating strategies adopted here to reduce incidents of cracking in pavement concrete slabs. Field slabs were instrumented with stressmeters and thermocouples. Cracking mitigating strategies studied here were reduction of cementitious paste volume through aggregate grading optimization, internal curing using saturated lightweight aggregates, fiber reinforcement to inhibit plastic cracking, use of shrinkage-reducing admixtures, reduction of base restraint using geotextile and plastic sheeting. DIANA and HIPERPAV software programs were used to identify the main factors affecting cracking potential in pavement slabs. The findings indicate that the initial stress development in most of the field-placed slabs was affected by moisture migration to the base; tensile stresses were observed due to an increased autogenous shrinkage within the slab. DIANA finite element analysis indicated that the initial temperature gradient within the slab would not contribute to the development of tensile stresses at early age. The cracking risks of HES concrete can be greatly reduced by increasing the aggregate packing density and lowering the paste content. The cracking probability of HES concrete slabs can be minimized by incorporating LWA as a means of internal curing to extend hydration and reduce autogenous shrinkage effects. The base friction-reducing mediums showed more pronounced effects on early-age stress development by affecting moisture absorption than by reducing friction. The geotextile augmented the absorption of moisture from concrete, which increased cracking risks during early age.

17. Key Word
High-early strength concrete, aggregate optimization, internal curing, geotextile and plastic membranes, activation energy, stressmeter, replacement slab concrete mixtures.

18. Distribution Statement
No restrictions

19. Security Classif. (of this report)
Unclassified

20. Security Classif. (of this page)
Unclassified

21. No. of Pages
283

22. Price

Form DOT F 1700.7 (8-72) Reproduction of completed page authorized

Acknowledgement

This work has been sponsored by the Florida Department of Transportation (FDOT). The Principal Investigator appreciates the valuable discussions with Dr. Harvey DeFord, Project Manager. The authors would like to thank Mr. Gregory Deese (PE), with the Florida Department of Transportation District 7 Office, for providing the site for slab placement and for assistance with form construction and slab sub-base preparation.

Executive Summary

1.1 Background

Concrete slab replacement projects in Florida frequently encounter high incidences of replacement slab cracking. Cracking rates in recent slab replacement projects have ranged from a desirable rate of less than 1% to a completely unacceptable rate of greater than 40%. Typically, the causes of the cracking are not reliably determined. Research is needed to determine the contributing factors that lead to cracking. From this information, procedures can be developed which minimize the tendency of replacement slabs to crack.

1.2 Research Objectives

The objective of the proposed research is to identify concrete mixture combinations, slab base-restraint and placement conditions that can reduce the risk of early-age cracking potential of concrete pavement repair slabs for the Florida department of Transportation construction projects. The second objective is to quantify the benefits of different methods for reducing cracking potential and provide corresponding recommendations to the Florida Department of Transportation for specification changes.

1.3 Main Findings

- The initial stress development in most of the field-placed slabs was affected by the moisture migration to the base; tensile stresses were observed due to an increased autogenous shrinkage within the slab. DIANA finite element analysis confirmed that the initial temperature gradient would not contribute significantly to the development of tensile stresses within the slab at early age.
- The cracking risks of high early strength (HES) concrete can be greatly reduced by increasing the aggregate packing and lowering the paste content. A decrease in cement content decreased the temperature rise and overall autogenous shrinkage in concrete and, consequently, its tendency to crack.
- High early-age strengths in concrete can be achieved even with low paste volume in concrete mixtures.

- The cracking probability of HES concrete slabs can be minimized by incorporating saturated lightweight aggregate (LWA) as a means of internal curing to extend hydration and reduce autogenous shrinkage effects.
- The low shrinkage-reducing admixture (SRA) dosage and fiber volume utilized in this study showed a reduction in cracking risks during the most critical time period for HES slabs, the first 24 hours after placement. They did not, however, reduce the cracking probability significantly after that time.
- The base friction-reducing media showed more pronounced effects on early-age stress development through base moisture absorption than by reducing friction.
    - The double layers of plastic sheeting at the slab-base interface prevented moisture loss to the base at early age. However, later on, its bond-breaking ability was questionable as no significant effect on cracking potential was observed; either the plastic did not change the friction coefficient between the slab and the base or curling lifted the slab off of the subbase slightly.
    - The geotextile augmented the absorption of moisture from concrete and increased cracking risks during early age. However, later on, the cracking tendency was somewhat reduced.

1.4 Recommendations

Based on the findings of this study, the following can be recommended:

- Require that the bases be prewetted prior to concrete placement to prevent moisture migration and the resultant increase in tensile stresses.
- Require that geotextiles be prewetted prior to concrete placement.
- Use of an HES mix with optimized aggregate gradation and reduced paste content to overcome thermal and shrinkage effects, which promote cracking.
- Concrete mixtures with optimized aggregate gradation (denser particle packing) and reduced cement content are recommended for use for full-depth repairs in HES pavement slabs.

1.5 Recommendations for Future Study

The findings of the current study identified several strategies that, if implemented, can reduce the cracking potential in HES pavement replacement slabs. It would be desirable to combine several of the identified strategies in a single mixture and assess the enhancement of the crack mitigation effects when strategies are applied simultaneously.

TABLE OF CONTENTS

Contents page

LIST OF FIGURES

LIST OF TABLES

Chapter 1 Literature Review

1.1 Introduction

Early opening-to-traffic (EOT) of concrete construction has become prevalent as a consequence of rational approaches to estimated economic costs from work zone activities and lane closures that have been implemented by state transportation agencies. EOT concrete mixtures usually allow traffic to be opened six hours after placement, requiring high-early age strengths. The low water-to-cementitious material ratios (w/cm) and accelerating admixtures used can create a high amount of volume change at early ages that, when restrained by the pavement base during curing, generates high tensile stresses. High early-age stresses can result in cracks and failed repairs.

The Florida Department of Transportation (FDOT) has experienced high incidences of cracking of replacement slabs on some concrete slab replacement projects. The range of cracking rates in these recent slab replacement projects varied from a desirable rate of less than 1% to a completely unacceptable rate of greater than 40% [1]. Inadequate saw depths, late sawing, and restrained shrinkage stresses have been identified as contributing factors to uncontrolled cracking. Concrete pavement repair performance could be improved by identification of effective methods of mitigating early-age restrained shrinkage stresses.

This study was initiated with the objective of improving performance of EOT pavement repairs by reducing concrete autogenous and thermal shrinkage and reducing base restraint. A literature review was conducted to determine a refinement process for mix designs to optimize the amount of cementitious materials needed for mix designs in order to reduce shrinkage, identify causes of cracking, and develop potential methods to minimize cracking potential in high early-strength (HES) concrete for jointed plain concrete pavement (JPCP) repairs. The factors thought to contribute to slab cracking were examined and included [1] slab base-restraints, construction methods, properties of HES concrete, HES mixture design, and concrete curing methods. Experimental procedures to quantify the effects of these contributing factors on cracking at early ages were examined. Although there are nationwide common practices for JPCP construction, each state has its own practices due to the regional weather conditions and available materials. FDOT specifications related to HES concrete pavement construction were reviewed and compared to those adopted in other states.

1.2 High Early-Strength Concrete Materials Requirements

Opening criteria for HES slabs vary between transportation agencies and the details of the project. Some of these criteria specified for various state agencies are compiled in Table 1-1. The strength criteria specified could either be a minimum flexural or compressive strength threshold or both. While some states specify both an opening time and a strength criteria, other agencies specify the strength needed to open pavement to traffic [2]. This is in consonance with the ACPA (American Concrete Pavement Association) fast track paving guide, which suggests defining a criteria based on a minimum opening strength for HES pavements [3] . Opening to traffic might be based on third point loading for HES mixes used in repairs that are less than 3 ft in length [4]. The ACPA guide also defines early age strength thresholds depending on the thickness of the pavement [3]. Agencies base compliance with the strength required for opening to traffic on a specified maturity-strength relationship (corresponding to opening strength according to ASTM C1074) as demonstrated in the WSDOT (Washington Department of Transportation) and FDOT (Florida Department of Transportation) manuals or other nondestructive techniques such as rebound hammer [5].

Table 1-1: State requirements for opening to traffic

State	Minimum age at opening to traffic	Compressive strength requirement	Flexural strength requirement
Arkansas	6 hours	2,000 psi	
California	8 hours [6]	-	400 psi [6]
Colorado	Constractor specified [7]	3,000 psi at opening[2]	650 psi at 28 days[7]
Delaware	Contractor Specified [8]	2,000 psi for opening to traffic [8]	

Table 1-1: State requirements for opening to traffic (Contd.)

State	Minimum age at opening to traffic	Compressive strength requirement	Flexural strength requirement
Florida	Contractor Specified [8]	1,600 psi at opening to traffic (Amended July 2016) [8]	
Georgia	> 4 hours [9]	3,000 psi at 3 days for acceptance [9]	-
Illinois	4-8 Hours [10]	3,500 psi at opening [10]	
Kansas	4-6 hours [11]	3,500 psi [11]	
Maryland	12 hours [11]	2,500 psi [11]	
Michigan	8 hours [11]		290 psi at opening [11]
Minnesota	12-hours		
Missouri	4 hours [11]	3,500 psi [11]	
New Jersey	6.5 hours [11]	-	350 psi at opening [11]
New York	Contractor specified [12]	3,000 psi at opening [12]	
North Carolina	Contractor specified [5]	2,500 psi [5]	
Ohio	4 hours [11]		400 psi at opening [11]
Pennsylvania	Less than 7 Hours [11]	1,200 psi at opening, 1,450 psi at 7 hours [8]	
Texas	24 hours [11]		420 psi[11]
Virginia	Contractor specified [14]	2,500 psi at opening to traffic [14]	600 psi at 28 days for mix design
Washington	Contractor specified [15]	2,500 psi at opening to traffic as estimated using ASTM C1074 [15]	
Wisconsin	8 hours [11]	3,000 psi at opening [11]	

In order to achieve these high concrete strengths in the short time requirements for traffic opening, large dosages of accelerating admixtures are typically used. Further, high cement factors are usually specified and adopted [11]. Calcium nitrate and calcium chloride are two of the most commonly used types of concrete accelerators. While some state agencies like California and Illinois prohibit the use of chloride based accelerators in accelerated paving, their use is allowed in non-reinforced pavements by the FDOT. A draft specification of the FHWA specifies a minimum cementitious content of 750 lb/yd^3 [2]. Concrete suppliers must be careful to avoid overdosing, which can lead to weakening of the concrete and increase the probability of cracking

[1]. Most state agencies additionally specify a minimum cement content typically in the range of 670-890 lb/yd^3 for this class of pavements, while other agencies such as Missouri suggest increasing the cement content by 30% relative to mixes used in conventional concrete pavement for achieving high early strength. Typical cement requirements vary ranging from 650 to 890 lb/yd^3, with more cement being used when earlier opening times are required [7]. The use of type III is allowed by some agencies but not by the FDOT.

Depending on the length of the repair, minimum strength requirements can be obtained from center-point (3-point loading) or third-point (4-point loading) modulus of rupture tests. A modulus of rupture from center-point loading reaching 300 psi or third-point loading yielding 250 psi is considered an acceptable minimum by the FHWA [6]. In California, depending on the type of project, the required value for modulus of rupture can vary from 400 psi to 600 psi for opening to traffic [16].

The variation in EOT times imposed by state DOTs results in a range of concrete mix designs tailored to meet the EOT criteria. For the Florida Department of Transportation (FDOT), the concrete must have an air content between 1% and 6%, and a placement temperature not to exceed 100°F (38° C) [17]. Other agencies have a higher lower bound for the air content [1] likely due to freeze-thaw durability considerations.

1.3 Causes for Early-Age Concrete Failure

In order to understand the causes for early-age concrete failure, the early-age behavior of concrete must be known. The “early age” is defined as the period after final setting, during which the properties are changing rapidly. This period is generally considered to be about 7 days for normal concrete, but much less for HES concrete. During this period, tensile stresses are developed due to volumetric changes. Since the tensile strength of concrete is low and still developing throughout this stage while the stresses are being generated, it can lead to cracking. The behavior of concrete at an early age is influenced by several factors such as [18]:

- The rate of heat generation and resulting rate of temperature rise
- Accelerator content for HES concrete

- Climatic conditions such as air temperature, solar radiation, relative humidity of the air, and wind speed
- Concrete temperature and base temperature during placement
- The concrete coefficient of thermal expansion (CTE)
- Slab-base interface restraint
- Concrete shrinkage
- Curling and warping of the concrete slab as a result of temperature gradients
- Creep/relaxation phenomena
- Construction procedures

Thus, new pavement and repair slab failure can be as attributed to the combined effects of volume change, restrained stress, and stress relaxation.

1.3.1 Volume Change Mechanisms in Concrete

Thermal and moisture-related concrete volume changes have been identified as significant causes of early-age concrete cracking.

1.3.1.1 Thermal Volume Change

1.3.1.1.1 Heat of Hydration

Cement hydration reactions are exothermic. This means that heat is released during concrete curing. The progress of cement hydration can be monitored by following the rate of heat release with time. The cement hydration process and heat release are generally divided into five stages: (1) initial hydrolysis, (2) induction period, (3) acceleration period, (4) deceleration period, and (5) steady state, as shown in Figure 1-1 for a portland cement-water mixture (paste) at 30^{o}C [1].

A rapid heat evolution occurs in stage 1 due to rapid ionic dissolution once cement is mixed with water. The initial hydrolysis period is short and will typically cease within 15 minutes. Dissolution continues during the induction period until a critical concentration of calcium and hydroxyl ions is reached, after which precipitation of C-S-H begins. The induction period is the period in which the concrete can be placed and consolidated, since it is still workable. The length of the induction period can increase or decrease with admixture addition. The use accelerators will shorten the length of the induction period, while retarder extends the time associated with this period. Generally, after this period and at the beginning of the acceleration period, initial set occurs. During stage 3, calcium-silicate-hydrate (C-S-H) and calcium hydroxide (CH) start to precipitate from solution and the rate of C_3S reaction increases. Hence, a higher temperature (if the concrete or cement paste is hydrating in a non-isothermal system) can be observed. Final set is achieved when enough C-S-H has formed and connected to form a solid skeleton capable of bearing some load. The hydration of calcium silicate phases decelerates in stage 4 because the continued dissolution of reactants and precipitation of C-S-H (1) reduces the surface area of exposed, unreacted cementitious phases available for reaction, (2) reduces the volume of water in the pore network that is available for hydration, and (3) decreases transport of reactants (permeability) by reducing the cross section and volume of interconnected, water-filled capillaries needed for fluid transport of reactants [19]. Hydration is thought to be diffusion limited in the steady state, stage 5 [20]. It is also suggested that gradual filling of space by hydration products might be a factor controlling the rate of hydration in stages 4 and 5 [19].

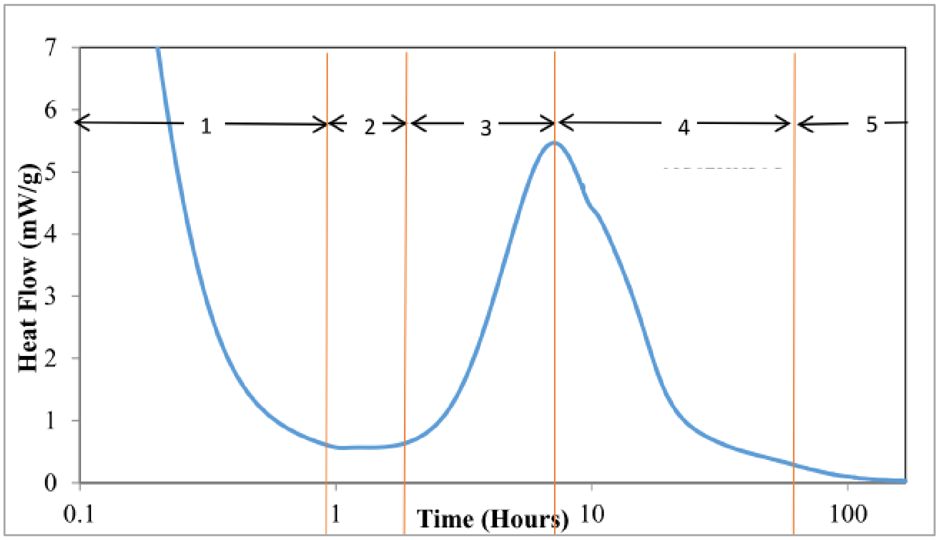

Figure 1-1: Typical stages of the hydration process [1]

1.3.1.1.2 Thermal Stress Development

Concrete heat of hydration raises the concrete pavement temperature. When the hydration and associated heat release slows down and is exceeded by the heat transfer with the environment, the concrete temperature will approach that of the ambient temperature. Concrete will contract during cooling. When restrained, this contraction will decrease any compressive stresses generated from the temperature rise, eventually inducing tensile stresses. The typical stress development in uniaxially restrained concrete, due to temperature variation, is illustrated in Figure 1-2 [21]. Once the developed tensile stresses exceed the tensile strength of concrete, cracking may occur [1]. Restrained stresses due to thermal changes can be calculated using Equation 1-1:

$$\sigma_t = K \cdot \alpha \cdot \Delta T \cdot \frac{E}{1+\phi} \qquad \text{Equation 1-1}$$

Where,

σ_t = restraint stress

K = level of restraint

α = concrete coefficient of thermal expansion

ΔT = change in temperature

E = elastic modulus of concrete

ϕ = creep coefficient

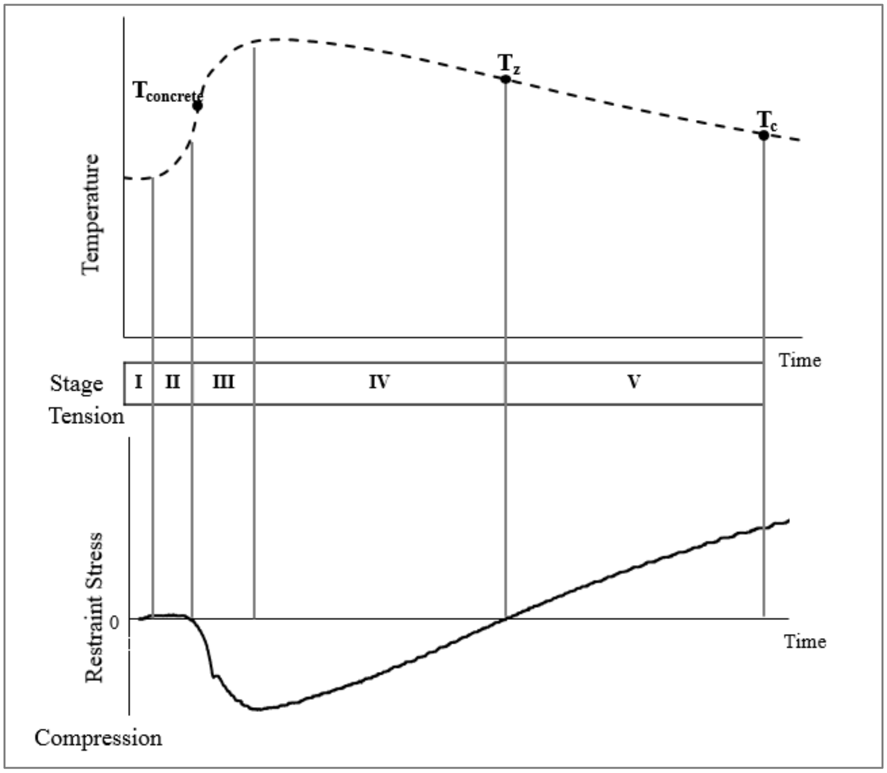

Figure 1-2: Typical temperature and stress development in restrained concrete members during hydration

Determination of the degree of restraint, K, is difficult and is a function of the ratio of local to surrounding stiffness of concrete or base conditions [22]. It is therefore likely that when the heat of hydration or moisture distribution varies spatially, restraint is created due to local differences in stiffness of the surrounding concrete [22]. During the concrete temperature rise phase, designated by phase III in Figure 1-2, restraint tensile stresses at the surface are created due to drying shrinkage or due to the expansion of the core that is restrained by the cooler outer surface that does not heat up and expand at the same rate. Surface cracks due to these stresses might close when these regions go into compression but can adversely affect durability [23]. The temperature at which the concrete goes from compression to tension is known as the second zero stress temperature (ZST). Cracking that is initiated during this cooling stage can be detrimental as it would likely not be confined locally but rather extending deeper [16],[17].

For pavements, night placements are used to offset the time of the maximum heat release from the ambient peak temperature. When the times coincide, the maximum temperature reached in the concrete will be higher. A higher peak concrete temperature also means a larger eventual temperature decrease and higher induced tensile stresses [24]. Equation 1-2 defines the maximum stress index (MSI), for continuously reinforced concrete pavements (CRCP), which describes the maximum potential stress the concrete can experience when cooled.

$$MSI = (T_{ZS} - T_{min}) * \alpha * E_c \qquad \text{Equation 1-2}$$

Where,

MSI = maximum stress index
α = concrete coefficient of thermal expansion (strain/°C),
E_c = creep adjusted Modulus of Elasticity (Pa),
T_{zs} = concrete zero-stress temperature (°C), and
T_{min} = minimum concrete temperature on the coldest winter night

The zero-stress temperature, T_{zs}, is a function of the maximum temperature and a reduction factor, which relates temperature development to stiffness. Concrete minimum temperature, T_{min}, is a function of the ambient temperature [25]. Equation 1-2 is derived from Equation 1-1, assuming a constant elastic modulus after setting, 100% restraint, and no stress relaxation.

The second zero stress temperature, derived from experimental testing using a rigid cracking frame, (phase IV), has been previously used as a metric to evaluate the relative level of tensile stresses generated and screen the suitability of different mixtures for massive concrete applications. However, recent work [26] has suggested that the effect of ZST on long-term performance of CRCPs is not as significant as previously thought and that the current models must account for early-age viscoelastic behavior of concrete.

McCullough and Rasmussen [27], modeled the early-age behavior of portland cement concrete pavement during the first 3 days. The model accounted for early stress development through incorporating the effects of temperature development due to cement heat of hydration, environmental effects, specific heat, thermal conductivity, creep, coefficient of thermal expansion, strength and elastic modulus development, restraint due to friction, and curling. HIgh PERformance PAVing software (HIPERPAV) predicts the critical stress that can lead to slab damage. Determination of critical tensile stress incorporates the following [27]:

- Models to determine strain evolution after the determination of temperature and moisture profiles. These account for axial, thermal, curling, and moisture differential-related strains
- A creep-adjusted elastic modulus.
- A restraint factor dependent on the nature of the slab-base interface or a finite element model to account for structural interactions.
- Tracking development of strength and modulus using maturity concepts to determine a stress-strength ratio.

The critical tensile stress $\sigma_{critical}$ is determined by HIPERPAV [27] using Equation 1-3:

$$\sigma_{critical} = MAX_{TENSILE} \left\{ \begin{matrix} \left(\epsilon_{axial,top} + \epsilon_{sh}\right) x\ R_F\ x\ E_{eff} + \sigma_{curl,top} \\ \epsilon_{axial,bottom}\ x\ R_F\ x\ E_{eff} + \sigma_{curl,bottom} \\ 0 \end{matrix} \right\} \tag{Equation 1-3}$$

Where,

$\sigma_{\mathrm{critical}}$ = critical stress

$\mathrm{MAX}_{\mathrm{TENSILE}}$ = maximum tensile stress

$\epsilon_{\mathrm{axial,top}}$ = strain in the axial direction of the top of the slab

ϵ_{sh} = shrinkage strain

R_{F} = restraint factor

E_{eff} = effective modulus of elasticity
$\sigma_{curl,top}$ = stress caused by the curling in the top of the slab
$\epsilon_{axial,bottom}$ = strain in the axial direction of the bottom of the slab
$\sigma_{curl,bottom}$ = stress caused by the curling in the bottom of the slab

1.3.1.1.3 Coefficient of Thermal Expansion (CTE)

The coefficient of thermal expansion (CTE) is a fundamental concrete material property [28]. Application of the rule of mixtures has been found to provide a reasonable approximation of the CTE of concrete, [29].The coefficient of thermal expansion can therefore be calculated from the volume-weighted average of the CTE of the individual concrete constituents, [30]. The concrete CTE is affected largely by the aggregate CTE due to the high volume of aggregates in concrete. The aggregate CTE is strongly influenced by the aggregate mineralogy. McCullough et al. [31] correlated the aggregate CTE with silicon oxide and calcium oxide content. They proposed a regression equation of the following form:

$$CTE_{agg} = 2.36(Na) - 0.757(A1) - 0.109(Ca) - 0.271(Fe) + 16.017 \quad \text{Equation 1-4}$$

Where,

CTE_{agg} = coefficient of thermal expansion of the aggregate
Na, Al, Ca, Fe = weight fraction of the elemental oxides

CTE of the cement paste is affected by the cement degree of hydration and moisture content [30],[32]. Typical CTE values for aggregates of different mineralogy together with cement pastes prepared with variable w/c ratios and concrete are presented in Table 1-2.

Table 1-2: Typical range of coefficient of thermal expansion of aggregates compared to cement paste (adapted from source: [33])

Coefficient of Thermal Expansion	10^{-6}/°C	10^{-6}/°F
Type of Aggregate		
Granite	7-9	4-5
Basalt	6-8	3.3-4.4
Limestone	6	3.3
Dolomite	7-10	4-5.5
Sandstone	11-12	6.1-6.7
Quartzite	11-13	6.1-7.2
Marble	4-7	2.2-4
Cement Paste (saturated)		
w/c = 0.4	18-20	10-11
w/c = 0.5	18-20	10-11
w/c = 0.6	18-20	10-11
Concrete	7.4-13	4.1-7.3

Mallela et al. [28] tested 673 core samples representing hundreds of pavement sections located throughout the United States according to AASHTO TP 60. The predominant aggregate in each test specimen was identified. The general range of portland cement concrete CTE values was between 4 and 7 x 10^{-6} in./in./°F (7.2 and 12.6 x 10^{-6} in./in./°C). The concrete made from igneous aggregates generally had a lower average CTE than concrete made from sedimentary aggregates. Typically, siliceous aggregates have a higher CTE than pure limestone aggregates. A sensitivity analysis conducted using the M-E PDG software to study the impact of concrete CTE on JPCP performance showed that pavements with chert, quartzite, and sandstone aggregates have higher cracking potential than those using limestone.

Jeong et al. [30] investigated the effect of age and moisture on concrete CTE by using laboratory testing and FE analysis. Equation 1-5 was used to calculate the CTE. The age effect was examined by observing changes in the thermal strain and temperature of the concrete over a period of time. The moisture effect was tested for up to six months by periodically moving the specimen between high and low humidity conditions. Initially high CTE values stabilized between

11 and 12 microstrain/°C, 8-10 hours after placement. The maximum value of CTE was observed at approximately 85% RH and the minimum CTE values were near 100% RH and below 50% RH.

$$\alpha_c = \frac{\Delta\varepsilon_{tot} - \Delta\varepsilon_{sh}}{\Delta T} \qquad \text{Equation 1-5}$$

Where,

α_c = CTE of concrete

$\Delta\varepsilon_{tot}$ = total strain change, including thermal and shrinkage strains

$\Delta\varepsilon_{sh}$ = shrinkage strain change

ΔT = temperature change between consecutive measurements

FE analysis results showed that the maximum tensile stress in the concrete slab increased with an increase in the CTE of concrete. The magnitude of the effect appears to be dependent on the slab length, with longer slabs showing a stronger effect of CTE on maximum tensile stress. The analysis showed that as the slab thickness decreased, the effect of the concrete CTE on stresses increased. Likewise, an increase in the base modulus increased the effect that the CTE has on the maximum tensile stress development in pavement.

1.3.1.2 Shrinkage Due to Moisture Loss

1.3.1.2.1 Autogenous Shrinkage

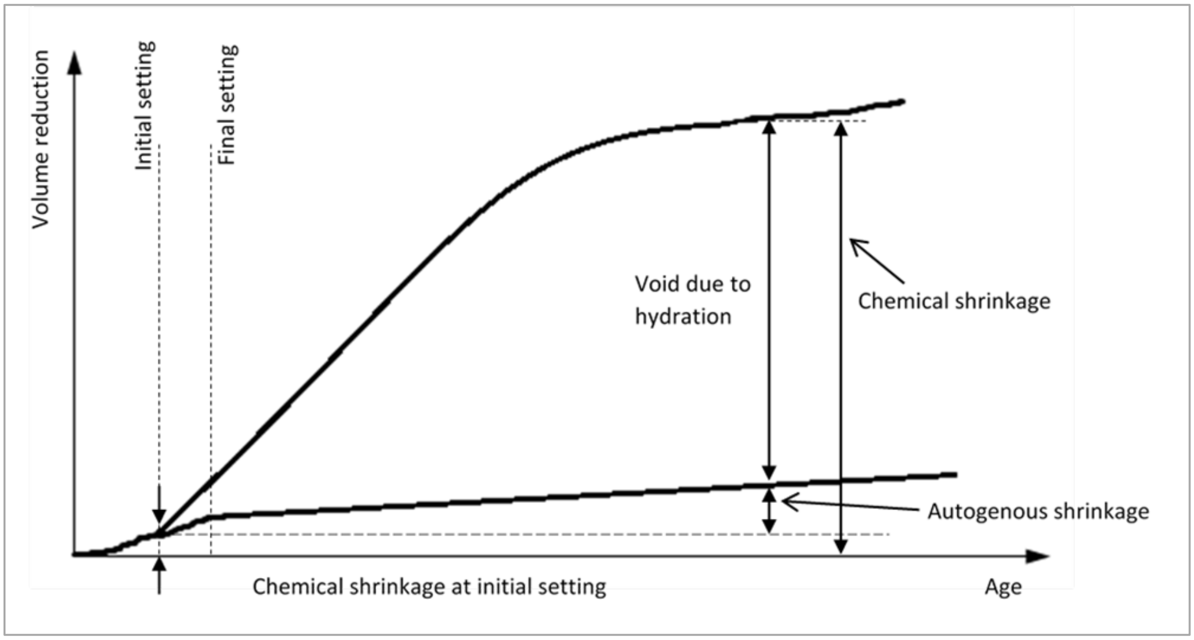

Figure 1-3: Relationship between chemical shrinkage and autogenous shrinkage [34]

Autogenous shrinkage is the macroscopic volume reduction due to chemical shrinkage in concrete as a result of cement hydration after the initial set. Chemical shrinkage is the phenomenon in which the total volume of hydration products is less than the total volume of reactants (cement and water), resulting in the emptying of previously filled capillary pores due to hydration [34]. The voiding of capillary pore space affects chemical shrinkage and hydration kinetics [35]. As hydration progresses, water needed for hydration is drawn from the adjoining saturated capillaries. The resulting capillary pressure tends to pull neighboring particles closer together, causing bulk shrinkage. The equation for saturation fraction is given by Equation 1-6 [36]:

$$S = \frac{V_{ew}}{V_p} \qquad \text{Equation 1-6}$$

Where,

V_{ew} = volume of evaporable water,

V_p = total pore volume of the paste

The Kelvin-Laplace equation shown in Equation 1-7 relates the capillary stress σ_{cap} to RH and size of pores. According to this equation, stresses increase as pore size or relative humidity decreases [35].

$$\sigma_{\mathrm{cap}} = - \frac{\ln\left(\frac{\mathrm{RH}}{100}\right) RT}{V_m} = \frac{2\gamma}{r}$$

Equation 1-7

Where,

RH = relative humidity

R = universal gas constant (8.314 J/(mol·K))

T = absolute temperature

V_m = molar volume of pore solution

γ = surface tension

r = pore meniscus radius

Concrete autogenous shrinkage strains can be calculated from the capillary stress using Equation 1-8:

$$\varepsilon = \frac{S \cdot \sigma_{cap}}{3} \cdot \left(\frac{1}{K} - \frac{1}{K_S}\right)$$

Equation 1-8

Where,

S = saturated fraction

σ_{cap} = capillary stress

K = bulk modulus of the whole porous body

K_s = bulk modulus of only the solid material of the porous body

This equation for autogenous shrinkage applies only for a saturated, linearly elastic material and does not account for creep. Lura et al. [36] attributes differences between the deformation calculated from Equation 1-8 and the measured autogenous deformation to concrete creep. Further, RH of the hydrated cementitious paste is typically lower than 100% due to the presence of alkali hydroxides in the pore solution. Any attempt to relate RH to the size of the largest filled pore, using the Kelvin-Laplace equation, should account for this drop in RH due to dissolved salts [36].

While some studies focus on capillary tension as the primary driving force relating to autogenous deformation, the role of disjoining pressure has warranted some attention as it is likely prevalent at high RH. According to disjoining pressure theory, the removal of water between opposing surfaces in the paste disrupts the overall force balance between surfaces, that would otherwise exist, due to repulsive forces in the presence of water. Removal of water could therefore cause contraction as the force balance becomes attractive [37]. Equation 1-7 can be modified to account for disjoining pressures and equilibrium of mechanical forces to obtain Equation 1-9:

$$P_c - \Pi = -\left(\frac{RT}{V_m}\right) ln\left(\frac{p}{p_s}\right) \qquad \text{Equation 1-9}$$

Where,

P_C = capillary pressure

Π = disjoining pressure

p = vapor pressure

p_s = saturation vapor pressure

1.3.1.2.2 Plastic Shrinkage

Plastic shrinkage can occur when all the bleed water at the surface of fresh concrete has evaporated. Once this occurs, water can evaporate from the concrete pores, thus inducing tensile stresses and possible cracking [38]. Ambient temperature, relative humidity, wind velocity, concrete temperature and bleeding characteristics of concrete are some of the influential factors that alter the evaporation rates of bleed water and plastic shrinkage cracking [39]. This is not thought to be a significant problem in Florida EOT repair slabs because of the short setting time [1].

1.3.1.2.3 Drying Shrinkage

Drying shrinkage of concrete is caused by evaporation of internal water in hardened concrete to the environment. The mechanism and equations governing this phenomenon are the same as those described in section 1.3.1.2.1, however the stimulus for emptying of pores and consequently shrinkage is humidity differentials between the concrete and the environment. Thus, capillary stresses are generated in the pores similar to what occurs in autogenous shrinkage, with the difference being the manner in which the relative humidity in the pores was lowered. For drying shrinkage, water loss can only occur at a concrete surface. Water that evaporates from the concrete surface is removed from adjoining capillary pores, generating capillary forces. This creates a moisture gradient between the capillaries near the surface and the interior. Water will then move from the center to the surface. This results in variations in the concrete moisture content in both space and time. This results in a non-uniform moisture distribution in the concrete cross section, which could lead to differential drying shrinkage. [40].

1.3.2 Base Restraint

Concrete movement caused by thermal expansion, autogenous shrinkage, drying shrinkage, or other forms of volume change can be restrained by the base [27]. This mechanism can be understood best by considering what occurs in the two extreme conditions of restraint [41] in concrete pavements, as shown in Figure 1-4. In the first extreme case, the slab is completely restrained from axial movement. The slab would, in this case, have zero measurable deformation or strain. This condition corresponds to a restraint factor of 1.0. The other extreme instance is that of a hypothetical slab resting on a frictionless surface where the restraint factor would be zero [42]. In this case, no stresses would be generated in the slab. The full volume change would, however, be measurable. In practice, the restraint level in jointed pavements would likely be somewhere in between these two extreme cases and is not constant along the length of the slab or width [43]. The highest restraint factor might be encountered at the center and decreases gradually as the free end is approached.

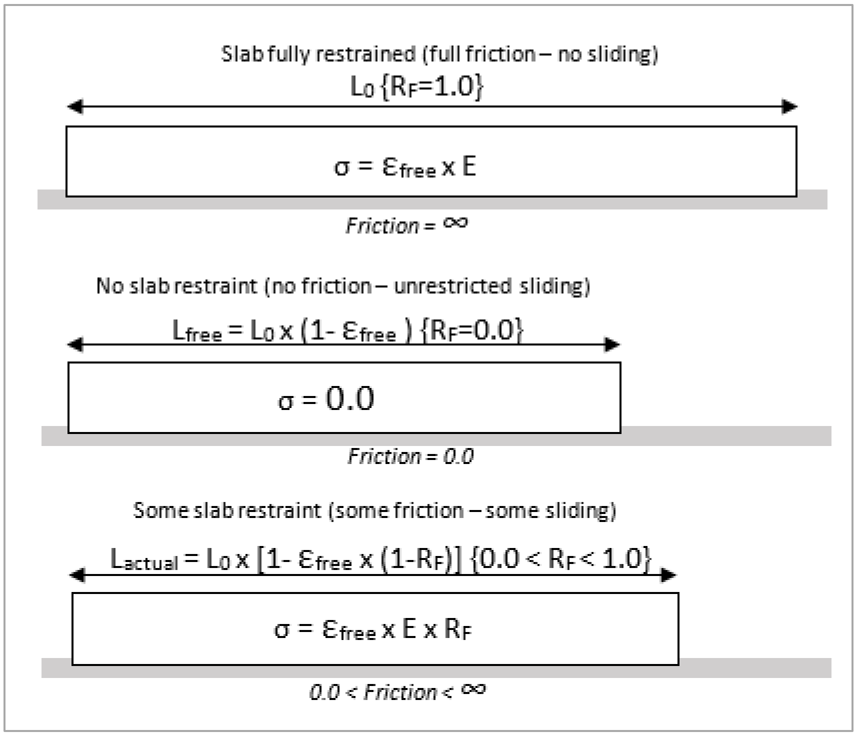

Figure 1-4: Idealized and practical axial restrain base conditions (adapted from [27])

The interaction between the slab and the base consists of adhesion, bearing, and shearing components [35],[36],[45]. The slab-base interface behavior cannot be adequately described by classical Coulomb friction theory because the behavior is also dependent on adhesion between the base and slab [44]. Adhesion is a function of the gluing action between the base and the slab and a function of the moisture condition [35],[36]. Bearing is a function of the base reaction to the force induced by the slab. This is influenced by the moisture and temperature conditions of the base. Shearing occurs when the concrete interacts with the rough base, resulting in shear stresses at the interface.

Figure 1-5 illustrates the effects of changing the base roughness and stiffness. Smoother and softer bases have lower levels of friction and restraint in the concrete pavement. A gradual decrease in the coefficient of friction of sliding occurs after movement of the slab [44]-[46]. Movement of the slab can cause aggregate particles to compact as the slab moves horizontally, decreasing interlock between the concrete and base. This can be idealized as linear-elastic behavior before sliding as shown in Figure 1-5a, with a slight decrease in the friction coefficient after sliding from the reduced interlock.

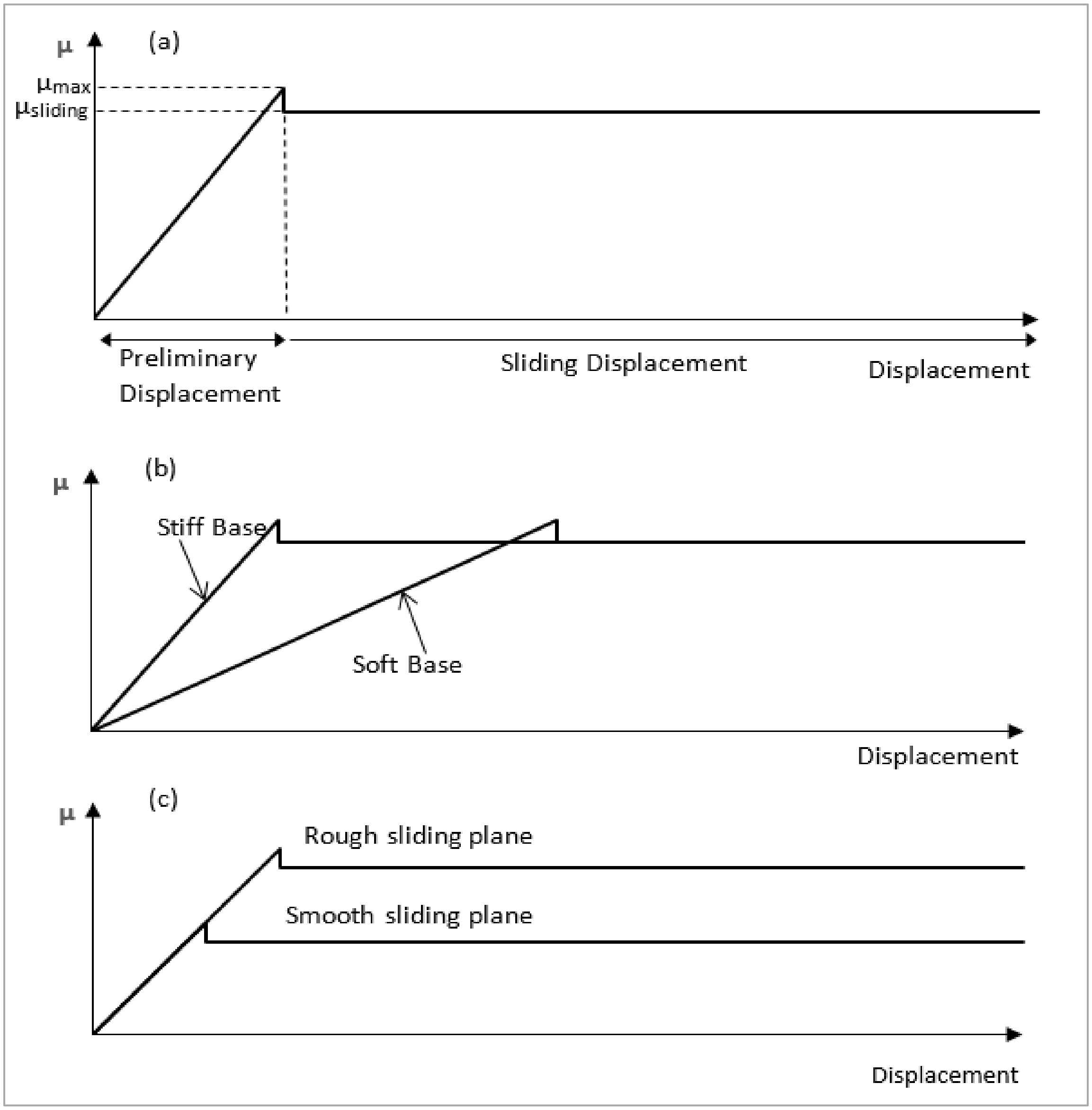

Figure 1-5: Coefficient of friction μ between concrete slab and base for (a) Linear elastic base, (b) Different base material stiffnesses, and (c) Different texture conditions (adapted from [46])

1.3.2.1 Base Restraint Modeling

The conceptual model used to quantify slab-base interface friction of a slab subjected to uniaxial restraint is shown in Figure 1-6, where it is observed that the slab displacement is highest at the free end, while restraint stresses are highest at the center of a slab. These constitute the likely boundary conditions for analysis used to determine the spatial and temporal variation of restraint stresses analytically [47], [48] or numerically [42]. The variation of thermal and shrinkage stresses with time is due to the changing environmental conditions and the progress of cement hydration. The assumptions underlying the determination of restraint stresses in modelling procedures are [47], [49]:

1. The response behavior of the slab is isotropic and linearly elastic,
2. Temperature and shrinkage strains are uniform through the depth of the slab,
3. Stresses from warping and curling are ignored,
4. The slab maintains complete contact with the base at all times (following from 3),
5. The friction force/stress displacement relationship is approximately bi-linear.

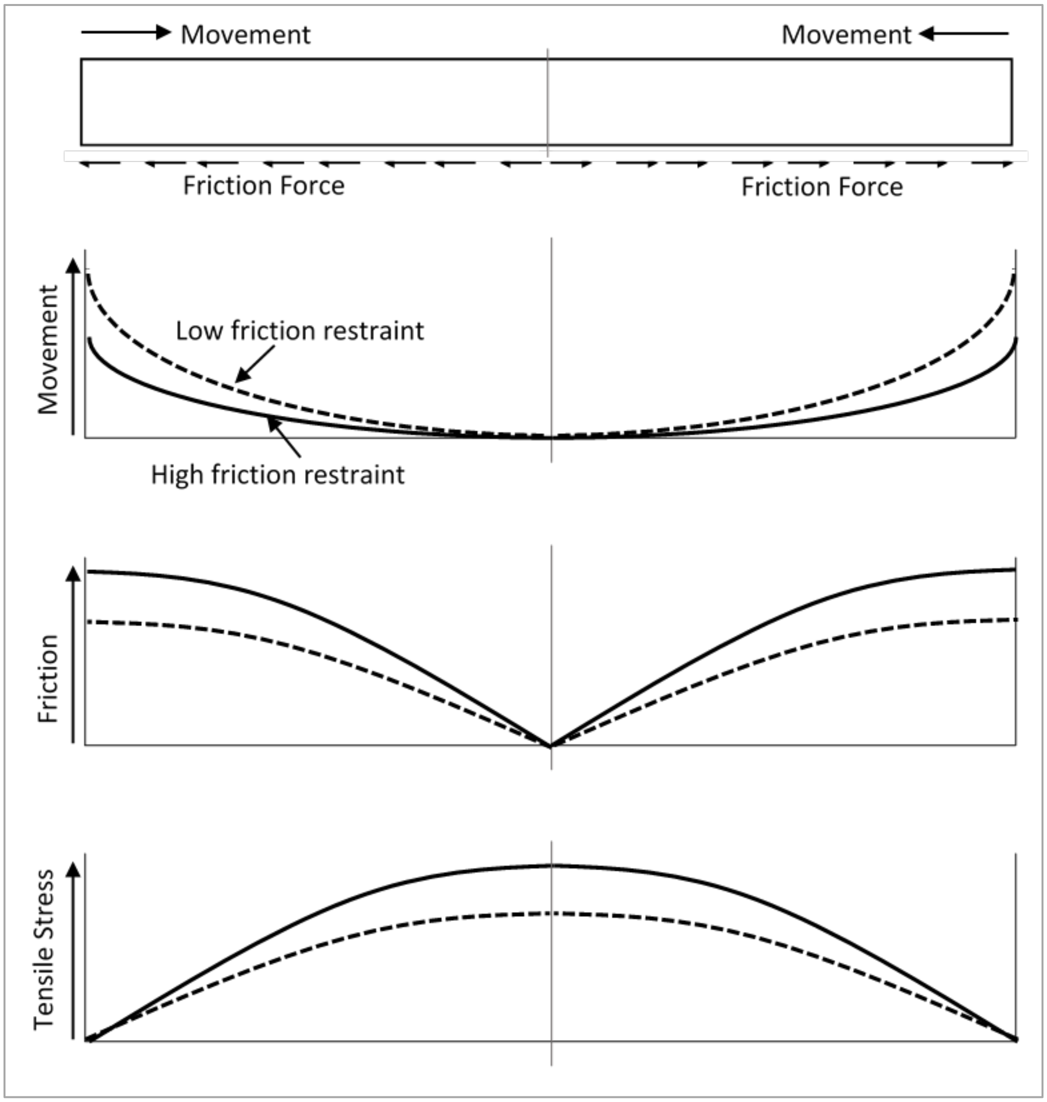

Figure 1-6: Variation of displacement, friction force, and cumulative tensile stress induced in a slab due to a temperature decrease (after [49])

Pittman and McCullough [49] describe the theory and operation of a program called "CRACK", which was developed to account for temperature and shrinkage stresses, in the determination of crack widths for controlling joint spacing in roller compacted concrete pavements. The algorithm for the program gives a general framework for computation of axial restraint stresses due to base friction. The analysis procedure is iterative and can be summarized as follows:

1. Determination of volumetric strains (incorporating the contributions from thermal changes, moisture-related changes, and restraint)

2. Determination of total movement (displacement at the free end) based on integrating volumetric strains along the half-length of the slab while exploiting symmetry
3. Determination of frictional force along the half-length of the slab based on a previously determined friction force-displacement relationship, which is characterized by the slab-base interface characteristics.
4. Determination of axial tensile or compressive stresses at different points along the length of the slab using results of (3) based on the slab dimensions.

Models developed to relate the friction between the concrete slab and sub-base to displacement typically adopt the aforementioned bilinear model [42]-[45],[50]. The bilinear model is an approximation of the parabolic function relating coefficient of friction, friction force, or shear stress developed at interface to displacement [44],[45]. These models typically ignore the effects of warping and curling on the base friction.

A description of a similar procedure is given in Rasmussen and Rozycki [42], who adopted a one-dimensional finite difference method (FDM)-based model for calculating the axial restraint stress for early-age jointed plain concrete pavements (JPCPs). The assumptions made in the analysis by this model are similar to what was described earlier for the CRACK program, and the analysis approach is identical in most respects. The cumulative displacements along the length of the slab at discrete points are determined numerically using the aforementioned FDM-based approach. The bilinear relationship used in this model relates frictional stress to displacement, as shown in Figure 1-7, which is similar to the frictional force-displacement plot shown in Figure 1-8. Some typical values of the parameters that are used to characterize frictional stress-slab displacement are shown in Table 1-3. The governing differential equation relating axial slab displacement and interfacial frictional is given below in Equation 1-10 [42], [51]:

$$\frac{d^2u}{dx^2} - \left[\frac{b}{E_C \cdot A_C}\right] \cdot \tau_f = 0 \qquad \text{Equation 1-10}$$

Here,

u = the axial displacement of the slab

b = the slab width

τ_f = the friction force per unit base area (psi or MPa)

E_c = the modulus of elasticity of concrete

A_c = the area of the pavement

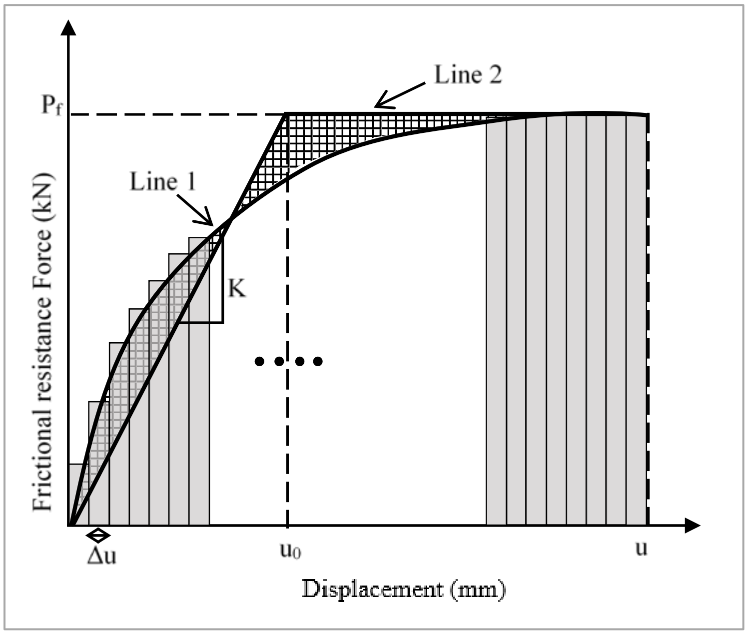

Figure 1-7: Bi-linear approximation of interface characteristics (adapted from [50])

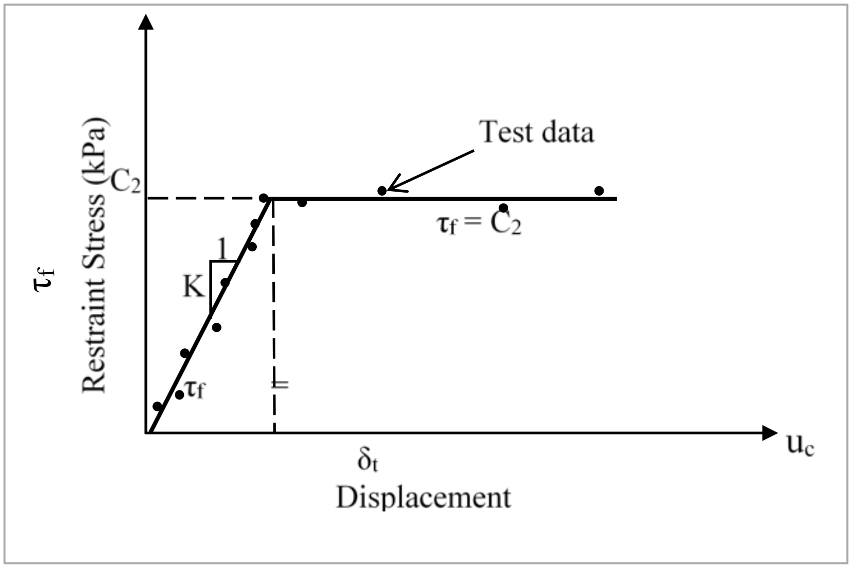

Figure 1-8: Restraint stress vs displacement (adapted from [42])

Table 1-3: Typical values of parameters characterizing bi-linear friction-displacement relationship

Base/Subbase Type	**C_2 in kPa (psi) (max. restraint)**	**δ_f in mm (in.) (displacement at sliding)**	**K_3 in kPa/mm (psi/in.) (restraint slope)**
Dense-Graded HMA (Rough)	69 (10.0)	0.25 (0.01)	270 (1000)
Dense-Graded HMA (Smooth)	35 (5.0)	0.51 (0.02)	68 (250)
Asphalt Stabilized (Rough)	103 (15.0)	0.51 (0.02)	200 (750)
Asphalt Stabilized (Smooth)	41 (6.0)	0.64 (0.025)	65 (240)
Cement Stabilized	103 (15.0)	0.025 (0.001)	4100 (15000)
Lime Treated Clay	10 (1.5)	0.76 (0.03)	14 (50)
Natural Clay	6.9 (1.0)	1.0 (0.04)	6.8 (25)
Granular	14 (2.0)	0.51 (0.02)	27 (100)

Roesler and Wang [48] proposed a base-restraint model that accounts for curling and warping behavior of the slab to model the factors contributing to joint opening. They provide an analytical closed-form solution to determine the slab displacement. For the hydrating concrete pavement slab studied, the modulus in their sample solution was taken as a function of time. Differences in modelled and measured joint openings was attributed to the inability of the model to account for reversible drying shrinkage, [48]. Lederle [52] proposed a model to predict reversible drying shrinkage, and applied it to the approach of Roesler and Wang to include reversible differential drying shrinkage.

A similar approach to that adopted by Roesler and Wang [48] for determination of stresses due to non-linear temperature gradients was used by Mohammed and Hansen, [53]. The following assumptions were used in this model:

- The slab is elastic, homogenous, and isotropic with mechanical properties that do not change based on temperature.
- Plane sections remain plane after bending.
- Stresses and strains in the z-direction are 0.
- The deflection of the slab is minimal compared to the size of the slab.
- Temperature/shrinkage strains only vary through the cross section.

With a temperature gradient, the deformation in an unrestrained slab at each location will be different because of the differential local strain. This nonhomogeneous strain causes restraining forces and stresses to be enacted on the surrounding elements. Hooke's law was used to quantify the amount of stress produced by restrained movement, which in turn allowed it to be characterized into moments (M) and normal forces (N) that are solely dependent on temperature gradation. Equilibrium in the slab is reached by using equal and opposite M and N to determine the internal restraint. Slab curvature can create additional stresses.

External restraint calculation can be made easier by using an equivalent linear temperature gradient. The stress in a pavement with a nonlinear temperature profile can be solved using the following steps:

1. Obtain a strain distribution in the z-axis
2. Determine the axial force and moment values
3. Calculate residual stress
4. Calculate an equivalent linear temperature gradient
5. Calculate the stresses due to the temperature gradient
6. Add stress from residual stress and temperature gradient

1.3.2.2 Experimental Determination of Pavement Friction

Push-off tests can be used to quantify the friction at the interface between a pavement and its base. A bilinear model is typically used to model push-off test results. A schematic of the test procedure is given in Figure 1-9. The setup consists of a slab placed on a base with a hydraulic jack that is used to apply a horizontal load on the slab. The slab displacement is measured using dial gauges positioned on the free end. The Texas test method includes a procedure conducted on a slab with dimensions of 4 ft x 8 ft [42] where displacement measurements are made at load increments of 0.5 kip (500 lb) to calculated stresses. An alternative field-testing version of this test has been developed on a slab with smaller dimensions. The Federal Highway Administration (FHWA) Mobile Concrete Laboratory (MCL) has used the field-testing version of the push-off test. In this method, four displacement transducers set at two heights are placed on the side of the slab. On the opposite side of the slab, a steel beam is situated to distribute the applied load. A hydraulic jack and a load cell are then positioned and a bulldozer or other piece of construction equipment is used to apply the load. Once the hydraulic jack and load cell are seated, the load is applied in 0.5-kip (500 lb) increments while slab displacements are read on the four transducers. The load is applied until the slab achieves sliding. The result is the minimum load necessary (corresponding to critical restraint stress) to continuously move the test slab across the base layer without stopping.

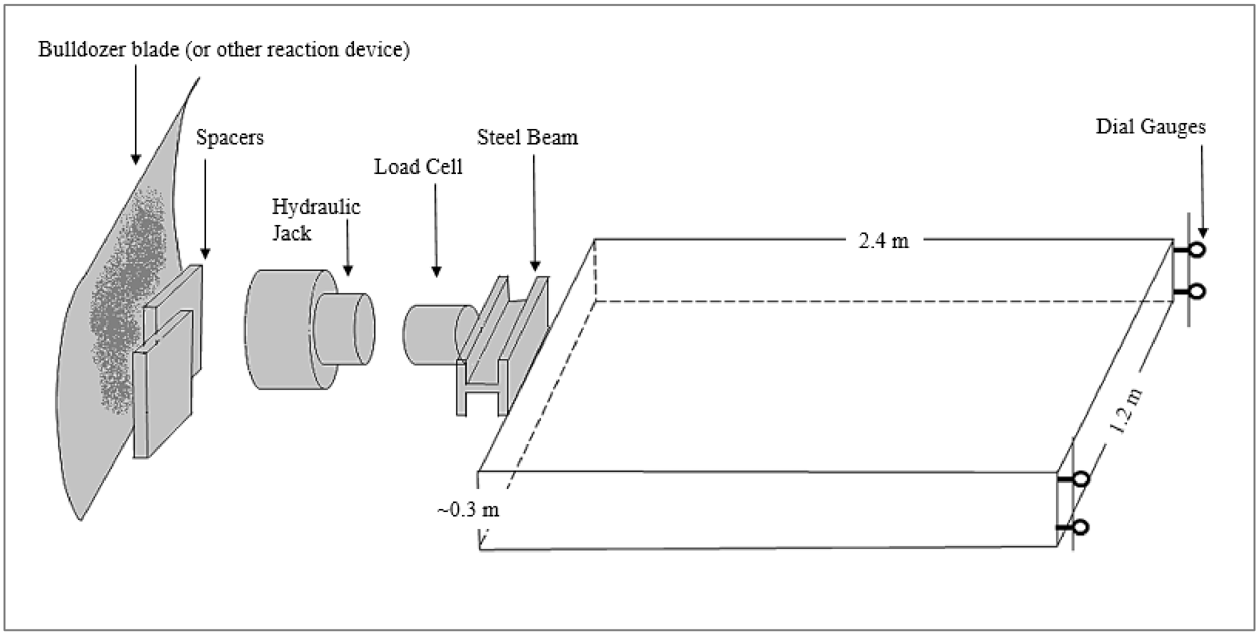

Figure 1-9: Schematic for the push-off test (adapted from [42])

1.3.3 Stress Relaxation

Creep and stress relaxation effects are significant during the concrete early-age period. When concrete is subjected to a constant load, elastic and plastic strain components occur. When the load is removed, the elastic strain is fully recovered, but not the plastic strain. This viscous behavior is known as creep [18]. On the other hand, when concrete is subjected to a constant strain, stress relaxation occurs. Concrete stress relaxation potential is higher at early ages and decreases with continued hydration. The typical creep/relaxation effect due to temperature loading is illustrated in Figure 1-10. After the concrete is placed, the concrete temperature increases as a result of heat of hydration as explained in section 1.3.1.1.1. Concrete develops strength after setting. Thermal expansion while axial movement is restrained results in the development of compressive stresses. Creep may cause some relaxation of stress. In the cooling period, the concrete begins to contract. Due to the continued relaxation and temperature decrease, the concrete compressive stresses decrease and eventually tensile stresses may occur. When these developed tensile stresses exceed the tensile strength of concrete cracking occurs [18].

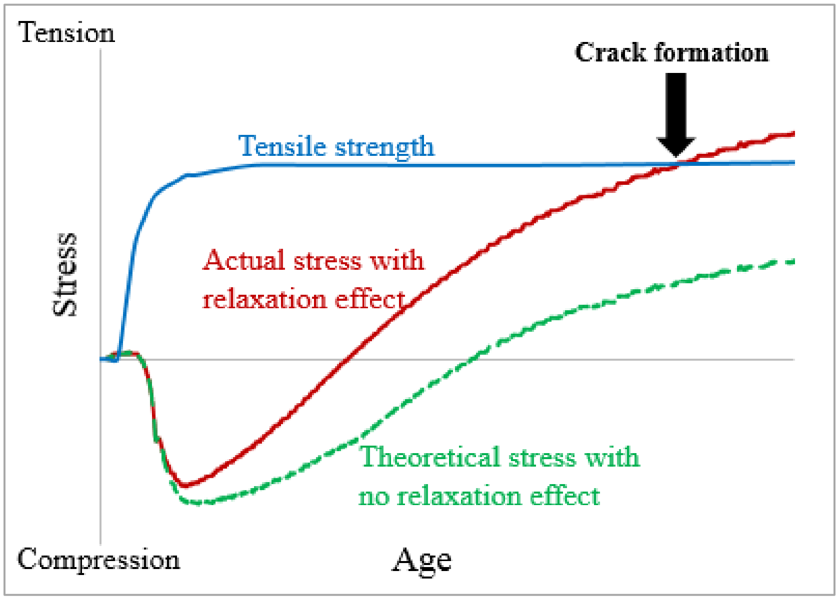

Figure 1-10: Stress development in concrete member without and after accounting for relaxation

1.4 Early-Age Cracking Mitigation Measures

Measures need to be taken to minimize volumetric changes and any resulting cracking due to thermal and moisture gradients, and dimensional changes that occur in concrete at early ages. These methods include mixture optimization by reduction of paste volume (by use of chemical admixtures and/or improved aggregate packing density by gradation optimization), use of shrinkage reducing admixtures, use of fibers to increase tensile strength, internal curing, and reduction of base friction.

1.4.1 Optimal Mix Design

Early-age autogenous shrinkage, drying shrinkage, and heat of hydration in concrete pavements originate in the paste fraction of the concrete. Mixture optimization methods could prove useful in maintaining high early strengths while reducing paste content, and is an objective of this research.

1.4.1.1 Optimizing Combined Aggregate Gradation

Dimensional changes caused by autogenous and drying shrinkage are attributed to the behavior of the paste fraction [41]. Volumetric variations related to temperature changes are also a function of the cement hydration reaction and consequently the paste volume contained in the mix. A reduction in paste content can result in lower early-age volume change, stress, and consequently the cracking probability. A reduction in paste volume through various means is an objective for improving the early-age performance of EOT concrete mixes. The paste fraction of concrete is used to a) bind aggregates, b) fill voids between coarse and fine aggregates, and c) ensure adequate workability for placement. The following section describes different techniques to optimize the combined particle gradation in concrete.

1.4.1.1.1 Continuous Grading Curves and Empirical Methods for Determining Aggregate Gradation

Several aggregate optimization methods have been developed to help increase aggregate volume percentage and decrease concrete paste content, while still maintaining adequate concrete workability. These methods include:

1. Use of the Fuller curve or the 0.45 power chart [54].
2. Use of the Shilstone workability chart [55].
3. Placing limits on the percent retained on selected sieves. This includes the 8-18 method and tarantula curve method [56], [57], [58].
4. Use of theoretical packing models to achieve an optimized gradation. This approach is more popular in Europe [59], [60], [61].

Ideal gradation curves such as the Fuller curve are based on a relationship between particle size distribution and particle diameter of the form:

$$P(d) = \left(\frac{d}{d_{max}}\right)^{q} \qquad \text{Equation 1-11}$$

Where,

$P(d)$ = particle size distribution function

d = particle size diameter being considered

d_{max} = maximum size particle

q = an exponential term whose value for the fuller curve is 0.5 to obtain a distribution that yields the greatest density

Modifications to '*q*' have been suggested and adopted by different authors through experimental methods. Reported q values vary based on particle characteristics, such as shape and texture, and range between 0.33-0.5 [62] and 0.45-0.7 [63]. The influence of particle shape and texture is important as it influences the degree of interlocking between particles during placement, and the bond between the paste and aggregate when hardened.

Shilstone defined two parameters, the coarseness factor (CF) and the workability factor (WF), Equation 1-12 and Equation 1-13, to help identify useful initial concrete particle size distributions [63]:

$$CF = \frac{R_{9.35}}{R_{2.36}} \quad \text{Equation 1-12}$$

$$\mathrm{WF} = \mathrm{P}_{2.36} + 0.045\,(\mathrm{C} - 335) \quad \text{Equation 1-13}$$

Where,

CF = coarseness factor

WF = workability factor

$R_{2.36}$ = cumulative percentage of material retained on the 2.36-mm (#8) sieve

$R_{9.35}$ = cumulative percentage of material retained on the 9.35-mm sieve (3/8”) sieve

C = cement content in kg/m^3

$P_{2.36}$ = percentage of material passing 2.36-mm (#8) sieve.

The Shilstone workability chart is based on plotting WF (y-axis) against CF (x-axis).The origins of the Shilstone workability chart are traced to analyses conducted in order to determine the cause of premature failure in concrete pavement, for which the cause was attributed in part to the absence of sufficient intermediate-sized aggregate between 9.35 and 2.33 mm [64]. This approach is strictly empirical, although it has been successfully applied to diagnose workability problems for some slabs-on-grade.

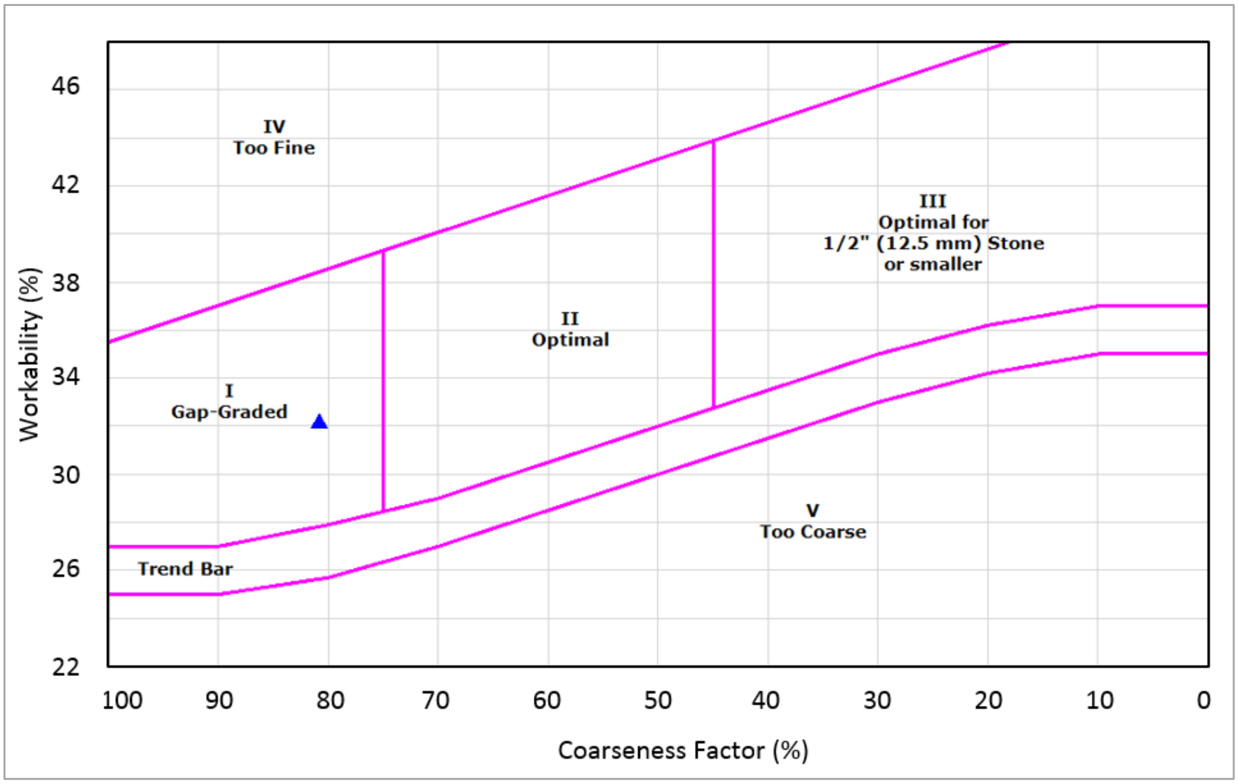

Figure 1-11: Shilstone workability chart (courtesy: Transtec Group)

Figure 1-11 is divided into distinct regions based on desirability of combined aggregate gradation and the likely effect the gradation has on workability:

- Zone I: "Gap-graded" mixtures which have a tendency to segregate
- Zone II: “Optimal” for mixtures with well-graded coarse aggregate, 38 to 13 mm (1-1/2 to 1/2 in.)
- Zone III: “Optimal” for mixtures with smaller coarse aggregate - 13 mm (1/2 in.) and finer
- Zone IV: “Too Fine” – aggregate distribution too fine, resulting in a “sticky” mixture
- Zone V: “Too Coarse” – aggregate distribution too coarse, resulting in a “rocky” mixture

The 8-18 retained chart, also called the haystack plot, sets limits on aggregate percentage retained for each sieve above the No. 30 sieve and one sieve size below the maximum aggregate size, to be between 8% and 18 % [56]. Recently [58], [65] , a modification of the 8-18 retained chart, called the ‘tarantula curve,’ was made to address workability concerns related to aggregate gradation. The tarantula curve was developed from the evaluation of over 300 different concrete mixtures.

A two-phase study by NRMCA [56] investigated the effect of the gradation, as defined by the location of the combined gradation in Zone II of the Shilstone chart, and the sieve size distribution. Aggregate gradations were kept within the optimal region defined by the 8-18 retained chart. The study compared the well-graded (Zone II) and the gap-graded (Zone I) zones. The results indicate that void content did not appear to be related to gradation as evaluated using Shilstone and 8-18 retained charts. The workability results seemed to show a similar trend in that the slumps of well-graded and poorly graded mixes did not show significant differences. However, it was determined the charts were successful in diagnosing and improving segregation resistance. Mixes having combined aggregate gradations in Zone II (classified as well-graded mixes) showed higher segregation resistance. This suggests that the greatest utility of the Shilstone workability chart and 8-18 retained charts is most likely as a qualitative check on combined aggregate gradations to prevent segregation, and fine tuning of gradations for pavement concrete [56], [66].

1.4.1.1.2 Particle Packing

Improvement made in the packing of materials, through the use of enhanced particle packing (space filling) methods, has application in many areas such as design of packed beds, ceramics, and metallurgy [60]. As applied to concrete technology, the determination and optimization of packing of aggregates could potentially be used to optimize packing in combined aggregate gradations to reduce voids. This would result in an improvement in strength and workability as a consequence of less paste needed to fill the void space and to coat the aggregate [67]. Packing density maybe defined mathematically as the ratio of solid volume to total volume.

The packing density can be calculated using Equation 1-14 or alternatively using the specific volume *v* in Equation 1-15:

$$\phi = 1 - \varepsilon \qquad \text{Equation 1-14}$$

Where,

ϕ = packing density

ε = porosity

$$\phi = \frac{1}{v} \qquad \text{Equation 1-15}$$

Where,

ν = specific volume of solids

Ideal packing, for spherically shaped particles in applications such as packed beds, was first described by Furnas (1929). The model considered packing of a binary mix. A binary mix is a mixture consisting of mono-sized spheres of coarse and fine sizes with diameters d_1 and d_2, and volume fractions y_1 and y_2, respectively.

More generally, the volume fraction of the ith component can be represented by:

$$Y_i = \frac{\left(\frac{m_i}{p_i}\right)}{\sum\left(m_i * p_i\right)} \qquad \text{Equation 1-16}$$

Where,

Y_i = Volume Fraction

m_i = mass of the ith constituent

p_i = specific gravity of the ith constituent

The two cases considered by Furnas were [68]:

1. The volume fraction of the fine particles is large
2. The volume fraction of the coarse particles is large

For Case 1, the packing density is given by Equation 1-17:

$$\phi = \frac{1}{\frac{y_1}{\phi_1} + y_2} \qquad \text{Equation 1-17}$$

For Case 2, the packing density is given by Equation 1-18:

$$\phi = \frac{\phi_2}{y_2} \qquad \text{Equation 1-18}$$

Where,

ϕ_1 = packing density of the fine particle fraction

ϕ_2 = packing density of the coarse particle fraction

y_1 = volume fraction of fine particles

y_2 = volume fraction of coarse particles

This follows from the observation that the small particles, if their size is sufficiently smaller than the coarse particles, would fill-in the interstitial space between coarser particles. In both instances, the packing density is larger than the individual packing densities of the independent systems consisting of coarse and fine particles. However, as noted earlier, for Furnas' model to be applicable, the condition $d_1 >> d_2$ has to be satisfied.

The Toufar packing model is based on the assumption that smaller particles having d_1 / d_2 ratio higher than 0.22 are too large to be situated in the interstices of the large particles [60], [61]. Thus a binary mix of monosized coarse and fine fractions consists of larger particles distributed discretely in a matrix of small particles [61]. The general packing density equation is of the form shown in Equation 1-19 [68]:

$$\phi = \frac{1}{\frac{y_1}{\phi_1} + y_2 + z \cdot \left\{ \frac{1}{\phi_2} - 1 \right\}}$$

Equation 1-19

Where,

z = correction for void space created by the volume of larger particles which are not densely packed and not distributed in a matrix of smaller particles

The parameter z is function of the diameter ratio and volume fraction of coarser particles. An estimation of z in the Toufar model considers the statistical probability of the coarser particles not being present in the fine particle matrix to obtain the following relationship for packing density in binary mixtures [68],[61] :

$$\phi = \frac{1}{\frac{y_1}{\phi_1} + \frac{y_2}{\phi_2} + y_2 \cdot \left\{ \frac{1}{\phi_2} - 1 \right\} \cdot \frac{d_1 - d_2}{d_1 + d_2} \cdot \left\{ 1 - \frac{1 + 4 \cdot \frac{y_1}{y_2} \cdot \frac{\phi_2}{\phi_1 \cdot (1 - \phi_2)}}{\left(1 + \frac{y_1}{y_2} \cdot \frac{\phi_2}{\phi_1 \cdot (1 - \phi_2)} \right)} \right\}}$$

Equation 1-20

Where,

ϕ = effective packing density of the binary mix

d_1 = diameter of the fine particles

d_2 = diameter of the coarse particles

ϕ_2 = packing densities of the coarse fractions

ϕ_1 = packing densities of the fine fractions

The assumptions made by the original Toufar model are [60]:

1) The aggregates are perfectly spherical
2) Aggregates are monosized
3) Fine and coarse aggregates have different sizes.

Assumptions (1) and (2) are problematic, as coarse and fine aggregates used in concrete are multi-component systems with a large range of particle sizes. In order to overcome deficiencies resulting from these assumptions, a characteristic diameter for each system (of each fine or coarse aggregate gradation being blended) is used [60], [68]. In theoretical packing models, most crushed materials are assumed, based on experimental studies [60], to follow a Rosin-Rammler-Sperling-Bennett (RRSB) distribution. The RRSB distribution is given by [60]:

$$R(d) = \exp\left(-\left(\frac{d}{d'}\right)^{n}\right) \qquad \text{Equation 1-21}$$

Where,

$R(d)$= cumulative probability that the diameter is less than d

d = diameter of the particle

d' = characteristics diameter for which the value of $R(d)$ is either 36.8 or 50

n = a parameter whose value is typically between 2 and 3

The characteristic diameter is defined by Goltermann et al. [60] as the diameter corresponding to a 36% residue, or particle size diameter corresponding to 36% cumulative retained on the RRSB distribution chart. The use of a characteristic diameter, termed eigen packing [60], is considered to be sufficient to overcome deficiencies of the original Toufar model assumptions. Thus, a characteristic diameter might be obtained for a coarse or fine aggregate gradation using a log-log RRSB distribution chart. However, with overlapping fractions, it is likely that the packing density would be overestimated with the use of the packing method [68].

After having obtained the individual packing densities of concrete particles, optimization of packing density using binary systems typically involves plotting the packing density of the combined system as a function of fine aggregate percentage (by mass or volume) or fine-to-coarse aggregate ratio as shown in Figure 1-12.

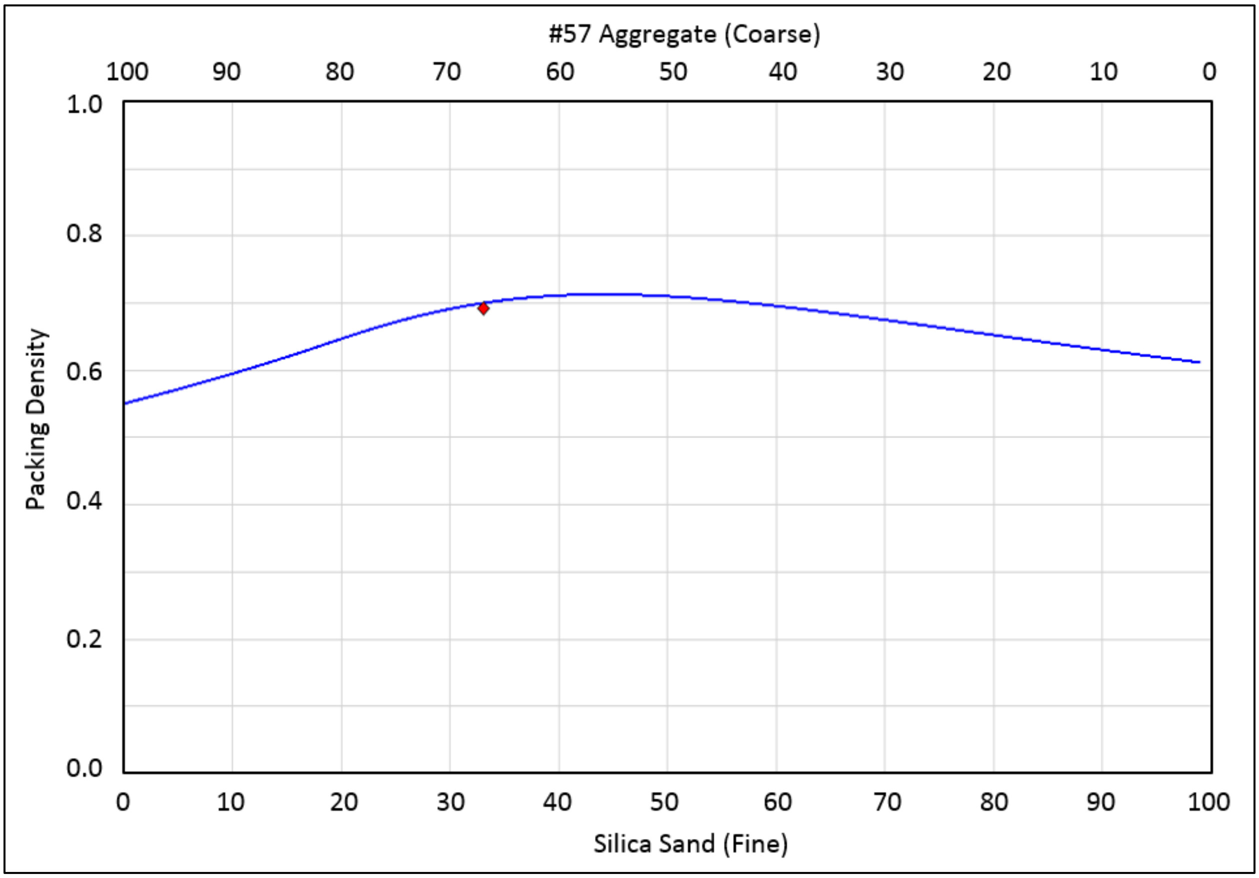

Figure 1-12: Typical plot of packing density vs. fine aggregate content (by mass) (courtesy: Transtec Group)

If the objective is to compute the packing densities in a system that has more than two constituents such as an intermediate aggregate, a ternary chart might be used. This is obtained by using a similar method to the one described previously for binary systems, except that the packing density calculations would have to be performed for two multiparticle systems at a time and continued stepwise until all systems have been included. The sequence in which these are performed is determined by the highest fine/coarse diameter ratio of the constituents [69].

The Toufar packing model has been found to adequately predict the packing density and void space, making it a potential candidate for HES mixtures [63],[70]. Jones et al. [70] studied the theoretical and experimentally-determined packing densities of combined aggregates using different models. The Toufar model was found to predict accurately the packing densities of the combined aggregates. Goltermann et al. [60] conducted experimental trials on 2 types of coarse and fine aggregates and found the packing densities predicted by the Toufar model to be within 3% of the experimentally determined packing degree.

1.4.1.2 Mixture Proportioning Protocols for Optimization of Paste Content

An objective of the literature survey in this section was the identification of a mix design protocol that would aid in reducing the current cement factors used in typical Florida high-early-strength mixtures, which can range between 850-1020 (lb/yd^3). Previous attempts at formalizing the use of packing theories discussed in 1.4.1.1 for the mix design of JPCP pavements in the US include "A Guide to Optimal Combined Aggregate Gradation" (SHRP C334) [61] and the "Concrete Components Handbook" (SHRP C624) [71], which seek to address purported deficiencies in the conventional procedures for proportioning and selection of combined aggregates (coarse and fine fractions) to attain optimal gradation. The reports consist of a series of packing density tables for binary and ternary aggregate combinations which were derived for commonly used coarse, fine and intermediate gradations. Packing densities for aggregate combinations were computed based on a model that combined Toufar and Aim packing models. The suggested mix design procedure involves the following steps:

1. Determination of characteristic diameter for fine and coarse fractions based on RRSB sieve size distribution chart.
2. Experimental determination of individual packing densities of sand and coarse aggregate fractions.
3. Determine the optimal combination of aggregates of each system corresponding to the desired or highest possible packing density.

Mixture proportioning methods that are used to optimize the paste fraction of Self Consolidating Concretes (SCC) can be borrowed for other concrete types and might therefore be of particular interest. These methods might be also instructive because just as in the mix design of HES concrete, reduction in paste content is desirable. Similar to HES mixes, there is likely a lower bound on the paste content required to attain the necessary properties [72]. Koehler [73] details a set of methods adopted to design SCC mixes. Many of these methods explicitly consider some function of the relationship between the required paste and either experimentally determined or theoretically calculated void volume. The paste-to-void volume ratio [67] or aggregate-void saturation ratio ([74]) are used as parameters in the mixture proportioning process.

The paste-to-void volume concept proposed by Yurdakul et al [59] offers a simple proportioning method to quantify any improvement in reduction in paste content made with the use of packing theories for combined aggregate gradation [59]. The mix design procedure, which is currently used by the Iowa DOT for concrete pavement mixes is of particular interest. It consists of the following steps:

- Select the combined aggregate gradation based on 8-18 retained, Shilstone and 0.45 power charts
- Select the paste-to-void volume ratio
- Make trial batches to obtain optimal properties

This method has the following advantages [67]:

- Since the paste volume is selected after optimizing the aggregate gradation, the paste content can be adjusted according to necessary requirements.
- This method could allow for the determination of an optimal paste volume beyond which increasing the cement content would likely not aid the development of mechanical properties.

Yurdakul et al. [67] attempted to determine the paste-to-void volume ratio thresholds by relating normalized contributions of cementitious material content to the gain of mechanical or plastic properties through the use of a parameter called cementing efficiency. The study tested 64 mixes for hardened and plastic properties of paving concrete. Although the range of cement factors (400-700 lb/yd^3) was lower than that encountered for HES mixes, the proportioning method adopted and the overall approach of relating paste volume to properties of the mix is of interest. The study found that paste-to-void volume ratios of 1.25-1.5 were optimal for 28-day compressive strength and 1.5-1.75 were optimal for slump. The study observed that beyond the 1.75 paste-to-void volume ratios, the performance of the mixes, based on transport properties as measured by air permeability and chloride penetration, were adversely affected. In a similar study for the Indiana Department of Transportation (INDOT), Rudy and Olek [72] suggested the use of paste contents in the range of 23 to 26% for paving mixes. However, they also observed that typical paste-to-void volume ratio thresholds adopted for conventional paving mixes may not be directly applicable for HES paving mixes [75]. Studies point to a steeper increase in early-age compressive stress with higher paste contents, which is likely related to the higher temperatures attained during curing due to higher cement content [76],[75]. Notwithstanding the arguments against direct applicability of paste-to-void thresholds of conventional paving mixes to HES mixes, it might be useful to quantify what the paste-to-void volume ratio would be for a typical Florida EOT mix to determine whether the potential for paste reduction exists. A standard mix from a previous study conducted at USF [1] was used for this purpose. Since information on void volume of the combined coarse and fine aggregate combination was not available, a mix design suite called "COMPASS" [77] was used to estimate packing density using the built-in Toufar model option. The software requires sieve size distribution data for fine and coarse fractions, specific gravities, and other properties as inputs to calculate the packing density of the combined aggregate gradation. After calculating the void volume from the packing density, the paste-to-void volume corresponding to the paste volume for the mix was calculated. The results are shown in Table 1-4 (along with computations made from the mix used for validation).

Table 1-4: Paste-to-void volume ratio calculated for mix from 2 studies

Mix	**Void Volume**	**Cement Factor at Vp/Vv =1 (lb/yd^3)**	**Cement Factor for Mixture (lb/yd^3)**	**Vp/Vv**
Mix 1 from [67]	0.198	400	400	1.00
Slab Mix 1 from [1]	0.302*	688	900	2.2

*Computed based on Toufar Model using COMPASS

As shown in Table 1-4, the paste-to-void volume ratio obtained for Slab Mix 1 from [1]was 2.2, which was close to the paste-to-void volume values adopted for self-consolidating concrete in [78].

1.4.2 Fiber-Reinforced Concrete

Cracking potential can be improved by increasing the concrete tensile capacity and by reducing restrained stresses. Fiber reinforced concrete could be used to attain high-early-compressive and -tensile strengths, and to ensure crack control. The increase in early strength is attributed to the confining effect of fibers [79]. The use of fibers in high-early-strength pavement, based on studies by DOTs in Michigan and Florida, appears to be somewhat promising. MDOT [80] evaluated the use of cellulose and polypropylene fibers in HES concrete mixes intended for rapid repair of pavement to control microcracking. They also saw an increase in early-age strength gain with their use, which could potentially be used to reduce the mixture cement factor. A normal strength (NS) concrete mixture, a plain HES mixture, and mixtures incorporating polypropylene fibers at 0.9 kg/m^3 and cellulose fibers at 1.2 kg/m^3 were used. Compressive and flexural strength tests were conducted at 4, 6, and 8 hours to assess the early-age development of mechanical properties. Restrained ring experiments were conducted to evaluate the effect of the addition of cellulose fibers on controlling crack widths. The mix incorporating cellulose fiber outperformed the control and the polypropylene fiber mix in all of the testing. Based on these results, a new mix, using cellulose fiber with a reduced cement content and accelerator dosage, was selected for placement. Companion beams were cast for testing the flexural strength for comparison with a plain HES mixture. The HES mix with cellulose fibers was found to have higher flexural strength at early ages [41].

Banthia et al. [81] evaluated the effectiveness of cellulose fibers in preventing shrinkage due to hygrothermal effects in concrete slabs in controlled environmental conditions (47°C and 5% RH). The expectation was that curling deflections would decrease with incorporation of these fibers at 3 dosages, with the level of curling decreasing with the level of dosage. In this study, a w/c ratio of 0.458 with a relatively high cement content of 480 kg/ m^3 (809 lb/yd^3) was used. Fiber contents were varied at 1.2, 2.4 and 3.6 kg/m^3 (volume fractions of 0.1, 0.2, and 0.3%). The inclusion of fibers was effective in reducing the shrinkage strains. An additional advantage of these fibers is that they have been shown to have an internal curing effect that reduces shrinkage. There are, however, concerns with the use of cellulose fibers. These concerns are:

1. Cellulose fibers are not durable in alkaline conditions [82]. Given their presence in the cement paste matrix, which is highly alkaline, their degradation would likely affect their performance in concrete. As early as 2002, a standard for evaluating the stability of these fibers for their use in fiber reinforced concrete was released (ASTM D735). Some proprietary fibers are known to be more resilient in service [82].
2. Cellulose fibers are hydrophilic in nature [83].

3. Other studies appear to indicate that the effect of cellulose fiber addition is not the same across the whole family of fibers. Retardation of hydration has been noted with some h-cellulose fibers [84]. This is significant because, as has been noted earlier, these fibers are used to reduce the cement content and accelerator dosages without compromising early-age strength.

Suksawang and Mirmiran [79] evaluated the use of fiber reinforced concrete for HES pavement for EOT applications. Mixes incorporating 9 distinct fiber types were evaluated for early-age hardened properties. Their use was found to increase early-age flexural and compressive strength of all mixes incorporating fibers. The use of fibrillated fibers was found to be particularly helpful in the gain of early-age strength.

1.4.3 Internal Curing

Conventional concrete is typically cured using external methods to primarily prevent evaporation and water loss to the environment, and supply some additional water for hydration near the exposed surface. External curing is difficult for EOT concrete pavements. Wet external curing is not possible and curing compound is rapidly removed once traffic is opened. Internal curing is a recently developed technique to prolong cement hydration by providing internal water reservoirs in the concrete, and could be a good method of providing curing for EOT concrete pavements.

High performance concrete mixtures were developed as a means of enhancing durability and are created using lower water-to-cementitious materials (w/cm) ratios, chemical admixtures, and supplementary cementitious materials (SCMs). Low w/cm ratios used in HES mixtures often do not provide enough water to fully hydrate the cement in the mixture. Hydration could be improved and autogenous shrinkage could be minimized by the use of internal curing [85].

Internal curing can be provided by highly absorptive materials that will desorb water into the cement pore structure after setting. Materials such as lightweight aggregate (LWA), super absorbent polymers (SAP), perlite, and wood pulp can be used in this process. LWA contribute to the structural capacity of the concrete mixture, while some SAP, perlite, and wood pulp do not [85].

1.4.3.1 Lightweight Aggregates (LWA)

Bentur et al. [86] tested high performance concrete (HPC) mixes incorporating silica fume at 0.33 water-to-binder (w/b) ratio to study autogenous deformation in restrained and unrestrained conditions using varying proportions of lightweight aggregate (LWA). The moisture state of the LWA was varied through the use of LWA aggregates in pre-soaked, air dry, and partial LWA replacement concrete. Use of lightweight aggregate was found to significantly reduce the shrinkage of concrete. Although the amount of water present in the aggregate had an impact on the shrinkage, at 28 days, there was roughly no difference between the strengths.

Cusson et al. [87] attempted to identify the amount of wet lightweight aggregate required as an internal source of water to counteract self-desiccation and the development of stresses in restrained conditions. To investigate the effect of initial water conditions and content of lightweight aggregate on the autogenous shrinkage of high-strength concrete, four high-performance concrete mixes with w/c of 0.34 were tested. Restrained autogenous shrinkage and free autogenous shrinkage tests were conducted for lightweight aggregate concretes in wet and air-dry states. Autogenous shrinkage was completely prevented in the lightweight concrete with wet aggregate. The tensile stresses induced in the lightweight concrete were considerably lower than in the normal-weight concrete mixture.

Henkensiefken et al. [88] studied the behavior of internally cured mixtures made with presoaked lightweight aggregate under sealed and unsealed conditions. The mix design used Type I portland cement, water, sand, two lightweight aggregates, and a high-range water-reducing admixture. The water and cement used were constant throughout the experiment with a w/c of 0.3. The sand was replaced with increasing amounts of prewetted lightweight aggregate (PLWA). The sand and lightweight aggregate together made up 55% of the mixture by volume. The relative humidity of all specimens decreased with time, but the mixes with greater replacement of PLWA decreased less than the mixes with lower replacement of PLWA. The higher relative humidity indicates the larger pore sizes remained saturated, thereby reducing the capillary stress.

1.4.3.2 Superabsorbent Polymers (SAP)

Shen et al. [89] studied the effect of superabsorbent polymers (SAP) on autogenous shrinkage in early-age concrete. Increased dosages of SAP increased the time of setting. The compressive strength was found to be lower for mixes with greater amounts of SAP because the SAP, when swollen with water, did not contribute to strength. The concrete with SAP expanded more than normal concrete after setting. The concrete with SAP experienced less autogenous shrinkage than regular concrete. The rate and ultimate amount of autogenous shrinkage decreased with the incorporation of SAP.

Craeye et al. [90] attempted to find an optimum dosage where the autogenous shrinkage reduction was as high as possible and the strength reduction as low as possible, using super absorbing polymers (SAP) as an internal curing agent. Four high-performance concrete mixes with w/c ratio 0.32 were selected with varying SAP content such that the internal curing water contents supplied were 0 kg/m^3, 50 kg/m^3, 70 kg/m^3, and 90 kg/m^3. Experiments were performed according to Belgian Codes to study the effect of internal curing on concrete properties: fresh concrete properties (slump, flow, and density), mechanical properties (autogenous shrinkage, basic creep, modulus of elasticity, compressive strength and tensile strength), and thermal properties (hydration heat production). Finite element analysis of a bridge deck, using the HEAT software package, was carried out to identify the temperature variation in the bridge deck the and possibility for early-age cracking when different mixes are used. Addition of SAP reduced the mechanical strength and modulus of elasticity and increased creep. A higher and earlier heat production rate due to hydration was found for higher amounts of SAP [90].

Savva & Petrou [91] studied the effect of normal-weight aggregate as an alternative to internal curing. The study was performed by comparing the effect high absorptive normal-weight aggregate to a control mix and concrete with SAP. The desorption properties of normal-weight aggregate were characterized by placing them in an environmental chamber where the RH was lowered and the water content was measured. The aggregate lost most of its water at an RH of 97%. The use of saturated-surface-dry (SSD), high-absorption, normal-weight aggregates for internal curing decreased autogenous shrinkage; however, increased temperature rise, increased porosity, and decreased compressive strength were observed. The shrinkage was less than the control but greater when SAP were used. The temperature was greater than both the control and when SAP were used. The porosity measured was less than that of the concrete samples containing SAP. The compressive strength was similar to the control mix.

1.4.3.3 Shrinkage-reducing Admixtures

Shrinkage reducing admixtures (SRA) belong to a class of materials called ‘surfactants’, which when adsorbed at interfaces (in this instance, the water-air interface created in capillary pores) cause a reduction in surface tension [92]. When water is lost from a pore, a water-vapor interface is created. SRAs reduce shrinkage by reducing the surface tension at the water-vapor interface and consequently reducing the tensile stresses on pore walls. This mechanism may not be effective below 50% RH [37], and functions less effectively above a certain concentration threshold called the critical micelle concentration (CMC). The reduction in rate of hydration associated with the addition of SRAs is related to lowering the affinity of alkalis to dissolve in water and thus delayed addition is suggested with their use [92]. This would appear to be a major deficiency considering that the rate of gain of early strength for EOT mixes is critical, but could potentially be offset by use of accelerating admixtures. A new class of admixtures called ‘crack reducing admixtures’ purports to avoid this effect and is claimed to more effectively reduce shrinkage stresses [93].

Folliard and Burke [94] studied the properties of high-performance concrete (HPC) incorporating SRAs. The use of SRAs greatly decrease the shrinkage of the concrete and the size of the cracks associated with the shrinkage in restrained-concrete ring experiments. These advantages came with consequences, most prominent of these being reduced strength at all ages, especially at 24 hours.

Weiss et al. (1998) [95] reviewed test methods, material compositions, theoretical modeling, and the use of a shrinkage-reducing admixture for restrained concrete. Six different mixes were tested using normal- and high-strength concrete, and with various amounts of shrinkage-reducing admixture. Compressive tests were performed to determine modulus and compressive strength using cylinders at ages of 1, 3, 7, 14, and 28 days. Fracture testing and free shrinkage testing were performed on the concrete. Tests were performed to simulate the restraint experienced in highway pavements and bridge decks. The restraint conditions simulated base friction and allowed for multiple cracks to occur. All mixes shrank, but the mixes that incorporated 2% shrinkage-reducing admixture shrank the least. The inclusion of shrinkage-reducing admixture increased the time-to-cracking for all mixes and eliminated cracking in the normal concrete with 2% SRA. The compressive strength of the concrete was reduced by 16% in the high-strength concrete with the 2% SRA. The inclusion of SRA increases the flow and workability, so less water may be used to counteract the drop in compressive strength. Shrinkage-reducing admixtures showed a reduction of up to 40% in free shrinkage.

1.4.4 Use of Separation Layer (Bond Breaker) between Base and Slab

The influence of base characteristics is quite significant on the development of early-age axial restraint stresses in concrete pavements. However, a reduction in these restraint stresses generated due to base friction can be achieved by introducing a separation layer that acts as a bond breaker at the slab-base interface.

Rozycki and Rasmussen [42] modified the interfacial properties of a concrete slab with a hot-mixed asphalt concrete (HMAC) base and found that frictional stress-slippage relationship was significantly affected. Application of a 2-mm sand layer or a polyethylene sheet between the slab and the HMAC base significantly reduced the maximum frictional stress.

The parameters in Table 1-5 were used as inputs to the model developed by Zhang and Li [47] to predict the shrinkage-induced stresses in concrete pavements. It was apparent from the model predictions that the shrinkage-induced stresses could be greatly reduced by applying a 2-mm sand layer or a polyethylene sheet between the slab and HMAC layer. In a study [43] which investigated the effect of polyethylene sheeting as a friction reducing medium, it was noted that application of a double layer of polyethylene sheeting significantly reduced the maximum coefficient of friction, which could eventually result in a reduction in the maximum tensile stress induced in the pavement.

Table 1-5: Restraint characteristics of HMAC base (32-mm max. aggregate size) (adapted from [47])

Base type	**Max. frictional stress – τ_0 (MPa)**	**Slippage at τ_0 δ_0 (mm)**
Untreated 32-mm HMAC	0.104	0.25
Untreated 32-mm HMAC with 2-mm sand	0.023	0.50
Untreated 32-mm HMAC with polyethylene sheet	0.007	0.60

In addition to the polyethylene, geotextile has been used as an interlayer/bond breaker in concrete pavements in Europe during the last two decades. Besides preventing cracks in the base from reflecting into the slab, its permeability also facilitates drainage of water at the slab-base interface. It was indicated that geotextiles, used as bond breakers, lower the critical axial restraint stress considerably in a cement-treated base-slab interface [96]. This is a clear indication of the effectiveness of geotextiles in maintaining a distinct separation between the slab and the support layers. Similar results were obtained in an analysis using HIPERPAV in the same study.

Table 1-6: Effect of geotextile on the maximum restraint stress (adapted from [96])

Max. restraint stress (psi)	Without geotextile	With geotextile
Slab 1	16 -17	4.5
Slab 2	10	1.4

1.5 Methods for Prediction and Measurement of Concrete Volume Change and Restrained Stresses

1.5.1 Autogenous Shrinkage

ASTM C1698 specifies the procedures to measure bulk strain of a sealed cement paste or mortar specimen with w/cm ratios less than 0.4, when no external force is imposed. The specification applies to testing of cementitious mixtures containing admixtures, various supplementary cementitious materials (SCM), and other fine materials. Samples are cured at a constant temperature from the time of final setting until ages of 1, 3, 7, 14 and 28 days.

Freshly mixed paste or mortar is placed in a corrugated mold, which provides little resistance for the expansion or contraction of the specimen. The mold should be sealed to prevent the loss of moisture to the environment due to evaporation. It is then stored at constant temperature. A dilatometer is used to measure the lengths of the samples until the designated age is reached. Autogenous strain is computed using the change in length and the original length of the specimen.

1.5.2 Drying Shrinkage

ASTM C596 is the governing standard for the determination of drying shrinkage of mortar. The test involves curing 1 × 1 × 11 ¼ in. mortar bars for 24 hours (in standard ASTM C490 molds), after which the mortar specimens are placed in lime-saturated water for 48 hours. A length reading is taken after removal from the lime bath and these specimens are subsequently placed in air storage for a period of 25 days, with length readings being taken at 4, 11, 18 and 25 days.

ASTM C157 is similar to ASTM C596, but is performed on mortar or concrete prisms with a 3-in. square cross section for aggregates with a maximum size smaller than 1-in., or a 4-in. square cross section for aggregates with a maximum size smaller than 2 in. Specimens are cured in lime water until 28 days before being placed in a room at 73 ± 3°F [23 ± 2°C]. Length change is measured throughout the testing period.

1.5.3 Free Shrinkage Frame (SF)

Free shrinkage frames are used to measure unrestrained concrete shrinkage from autogenous and thermal deformation. The concrete specimen is sealed with two layers of plastic within the frame to prevent moisture loss. A network of copper pipes transports temperature-controlled water throughout the frame to keep the concrete at predetermined temperature profiles with time. Two anchor disks connected by invar rods to displacement sensors are placed into the specimen 500 mm away from one another. The displacement of the two disks and the temperature are recorded. The shrinkage measured by the displacement of the two plates anchored in the concrete is due to both autogenous shrinkage and thermal expansion.

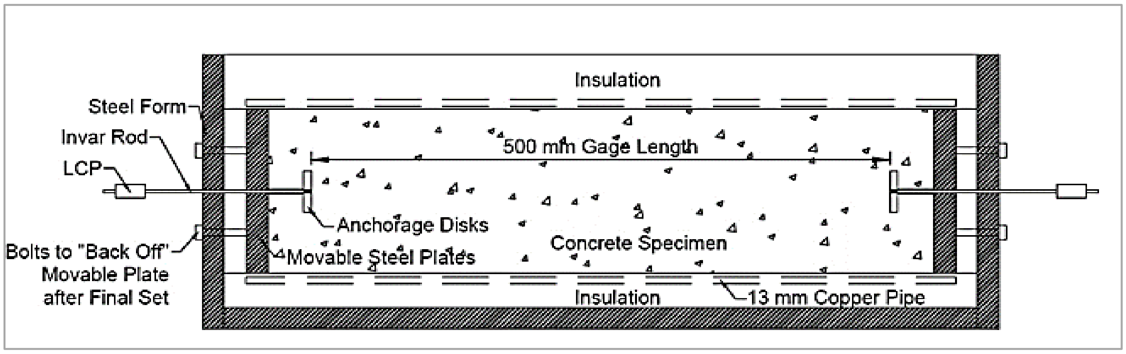

Figure 1-13: Schematic for free shrinkage frame [1]

1.5.4 In Situ Determination of Stresses

Stressmeters were introduced in Japan and have been used to advance concrete research. One of the main advantages of the stress meter is that it can measure thermal stresses even when the mechanical properties are still developing. The stress is not measured directly but is calculated using a load cell. In the stressmeter, there is a load cell adjacent to a cylindrical interior chamber with a bond-breaking material covering the interior walls of the chamber. The interior of the stressmeter is filled with concrete (the concrete prism shown in Figure 1-14) and then placed into the concrete comprising the slab or component to be tested. The external concrete is bonded to the load cell, the load cell to the concrete prism, and the prism to the external concrete using anchor bolts. Water is able to travel between the prism and the surrounding concrete so it is assumed that the concrete in the prism has the same moisture level as the external concrete. A schematic of the apparatus is given in Figure 1-14.

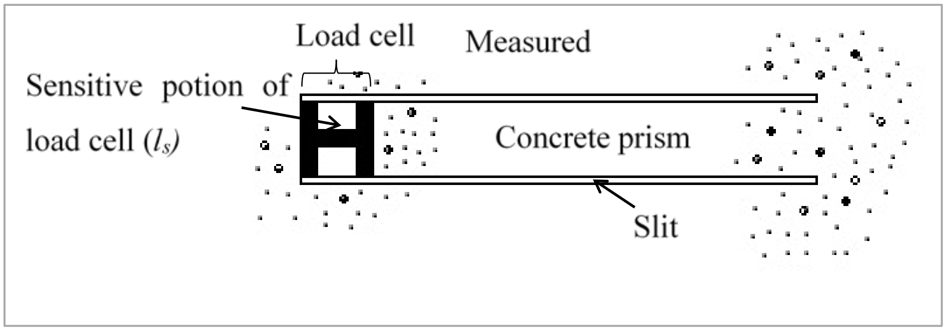

Figure 1-14: Schematic for stressmeter (adapted from [97])

Yeon et al. (2013) [98] details the use of a Vibrating Wire Strain Gauge (VWSG) used in conjunction with a Non-Stress Cylinder to determine the stress-dependent strain for CRCPs to compare modeled and measured ZST. The concrete inside the non-stress cylinder is non-restrained and is used to measure a stress-independent strain history. The resulting stress histories showed good agreement with those measured using a stressmeter.

1.5.5 Rigid Cracking Frame (RCF)

The rigid cracking frame is used to measure the restrained tensile stress developed during the curing of concrete specimens. Rigid cracking frames have a copper pipe network that allows water to heat the concrete to a temperature profile similar to the temperature experienced in the center of a concrete element. In the rigid cracking frame, the concrete prism is restrained by dovetailed crossheads on either end of the specimen. The crossheads and restraining bars restrict the concrete from expanding and contracting. The degree of restraint starts at 100% when the concrete is fresh, and decreases after setting as the concrete modulus increases. The stresses are measured using the strain gauges on the invar bars. The rigid cracking frame measures the uniaxial autogenous and thermal stresses and does not account for warping, curling, or drying shrinkage.

1.5.6 Thermal Stress Testing Machine

Thermal stress testing machine (TSTM) is an axial restraint test that measures the force in a dogbone-shaped concrete prism when kept at 100% restraint. The TSTM uses a similar concrete specimen as the RCF. It includes a load cell, cross-heads and a heating and cooling system. A load cell is placed in series with the specimen, the frame, and a motor. When the specimen deformation measured exceeds a given threshold, the motor is activated to move the specimen back to a state of zero strain. The stress measurements are initiated when the fresh concrete stiffens and measurements are taken continuously thereafter.

1.6 Transient Temperature and Stress Modeling

The assessment of cracking risk in early-age JPCP typically relies on the ability to model material behavior, geometry, and environmental conditions realistically. This is likely well suited for procedures using FEM- or FDM-based techniques. A modelling framework that is intended to model transient stresses is important so that a comparison between tensile stress and (either deterministic or probabilistic) tensile strength can be made. The flow chart in Figure 1-15 details the essential elements of such a framework.

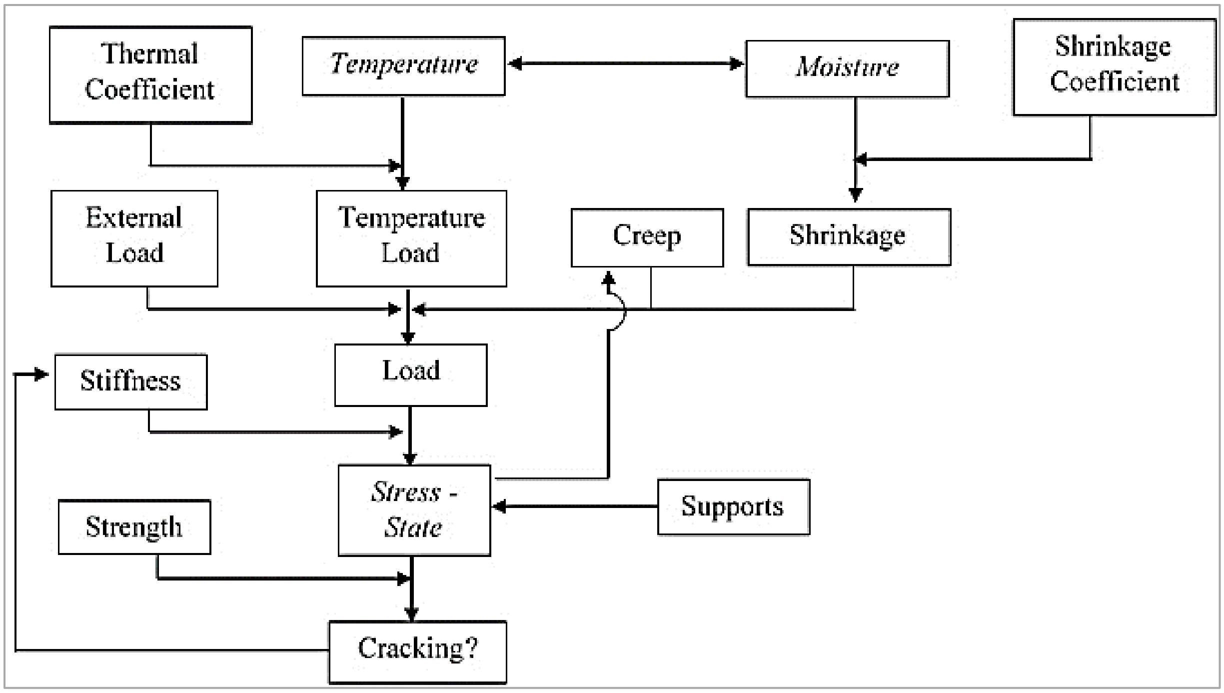

Figure 1-15: Flowchart for analysis early-age concrete behavior (adapted from [99])

Many researches have proposed different numerical approaches to reproduce early-age performance of concrete [100],[101],[102]. When performing numerical analysis, maturity, temperature, moisture, and stresses need to be incorporated [99].

1.6.1 Modeling of Stresses

Assessment of the stresses in early-age concrete involves [103];

- A transient thermal analysis which determines the temperature history. The temperature development is determining the development of material properties, and is also used later to calculate the thermal deformation in stress calculations.
- A transient stress analysis considering transient material properties such as autogenous shrinkage, thermal history, and boundary conditions.
- Material behavior as a function of degree of hydration, temperature, and moisture content.
- Stiffness of the adjoining elements or concrete.

The likelihood of cracking is determined by the ratio of tensile strength (typically the splitting tensile strength multiplied by a reduction factor) and the principal tensile stress. This ratio, also called the cracking index, is shown in Equation 1-22 and could be either deterministic [99] or probabilistic [100].

$$I(t) = \frac{f(t)}{\sigma_t}$$ Equation 1-22

Where,

$f(t)$ = tensile strength

σ_t = principal tensile stress

The general equation for stress modeling is provided by McCullough and Rasmussen [27]:

$$\sigma(t,x) = f[\alpha_c(t), \Delta T(t,x), Z_c(t,x), E_c(t,x), \nabla T(t,x), \nabla M(t,x), \ldots.]$$ Equation 1-23

Where,

σ = stress in concrete due to restrained movements

t = time variable

x = space variable

α_c = coefficient of thermal expansion of concrete

Z_c = shrinkage due to moisture loss

E_c = modulus of elasticity

ΔT = temperature change from the concrete set temperature

∇T = temperature gradient in the pavement

∇M = moisture gradient in the pavement

In addition to thermal and shrinkage stresses, curling stresses generated by the temperature gradient between the top and the bottom of the slab are also considered. Curling stresses at the mid-slab edge can be calculated using Equation 1-24 [104].

$$\sigma_t = \frac{C * E_c * \alpha_T * \Delta T}{(1 - \nu^2)}$$ Equation 1-24

Where,

σ_t = tensile stress

C = factor that accounts for slab length, thickness and subgrade stiffness

E_c = elastic modulus

α_t = coefficient of thermal expansion

ΔT = temperature difference between the top and the bottom of the slab

v = Poisson’s ratio

1.6.2 Modeling of Material Behavior

Material models are used to describe the behavior of a structure. Description of material behavior is complex because of the viscoelastic nature of concrete. The viscoelastic modelling can be simplified by the use of an incremental approach, where experimental data is made to fit a rheological model, rendering the modeling approach more amenable to FEM-based analysis. Creep modeling typically uses classical aging viscoelastic models, which are based on the assumption that all the loads such as stress, temperature and humidity variations could be predicted during the lifetime of the structure. This requires a complete loading history, σ (t) [99]. Equation 1-25 is an example of a viscoelastic model.

$$\varepsilon(t) = \int_0^t J(t,\tau) D d\sigma(\tau) + \varepsilon_0(t) \qquad \text{Equation 1-25}$$

Where,

ε(t) = strain at time t

J = compliance function

τ = time at loading

D = constant matrix given by Poisson ratio

σ = stresse

ε_0 = strain without relation to the stresse (due to thermal deformations and shrinkage)

Equation 1-25 is a relationship between actual strains and loading history. It can determine the variation of strains with time for an arbitrary stress history. The material properties are given by the compliance function, and it includes the effects due to the temperature and moisture distribution. However, use of such a model is inconvenient in a numerical analysis, as it includes computation of expansive sums, and requires a complete stress history. In order to avoid these difficulties, the compliance function J can be expanded, as shown in Figure 1-16 and Equation 1-26 (which is the incremental form). The strain in each element is a result of viscoelastic behavior, which is denoted by the elastic modulus (E_i) and coefficient of viscosity (η_i) in Figure 1-16.

$$\varepsilon(t) = \sum_{i=1}^{n} \varepsilon_i(t) + \varepsilon_0(t) \qquad \text{Equation 1-26}$$

Where,

n = number of terms in the expansion

ε_i = contribution from the i^{th} term

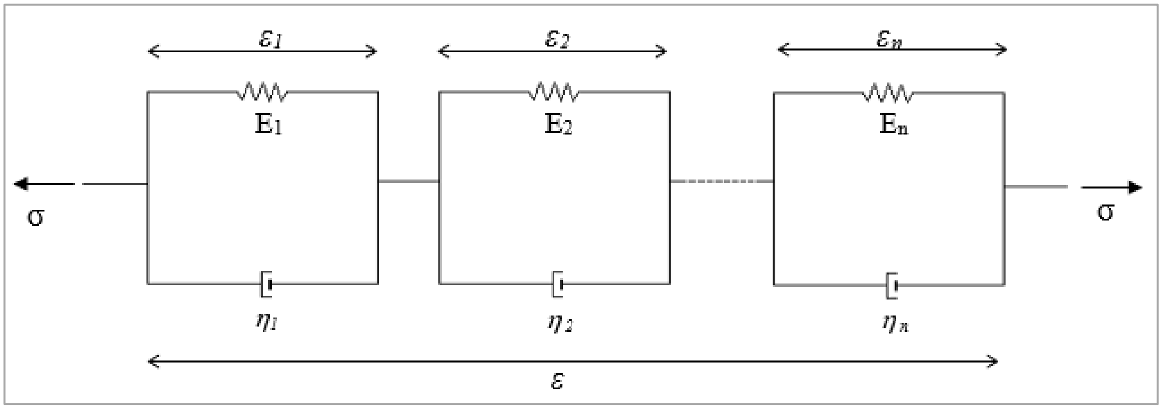

Figure 1-16: Rheological model obtained for the expansion of the compliance function (adapted from [99])

1.6.3 Modeling of Temperature

Thermal properties of early-age concrete, pavement geometry, and weather condition data are needed as inputs for thermal analysis of hardening concrete [105]. The temperature distribution due to hydration and ambient temperature conditions in the interior of the modelled concrete slab can be obtained via a solution to the volumetric Fourier heat balance equation shown in Equation 1-27 [102].

$$\frac{\partial}{\partial x}\left(k\frac{\partial T}{\partial x}\right) + \frac{\partial}{\partial y}\left(k\frac{\partial T}{\partial y}\right) + \frac{\partial}{\partial z}\left(k\frac{\partial T}{\partial z}\right) + Q_h = \rho C_p\left(\frac{\partial T}{\partial t}\right) \qquad \text{Equation 1-27}$$

Where,

T = temperature

k = thermal conductivity

Q_h = rate of heat generation due to the progress of cement hydration

ρ = density

C_p = specific heat capacity

Ruiz et al. [106] found that the variation of thermal conductivity (k) could be represented by Equation 1-28.

$$k = k_{\infty}(1.33 - 0.33\alpha) \qquad \text{Equation 1-28}$$

Where,

k_{∞} = thermal conductivity for hardened concrete

α = degree of hydration

The specific heat capacity C_p could be found using Equation 1-29 [100].

$$C_p = C_0(1.15 - 0.15r) \qquad \text{Equation 1-29}$$

Where,

C_p = Specific heat of hardening concrete

$C_0(r)$ = Specific heat of hardened concrete

r = degree of reaction

The heat source term present in the heat balance equation can be described in Equation 1-30. The coefficients used in Equation 1-30 are obtained from calorimetric testing [107] with the temperature dependence described by the Arrhenius equation [102].

$$Q_H(t) = H_u . C_c . \left(\frac{\tau}{t_e}\right)^{\beta} . \left(\frac{\beta}{t_e}\right) . \alpha(t_e) . \frac{E}{R}\left(\frac{1}{273 + T_r} - \frac{1}{273 + T_c}\right) \qquad \text{Equation 1-30}$$

Where,

H_u = total heat of hydration

C_c = cementitious material content

t_e = equivalent age

$\alpha(t_e)$ = degree of hydration at t_e

β = hydration shape parameter

τ = hydration time parameter

E = activation energy

R = universal gas constant, 8.3144 J/(mol.K)

T_r = reference temperature, ^{o}C

T_c = temperature of concrete, ^{o}C

1.6.4 Modeling of Moisture State

Different models have been developed in the past to simulate moisture content and transport due to drying, self-desiccation, or both. These were either mechanistic, empirical, or mechanistic-empirical models. Although most of these models considered moisture content as a function of w/c ratio, the degree of hydration was not taken into account [108], [109]. However, a nonlinear empirical model was later developed to capture the moisture loss due to self-desiccation, considering the moisture content as a function of w/c ratio and degree of hydration [110]. Xu et al. [111] then proposed a mechanistic-empirical moisture diffusion model for modeling moisture-related changes in concrete pavements during early age hydration.

Fick's Law shown in Equation 1-31 can be used to model changes in moisture due to drying and wetting.

$$\frac{\partial H}{\partial t} = \frac{\partial}{\partial x}\left[D(H) \cdot \frac{\partial H}{\partial x} \right] \qquad \text{Equation 1-31}$$

Where,

H = moisture content or relative humidity

D = moisture diffusivity (changes with degree of hydration and moisture content)

x = depth of the position of the point from the top of the slab

t = time

The model shown in Equation 1-32 and developed by Bazant and Najjar [112] can be used to determine the concrete moisture diffusivity coefficient as a function of moisture level.

$$D(H) = D_r \left[\alpha_0 + \frac{1-\alpha_0}{1+\left(\frac{1-H}{1-H_c}\right)^n} \right] \qquad \text{Equation 1-32}$$

Where,

D_r = maximum diffusivity coefficient

α_0 = constant (0.05)

H_c = moisture at ultimate degree of hydration

n = integer constant

The moisture loss due to self-desiccation can be expressed by Equation 1-33 and Equation 1-34 developed by Oh and Cha [110].

$$H_L = 1 - H_S = -\left(H_{s,max} - 1\right)\left(\frac{\alpha}{\alpha_{max}}\right)^s \quad \text{Equation 1-33}$$

$$\frac{H_s - 1}{H_{s,max} - 1} = \left(\frac{\alpha}{\alpha_{max}}\right)^s \quad \text{Equation 1-34}$$

Where,

H_L = moisture loss

H_S = moisture content at self-desiccation

$H_{S,max}$ = maximum moisture content due to self-desiccation

α = degree of hydration of cement

α_{max} = ultimate degree of hydration of concrete

S = material parameter, which is dependent on w/c ratio

Additionally, boundary conditions are defined considering the slab surface condition and curing condition.

1.6.5 Prediction Using Finite Element Modeling Software

Several software packages that incorporate numerical models for the prediction of material behavior, temperature, moisture, and stresses are available today for evaluating concrete performance and failure criteria. These software are tools that assess the effects of different mix parameters, environmental conditions, and construction practices on the cracking potential [1]. A commonly used software for pavement early-age analysis is HIPERPAV [105] sponsored by the Federal Highway Administration (FHWA). HIPERPAV is specifically designed for the control of the factors affecting concrete pavement behavior at early ages. Hence, it allows the analysis of the stress development and cracking risks in a pavement during the first 72 hours after construction.

In order to predict the magnitude of stresses in concrete pavements at early age, HIPERPAVE contains algorithms to model the parameters that influence the behavior of concrete. These are grouped into four major categories as mix design parameters, pavement design parameters, construction parameters, and environmental parameters as shown in Table 1-7 [104].

Table 1-7: Parameters considered in HIPERPAVE to model early-age behavior

Mix design parameters	**Pavement design parameters**	**Construction parameters**	**Environmental parameters**
- Cement type - Lab maturity data - Coarse aggregate type - Cement content - Silica fume/ fly ash content - Water content - Coarse/ fine aggregate content - Use of water reducer - Use of retarder - Use of accelerator	- Base type - Base friction - Transverse joint spacing - PCC flexural strength - PCC modulus of elasticity - Slab thickness	- Curing method - Time of day of construction - Initial PCC mix temperature - Age of concrete at time of opening to traffic - Age of concrete at time of saw cutting - Initial base temperature	- Air temperature - Temperature distribution - Relative humidity distribution - Solar radiation - Average wind speed

1.6.6 Summary

EOT concrete pavement repairs can experience high early-age volume change from thermal, autogenous, plastic, and drying shrinkage strains. These deformations, when restrained by the base, adjacent slabs, or misaligned dowels, can cause large stresses that can lead to undesirable cracking. Test methods have been developed that can quantify the early-age deformation in HES concrete mixtures, and potential mitigation methods, such as mixture optimization, internal curing, and base separation layers, have been identified.

1.7 References

[1] A. Zayed, K. Riding, C. C. Ferraro, A. Bien-aime, N. Shanahan, D. Buidens, T. Meagher, V. Tran, J. D. Henika, J. M. Paris, C. M. Tibbetts, and B. E. Watts, “Final Report Long-Life Slab Replacement Concrete FDOT Contract Number : BDV25-977-01,” University of South Florida, Tampa, FL, 2015.

[2] M. Yang, M. Abdelrahman, S. Ahmari, and H. Alanazi;, “Survey and Literature Review of Fast-Track PCC Pavement Repair Processes and Materials,” North Dakota State University, Fargo, ND, 2013.

[3] American Concrete Pavement Association, “Fast Track Concrete Pavement,” *Wikipave*. 1994.

[4] M. Yu, Thomas; Mallela, J; Darter, “Highway Concrete Pavement Technology Development and Testing : Volume IV — Field Evaluation of Strategic Highway Research Program (SHRP) C-206 Test Sites (Early Opening of Full-Depth Pavement Repairs) - FHWA-RD-02-085,” ERES Division of Applied Research, Champaign, IL, 2006.

[5] North Carolina Department of Transportation, “Standard Specifications for Roads and Structures,” Raleigh, NC, 2012.

[6] California Department of Transportation, “Chapter 8 Full Depth Concrete Repair,” in *Maintenance Technical Advisory Guide Volume II - Rigid Pavement Preservation 2nd Edition*, Caltrans, 2008, p. (8)1-19.

[7] Colorado Department of Transportation, “Standard Specifications for Road and Bridge Construction,” Denver, Co, 2011.

[8] Delaware Department of Transportation, “Supplemental Specifications to the August 2001 Standard Specifications,” Dover DE, 2014.

[9] Georgia Department of Transportation, “Standard Specifications Construction of Transportation Systems,” Atlanta, GA, 2013.

[10] Illinois Department of Transportation, “Standard Specifications for Road and Bridge Construction,” Illinois, 2012.

[11] T. J. Van Dam, K. R. Peterson, L. L. Sutter, A. Panguluri, and J. Sytsma, “Guidelines for

Early-Opening to Traffic Portland Cement Concrete for Pavement Rehabilitation, NCHRP Report 540," National Cooperative Highway Research Program, Transportation Research Board, Washington, DC, 2005.

[12] New York Department of Transportation, "Standard Specification for Roads and Bridges," Albany, NY, 2014.

[13] R. Dowling, "Multimodal Level of Service Analysis for Urban Streets: Users Guide - NCHRP Web-Only Document 128," Dowling Associated, Inc, Oakland, CA, 2009.

[14] Virginia Department of Transportation, "Road and Bridge Specifications," Richmond, VA, 2016.

[15] Washington Department of Transportation, "Standard Specifications for Road, Bridge, and Municipal Construction," Olympia, WA, 2016.

[16] California Department of Transportation, "Standard Specifications for Road and Bridge Construction," Sacramento, CA, 2015.

[17] Florida Department of Transportation, "Standard Specifications for Road and Bridge Construction," Tallahassee, FL, 2015.

[18] J. Mauricio Ruiz, R. O. Rasmussen, G. K. Chang, J. C. Dick, and P. NelsonK., "FHWA-HRT-04-122: Computer-Based Guidelines For Concrete Pavements Volume II—Design and Construction Guidelines and HIPERPAV II User's Manual," Federal Highway Administration, 2005.

[19] K. L. Scrivener, P. Juilland, and P. J. M. Monteiro, "Advances in Understanding Hydration of Portland Cement," *Cem. Concr. Res.*, vol. 78, pp. 38–56, 2015.

[20] S. Mindess, F. J. Young, and D. Darwin, *Concrete*. Upper Saddle River, NJ: Pearson Education, Inc., 2003.

[21] R. Breitenbücher, "Investigation of Thermal Cracking with the Cracking-Frame*," *Mater. Stuctures Mater. Constr.*, vol. 23, pp. 172–177, 1990.

[22] H. Mihashi and J. P. D. B. Leite, "State-of-the-Art Report on Control of Cracking in Early Age Concrete," *J. Adv. Concr. Technol.*, vol. 2, no. 2, pp. 141–154, 2004.

[23] A. Jensen, O. M., Christensen, S. L., Dela, B. F., Hansen, J. H., Hansen, P. F., & Nielsen,

"HETEK-Control of Early-Age Cracking in Concrete: State of the Art," Denmark Ministry of Transport, Copenhagen, Denmark, 1996.

[24] A. Schindler and F. McCullough, "Importance of Concrete Temperature Control During Concrete Pavement Construction in Hot Weather Conditions," *Transp. Res. Rec.*, vol. 1813, pp. 3–10, 2002.

[25] A. K. Schindler, "Concrete Hydration, Temperature Development, and Setting at Early-Ages," University of Texas at Austin, Austin, 2002.

[26] J. H. Yeon, "Implications of Zero-Stress Temperature for the Long-Term Behavior and Performance of Continuously Reinforced Concrete Pavement," *Constr. Build. Mater.*, vol. 91, pp. 94–101, 2015.

[27] B. F. McCullough and R. O. Rasmussen, "Fast Track Paving: Concrete Temperature Control and Traffic Opening Criteria for Bonded Concrete Overlays Volume I -Final Report," Transtec Inc., Austin, TX, 1998.

[28] J. Mallela, A. Abbas, T. Harman, C. Rao, R. Liu, and M. Darter, "Measurement and Significance of the Coefficient of Thermal Expansion of Concrete in Rigid Pavement Design," *Transp. Res. Rec.*, vol. 1919, pp. 38–46, 2005.

[29] M. S. Siddiqui and D. W. Fowler, "A Systematic Optimization Technique for the Coefficient of Thermal Expansion of Portland Cement Concrete," *Constr. Build. Mater.*, vol. 88, pp. 204–211, 2015.

[30] J. Jeong, D. Zollinger, J. Lim, and J. Park, "Age and Moisture Effects on Thermal Expansion of Concrete Pavement Slabs," *J. Mater. Civ. Eng.*, vol. 24, no. 1, pp. 8–15, 2012.

[31] B. F. McCullough, D. Zollinger, and T. Dossey, "Evaluation of the Performance of Texas Pavements Made With Different Coarse Aggregates-TX-01/7-3925-1," Center for Transportation Research, The University of Texas at Austin, Austin, TX, 2000.

[32] S. L. Meyers, "How Temperature and Moisture Changes may Affect the Durability of Concrete," *Rock Prod. devoted to Prod. sale rock clay Prod.*, vol. 54, pp. 153–158, 1951.

[33] Federal Highway Administration Research and Technology, "Thermal Coefficient Of

Portland Cement Concrete," *Portland Cement Concrete Pavements Research*, 2016. [Online]. Available: https://www.fhwa.dot.gov/publications/research/infrastructure/pavements/pccp/thermal.cfm. [Accessed: 01-Nov-2016].

[34] E. Tazawa, Ed., *Autogenous Shrinkage of Concrete*. London: E & FN Spon, 1998.

[35] D. P. Bentz, K. A. Snyder, and P. E. Stutzman, "Microstructural Modelling of Self-Desiccation During Hydration," in *Self-Desiccation and Its Importance in Concrete Technology*, 1997, pp. 132–140.

[36] P. Lura, O. M. Jensen, and K. Van Breugel, "Autogenous Shrinkage in High-Performance Cement Paste : An Evaluation of Basic Mechanisms," *Cem. Concr. Res.*, vol. 33, pp. 223–232, 2003.

[37] A. B. Eberhardt and R. J. Flatt, "Working Mechanisms of Shrinkage-Reducing Admixtures," in *Science and Technology of Concrete Admixtures*, Elsevier Ltd, 2016, pp. 305–320.

[38] P. J. Uno, "Plastic Shrinkage Cracking and Evaporation Formulas," *ACI Mater. J.*, vol. 95, no. 4, pp. 365–375, 1998.

[39] A. Almusallam, M. Maslehuddin, M. Abdul-Waris, and M. Khan, "Effect of Mix Proportions on Plastic Shrinkage Cracking of Concrete in Hot Environments," *Constr. Build. Mater.*, vol. 12, no. 6–7, pp. 353–358, 1998.

[40] J. K. Kim and C.-S. Lee, "Prediction of Differential Drying Shrinkage in Concrete," *Cem. Concr. Res.*, vol. 28, no. 7, pp. 985–994, 1998.

[41] P. K. Mehta and P. J. M. Monteiro, *Concrete: Microstructure, Properties and Materials*, 3rd ed. New York, NY: McGraw-Hill, 2006.

[42] R. Otto Rasmussen and D. K. Rozycki, "Characterization and Modeling of Axial Slab-Support Restraint," *Transp. Res. Rec. J. Transp. Res. Board*, vol. 1778, pp. 26–32, 2001.

[43] J. W. Wesevich, B. F. McCullough, and N. H. Burns, "Stabilized Subbase Friction Study For Concrete Pavements," Texas DOT, 1987.

[44] S. Lee, "Characteristics of Friction Between Concrete Slab and Base," *KSCE J. Civ. Eng.*,

vol. 4, no. 4, pp. 265–275, 2000.

[45] S. Li, B. Tian, K. Niu, Z. Sun, and W. Zhou, “Characteristics of Base Friction for Concrete Pavement Structure in China,” *Transp. Res. Rec. J. Transp. Res. Board*, vol. 2367, pp. 107–112, 2013.

[46] S. W. Lee, “Behavior of Concrete Slab Under Frictional Drag,” *KSCE J. Civ. Eng.*, vol. 5, no. 2, pp. 141–145, 2001.

[47] J. Zhang and V. C. Li, “Influence of Supporting Base Characteristics on Shrinkage - Induced Stresses in Concrete Pavements,” *ASCE J. Transp. Eng.*, vol. 127, no. 6, pp. 455–462, 2001.

[48] J. R. Roesler and D. Wang, “An Analytical Approach to Computing Joint Opening in Concrete Pavements,” in *Proceedings of the 6th RILEM International Conference on Cracking in Pavements: Pavement Cracking: Mechanisms, Modeling, Detection, Testing and Case Histories*, 2008, pp. 79–88.

[49] D. W. Pittman and B. McCullough, “Development of a Roller-Compacted Concrete Pavement Crack and Joint,” *Transp. Res. Rec. J. Transp. Res. Board*, vol. 1568, pp. 52–64, 1997.

[50] J. H. Jeong, J. Y. Park, J. S. Lim, and S. H. Kim, “Testing and Modelling of Friction Characteristics Between Concrete Slab and Subbase Layers,” *Road Mater. Pavement Des.*, vol. 15, no. 1, pp. 114–130, 2014.

[51] D. Xin, D. G. Zollinger, and R. W. James, “One-dimensional Model for Analysis of CRC Pavement Growth,” *ASCE J. Transp. Eng.*, vol. 118, no. 4, pp. 557–575, 1992.

[52] R. E. Lederle, “Accounting for Warping and Differential Drying Shrinkage Mechanisms in the Design of Jointed Plain Concrete Payments,” Michigan Technological University, 2011.

[53] A. R. Mohamed and W. Hansen, “Effect of Nonlinear Temperature Gradient on Curling Stress in Concrete Pavements,” *Transp. Res. Rec.*, vol. 1568, pp. 65–71, 1997.

[54] W. B. Fuller and S. E. Thompson, “The Laws of Proportioning Concrete,” *Asian J. Civ. Eng. Transp.*, vol. 59, pp. 67–143, 1907.

[55] J. M. Shilstone SR and J. M. Shilstone JR, “Performance-Based Concrete Mixtures and Specifications for Today,” *Concr. Int.*, no. 2, pp. 80–83, 2002.

[56] K. Obla, H. Kim, and C. Lobo, “Effect of Continuous (Well-Graded) Combined Aggregate Grading on Concrete Performance, Phase A: Aggregate Voids Content (Packing Density),” National Ready Mixed Concrete Association Research Laboratory, Silver Spring, MD, 2007.

[57] M. D. Cook, A. Ghaeezadeh, M. T. Ley, and B. . Russell, “Final Report-Investigation of Optimized Graded Concrete for Oklahoma–Phase 1-FHWA-OK-13-12,” Oklahoma State University, Stillwater, OK, 2013.

[58] M. Cook, N. Seader, T. Ley, and B. Russell, “Final Report-Investigation of Optimized Graded Concrete for Oklahoma- Phase 2- FHWA-OK-15-07,” Oklahoma State University, Stillwater, OK, 2015.

[59] E. Yurdakul, “Proportioning for Performance-Based Concrete Pavement Mixtures,” Iowa State University, 2013.

[60] P. Goltermann, V. Johansen, and L. Palbol, “Packing of aggregates: An Alternative Tool to Determine the Optimal Aggregate Mix,” *ACI Mater. J.*, vol. 94, no. 5, pp. 435–443, 1997.

[61] P. Anderson and V. Johansen, “A Guide to Determining the Optimal Gradation of Concrete Aggregates,” Strategic Highway Research Program, Washington, DC, 1993.

[62] S. A. A. M. Fennis and J. C. Walraven, “Using Particle Packing Technology for Sustainable Concrete Mixture Design,” *Heron*, vol. 57, no. 2, pp. 73–101, 2012.

[63] M. Moini, I. Flores-Vivian, A. Amirjanov, and K. Sobolev, “The Optimization of Aggregate Blends for Sustainable Low Cement Concrete,” *Constr. Build. Mater.*, vol. 93, pp. 627–634, 2015.

[64] J. R. Shilstone Sr, James M. LaFrenz, “The Aggregate, the Key to High Performance Concrete,” in *Transportation Research Board 77th Annual Meeting*, 1998.

[65] D. Cook, N. Seader, A. Ghaeezadeh, B. Russell, and T. Ley, “Aggregate Proportioning and Gradation for Slip Formed Pavements,” 2014. [Online]. Available:

http://www.cptechcenter.org/ncc/TTCC-NCC-documents/F2014 NC2 Omaha/11F2014 Ley Optimized Graded Concrete2.pdf.

[66] K. Obla, H. Kim, and C. Lobo, “Effect of Continuous (Well-Graded) Combined Aggregate Grading on Concrete Performance, Phase B: Concrete Performance,” National Ready Mixed Concrete Association Research Laboratory, Silver Spring, MD, 2007.

[67] E. Yurdakul, P. C. Taylor, H. Ceylan, and F. Bektas, “Effect of Paste-to-Voids Volume Ratio on the Performance of Concrete Mixtures.,” *J. Mater. Civ. Eng.*, vol. 25, no. 12, pp. 1840–1851, 2013.

[68] P. J. Andersen and V. Johansen, “Particle Packing and Concrete Properties,” in *Material Science of Concrete II*, S. Skalny, J.; Mindess, Ed. American Ceramic Society, 1995, pp. 111–146.

[69] M. Anson-Cartwright, “Optimization of Aggregate Gradation Combinations to Improve Concrete Sustainability,” University of Toronto, 2011.

[70] R. Jones, L. Zheng, and M. Newlands, “Comparison of Particle Packing Models for Proportioning Concrete Constituents for Minimum Voids Ratio,” *Mater. Struct.*, vol. 35, no. 5, pp. 301–309, 2002.

[71] D. M. Roy, B. E. Scheetz, R. I. a Malek, and P. J. Andersen, “SHRP C-624: Concrete Components Packing Handbook,” Materials Research Laboratory, The Pennsylvania State University, Washington D.C, 1993.

[72] A. Rudy and J. Olek, “Optimization of Mixture Proportions for Concrete Pavements—Influence of Supplementary Cementitious Materials, Paste Content and Aggregate Gradation,” Purdue University, West Lafayette, IN, 2012.

[73] E. P. Koehler and D. W. Fowler, “Aggregates in Self-Consolidating Concrete,” University of Texas at Austin, Austin, TX, 2007.

[74] S. Jacobsen and B. Arntsen, “Aggregate Packing and Void Saturation in Mortar and Concrete Proportioning,” *Mater. Struct.*, vol. 41, no. 4, pp. 703–716, 2008.

[75] P. Zia, S. Ahmad, and M. Leming, “High-Performance Concretes A State-Of-Art Report (1989-1994),” Federal Highway Administration, Washington D.C, 1997.

[76] M. S. Smit, “The Effect of Mixture Proportions on the Properties of High Strength Concrete Used in Pavement,” University of Pretoria, 2015.

[77] S. K. Reinert, “Optimizing Portland Cement Concrete Mix Design to Environmental and Construction Variables with the Aid of Computer Design Software,” Iowa State University, 2007.

[78] X. Wang, P. Taylor, K. Wang, and G. Morcous, “Effects of Paste-to-Voids Volume Ratio on Performance of Self-Consolidating Concrete Mixtures,” *Mag. Concr. Res.*, vol. 67, no. 14, pp. 771–785, 2014.

[79] N. Suksawang and A. Mirmiran, “Use of Fiber Reinforced Concrete for Concrete Pavement Slab Replacement,” Florida Institute of Technology and Florida International University, 2014.

[80] P. Soroushian and S. Ravanbakhsh, “High-Early Strength Concrete: Mixture Proportioning with Processed Cellulose Fibers for Durability,” *ACI Mater. J.*, vol. 96, no. 5, pp. 593–599, 1999.

[81] N. Banthia, V. Bindiganavile, F. Azhari, and C. Zanotti, “Curling Control in Concrete Slabs Using Fiber Reinforcement,” *J. Test. Eval.*, vol. 42, no. 2, p. 20120111, 2014.

[82] H. J. Brown, J. D. Speakman, and J. H. Morton, “Applications of Alkaline-Resistant Cellulose Polymer Fiber in Ready Mixed Concrete,” vol. 268, pp. 55–62, 2010.

[83] D. P. Bentz and W. J. Weiss, “Internal Curing : A 2010 State-of-the-Art Review,” *Civ. Eng.*, 2011.

[84] A. Mezencevova, V. Garas, H. Nanko, and K. E. Kurtis, “Influence of Thermomechanical Pulp Fiber Compositions on Internal Curing of Cementitious Materials,” *J. Mater. Civ. Eng.*, vol. 24, no. 8, pp. 970–975, 2012.

[85] B. E. Byard and A. K. Schindler, “Cracking Tendency of Lightweight Concrete,” Highway Research Center, Auburn University, 2010.

[86] A. Bentur, S. I. Igarashi, and K. Kovler, “Prevention of Autogenous Shrinkage in High-Strength Concrete by Internal Curing Using Wet Lightweight Aggregates,” *Cem. Concr. Res.*, vol. 31, no. 11, pp. 1587–1591, 2001.

[87] D. Cusson and T. Hoogeveen, “Internal Curing of High-Performance Concrete with Pre-Soaked Fine Lightweight Aggregate for Prevention Of Autogenous Shrinkage Cracking,” *Cem. Concr. Res.*, vol. 38, no. 6, pp. 757–765, 2008.

[88] R. Henkensiefken, D. Bentz, T. Nantung, and J. Weiss, “Volume Change and Cracking in Internally Cured Mixtures Made with Saturated Lightweight Aggregate Under Sealed and Unsealed Conditions,” *Cem. Concr. Compos.*, vol. 31, no. 7, pp. 427–437, 2009.

[89] D. Shen, T. Wang, Y. Chen, M. Wang, and G. Jiang, “Effect of Internal Curing with Super Absorbent Polymers on the Relative Humidity of Early-Age Concrete,” *Constr. Build. Mater.*, vol. 99, no. January, pp. 246–253, 2015.

[90] B. Craeye, M. Geirnaert, and G. D. Schutter, “Super-absorbing Polymers as an Internal Curing Agent for Mitigation of Early-Age Cracking of High-Performance Concrete Bridge Decks,” *Constr. Build. Mater.*, vol. 25, no. 1, pp. 1–13, 2011.

[91] P. A. Savva and M. F. Petrou, “High-Absorptive Normal-Weight Aggregates used as Internal Curing Agent,” in *27th Biennial National Conference of the Concrete Institute of Australia in conjuction with the 69th RILEM week*, 2015, pp. 1305–1313.

[92] F. Rajabipour, G. Sant, and J. Weiss, “Interactions Between Shrinkage Reducing Admixtures (SRA) and Cement Paste’s Pore Solution,” *Cem. Concr. Res.*, vol. 38, no. 5, pp. 606–615, May 2008.

[93] C. Nmai, D. Vojtko, S. Schaef, E. K. Attiogbe, and M. A. Bury, “Crack Reducing Admixture,” *Concr. Int.*, vol. 36, no. 1, pp. 53–57, 2014.

[94] K. J. Folliard and N. S. Berke, “Properties of High Performance Concrete Containing Shrinkage-Reducing Admixture,” *Cem. Concr. Res.*, vol. 27, no. 1, pp. 1357–1364, 1997.

[95] W. J. Weiss, W. Yang, and S. P. Shah, “Shrinkage Cracking of Restrained Concrete Slabs,” *J. Eng. Mech.*, vol. 124, no. July, pp. 765–774, 1998.

[96] Federal Highway Administration, “I-29 Reconstruction Evaluation of Geotextile Interlayer,” Federal Highway Administration, Washington, DC, 2007.

[97] J. H. J. Kim, S. E. Jeon, and J. K. Kim, “Development of New Device for Measuring Thermal Stresses,” *Cem. Concr. Res.*, vol. 32, no. 10, pp. 1645–1651, 2002.

[98] J. H. Yeon, S. Choi, and M. C. Won, "Evaluation of Zero-Stress Temperature Prediction Model for Portland Cement Concrete Pavements," *Constr. Build. Mater.*, vol. 40, pp. 492–500, 2013.

[99] A. Boe Hauggaard, L. Damkilde, P. F. Hansen, E. S. Pedersen, and A. Nielsen, "Hetek Control of Early Age Cracking in Concrete, Phase 4 and 5: Material Modelling - Continuum Approach," Denmark Ministry of Transport, 1997.

[100] G. De Schutter, "Finite Element Simulation of Thermal Cracking in Massive Hardening Concrete Elements Using Degree of Hydration Based Material Laws," *Comput. Struct.*, vol. 80, no. 27–30, pp. 2035–2042, 2002.

[101] J. Jonasson, "Modelling of Temperature, Moisture and Stresses in Young Concrete," Lulea University of Technology, 1994.

[102] R. Faria, M. Azenha, and J. A. Figueiras, "Modelling of Concrete at Early Ages: Application to an Externally Restrained Slab," *Cem. Concr. Compos.*, vol. 28, no. 6, pp. 572–585, 2006.

[103] E. S. Pedersen, H. Spange, E. J. Pedersen, A. Boe Hauggaard, O. M. Jensen, and B. Friis Dela, *Hetek Control of Early Age Cracking in Concrete, State of the Art*. Copenhagen, Denmark: Denmark Ministry of Transport, 1996.

[104] E. B. Lee, V. Lamour, J. H. Pae, and J. Harvey, "Analysis of Sensitivity of Plain Jointed Concrete Pavement in California to Early-age Cracking using HIPERPAV," University of California, Pavement Research Center, Davis, CA, 2003.

[105] R. Otto Rasmussen, J. Mauricio Ruiz, D. Rozycki, and B. Frank McCullough, "Constructing High-Performance Concrete Pavements with FHWA HIPERPAV Systems Analysis Software," *Transp. Res. Rec. J. Transp. Res. Board*, vol. 1813, pp. 11–20, 2002.

[106] J. M. Ruiz, A. K. Schindler, R. O. Rasmussen, P. K. Nelson, and G. K. Chang, "Concrete Temperature Modeling And Strength Prediction Using Maturity Concepts In The FHWA HIPERPAV Software," in *Seventh International Conference on Concrete Pavements. The Use of Concrete in Developing Long-Lasting Pavement Solutions for the 21st Century*, 2001, pp. 97–11.

[107] A. K. Schindler and K. J. Folliard, "Heat of Hydration Models for Cementitious Materials,"

ACI Mater. J., vol. 102, no. 1, pp. 24–33, 2005.

[108] B. Persson, “Moisture in Concrete Subjected to Different Kinds of Curing,” *Mater. Struct.*, vol. 30, pp. 533–544, 1997.

[109] L. J. Parrott, “Moisture Profiles in Drying Concrete,” *Adv. Cem. Res.*, vol. 1, pp. 164–170, 1988.

[110] B. Oh and S. W. Cha, “Nonlinear Analysis of Temperature and Moisture Distributions in Early-Age Concrete Structures Based on Degree of Hydration. ,” *ACI Mater. J.*, vol. 100, no. 361–370, 2003.

[111] Q. Xu, J. M. Ruiz, G. K. Chang, R. O. Rasmussen, and D. K. Rozycki, “Moisture Transport Model for Enhancing FHWA HIPERPAV Predictions,” *Transp. Res. Rec. J. Transp. Res. Board*, vol. 2113, pp. 1–12, 2009.

[112] Z. P. Banzant and L. J. Najjar, “Nonlinear Water Diffusion in Non- Saturated Concrete,” *Mater. Constr.*, vol. 5, pp. 3–20, 1972.

Chapter 2 Stress Measurements in Field Pavement Replacement Slabs

2.1 Introduction

2.1.1 Importance of Stress in Concrete

There is a desire to quantify stress development in concrete replacement slabs especially during early age when concrete has low strength. The implementation of a stressmeter is a novel method to directly monitor the stress development in concrete. The device has been used in both field and laboratory settings; its capability in data collection as well as its impact on the concrete system in which it is embedded has been verified [1]–[4].

Conventionally, strain gauges have been used to convert a measured strain to stress using Hooke's law. These gauges contain electric wires. A change in the length of the wires results in a change in the wire resistance that is used to measure the strain. Strain gauges are cheap and effective for measuring stresses in structural elements that behave elastically under load. Strain gauges are not adequate; however, for determining stresses in restrained concrete. The concrete elastic stress under restraint can be calculated according to Equation 2-1:

$$\sigma = \alpha \cdot \Delta T \cdot E \cdot R \qquad \text{Equation 2-1}$$

Where,

σ = concrete stress (psi),
α = concrete coefficient of thermal expansion (1/°F),
ΔT = concrete change in temperature (°F),
E = concrete elastic modulus (psi), and
R = concrete degree of restraint (0 to 1, where R= 0 is free movement and R=1 is fully restrained).

For a non-zero temperature change, the measured strain in concrete for a fully restrained condition would be zero because by definition a fully restrained condition must have no deformation. That same fully restrained concrete could have non-zero stresses, however. A strain gauge used to measure the concrete strain would therefore give misleading results. Stress relaxation in the concrete would further decouple concrete strain measurements from the concrete stress in a restrained concrete element.

A stressmeter device was developed in Japan in the early 1990s to measure in situ concrete stresses [1]. The stressmeter has a load cell that can be embedded in concrete. It is attached to a 5-cm x 5-cm x 50-cm wire mesh basket to maintain the same moisture conditions inside and outside of the wire cage. The load cell has metal anchors on each side that bond to the concrete to ensure load transfer between the concrete and load cell. However, the small size of the cage can cause some difficulties in application of the device including, limitation on aggregate size and problems with execution of proper mixture compaction.

A newer version of the stressmeter was recently introduced by Geokon. Collaboration between Scanrock GmbH and the Geokon resulted in the development of the Geokon 4370 concrete stressmeter. This stressmeter is an improvement from the earlier types as it uses a vibrating wire gauge load cell. Vibrating wire gauge load cells are known to be very stable and do not significantly drift with time. The stressmeter is essentially a permeable tube that allows for similar environmental conditions inside and outside the tube. The tube is filled with the same concrete as in the structure [5]. A picture and schematic of the stressmeter used in this study are shown in Figure 2-1 and Figure 2-2, respectively. Technical specifications for the Geokon 4370 stressmeter are outlined in Table 2-1.

Figure 2-1: Picture of Geokon concrete stressmeter, Model 4370

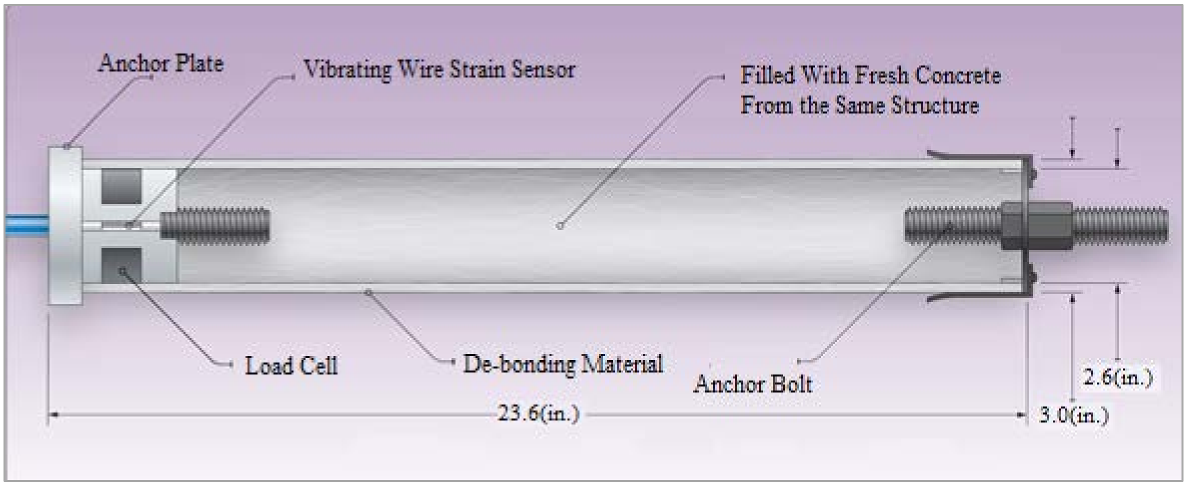

Figure 2-2: Schematic of Geokon concrete ctressmeter, Model 4370 (image provided courtesy of *GEOKON, INCORPORATED* | www.geokon.com)

Table 2-1: Geokon concrete stressmeter Model 4370 technical specifications

Technical Specifications	
Standard Range	-3 MPa to +25 MPa
Resolution	10 kPa
Accuracy[1]	± 0.25% F.S.
Temperature Range[2]	-20°C to + 80°C
Length x Diameter	600 X 76 mm (I.D. 66 mm)
[1] Load cell accuracy [2] Other ranges available on request	

2.2 Experimental

2.2.1 Fabrication of the Concrete Specimen

Prior to field implementation, the stressmeters devices were tested in the laboratory. Two concrete beams (6”x 6”x 60”) were prepared in the laboratory and each had an embedded stressmeter. They were loaded in a hydraulic testing machine in order to determine the sensor accuracy. Wood formwork was constructed for the concrete specimens as shown in Figure 2-3. Holes were drilled into both end panels to allow for a 1” diameter A-36 all-threaded steel bar to pass through. The all-threaded steel bar was embedded 11 inches into the concrete and extended 4 inches out of the formwork. The all-threaded steel bar was used to secure proper gripping of the concrete specimen while loading in tension, Figure 2-4. A nut was threaded onto the end of the bar embedded in the concrete in order to provide additional mechanical anchorage. Concrete specimen 1 was tested in tension only, whereas specimen 2 was tested in both tension and compression.

Figure 2-3: Wooden forms for 6” x 6” x 60” concrete specimen

Figure 2-4: Concrete specimen fabrication

The stressmeter was centered in the specimen using a suspension system constructed of a 22-gauge wire mesh loop as shown in Figure 2-5. The wire mesh was pulled up through the holes (on the sides, bottom and top centers) until the stressmeter and the steel bar were leveled and centered horizontally and vertically. Three layers of plastic were used to seal the wooden frame against moisture loss and to facilitate form removal. Tamping rods and a vibrator were used to consolidate concrete within the wooden form and around the stressmeter.

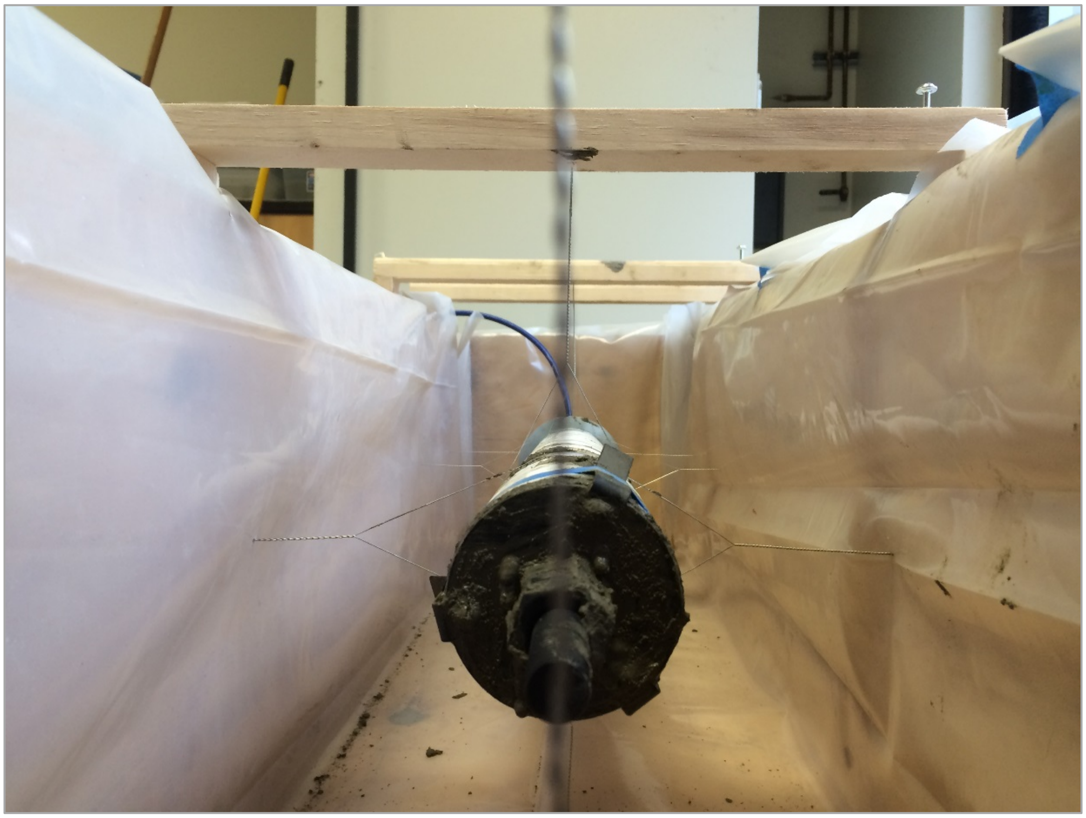

Figure 2-5: Centering of stressmeter in the cast using a 22-gauge wire mesh loop

Due to limitations on the size of the concrete mixer (1-ft^3mixer), the concrete for the 6” x 6” x 60” specimens were prepared in two 0.75-ft^3 batches. A high-early-strength concrete mixture design was used to achieve the required strength in a shorter period of time. Table 2-2 and Table 2-3 show the concrete mixture proportions used for specimen 1 and specimen 2, respectively. Specimen 1 was tested at 14 days after placement while the second specimen was tested at 5 days after placement.

Table 2-2: Concrete mixture proportions used for first specimen

Materials	**Weight (lb/y^3)**
ACO4 Cement	750.0
Oolite #67 Coarse Aggregate (OD)	1543.4
Ottawa Sand Fine Aggregate (OD)	1045.5
Deionized Water	262.4
AEA	0.05
Type F High-Range Water-Reducing Admixture	3.14
Type D Water-Reducing and RetardingAdmixture	2.62

Table 2-3: Concrete mix proportions used for second specimen

Materials	**Weight (lb/y^3)**
ACO4 Cement	900.0
Oolite #67 Coarse Aggregate (OD)	1688.7
Ottawa Sand Fine Aggregate (OD)	828.2
Deionized Water	321.9
AEA	0.20
Set-Accelerating Admixture	33.60
Type D Water-Reducing and RetardingAdmixture	3.37

2.2.2 Programming

A Campbell Scientific CR6 datalogger was used to collect and record the data. In this study, the Shortcut for Windows (SCW) [6] was used to write the datalogger program and the PC200W software [7] was used to send the program to the datalogger and retrieve the stored data. Both software are made by the manufacturer of the datalogger and can be downloaded for free. A scan interval of 1 second was determined based on both the sampling rate and processing rate of the data logger.

The concrete specimen was placed in a universal testing machine (UTM), MTS Systems, for load application. The MTS was connected to the Campbell Scientific CR6 data logger to collect the applied force. The GeoKon stressmeter calibration equations and values, reported by the manufacturer, were used in this study. Calibration values are specific to each stressmeter. Two different calculation methods were offered by GeoKon to convert the digit values that the stressmeter reads into stress. The digits value is a simple conversion from the frequency of the vibrating strain gauge, as indicated in Equation 2-2 [8].

$$\mathrm{Digits} = \left(\frac{\mathrm{f}}{1000}\right)^2 \times 1000 \qquad \text{Equation 2-2}$$

Where,

f = frequency (hz)

A Linear Gauge Factor was specified to convert digits into a stress using a Linear model (Equation 2-3).

$$\mathrm{LinearPSI} = \mathrm{G} * (\mathrm{R}_1 - \mathrm{R}_0) \qquad \text{Equation 2-3}$$

Where,

G = Linear gauge factor (psi/digit)
R_0 = Regression zero
R_1 = Initial field zero reading

A polynomial model can also be used to calculate the stressmeter stress from the digits as shown in Equation 2-4.

$$\mathrm{PolyPSI} = \mathrm{A} * \mathrm{R}_1{}^2 + \mathrm{B} * \mathrm{R}_1 + \mathrm{C} \qquad \text{Equation 2-4}$$

Where,

A = Polynomial gauge factor A from Stressmeter calibration report
B = Polynomial gauge factor B from Stressmeter calibration report
C = Polynomial gauge factor C from Stressmeter calibration report
R_1 = Initial field zero reading (digits)

To determine the stress in the concrete specimen, based on the load applied by the UTM, the applied load was divided by the cross-sectional area of the specimen as indicated in Equation 2-5.

$$\text{Beam Stress} = \frac{\text{Force by UTM (lb)}}{\mathrm{Area}_{\mathrm{beam}}\ (in^2)} \qquad \text{Equation 2-5}$$

A data table was built in the software to determine what data was saved and where in the datalogger memory. The program was then sent to the CR6 data datalogger via USB. The wiring diagram to attach the sensors to the datalogger is automatically generated by the SCW software.

2.3 Evaluation of Concrete Specimens and Stressmeters

Specimen 1 was tested in tension using the MTS load frame as shown in Figure 2-6. The specimen was loaded in increments of 500 pounds until failure. At every stage of load application, the load was sustained for a short period of time to obtain a stable force on the concrete specimen. The concrete specimen fractured when the load was transitioning from 6,000 pounds to 6,500 pounds. The tensile stress developed in specimen 1 with time is shown in Figure 2-7. The applied versus measured stress is plotted in Figure 2-8, calculated using the LinearPSI and PolyPSI methods. As can be seen from Figure 2-7 and Figure 2-8, the Linear method provides more accurate stress measurement compared to PolyPSI method. The measured stress development using the LinearPSI model overestimated the applied stress by 17.6%. To understand the root of the issue, the specimen was visually evaluated. It appeared that there was a slight eccentricity in the stressmeter placement. Testing performed by Geokon [1] showed a similar 10-15% deviation between applied and measured tensile stresses. To better evaluate the situation and the cause of this discrepancy, a second specimen was fabricated and tested in compression and tension separately.

Figure 2-6: Concrete specimen 1 fractured in tension

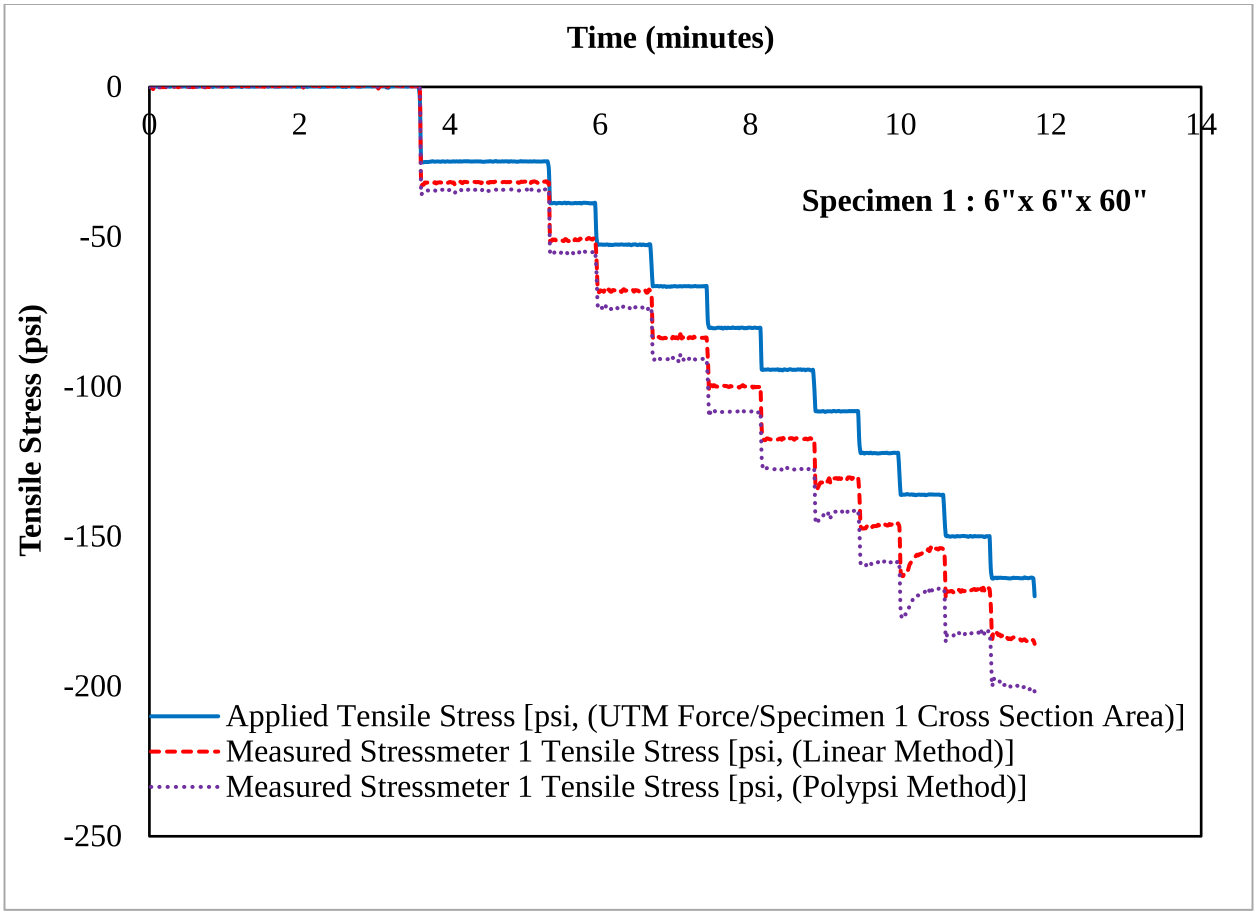

Figure 2-7: Concrete specimen 1 stress development evaluation

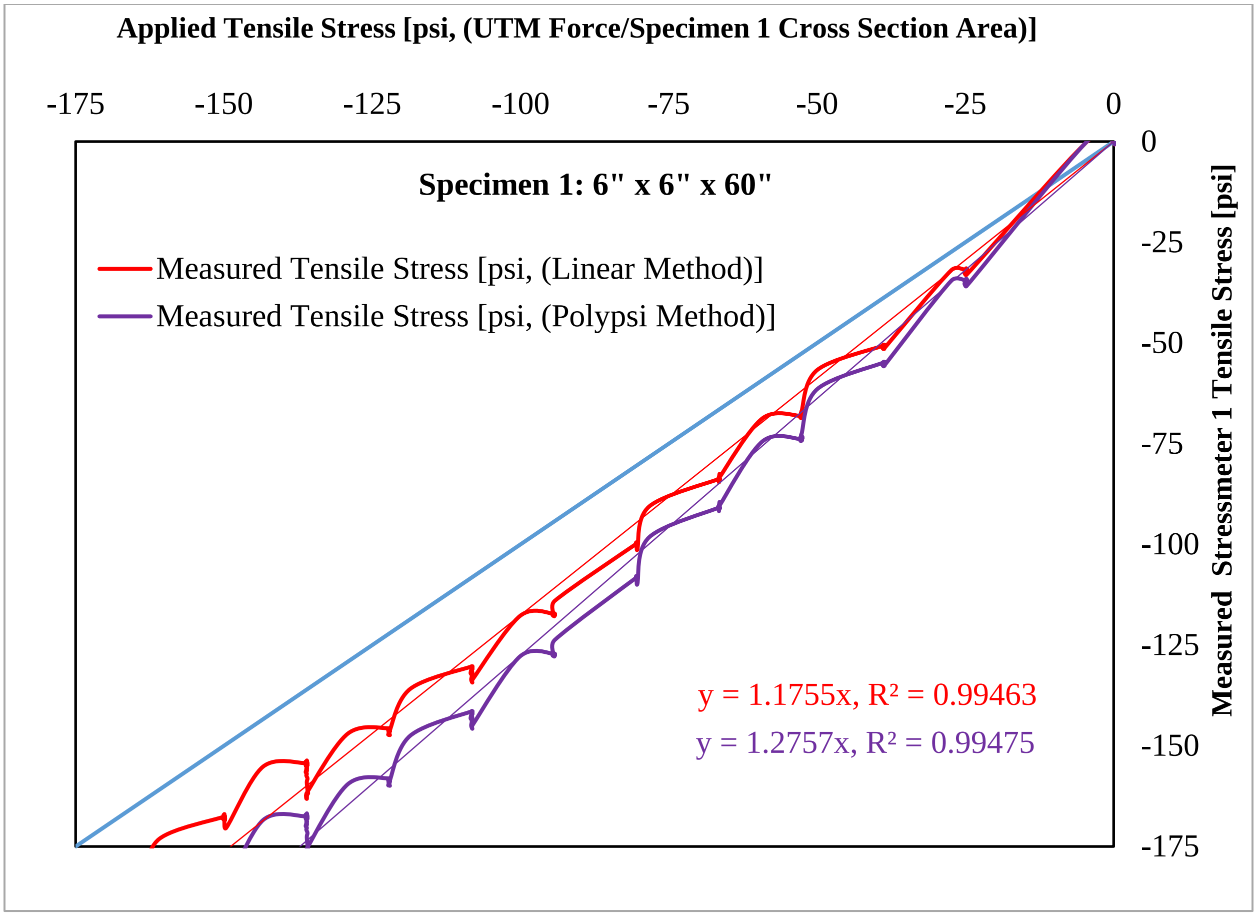

Figure 2-8: Concrete specimen 1 stress development evaluation

Some changes were made to specimen 2 based on specimen 1 testing (See Figure 2-9). Initially the stressmeter was secured in the wooden form using very thin wires. A laser pointer (See Figure 2-10) was used to align the stressmeter carefully. Mounting fixtures were fabricated and implemented to apply the compression and tensile forces on the specimens (See Figure 2-11 and Figure 2-12). Figure 2-13 shows specimen 2 after form removal. The applied and measured tensile and compressive stresses in specimen 2 are shown in Figure 2-14 through Figure 2-16. Figure 2-17 shows specimen 2 failed in tension testing. Similar to specimen 1, the stressmeter in specimen 2 overestimated the applied stress. The measured stress in specimen 2 was on average 20% higher than the applied stress calculated using the LinearPSI method.

Figure 2-9: Testing of 6” x 6” x 60” concrete specimen 2 in tension

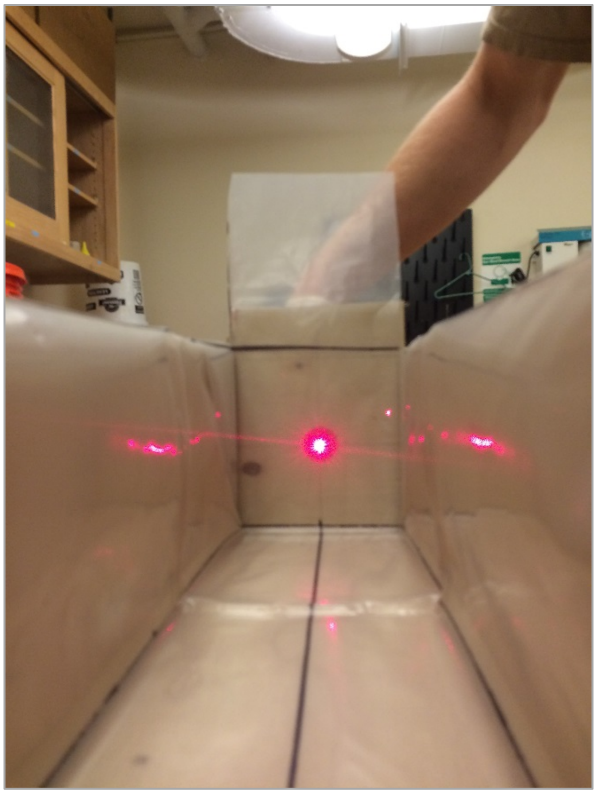

Figure 2-10: Laser pointer application

Figure 2-11: Mounting fixtures for specimen 2

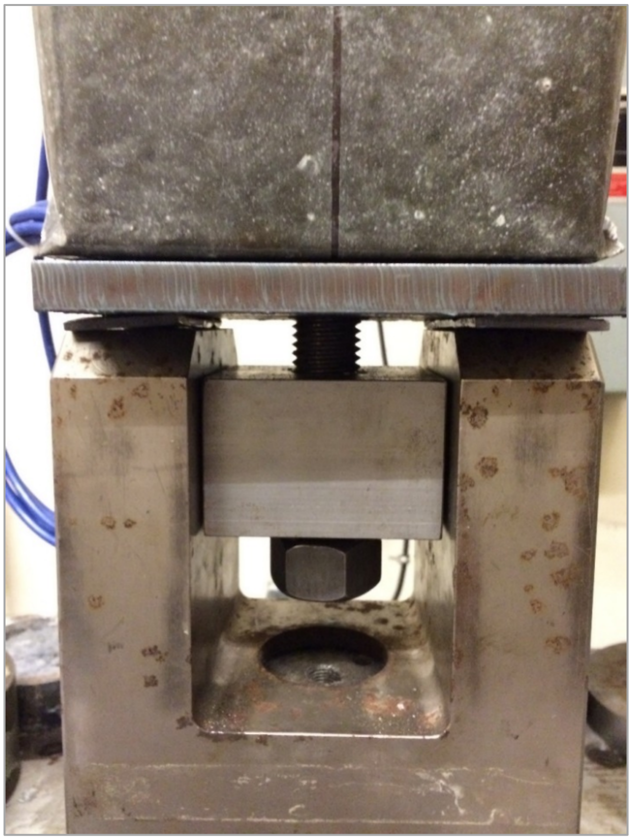

Figure 2-12: Mounting fixtures for specimen 2

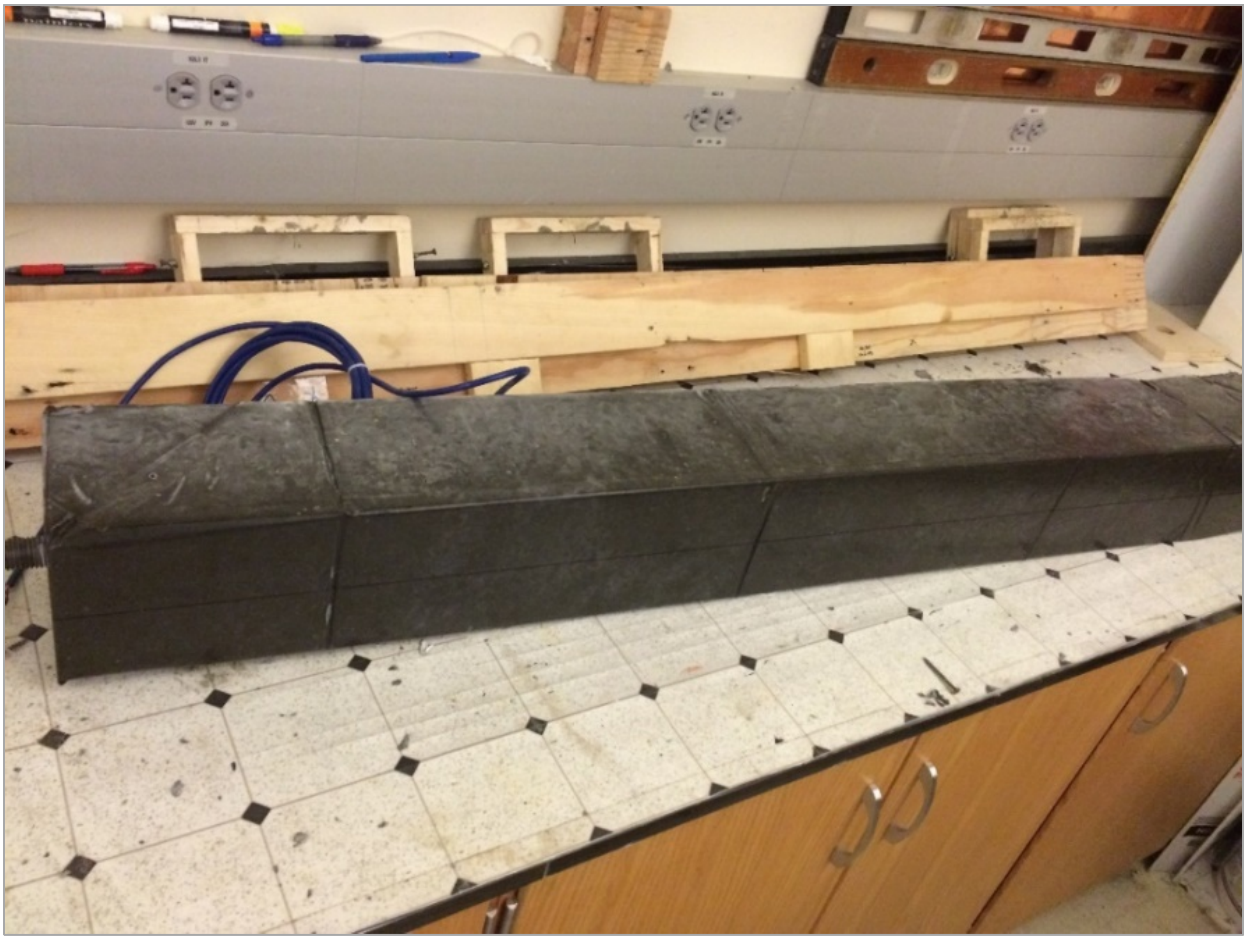

Figure 2-13: Specimen 2 after form removal

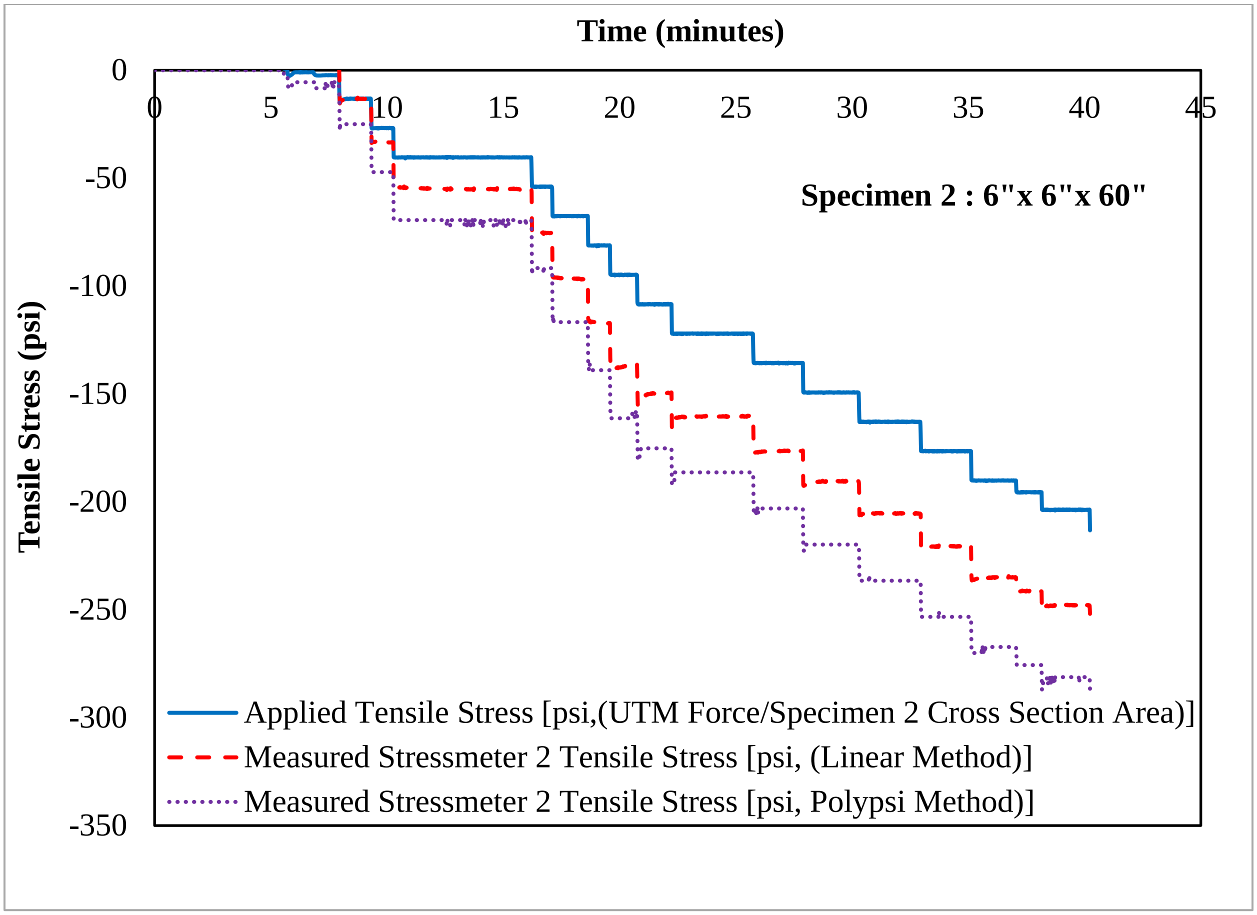

Figure 2-14: Concrete specimen 2 stress development evaluation

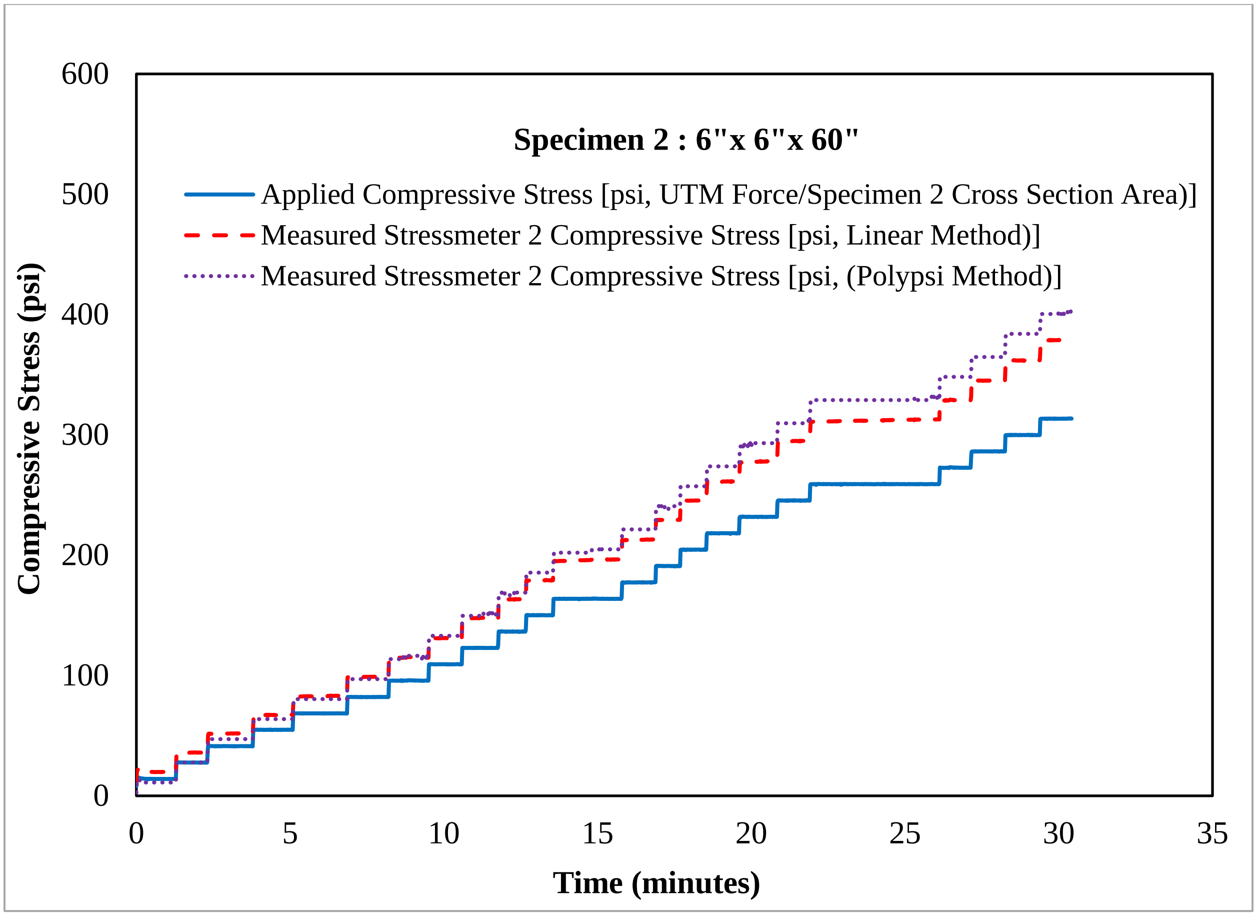

Figure 2-15: Concrete specimen 2 stress development evaluation

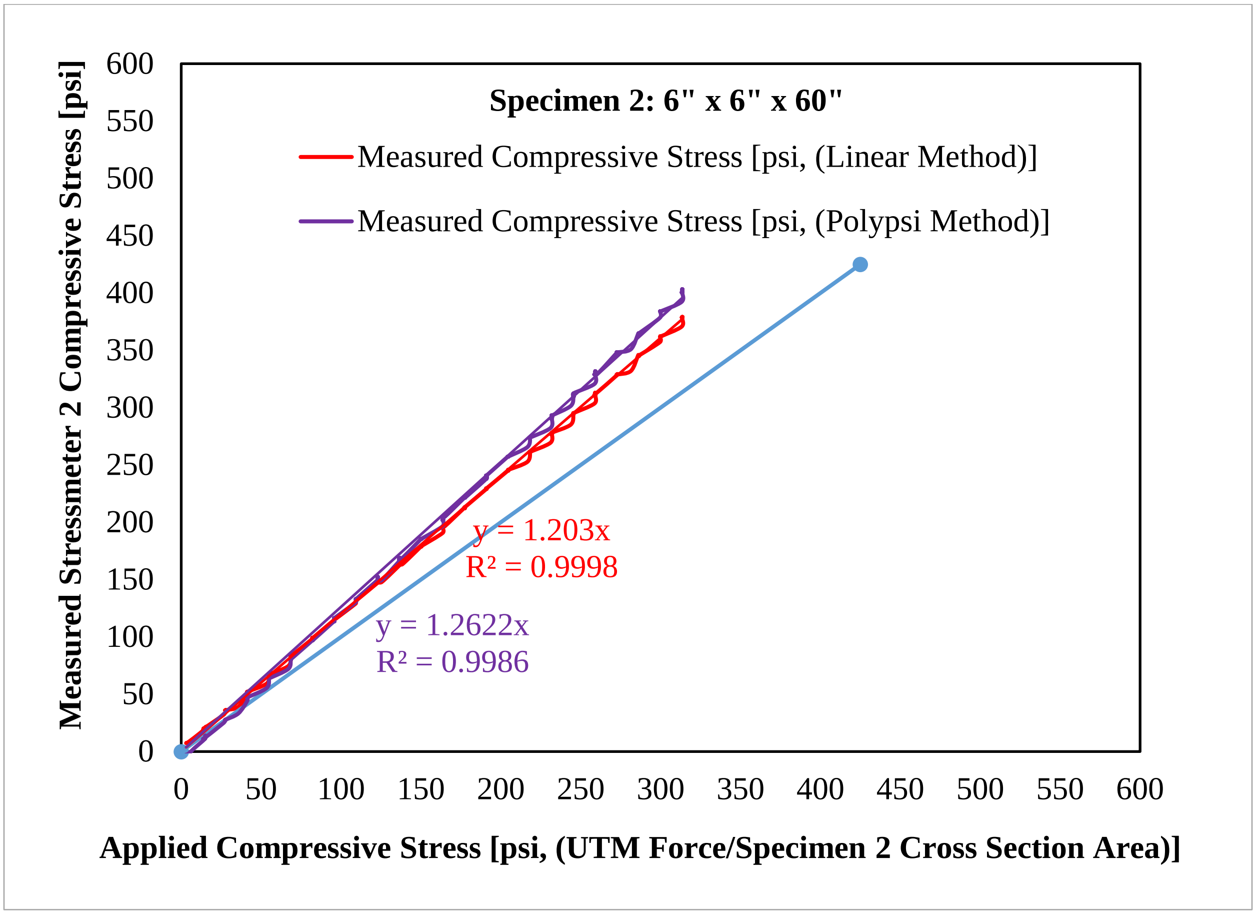

Figure 2-16: Specimen 2 stress development evaluation

Figure 2-17: Specimen 2 failure in tension

The stressmeter documentation provided by GeoKon indicates that the measuring error associated with the stressmeter can be attributed to the different rigidities of the dynamometer (constant) and the concrete (changes with age). This does not mean that the load cell on the stressmeter is improperly calibrated, only that differences in stiffness between the surrounding concrete and stressmeter affect the stress distribution. The act of measuring the stresses in the concrete with the stressmeter slightly changes the flow of the concrete stresses. At early concrete ages, the dynamometer is more rigid than the concrete and as a result provides concrete stress values that are higher than the applied stresses. At later ages, the elastic modulus of the concrete exceeds that of the dynamometer, and the measured stress values are lower than those of the applied stresses. Specimen 2 was tested at a younger age (5 days) than specimen 1 (14 days); based on the error information provided from GeoKon, specimen 2 would be expected to have a lower elastic modulus than specimen 1. As a result, the stress measured for Specimen 2 would be lower than that measured for specimen 1. For these specimen ages, the elastic modulus of the dynamometer was higher, and the stresses measured for the concrete specimens were lower than the applied stresses by 20.3% for specimen 2 and 17.5% for specimen 1, calculated based on the LinearPSI method.

2.4 Stressmeter Evaluation after Removal from Concrete Specimen

To evaluate the performance of the stressmeter by itself, stressmeter 1 was removed from the first concrete specimen and was placed in the UTM load frame for compression testing. The Model GK-404 vibrating wire readout provided by GeoKon was used to verify the validity of the data collected by CR6 DAQ by comparing the output values. The handheld reader (GK-404) and CR6 hardware were used separately to record the readings with an applied load ranging from 200 lb to 2,000 lb. To optimize the precision of the CR6, the settings for the vibrating wire with thermistor were altered in the program to assess the effects of changing the voltage output excitation and varying the output resolution. The voltages used were 5 and 12 volts, while the resolutions were adjusted to high and low levels.

It is demonstrated in Figure 2-18 that the Geokon readout underestimates the compression stress by 4%, using the LinearPSI Method, which indicates a good precision of the instrument to monitor the induced compressive stresses. On the other hand, the CR6 overestimates the compressive stresses by different values depending on the adjustment value of the excitation voltage and mode of resolution. As indicated in Figure 2-19, the CR6 shows the best stress reading when the excitation voltage was adjusted to 12 V and when the data was collected in low resolution mode. In this adjustment mode, the compressive stresses measured using the stressmeter had a 1% deviation from the UTM-measured stress using the LinearPSI Method. Setting of the program (Shortcut for Windows) to 12 V/high res., 5 V/High res., 5 V/Low res., respectively, resulted in 5%, 9%, and 6% overestimation of the compression stress (linear method), as shown in Figure 2-20 through Figure 2-22.

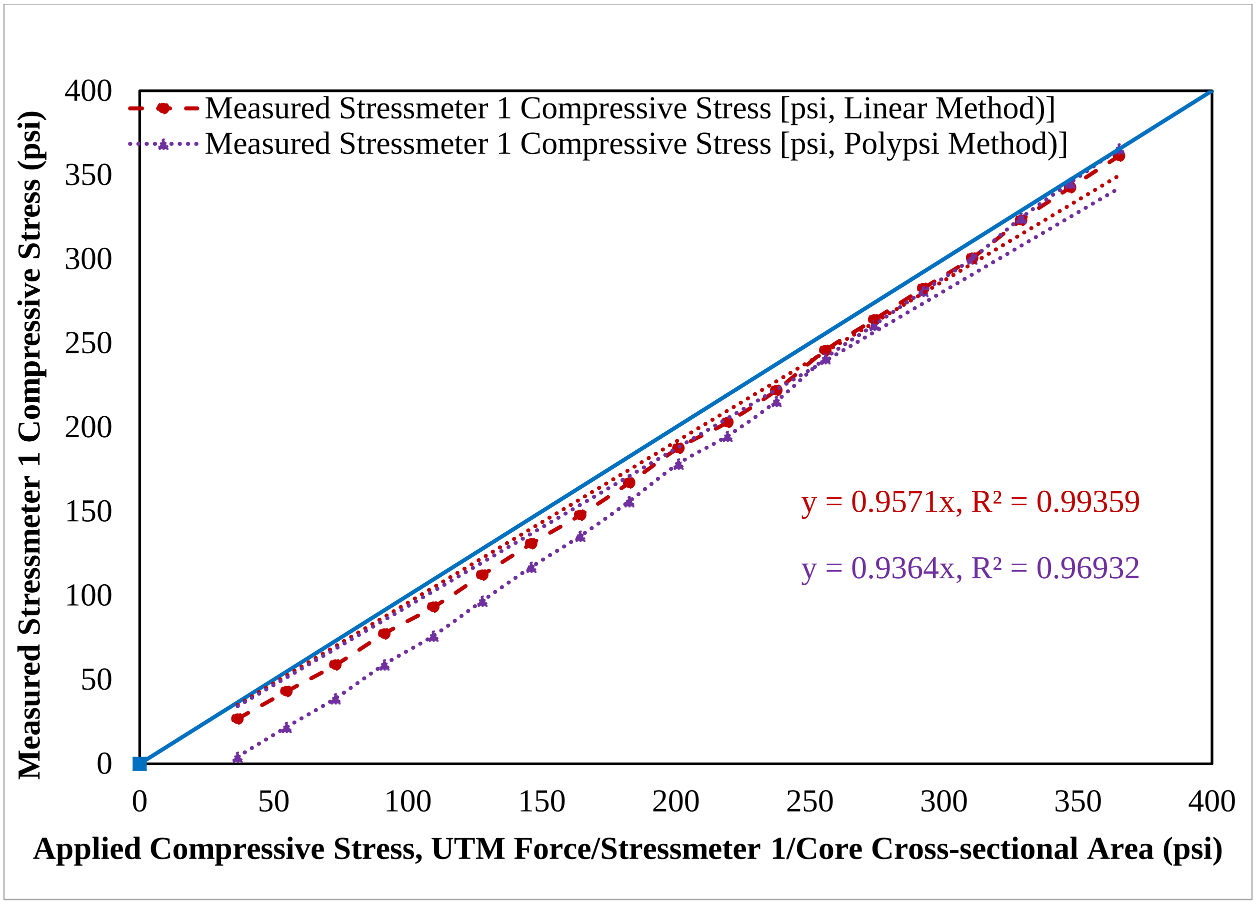

Figure 2-18: First concrete stressmeter, Model GK-404 vibrating wire readout

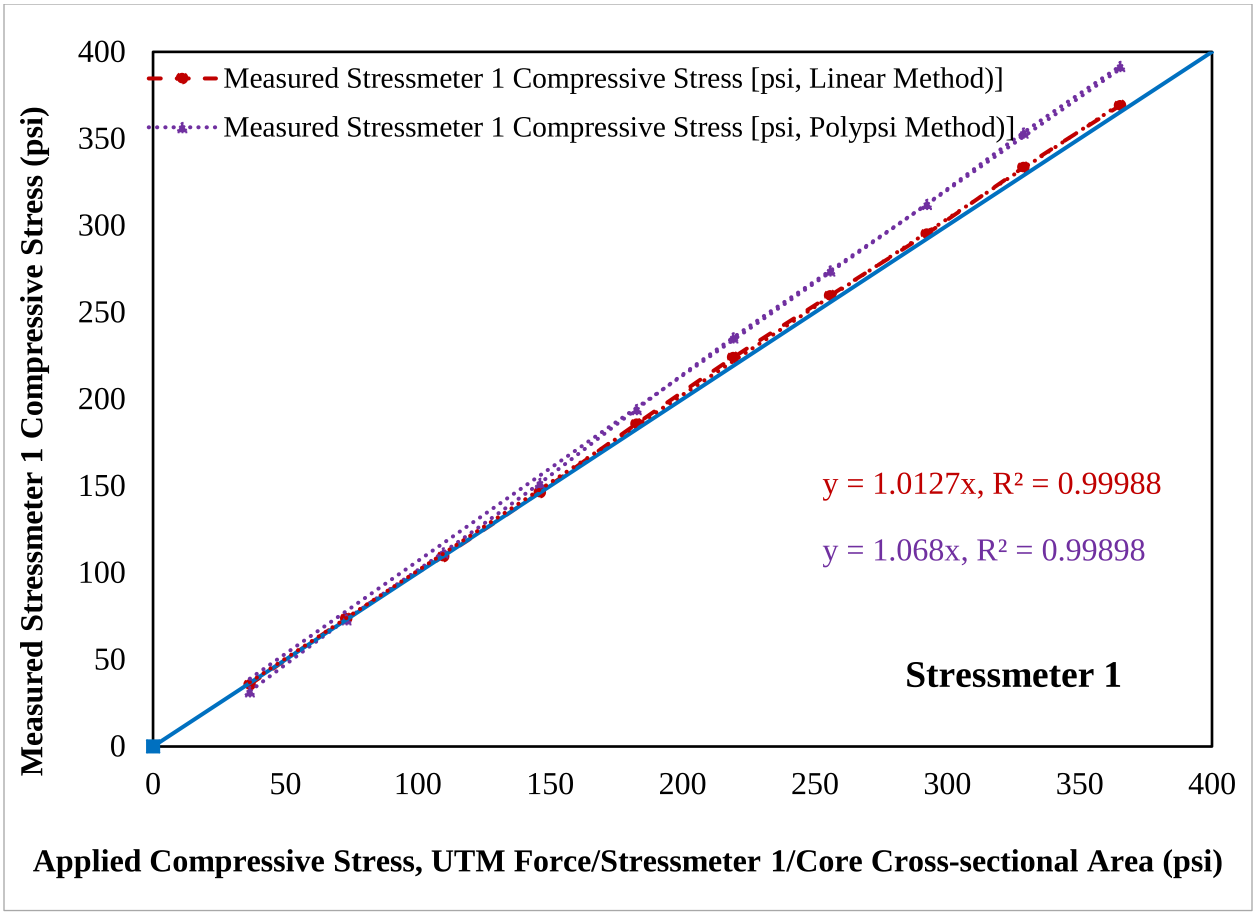

Figure 2-19: First concrete stressmeter, 12 volt and low resolution

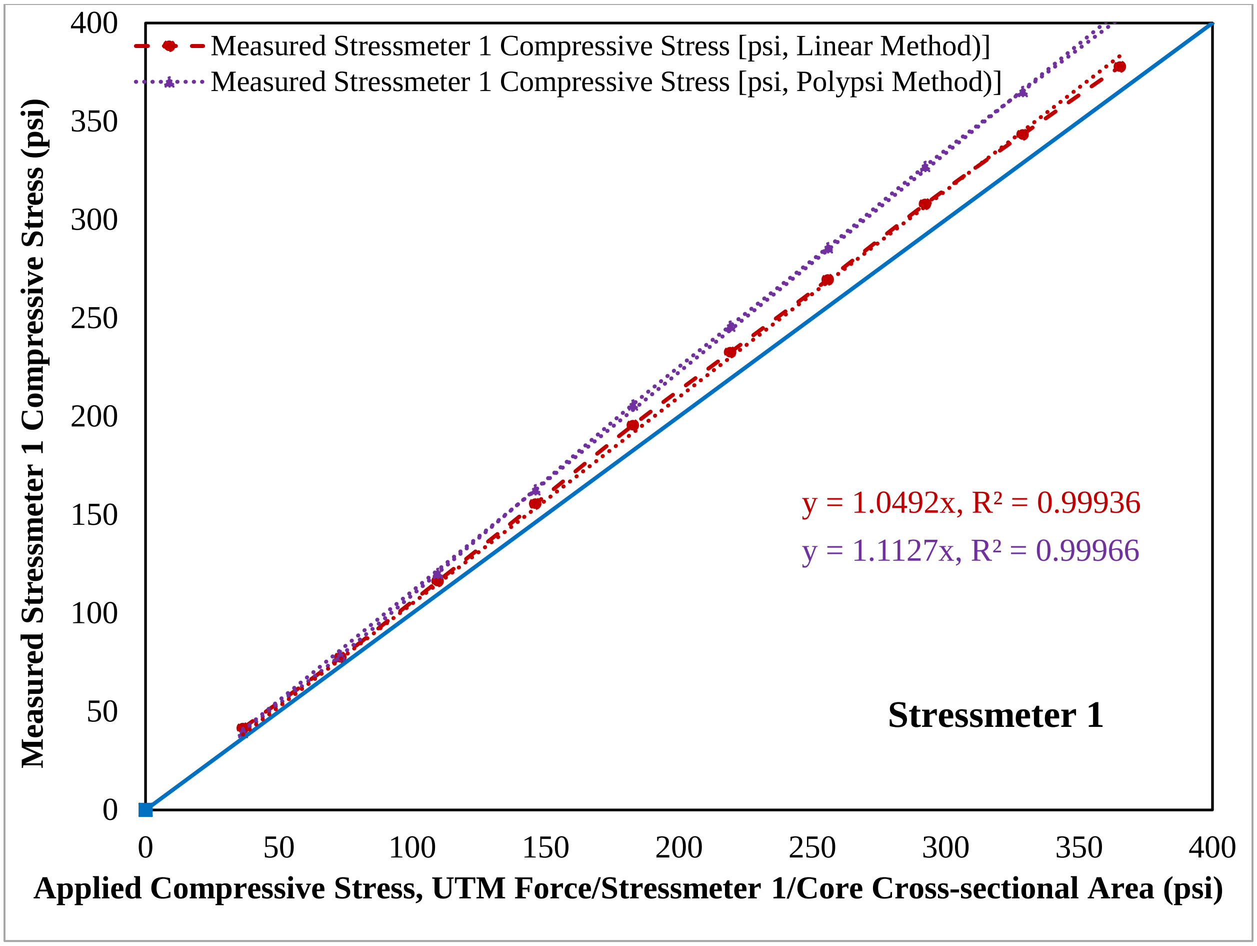

Figure 2-20: First concrete stressmeter, 12 volt and high resolution

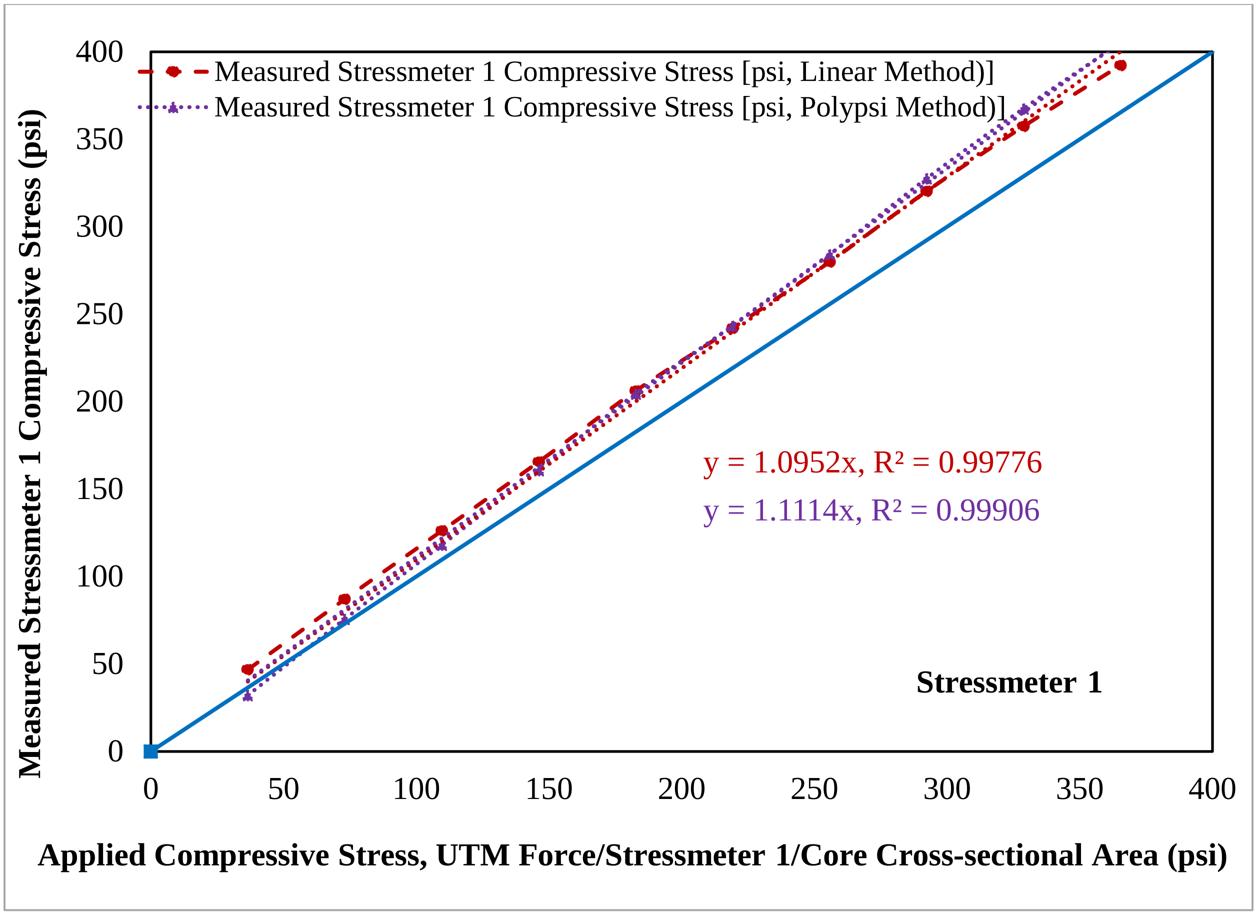

Figure 2-21: First concrete stressmeter, 5 volt and high resolution

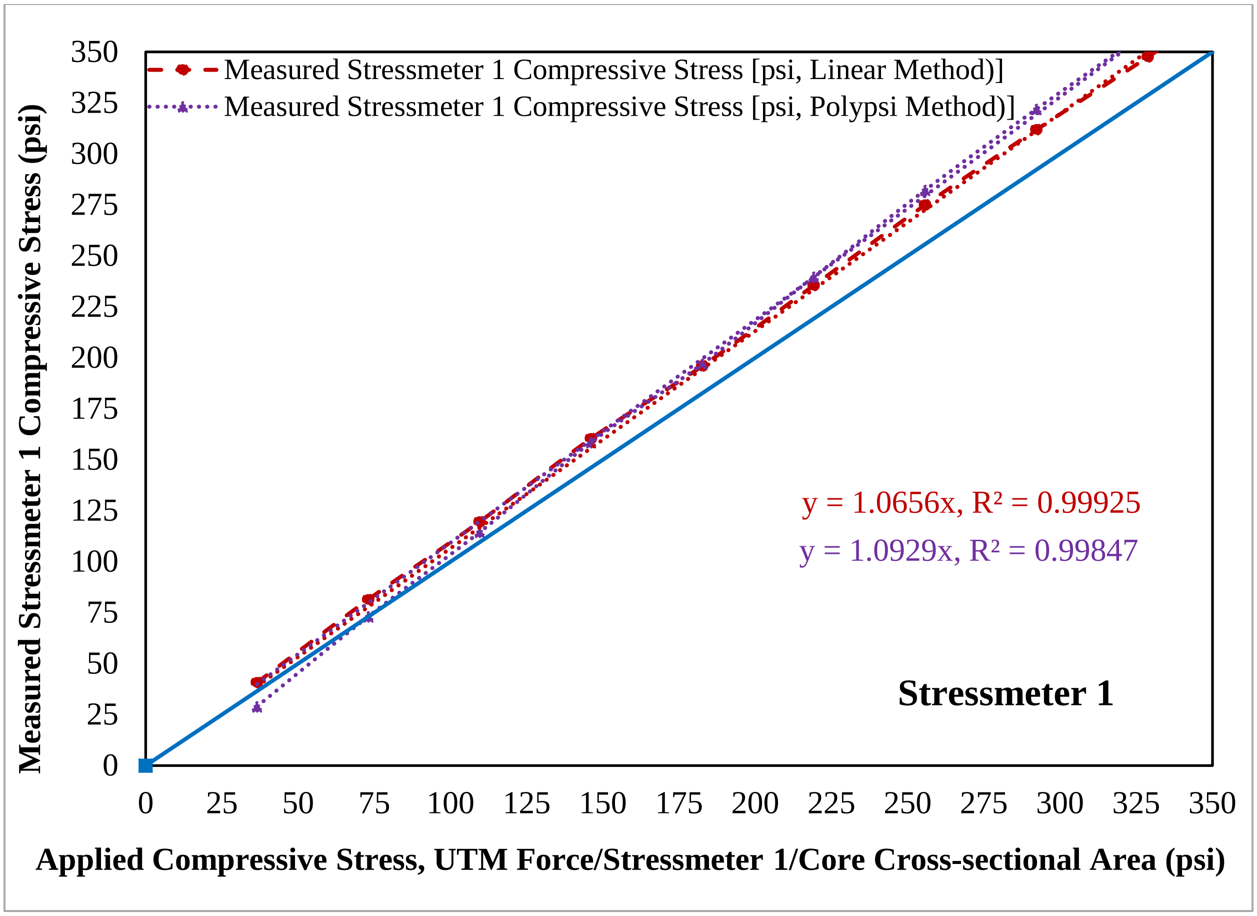

Figure 2-22: First concrete stressmeter, 5 volt and low resolution

2.5 Conclusion

Implementation of the GeoKon Model 4370 Concrete stressmeter is a novel method to directly monitor the stress development in concrete. There is some difference in the stress registered by the stressmeter and the actual/applied stress. It is indicated in the technical document provided by GeoKon that the measuring error associated with the stressmeter can be attributed to the different rigidities of the dynamometer and the concrete. This difference in the rigidities causes small differences in the stress distribution between the stressmeter and concrete. The use of the stressmeter should still allow for the quantification of the percentage benefit of pavement repair slab crack mitigation strategies.

2.6 References

[1] M. Laube and T. Rusack, “Concrete Stress Measurement – Device and Applications,” in *1st IMEKO TC20 Conference on Civil Engineering Metrology*, 2002, pp. 7–14.

[2] T. Kawaguchi and S. Nakane, “Investigations on Determining Thermal Stress in Massive Concrete Structures,” *ACI Mater. J.*, vol. 93, no. 1, pp. 96–101, 1996.

[3] M. Conrad, “A Contribution to the Thermal Stress Behavior of Roller-Compacted-Concrete (RCC) Gravity Dams-Field and Numerical Investigations,” Technical University of Munich, 2006.

[4] RILEM Technical Committee 119-TCE, “Adiabatic and Semi-Adiabatic Calorimetry to Determine the Temperature Increase in Concrete due to Hydration Heat of the Cement,” *Mater. Struct.*, vol. 30, no. 8, pp. 451–464, 1998.

[5] Geokon Incorporated, “Instruction Manual Model 4370 Concrete Stressmeter.” 2015.

[6] Campbell Scientific Inc., “Campbell Scientific Software Overview.” pp. 1–8, 2016.

[7] Campbell Scientific Inc., “PC200W,” *PC200W Datalogger Starter Software*, 2016. [Online]. Available: https://www.campbellsci.com/pc200w.

[8] Campbell Scientific Inc., “CR6 Measurement and Control System.” 2015.

Chapter 3 Characterization of Materials Used in Concrete Mixtures

3.1 Introduction

The goal of this project is to assess the effect of concrete mixture proportions, base restraint, shrinkage reducing admixtures, microfibers, and internal curing on early-age cracking potential of jointed plain concrete pavement (JPCP). In addition to placement of field slabs and laboratory assessment of concretes, HIPERPAV software sponsored by the Federal Highway Administration (FHWA) will be used to assess the cracking potential for each concrete mixture. It has been well-established that cement and aggregate properties have a significant effect on fresh and hardened concrete properties. This chapter discusses the laboratory experiments performed to characterize the materials used in the field and laboratory portions of the study. It is to be noted that the first set of the as-received cement, coarse, and fine aggregates had to be replaced, after conducting characterization testing, due to the unavailability of a ready-mix concrete supplier willing to supply the field concrete using the designated mixture design materials. Subsequently, the PI secured the next set of as-received cements and aggregates that matched the ready-mixed concrete to be used in field slabs. Only analyses conducted on the second set of the as-received materials are reported here.

3.2 Cement Characterization

3.2.1 Elemental Oxide Composition

The elemental oxide composition of the as-received cement used in this study was determined using x-ray fluorescence spectroscopy (XRF) according to ASTM C114 [1] and is listed in Table 3-1. Based on these results, the potential compound composition of the as-received cement was calculated following ASTM C150 [2], and the results are depicted in Table 3-2.

Table 3-1: Oxide chemical analysis for as-received cement*

Analyze	**CMX (wt %)**
SiO_2	21.20
Al_2O_3	5.15
Fe_2O_3	3.61
CaO	63.91
MgO	0.70
SO_3	2.59
Na_2O	0.14
K_2O	0.31
TiO_2	0.29
P_2O_5	0.15
Mn_2O_3	0.03
SrO	0.06
Cr_2O_3	0.02
ZnO	0.06
L.O.I(950°C)	1.66
Total	99.89
Na_2O_{eq}	0.35
SO_3/Al_2O_3	0.50

*Test conducted in a certified laboratory

Table 3-2: Bogue-calculated potential compound content for as-received cement

Phase	Without Processing Addition Correction
C_3S	52
C_2S	22
C_3A	8
C_4AF	11
C_4AF+2C_3A	26
$C_3S+4.75C_3A$	88

3.2.2 Mineralogical Analysis

The mineralogical composition of the as-received cement was determined using x-ray diffraction (XRD) measurements conducted in accordance with ASTM C1365 [3]. Prior to XRD measurements, the cement was wet-ground in ethanol in a McCrone micronizing mill to a particle size between 1 and 10 µm. The wet grinding method was used to avoid the effect of temperature on gypsum and its possible phase transformation to hemihydrate or anhydrite. The samples were then dried in an oven at 40°C.

In addition to analyzing the as-received cement, selective dissolutions (extractions) were performed to aid the identification of the minor phases as well as the C_3S and C_3A crystal structures. Salicylic acid/methanol (SAM) extraction was performed to dissolve the silicates and free lime and isolate a concentrated residue of aluminates, ferrites, and minor phases, such as periclase, carbonates, alkali sulfates and double alkali sulfates [4], [5]. Potassium hydroxide/sucrose extraction was used to dissolve aluminates and ferrites and obtain a residue of C_3S, C_2S, alkali sulfates and MgO [4].

XRD scans were collected using the Phillips X'Pert PW3040 Pro diffractometer equipped with the X'Celerator Scientific detector and a Cu-Kα x-ray source. Tension and current were set to 45 kV and 40 mA, respectively; 5 mm divergence and anti-scatter slits were used in the automatic mode. Scans were collected for the 7-70˚ 2θ angular range. The back-loading technique was used to load samples into the sample holder in order to minimize preferred orientation. The sample was rotated at 30 ppm, during data collection, to improve counting statistics [6]. Phase quantification was performed using the Rietveld refinement functionality of the Panalytical HighScore Plus 4.5 software. Three scans were collected for the as-received cement; the sample was re-loaded into the XRD holder prior to each scan in order to assess the precision of measurement. Table 3-3 lists the average values for each phase together with their corresponding standard deviations.

Table 3-3: Phase content using QXRD

Cement Phase	**CMX (wt %)**	**Standard Deviation**
C_3S	48.1	0.1
C_2S	23.1	0.2
C_3A	5.5	0.2
Ferrite	9.9	0.1
Gypsum	2.6	0.2
Hemihydrate	1.5	0.1
Calcite	1.2	0.2
Syngenite	0.7	0.1
Quartz	0.1	0.0
Amorphous/unidentified	7.2	0.4

Rietveld refinement is based on the assumption that all the phases present in the sample are crystalline and are accounted for. The XRD patterns of portland cements are very complex, with a number of phases that can potentially be present in small quantities and may be overlooked during the analysis. This would result in overestimation of the identified compounds. Although extractions greatly improve identification of minor phases, overestimation can also result from the presence of amorphous content. Previous studies reported that amorphous content in OPC of a few percent can be a result of the grinding process [7]. Additionally, amorphous content of cement may be increased from the use of processing additions in cement production. An external standard method was selected in order to correct for the potential presence of amorphous and/or unidentified content in the cement sample. In this method, an external standard is measured separately from the sample and is used to determine the experimental calibration factor (G) [8]–[11].

$$G = \frac{S_S \rho_S V_S^2 \mu_S^*}{W_S} \qquad \text{Equation 3-1}$$

where S_S, ρ_S, V_S, μ_S^*, and W_S are the Rietveld scale factor determined by the refinement software, density, unit cell volume, mass absorption coefficient, and crystalline weight fraction of the standard material in the external standard, respectively. Madsen et al. [11] state that this calibration factor "is dependent only on the instrumental and data collection conditions and is independent of individual phase and overall sample-related parameters." The calibration factor G is then used to determine the weight fraction of the crystalline phase "W_p" from Rietveld analysis of the sample according to:

$$W_p = \frac{S_p \rho_p V_p^2 \mu_{Sample}^*}{G} \text{ (wt.\%)} \qquad \text{Equation 3-2}$$

where μ^*_{sample} is the mass absorption coefficient (MAC) of the sample, determined independently of the Rietveld analysis [9], [10]. Typically, μ^*_{sample} is calculated using the tabulated elemental mass absorption coefficients for the oxides present in the sample as determined by x-ray fluorescence spectroscopy [9]. The amorphous/unidentified content is calculated by subtracting the sum of identified crystalline phases from 100%.

In this study, corundum (Standard Reference Material 676a) obtained from the National Institute of Standards and Technology (NIST) was selected as an external standard. MAC of corundum was calculated using the MAC calculator functionality in the Panalytical HighScore Plus 4.5 software and was equal to 30.91 cm^2/g. MAC of cement was determined to be 95.82 cm^2/g and was based on the chemical oxide composition listed in Table 3-1; loss on ignition content was attributed to CO_2.

3.2.3 Cement Physical Characteristics

Cement fineness has a significant effect on cement hydration, especially during the early stages of hydration [12]. In this study, cement fineness was measured using the Blaine (air permeability) method as described in ASTM C204 [13]. The measurements were performed in triplicate and the average value is reported in Table 3-4. While the method is widely used in the cement industry for quality control, it offers some drawbacks. For example, a single averaged value may be given to two cements with different proportion of fines; that is, two different cements having the same surface area will give the same Blaine value even though they have very different particle size distributions (PSDs) [14]. In contrast, particle size distribution measurements provide more accurate insight on the quality and grading of the cement.

PSD measurement describes the frequency and size of particles contained in a sample [15]. Typical particle sizes in portland cement vary from < 1 μm to 100 μm in diameter [14]. The characterization of the particles of the as-received cements was conducted using the principle of laser diffraction. Mastersizer 2000 laser scattering particle size analyzer manufactured by Malvern Instruments was used to analyze the particle size distribution of the cements using the dry method. The obtained differential and cumulative particle size distributions are plotted in Figure 3-1 and Figure 3-2, respectively. The results of cement density measurements, conducted in accordance to ASTM C188 [16], are presented in Table 3-4.

Table 3-4: Cement particle size analysis, Blaine fineness and density

Physical Properties	**CMX**
D_{10} (μm)	2.050
D_{50} (μm)	11.779
D_{90} (μm)	34.901
Mean size (MPS) (μm)	5.378
ASTM C204-Blaine Fineness (m^2/kg)	516
Density (g/cm^3)	3.15

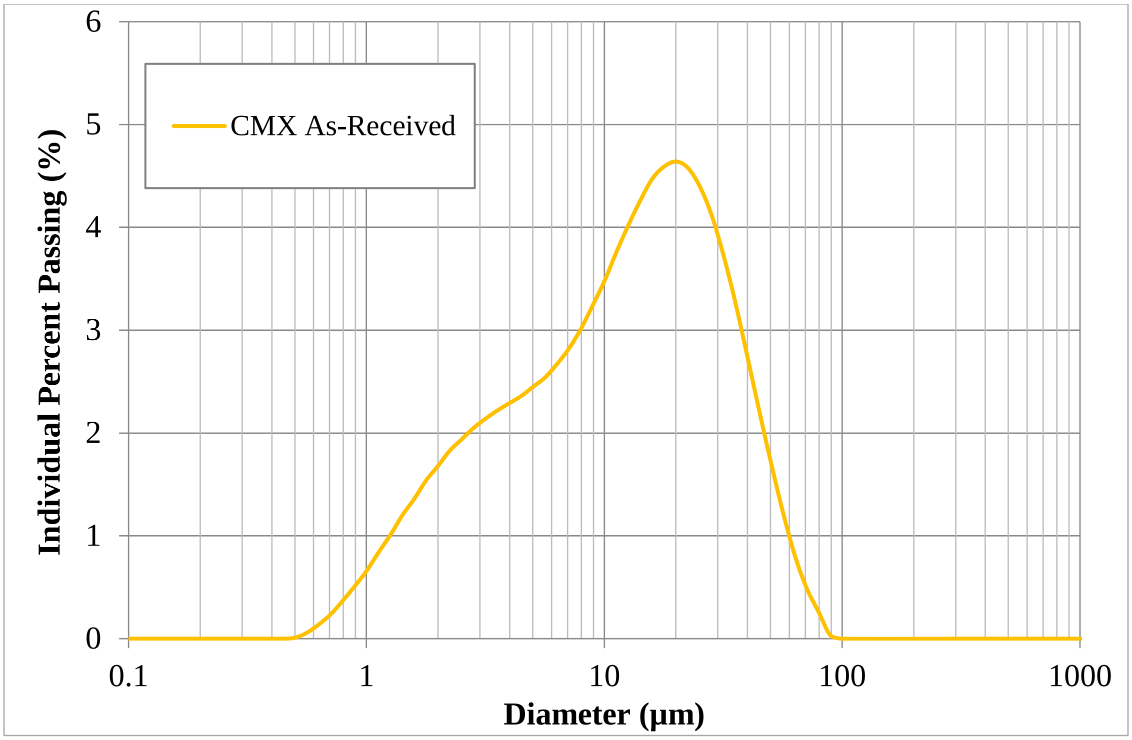

Figure 3-1: Differential particle size distribution for CMX cement

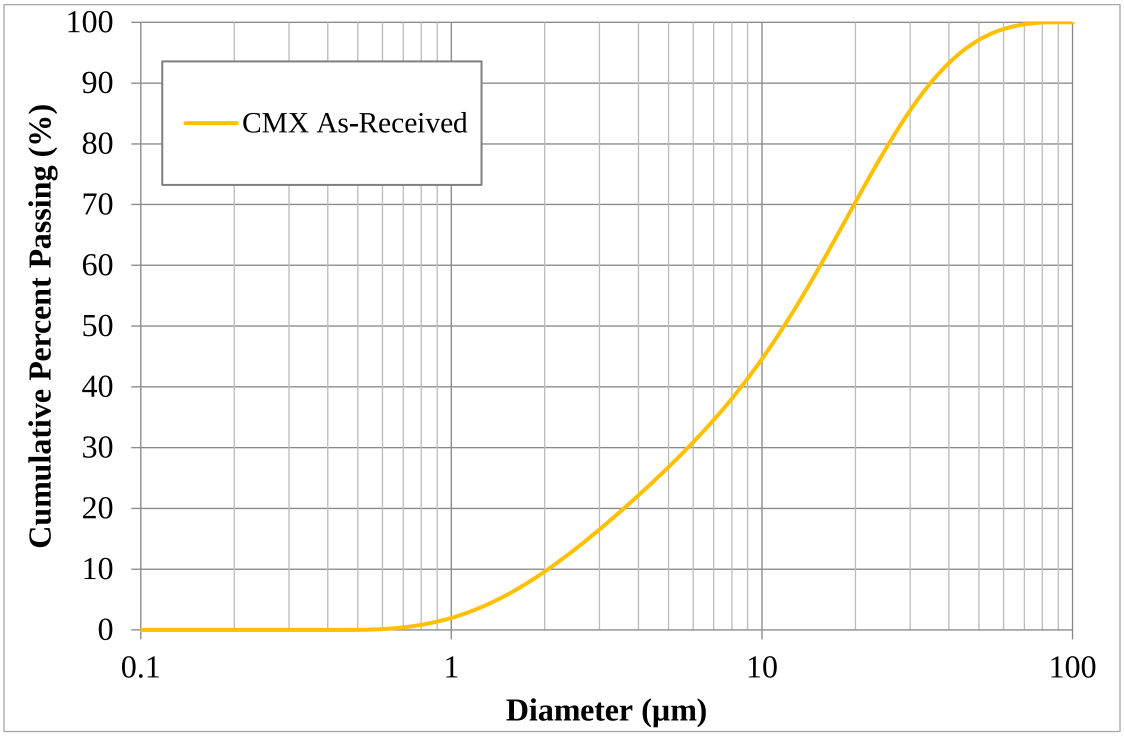

Figure 3-2: Cumulative particle size distribution for CMX Cement

3.3 Aggregate Properties

In order to characterize the aggregates used in this study, a representative sample of coarse and fine aggregate was obtained from stockpiles. The aggregates were collected from 5-6 locations in the stockpile following the guidelines specified in Alexander and Mindess [17]. Aggregates were then tested in the laboratory to determine their gradation, fineness modulus, bulk specific gravity (BSG), absorption capacity and dry-rodded unit weight (DRUW). The tests were conducted in accordance to ASTM C33 [18], ASTM C127 [19] and C128 [20] for coarse and fine aggregates, respectively.

In order to determine aggregate gradation, a 22-lb sample of #57 aggregate, a 5-lb sample of #89 aggregate, and a 5-lb sample of fine aggregate were oven-dried at 105°C to constant mass conforming to ASTM C136 [21]. Sieve analysis was performed on 4 samples, and the averages are plotted in Figure 3-3 through Figure 3-5. Aggregate gradation reported by the aggregate producer is also included in the figures for reference. Both the producer and USF-graded sand are marginally outside the ASTM limits for coarser sizes (#4, #8 and #16), which is somewhat typical for Florida sands.

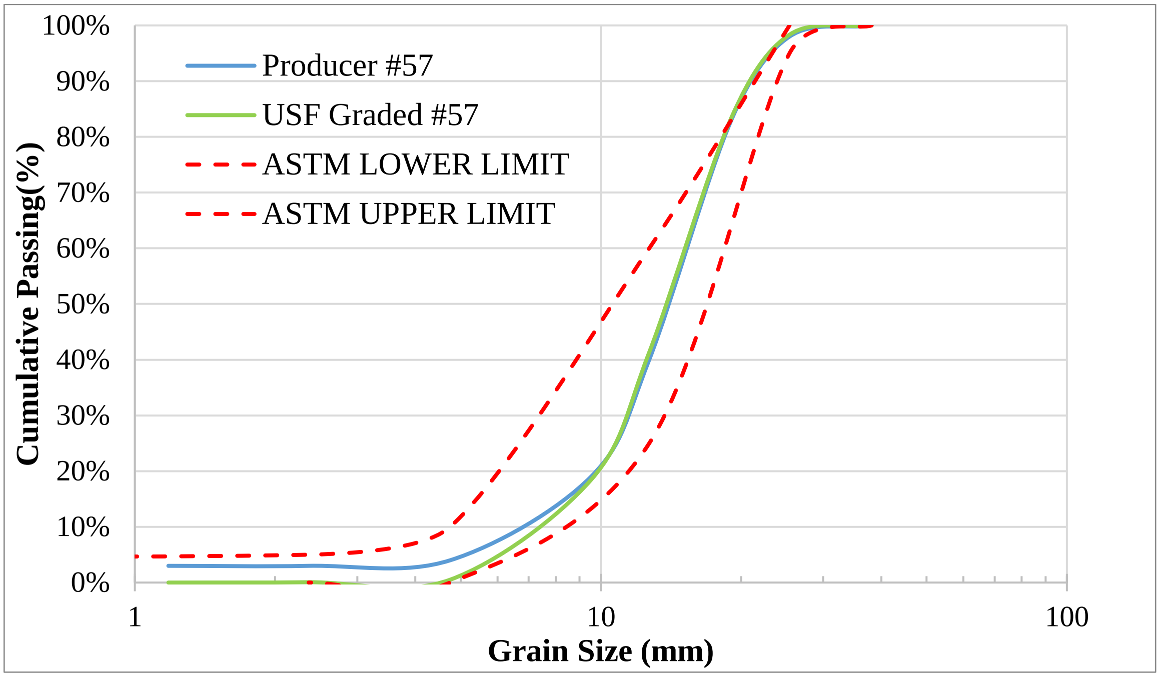

Figure 3-3: Aggregate grading for #57 stone

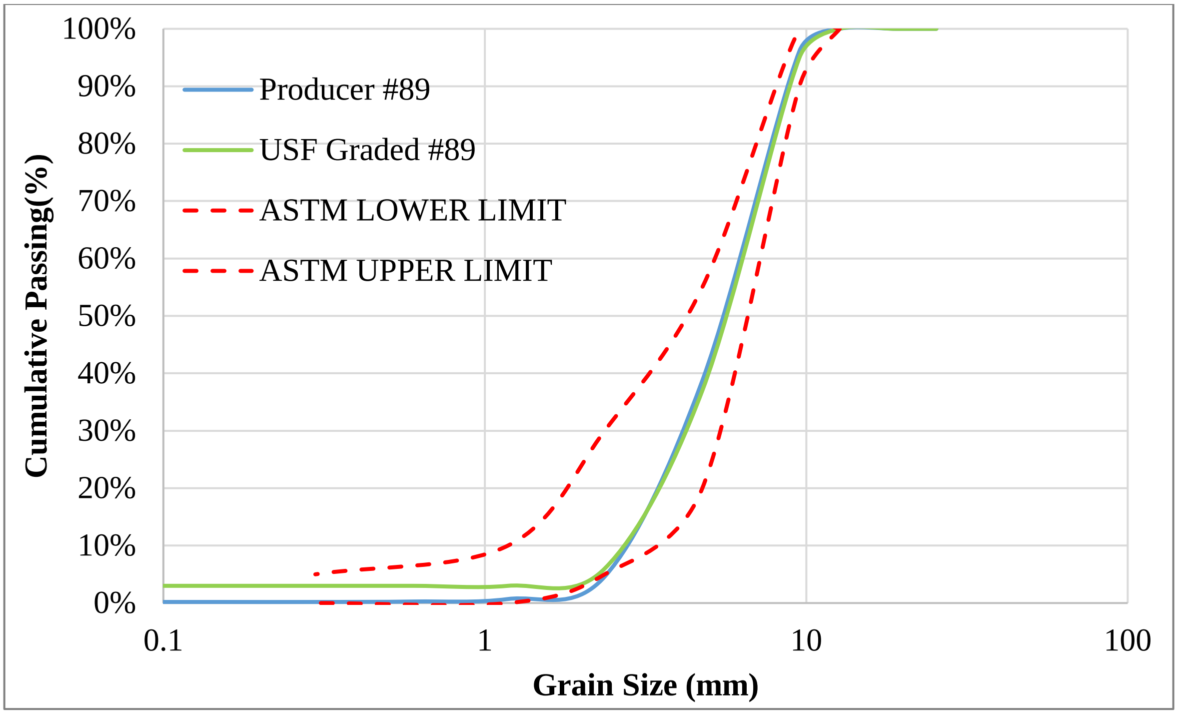

Figure 3-4: Aggregate grading for #89 stone

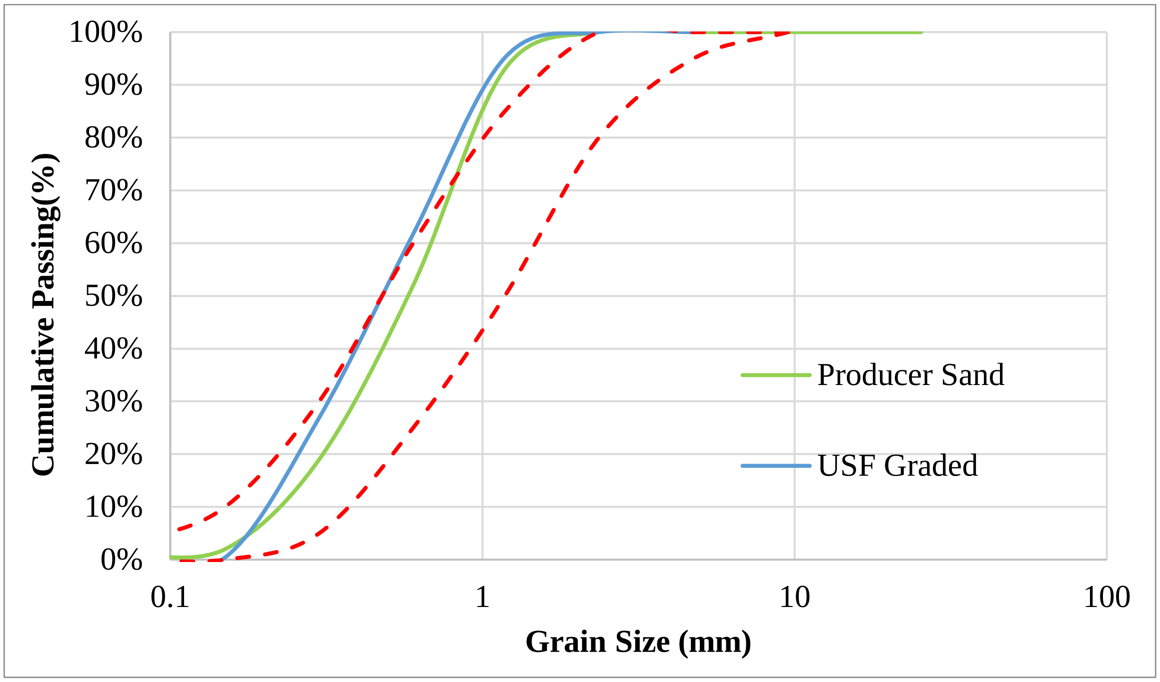

Figure 3-5: Aggregate grading for sand

Based on sieve size analysis, the following fineness moduli values were obtained as shown in Table 3-5:

Table 3-5: Fineness moduli for aggregates

Aggregate	Fineness Modulus
#57	6.98
#89	5.62
Sand	2.16

For the determination of the bulk specific gravity (BSG) and the absorption capacity (AC) of aggregates in the Saturated-Surface-Dry (SSD) moisture state, an oven-dried weight of aggregate in excess of 10 lb was used for #57, while for #89 sample weight in excess of 6 lb was used for adequate representation of all sizes as required by ASTM C127. The samples tested for $BSG_{(SSD)}$ and absorption were graded as shown in Figure 3-3 through Figure 3-5.

Testing to characterize the specific gravities of coarse and fine aggregates was performed conforming to procedures specified in ASTM C127 [19] and C128 [20], respectively, and the results are listed in Table 3-6. The dry rodded unit weights (DRUW) for coarse aggregates were obtained as specified by ASTM C29 for samples using a 0.33 ft^3 cylinder for #57 and a 0.25 ft^3 cylinder for #89 stone. Four determinations were made for each aggregate and the average value is reported in Table 3-6.

Table 3-6: Bulk specific gravity and absorption capacity for #57, #89 aggregates and sand

Aggregate	BSG_{SSD}	BSG_{OD}	AC (%)	DRUW (lb/ft^3)
#57	2.41	2.32	3.95%	88.59
#89	2.39	2.28	5.00%	81.85
Sand	2.64	2.64	0.56%	-

In addition to coarse and fine aggregate, lightweight aggregate (LWA) was obtained for this study. The use of pre-wetted lightweight aggregate (LWA) in concrete mixes is a common strategy to mitigate the development of autogenous shrinkage, as LWA provides an internal source of moisture thereby preventing self-desiccation. For this project, an expanded clay material with the properties listed in Table 3-7 was used for mixture proportioning. Figure 3-6 presents the gradation of LWA. This lightweight aggregate material was previously used and characterized in a recent FDOT study [22].

Table 3-7: Properties of lightweight aggregate characterized in [22]

Aggregate	**BSG$_{SSD}$**	**BSG$_{OD}$**	**AC (%)**
LWA	1.54	1.28	25.22% (96.5*)

*Desorption in 94% RH environment

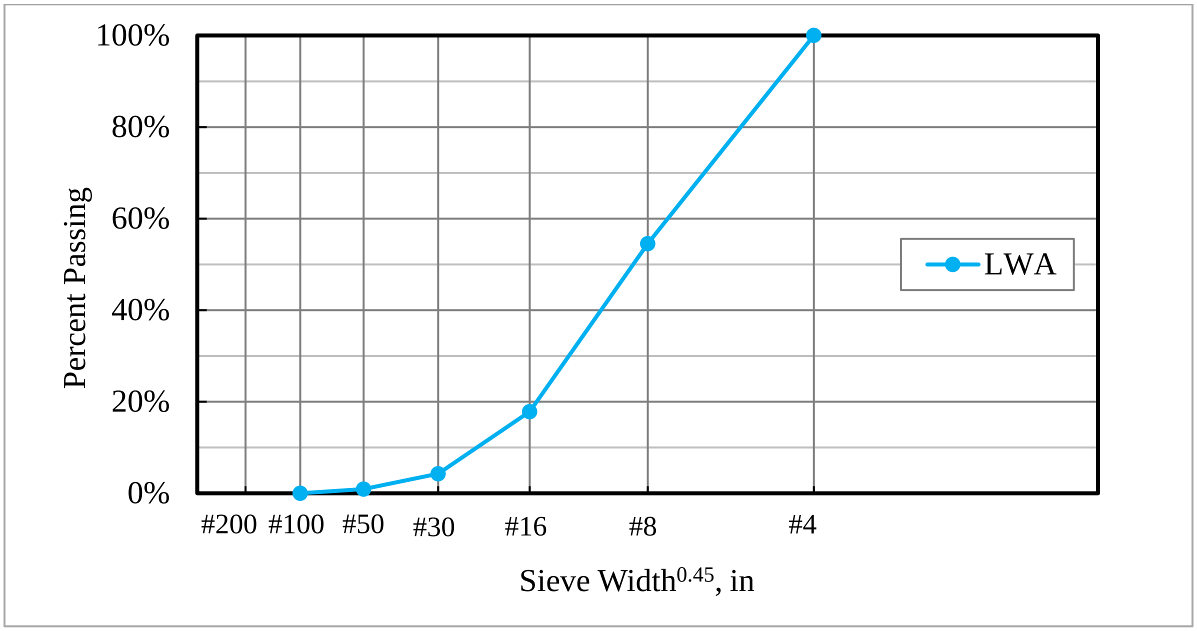

Figure 3-6: Gradation of LWA (adapted from [22])

ASTM C1761 [23] specifies the following equation for mixture proportioning based on chemical shrinkage, absorption capacity of aggregate, and cementitious material content:

$$M_{LWA} = \frac{C_f \cdot C_s \cdot \alpha_{\max}}{S \cdot W_{LWA}} \qquad \text{Equation 3-3}$$

Where,

M_{LWA} = mass of lightweight aggregate required in oven-dry condition (lb/yd^3)

C_f = cement factor (lb/yd^3)

α_{max} = maximum degree of hydration attainable based on the w/b ratio used

C_s = chemical shrinkage (lb/lb of cementitious)

S = saturation level of the aggregate (between 0 and 1)

W_{LWA} = mass of water released by the LWA to equilibrium mass in a 94% RH environment (lb)

The LWA is added to a concrete mixture by replacing an equal volume of fine aggregate present in the original concrete mix design as prescribed in [23] and [24] . A chemical shrinkage value of 0.07 lb/lb of cementitious material, as suggested in ASTM C1761 [23], was used for mixture proportioning. One half of the LWA dosage suggested by Equation 3-3 was used in mixture proportioning. This is done in order to reduce the concomitant loss in strength that would likely follow from placing the specified quantity of fine aggregate with LWA.

3.4 References

[1] ASTM C114-11b, “Standard Test Method for Chemical Analysis of Hydraulic Cement,” West Conshohocken, PA: ASTM International, 2012.

[2] ASTM C150/C150M-12, “Standard Specification for Portland Cement,” West Conshohocken, PA: ASTM International, 2012.

[3] ASTM C1365-06 (2011), “Standard Test Method for Determination of the Proportion of Phases in Portland Cement and Portland-Cement Clinker Using X-Ray Powder Diffraction Analysis,” West Conshohocken, PA: ASTM International, 2012.

[4] P. E. Stutzman, “Guide for X-Ray Powder Diffraction Analysis of Portland Cement and Clinker,” Gaithersburg, MD, 1996.

[5] W. A. Gutteridge, “On the Dissolution of the Interstitial Phases in Portland Cement,” *Cem. Concr. Res.*, vol. 9, no. 3, pp. 319–324, 1979.

[6] D. Bish and R. J. Reynolds, “Sample Preparation for X-Ray Diffraction,” in *Modern Powder Diffraction*, D. Bish and J. Post, Eds. Washington, DC: The Mineralogical Society of America, 1989, pp. 73–99.

[7] J. P. Cline, R. B. Von Dreele, R. Winburn, P. W. Stephens, and J. J. Filliben, “Addressing the amorphous content issue in quantitative phase analysis: the certification of NIST standard reference material 676a,” *Acta Crystallogr. A.*, vol. 67, no. Pt 4, pp. 357–67, Jul. 2011.

[8] B. H. O’Connor and M. D. Raven, “Application of the Rietveld Refinement Procedure in Assaying Powdered Mixtures,” *Powder Diffr.*, vol. 3, no. 01, pp. 2–6, Jan. 1988.

[9] D. Jansen, C. Stabler, F. Goetz-Neunhoeffer, S. Dittrich, and J. Neubauer, “Does Ordinary Portland Cement Contain Amorphous Phase? A Quantitative Study Using an External Standard Method,” *Powder Diffr.*, vol. 26, no. 01, pp. 31–38, Mar. 2012.

[10] M. A. G. Aranda, A. G. De la Torre, and L. Leon-Reina, “Rietveld Quantitative Phase Analysis of OPC Clinkers, Cements and Hydration Products,” *Reviews in Mineralogy and Geochemistry,* vol. 74, no. 1. pp. 169–209, 2012.

[11] I. C. Madsen, N. V. Y. Scarlett, and A. Kern, “Description and survey of methodologies

for the determination of amorphous content via X-ray powder diffraction," *Zeitschrift für Krist.*, vol. 226, no. 12, pp. 944–955, Dec. 2011.

[12] S. Mindess, F. J. Young, and D. Darwin, *Concrete*. Upper Saddle River, NJ: Pearson Education, Inc., 2003.

[13] ASTM C204-16, "Standard Test Method for Fineness of Hydraulic Cement by Air Permeability Apparatus," West Conshohocken, PA: ASTM International, 2016.

[14] P. K. Mehta and P. J. M. Monteiro, *Concrete: Microstructure, Properties and Materials*, 3rd ed. New York, NY: McGraw-Hill, 2006.

[15] A. Jillavenkatesa, S. J. Dapkunas, and L. Lum, *Particle Size Characterization*. National Institute of Standards and Technology (NIST), Special Publication 960-1, 2001.

[16] ASTM C188-09, "Standard Test Method for Density of Hydraulic Cement," West Conshohocken, PA: ASTM International, 2012.

[17] M. Alexander and S. Mindess, *Aggregates in Concrete*, 1st ed. CRC Press, 2005.

[18] ASTM C33/C33M-16, "Standard Specification for Concrete Aggregates," West Conshohocken, PA: ASTM International, 2016.

[19] ASTM C127-15, "Standard Test Method for Relative Density (Specific Gravity) and Absorption of Coarse Aggregate," West Conshohocken, PA: ASTM International, 2015.

[20] ASTM C128-15, "Standard Test Method for Relative Density (Specific Gravity) and Absorption of Fine Aggregate," West Conshohocken, PA: ASTM International, 2015.

[21] ASTM C136-06, "Standard Test Method for Sieve Analysis of Fine and Coarse Aggregates," West Conshohocken, PA: ASTM International, 2006.

[22] M. Tia, T. Subgranon, K. Kim, A. M. Rodriguez, and A. Algazlan, "Internally Cured Concrete for Pavement and Bridgedeck Applications," University of Florida, Gainsville, FL, 2015.

[23] ASTM C1761/C1761M-15, "Standard Specification for Lightweight Aggregate for Internal Curing of Concrete," West Conshohocken, PA: ASTM International, 2015.

[24] D. P. Bentz and W. J. Weiss, "Internal Curing : A 2010 State-of-the- Art Review," *Civ.*

Eng., 2011.

Chapter 4 Effect of Cementitious Materials on Heat of Hydration Activation Energy

4.1 Introduction

One of the objectives of this project was to quantify the effects of concrete temperature rise, stress development and evolution of mechanical properties on early-age cracking of rapid repair materials. The cementitious material apparent activation energy (E_a) is needed when using modeling software to analyze the concrete early-age cracking tendency. In chemistry, E_a is defined as the "energy barrier between reactants and products" [1]. The rate of reaction (k) is proportional to the temperature as shown by the Arrhenius equation (Equation 4-1). There is a linear relationship between the natural logarithm of k and the reciprocal of the temperature (T), as shown in Equation 4-2 [2].

$$k = \mathrm{A}\,\mathrm{e}^{-\left(\frac{\mathrm{E_a}}{\mathrm{RT}}\right)} \qquad \text{Equation 4-4}$$

$$\ln k = -\frac{E_a}{\mathrm{RT}} + \ln \mathrm{A} \qquad \text{Equation 4-5}$$

Where,

k = Specific rate of reaction

A = Pre-exponential term

E_a = Activation energy (kJ/mol)

R = Universal gas constant [8.314 J/(mol·K)]

T = Temperature (K)

Cement is a multi-component material that experiences multiple simultaneous reactions during hydration. The term "apparent" is added to reflect that the E_a value is indicative of the whole system rather than a single chemical reaction [2] - [5]. The apparent activation energy is affected not only by cement chemistry, but also by the concrete mixture parameters such as w/c ratio, presence of supplemental cementitious materials (SCMs) and/or chemical admixtures [6] - [8]. In essence, apparent E_a, which hereinafter will be referred to as E_a, describes the temperature sensitivity of the hydration rate of a concrete mixture. E_a can be calculated by plotting ln(k), determined for at least three different temperatures, against 1/T. E_a is the product of the negative slope and the universal gas constant [1].

In cement and concrete research, E_a is typically determined from heat of hydration (HOH) or compressive strength measurements. This task report focuses on the determination of HOH-based activation energy, while strength-based E_a will be discussed in Chapter 6. HOH-based E_a is used with semi-adiabatic calorimetry to model the concrete temperature rise [9]–[12].

4.2 Methodology

Isothermal conduction calorimetry was used to measure the heat of hydration of paste samples at 23, 30 and 40°C conforming to ASTM 1702 Method A internal mixing procedure [13]. Heat flow measurements were conducted using a TAM Air isothermal conduction calorimeter produced by TA Instruments. The paste samples were prepared following the concrete mix design outlined in Table 4-1. A typical mix design, currently used in concrete pavement construction, was adopted for Mix #1, which was taken as the Control mix. As the project focus was on methods of reducing cracking potential for high high-early-strength mixtures, several strategies were implemented to achieve this objective through concrete mixture design modification. For Mixes #2 and #3, aggregate gradation was optimized to reduce cement content by reducing the required paste volume. In Mix #2, the w/c ratio was maintained the same as in Mix #1 (0.384), while for Mix #3 it was reduced to 0.34 to compensate for the anticipated reduction in mechanical properties due to cement reduction. Mix #4 was prepared with the Control mix proportions but with the addition of a shrinkage-reducing admixture (SRA), which was expected to reduce capillary stresses and, consequently, concrete cracking potential due to shrinkage.

The summary of the paste mixes is outlined in Table 4-2. Volumetric solutions of chemical admixtures were prepared for each mix. The admixers used for mixing purposes contained 4 individual syringes that facilitated isolation of the chemical admixture solutions before mixing, per recommendations of admixture manufacturers. Before mixing, the cement was weighed in an ampoule and was attached to the admixer containing the weighed amounts of chemical admixture solutions. All the admixers were lowered into the calorimeter at the same time and kept there until calorimetry heat flow equilibrium was achieved. After the calorimeter achieved equilibrium, the experiment was started and the chemical admixture solutions were injected in the following order and timing: 10 seconds for water reducer solution injection, 15 seconds of constant internal mixing, 5 seconds for air-entraining admixture (AEA) solution injection, 15 seconds of constant internal mixing, 5 seconds for superplasticizer solution injection, 10 seconds of constant internal mixing, 5 seconds for shrinkage-reducing admixture (SRA) injection (if needed), mixing for 10 seconds if an SRA was used, 10 seconds for injection of accelerator, 10 seconds of constant internal mixing, and heat flow measurements were collected for 7 days.

Table 4-1: Concrete mix design per 1 m^3 (1 yd^3)

Mix Constituents	Mix #1	Mix #2	Mix #3	Mix #4
Cement, kg (lb)	534 (900)	415 (700)	415 (700)	534 (900)
Coarse Aggregate #57 limestone (SSD), kg (lb)	997 (1,680)	682 (1,150)	700 (1,180)	997 (1,680)
Intermediate Aggregate #89 limestone (SSD), kg (lb)	0.0	409 (690)	421 (710)	0.0
Fine Aggregate (SSD), kg (lb)	492 (829)	610 (1,028)	625 (1,054)	501 (844)
Water, kg (lb)	193 (325)	150 (252)	131 (221)	189 (319)
Type F Superplasticizer, ml (fl oz)	0.0	948 (24.5)	1354 (35.0)	0.0
Type E Accelerator, ml (fl oz)	14853 (384)	11554 (298.7)	11554 (298.7)	14853 (384)
Air Entrainer, ml (fl oz)	38 (1.0)	38 (1.0)	38 (1.0)	38 (1.0)
Type D Water Reducer, ml (fl oz)	874 (22.6)	696 (18.0)	696 (18.0)	874 (22.6)
Shrinkage Reducing Admixture, ml (gal)	0.0	0.0	0.0	3713 (0.75)
(w/c)	0.384	0.384	0.34	0.384

Table 4-2: Isothermal calorimetry paste mix design

Paste Mix Constituents	**Mix #1**	**Mix #2**	**Mix #3**	**Mix #4**
Cement (g)	4.070	4.070	4.395	4.075
Type F Superplasticizer (ml/100kg of cement)	0	228.2	325.9	0
Type E Accelerator (ml/100kg of cement)	2,781.5	2,781.5	2,781.5	2,781.5
Air Entrainer (ml/100kg of cement)	7.3	9.3	9.3	7.3
Type D Water-reducing Admixture (ml/100kg of cement)	167.6	167.6	167.6	167.6
Shrinkage Reducing Admixture (ml/100kg of cement)	0	0	0	695.4
(w/c)	0.384	0.384	0.34	0.384

Heat flow and cumulative heat of hydration were normalized per gram of cement in the sample. Evolution of the degree of hydration was calculated from the measured cumulative heat using Equation 4-3 and Equation 4-4 [9]–[11] and plotted as a function of time.

$$\alpha(t) = \frac{H(t)}{H_u} \qquad \text{Equation 4-6}$$

Where,

$\alpha(t)$ = Degree of hydration at time (t)

$H(t)$ = Heat evolved from time 0 to time t (J/gram),

H_u = Total available heat (J/gram)

$$H_{cem} = 500\, P_{C_3S} + 260\, P_{C_2S} + 866\, P_{C_3A} + 420\, P_{C_4AF} + 624\, P_{SO_3} + 1186\, P_{FreeCaO} + 850\, P_{MgO} \qquad \text{Equation 4-7}$$

Where,

H_{cem} = Total heat of hydration of portland cement as describe above (J/gram)

P_i = Ratio of mass of i^{th} component to total cement content

The exponential function (Equation 4-5) was then used to determine the E_a [11].

$$\alpha(t) = \alpha_u\, e^{-\left(\frac{\tau}{t}\right)^{\beta}} \qquad \text{Equation 4-8}$$

Where,

α_u = Ultimate degree of hydration

τ = Hydration time constant (hours)

t = Elapsed time since start of cement–water interaction (hours)

β = Shape parameter (dimensionless)

The α_u, τ, and β parameters were obtained by using the Solver function in Microsoft Excel to minimize the residuals between the measured values of α(t) (Equation 4-3) and the modeled values (Equation 4-5). The rate of reaction "*k*" was then obtained by taking the reciprocal of the hydration time constant τ. The activation energy was determined using the Arrhenius relationship in Equation 4-2. Additional curve fitting data are presented in Appendix A.

4.3 Results and Discussion

The heat of hydration of the cement paste mixtures (Mix #1 - Mix #4) are shown in Figures 4-1 through 4-3, at three temperatures (23, 30, and 40°C). At all temperatures, a lower w/c ratio yielded the lowest cumulative heat of hydration followed by SRA Mix #3.

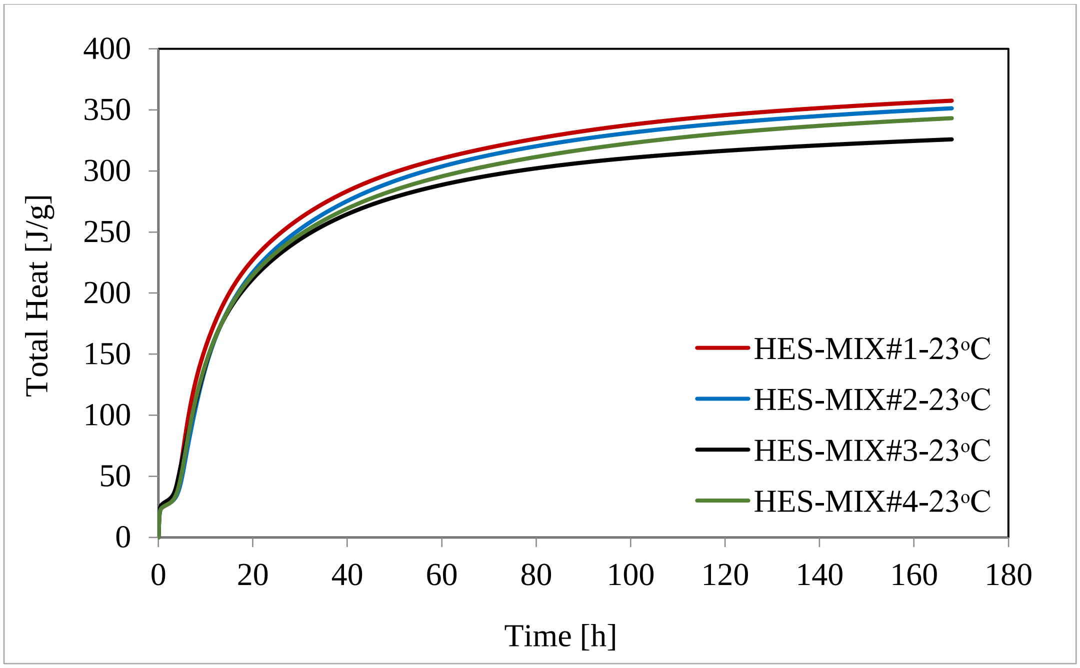

Figure 4-1: Heat of hydration of cement paste mixes at 23°C

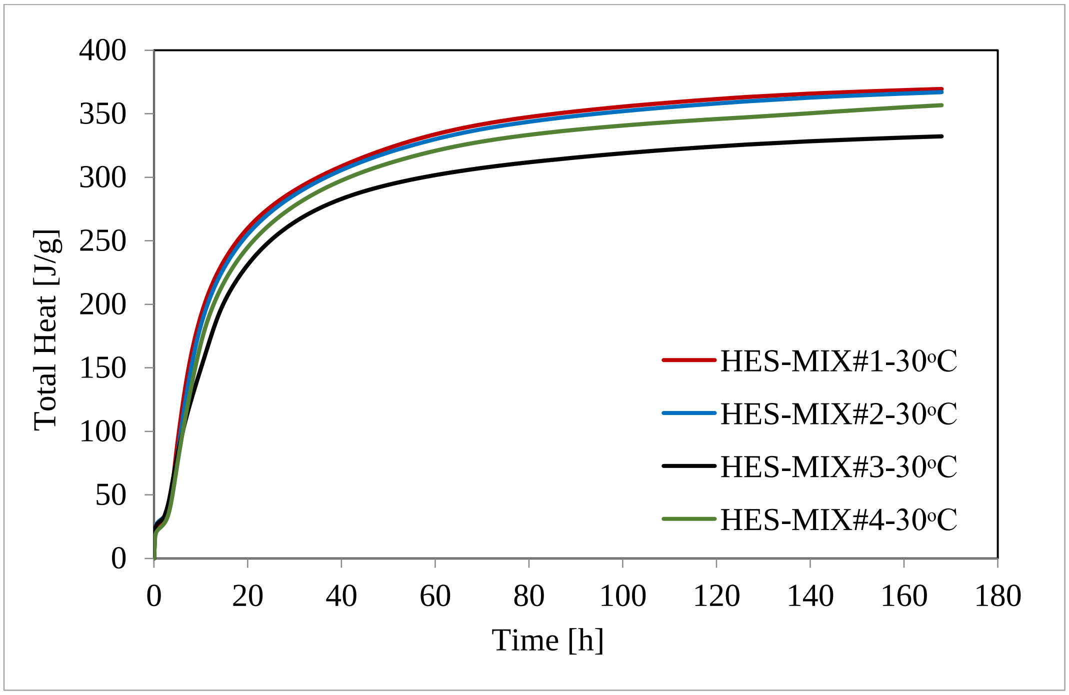

Figure 4-2: Heat of hydration of cement paste mixes at 30°C

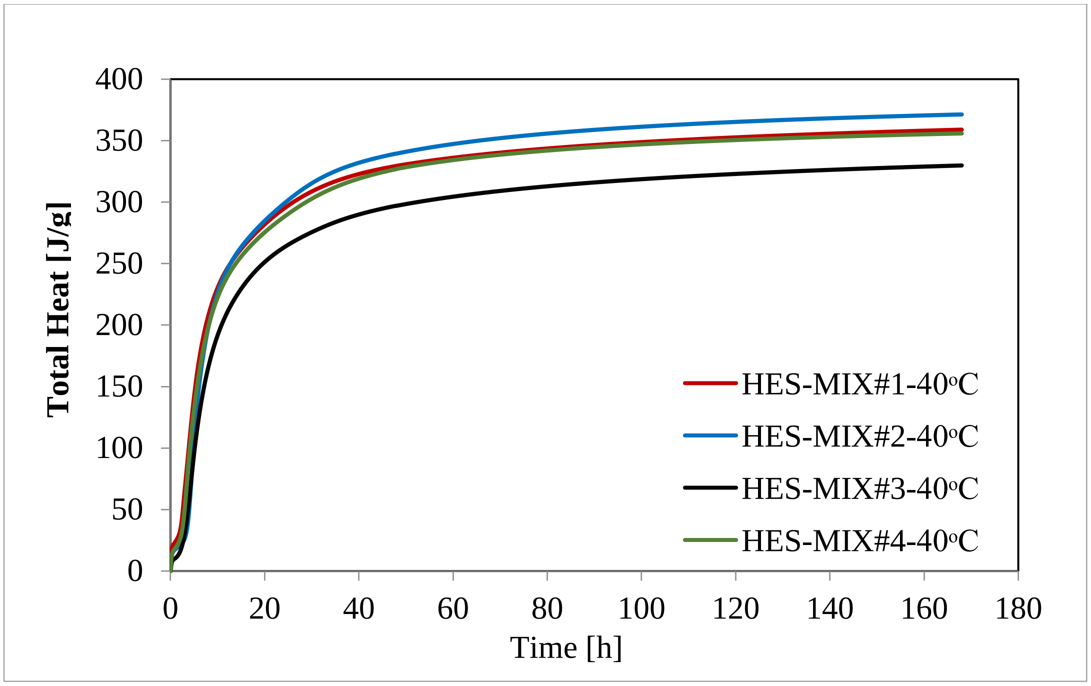

Figure 4-3: Heat of hydration of cement paste mixes at 40°C

Typically, E_a is calculated by keeping α_u and β parameters fixed, and only allowing τ to vary. This method is based on the assumption that α_u is not affected by the curing temperature; however, it has been reported that E_a values can vary depending on the temperature range selected for the E_a determination. Several researchers [8], [14] reported E_a values calculated by allowing α_u, β, and τ parameters to vary in order to eliminate the assumption of the constant α_u at all temperatures. This approach was utilized in this study as well, and the calculated E_a values are listed in Table 4-3.

Comparing Mix #2 to Mix#1, it appears that the addition of a superplasticizer resulted in a decrease in E_a. This is contradictory to the observations of Wirquin et al. [5], who reported a slight increase in E_a with superplasticizer addition. Unfortunately, the authors did not report the chemical composition of the superplasticizer, so it is difficult to compare their finding to the result obtained in this study. In contrast, Poole et al. [7] reported a decrease in E_a with addition of naphthalene sulfonate–based and polycarboxylate-based superplasticizers. A decrease in the w/c ratio (Mix #3 compared to Mix #2) and an increase in the superplasticizer dosage resulted in a decrease in α_u, which is consistent with reported results [10], [15]. Addition of SRA (Mix #4 compared to Mix #1) did not have a significant effect on E_a, which is consistent with previously reported findings [16].

Table 4-3: HOH-based activation energy

Mix ID	**Temp(°C)**	**α_u**	**β**	**τ**	***Ea* (kJ/mol)**	**R^2**
Mix #1	23	0.984	0.743	9.64	32.2	0.998
	30	0.975	0.824	7.31		
	40	0.908	0.914	4.74		
Mix #2	23	0.956	0.801	10.65	25.9	0.972
	30	0.966	0.839	7.65		
	40	0.927	1.073	5.97		
Mix #3	23	0.875	0.817	9.18	18.6	0.998
	30	0.865	0.896	7.83		
	40	0.828	1.006	6.10		
Mix #4	23	0.944	0.756	10.25	31.0	0.995
	30	0.926	0.893	8.02		
	40	0.902	0.943	5.19		

4.4 Conclusion

Isothermal calorimetry measurements were conducted to determine the HOH-based activation energy values. E_a decreased with the addition of superplasticizer and with a decrease in the w/c ratio. Addition of shrinkage-reducing admixture did not have a significant effect on E_a. The degree of hydration decreased with increasing the hydration temperature, which is in line with lower strengths and durability that are typical encountered with higher concrete hydration temperatures.

4.5 References

[1] J. E. McMurray and R. C. Fay, *Chemistry*, 5th ed. Upper Saddle River, NJ: Pearson Education, 2008.

[2] H. Kada-Benameur, E. Wirquin, and B. Duthoit, “Determination of Apparent Activation Energy of Concrete by Isothermal Calorimetry,” *Cem. Concr. Res.*, vol. 30, no. 2, pp. 301–305, 2000.

[3] K. O. Kjellsen and R. J. Detwiler, “Later Ages Strength Prediction by a Modified Maturity Method,” *ACI Mater. J.*, vol. 90, no. 3, pp. 220–227, 1993.

[4] L. D’Aloia and G. Chanvillard, “Determining the ‘Apparent’ Activation Energy of Concrete: Ea—Numerical Simulations of the Heat of Hydration of Cement,” *Cem. Concr. Res.,* vol. 32, no. 8, pp. 1277–1289, 2002.

[5] E. Wirquin, M. Broda, and B. Duthoit, “Determination of the Apparent Activation Energy of one Concrete by Calorimetric and Mechanical Means: Influence of a Superplasticizer,” *Cem. Concr. Res.*, vol. 32, pp. 1207–1213, 2002.

[6] A. K. Schindler, “Effect of Temperature on Hydration of Cementitious Materials,” *ACI Mater. J.*, vol. 101, no. 1, pp. 72–81, 2004.

[7] J. L. Poole, K. a. Riding, M. C. G. Juenger, K. J. Folliard, and A. K. Schindler, “Effect of Chemical Admixtures on Apparent Activation Energy of Cementitious Systems,” *J. Mater. Civ. Eng.*, vol. 23, no. 12, pp. 1654–1661, 2011.

[8] N. Shanahan, A. Bien-aime, D. Buidens, T. Meagher, A. Sedaghat, K. Riding, and A. Zayed, “Combined Effect of Water Reducer – Retarder and Variable Chloride-Based Accelerator Dosage on Rapid Repair Concrete Mixtures for Jointed Plain Concrete Pavement,” *J. Mater. Civ. Eng.*, pp. 1–10, 2016.

[9] A. K. Schindler, “Concrete Hydration, Temperature Development, and Setting at Early-Ages,” University of Texas at Austin, Austin, 2002.

[10] A. K. Schindler and K. J. Folliard, “Heat of hydration models for cementitious materials,” *ACI Mater. J.*, vol. 102, no. 1, pp. 24–33, 2005.

[11] J. L. Poole, K. A. Riding, K. J. Folliard, M. C. G. Juenger, and A. K. Schindler, “Methods

for Calculating Activation Energy for Portland Cement," *ACI Mater. J.*, vol. 104, no. 1, pp. 303–311, 2007.

[12] J. L. Poole, "Modeling Temperature Sensitivity and Heat Evolution of Concrete," The University of Texas at Austin, 2007.

[13] ASTM C1072-9a, "Standard Test Method for Measurement for Measurement of Heat of Hydration of Hydraulic Cementitious Materials Using Isothermal Conduction Calorimetry," West Conshohocken, PA: ASTM International, 2012.

[14] Q. Xu, J. Hu, J. M. Ruiz, K. Wang, and Z. Ge, "Isothermal Calorimetry Tests and Modeling of Cement Hydration Parameters," *Thermochim. Acta*, vol. 499, pp. 91–99, 2010.

[15] K. A. Riding, J. L. Poole, K. J. Folliard, M. C. G. Juenger, and A. K. Schindler, "Modeling Hydration of Cementitious Systems," *ACI Mater. J.*, vol. 109, no. 2, pp. 225–234, 2012.

[16] G. Sant, "The Influence of Temperature on Autogenous Volume Changes in Cementitious Materials Containing Shrinkage Reducing Admixtures," *Cem. Concr. Compos.*, vol. 34, no. 7, pp. 855–865, Aug. 2012.

Chapter 5 Effect of Cementitious Materials on Strength-Based Activation Energy

5.1 Introduction

As discussed in Chapter 4, the concept of apparent activation energy (E_a) can be applied not only to describe variation of the rate of cement reaction with temperature, but also to the development of various concrete properties, such as compressive strength, since their rate development is a function of the cement hydration rate development. In this case, the apparent activation energy is referred to as strength-based E_a. Activation energy obtained from strength development is primarily used in determining the early-age concrete maturity-strength relationship via the equivalent-age concept. ASTM C1074 defines equivalent age as "the number of days or hours at a specified temperature required to produce a maturity equal to the maturity achieved by a curing period at temperatures different from the specified temperature." Equivalent age is calculated using Equation 5-1.

$$t_e(Tr) = \sum_{t=0}^{t} e^{\frac{-E_a}{R}\left(\frac{1}{273+Tc} - \frac{1}{273+Tr}\right)} \Delta t \qquad \text{Equation 5-9}$$

Where,

t_e (Tr) = equivalent age at the reference curing temperature (hours)

T_c = temperature of concrete during time interval Δt (hr), °C,

T_r = reference temperature, °C

E_a = activation energy, J/mol

R = universal gas constant, 8.3144 J/ (mol·K)

In this investigation, the equivalent-age and/or maturity function will be used to model and compare compressive strength development of field-cast cylinders of different concrete mixture designs. Since concrete strength development is a function of both age and curing temperature, comparing concrete strength development at the same equivalent age/maturity reveals strength differences that are due solely to the differences in concrete mixture proportions. Strength comparisons based on chronological age are affected by concrete mix proportions as well as differences in curing temperatures resulting from different placement times. Equivalent-age strength development plots for field-cured cylinders cast for each concrete mixture are included in Chapter 10.

Strength-based *E_a* can be calculated by determining the strength development at 3 isothermal curing temperatures. Two mathematical functions have been proposed for E_a calculation: a hyperbolic function presented in Equation 5-2 [1]–[6] and an exponential function presented in Equation 5-3 [1], [5]–[8].

$$S = S_u \frac{k(t-t_0)}{1+k(t-t_0)} \qquad \text{Equation 5-10}$$

Where,

S = Average compressive strength at age t (MPa)
t = Test age (days)
S_u = Limiting strength (MPa)
k = Rate constant or rate of reaction (days^{-1})
t_o = Age at which strength development is assumed to begin (days)

$$S = S_u \, e^{-(\frac{\tau}{t})^{\beta}} \qquad \text{Equation 5-11}$$

Where,

S = Average compressive strength at age t (MPa)
t = Test age (days)
S_u = Limiting strength (MPa)
τ = Time constant (days) [1/k in the hyperbolic function]
β = Curve shape parameter (dimensionless)

The parameters (S_u, k, t_o, β, and τ) for both functions are determined using computer software such as the solver function in Microsoft Excel [5], [6], [9], [10]. The software uses least squares to optimize the best-fit parameters through the measured strength versus age data at various curing temperatures, and the E_a is calculated using the Arrhenius law (Equation 5-1).

5.2 Methodology

Concrete mix proportions used to determine strength-based E_a are listed in Table 5-1. All the mixtures contained a constant dosage of air-entraining admixture (AEA) meeting ASTM C260 [11] and chloride-based accelerator meeting Type E admixture classification according to ASTM C494 [12]. In addition, all mixtures contained a lignosulfonate-based Type D water-reducing and retarding admixture [12]. Mixes #2 and #3 also included a polyacrylate-based Type F high-range water-reducing admixture (superplasticizer) [12], and mix #4 contained a shrinkage-reducing admixture (SRA). Mix #1 was designated as the control, which is an approved FDOT mixture for concrete pavement. As one of the main objectives of the current project was to optimize high-early-strength concrete mixtures using for pavement repair while enhancing durability by lowering the cracking potential, several strategies were studied. In Mix #2, aggregate gradation was optimized to minimize the required paste volume with the goal of lowering the cement content of the mixture. Lowering the cement content as well as the paste volume in a concrete mixture will directly affect the temperature rise experienced by a concrete element and consequently enhance the hardened concrete volumetric dimensional stability. Since the w/c ratio was the same for Mix #2 and Mix #1, compressive strengths were expected to decrease with a decrease in cement content. In order to compensate for this, Mix #3 was prepared at a lower w/c ratio compared to Mix #2. Mix #4 was proportioned to evaluate the effect of SRA on stress development. Mix #5 contained lightweight aggregate and was used to evaluate the effectiveness of internal curing in reducing the cracking potential of concrete. Mix #6 contained fibers to assess the effect of microfibers on enhancing concrete tensile strength.

Table 5-1: Concrete mix proportions per 1 m^3 (1 yd^3)

Materials	**Mix #1**	**Mix #2**	**Mix #3**	**Mix #4**	**Mix #5**	**Mix #6**
Cement, kg (lb)	534 (900)	415 (700)	415 (700)	534 (900)	534 (900)	534 (900)
Coarse Aggregate #57 limestone (SSD), kg (lb)	997 (1680)	682 (1150)	700 (1180)	997 (1680)	997 (1680)	997 (1680)
Intermediate Aggregate #89 limestone (SSD), kg (lb)	0.0	409 (690)	421 (710)	0.0	0.0	0.0
Fine Aggregate (SSD), kg (lb)	492 (829)	610 (1028)	625 (1054)	501 (844)	326 (549)	491 (827)
Lightweight Aggregate (SSD), kg (lb)	0.0	0.0	0.0	0.0	97 (163)	0.0
Water, kg (lb)	193 (325)	150 (252)	131 (221)	189 (319)	193 (325)	193 (325)
Type F Superplasticizer, ml (fl. oz)	0.0	948 (24.5)	1354 (35.0)	0.0	0.0	0.0
Type E Accelerator, ml (fl. oz)	14853 (384)	11554 (298.7)	11554 (298.7)	14853 (384)	14853 (384)	14853 (384)
AEA, ml (fl. oz)	38 (1.0)	38 (1.0)	38 (1.0)	38 (1.0)	38 (1.0)	38 (1.0)
Type D water-reducing admixture, ml (fl. oz)	874 (22.6)	696 (18.0)	696 (18.0)	909 (23.5)	874 (22.6)	874 (22.6)
SRA, ml (gal)	0.0	0.0	0.0	3713 (0.75)	0.0	0.0
Fiber, kg (lb)	0.0	0.0	0.0	0.0	0.0	0.297 (0.5)
w/c	0.384	0.384	0.34	0.384	0.384	0.384

Mortar mixes were proportioned following ASTM C1074 [13] specifications. Accordingly, the same fine aggregate-to-cement ratios (by mass) as the coarse aggregate–to-cement ratios of the concrete mixes were used to prepare mortar mixtures. Since Mix #5 and Mix #6 had the same cement content, w/c ratio, chemical admixture dosages, and coarse aggregate–to-cement ratios as Mix #1, their activation energy was expected to be the same as well. Mortar mix designs are listed in Table 5-2. When chemical admixtures were used, mix water was adjusted to correct for water content in all chemical admixtures.

Table 5-2: Mortar mix proportions (6-cube mix)

Materials	**Mix #1**	**Mix #2**	**Mix #3**	**Mix #4**
Cement (g)	650.66	541.60	548.07	654.36
Fine Aggregate (SSD) (g)	1210.93	1419.37	1475.36	1217.81
Water (g)	238.59	199.23	177.46	235.59
Type F Superplasticizer (g)	0.0	1.33	1.95	0.0
Type E Accelerator (g)	24.32	20.25	20.49	24.46
AEA (g)	0.05	0.05	0.05	0.05
Type D water-reducing admixture (g)	1.22	1.04	1.06	1.28
SRA (g)	0	0	0	4.18
w/c	0.384	0.384	0.34	0.384

Mortar cubes were cured at three isothermal temperatures of 23, 35, and 50°C in accordance with ASTM C1074 [13] and tested at 3, 6, 12, 24, 48, 72, 168, and 672 hours. The selection of curing temperatures for strength-based E_a determination was based on the expected temperature range that the concrete will be subjected to in the field. The compressive strength data was plotted versus age and the solver function in Microsoft Excel was used to obtain the best fit between the collected data and the hyperbolic (Equation 5-2) and exponential (Equation 5-3) functions. Strength-based E_a was then calculated using the Arrhenius law (Equation 5-1). Additional collected data are presented in Appendix B.

5.3 Results and Discussion

Figure 5-1 through Figure 5-4 present compressive strength development of mortar cubes at three isothermal temperatures. Increased curing temperatures resulted in increased compressive strength at early ages, while later-age compressive strengths were decreased. This phenomenon has been previously described in the literature and is frequently referred to as the cross-over effect [3], [14], [15].

For Mix #1, which was taken as the base mix design, the highest compressive strengths up to 1 day were observed for cubes cured at 50°C. The cross-over effect between the compressive strengths for cubes stored at 50°C and 35°C was observed at approximately 2 days, after which the highest compressive strengths were measured for the cubes stored at 35°C. At 28 days, compressive strength of cubes stored at 23°C was similar to that of the cubes stored at 35°C.

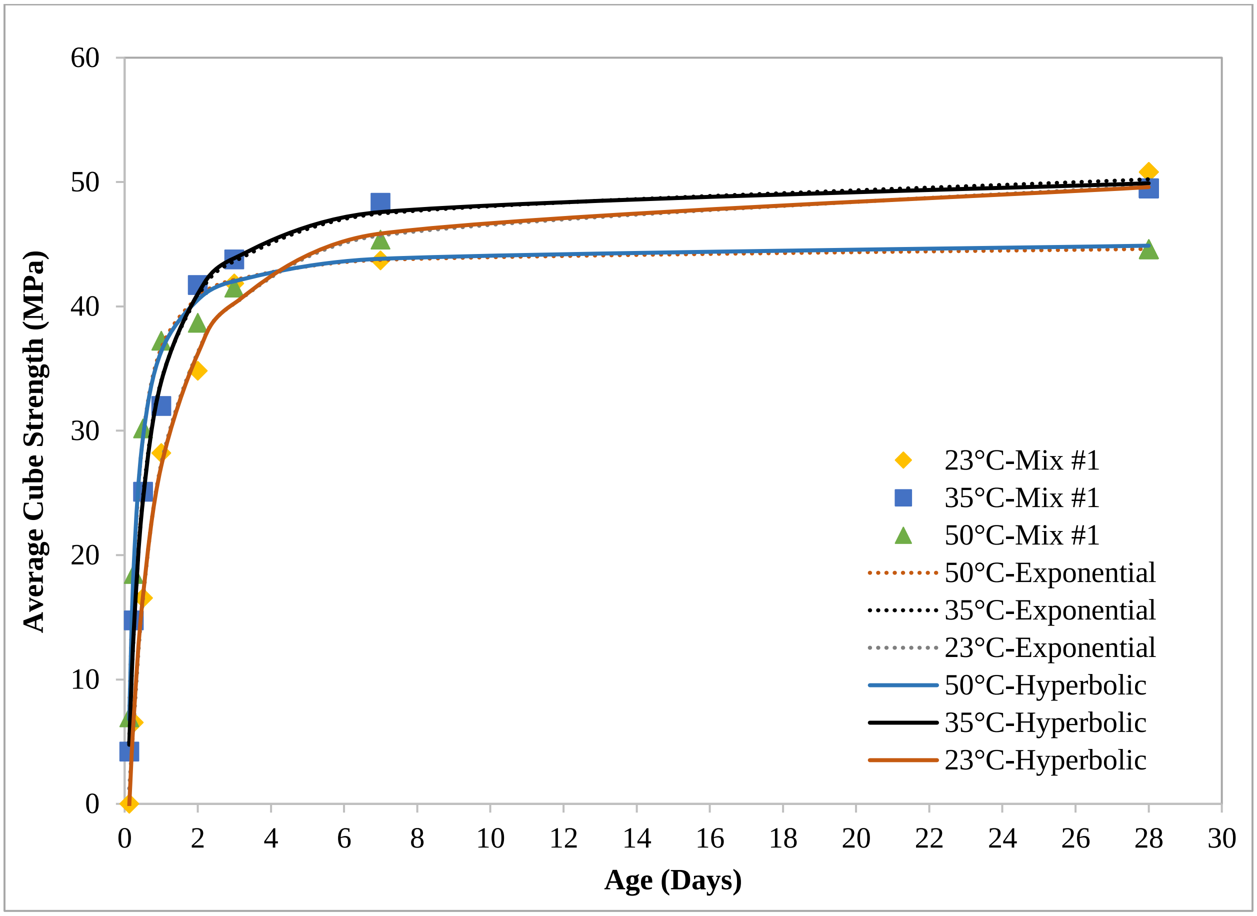

Figure 5-1: Compressive strength development for Mix #1 mixture

For Mix #2, the amount of cement was reduced from 900 to 700 lb, while maintaining the same w/c ratio as in Mix #1 mix. As expected, this resulted in a decrease in compressive strength for all temperatures up to 7 days. Although highest compressive strengths were observed for the 50°C curing temperature up to 1 day as for Mix #1, the cross-over effect for the 23°C curing temperature was observed at 2 days, after which time the cubes stored at 23°C maintained the highest compressive strength, while the compressive strength for the 50°C curing temperature was the lowest.

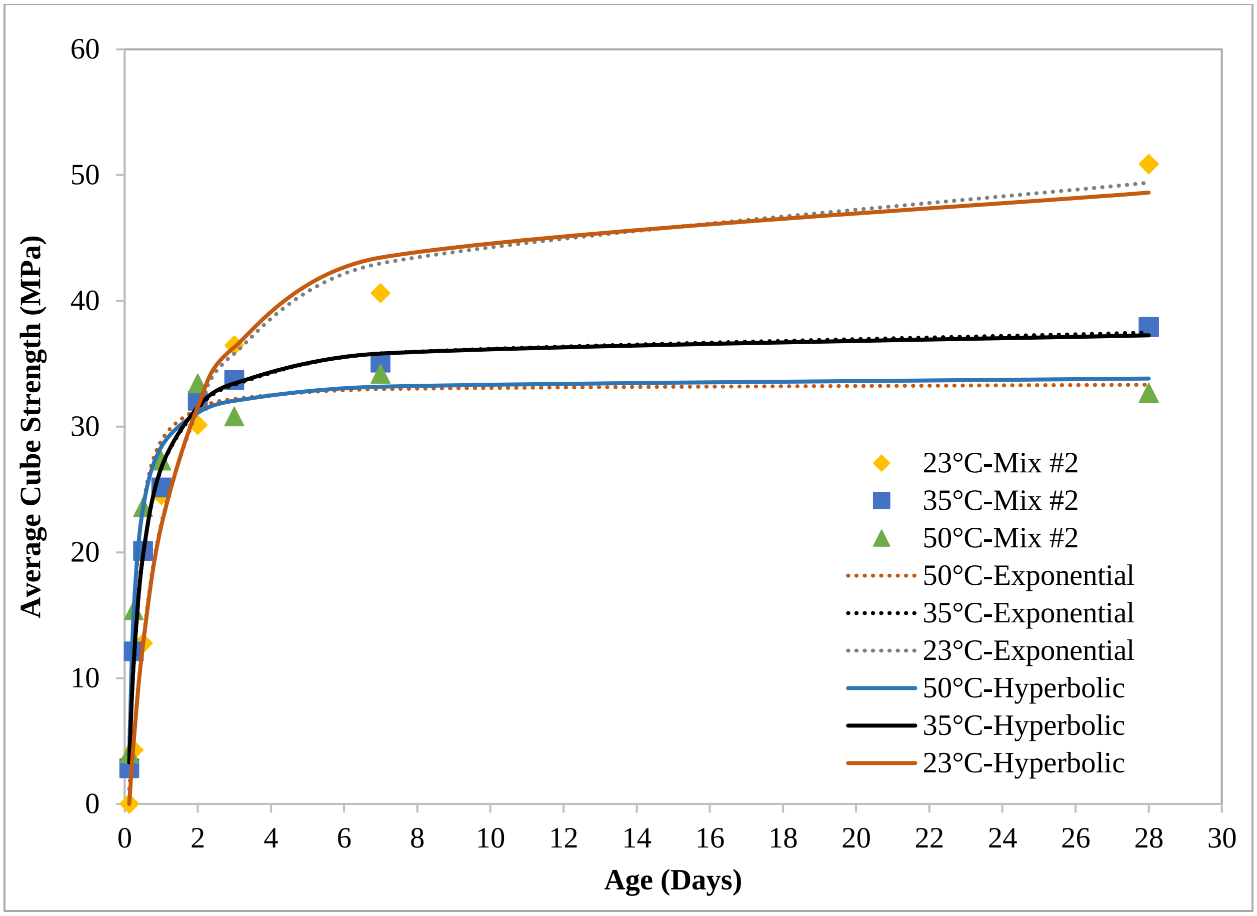

Figure 5-2: Compressive strength development for Mix #2 mixture

In Mix #3, the cement content was maintained at 700 lb, but the w/c ratio was reduced to 0.34. The measured compressive strength showed improvement at all ages and curing temperatures, not only when compared to Mix #2, but also Mix #1. As with the previous mix, the highest compressive strength, up to 1 day, was observed for the 50°C curing temperature. The cross-over effect was observed between 1 and 2 days, after which time the highest compressive strength was observed for the 35°C curing temperature. The highest rate of compressive strength gain after 3 days was observed for the 23°C; the cross-over effect for the 23°C and 50°C curing temperatures was observed at approximately 5 days. As with Mix #1, the 28-day compressive strength was very similar for cubes stored at 23°C and 35°C.

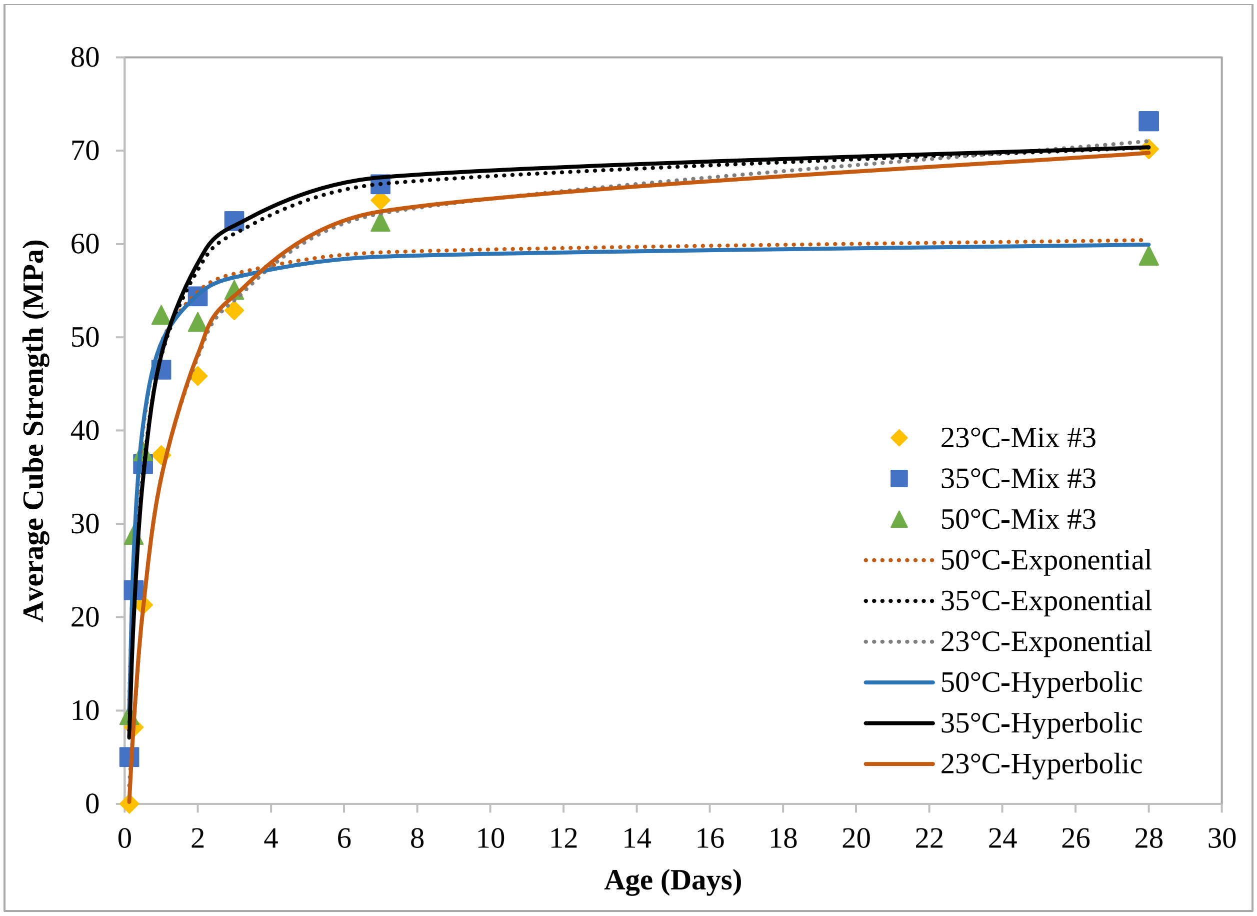

Figure 5-3: Compressive strength development for Mix #3 mixture

The mixture proportions for Mix #4 was identical to Mix #1, except for the presence of SRA. Compressive strengths of this mix during the first 12 hours were very similar to those of Mix #1 at all temperatures, after which time the strengths of Mix #4 exceeded those of the Mix #1. As with the other mixtures, the highest compressive strengths, up to 1 day, were observed for the 50°C curing temperature. The cross-over effect for the 50°C and 35°C curing temperatures was observed at approximately 2 days. After the age of 2 days, highest compressive strengths were observed for the cubes stored at 35°C.

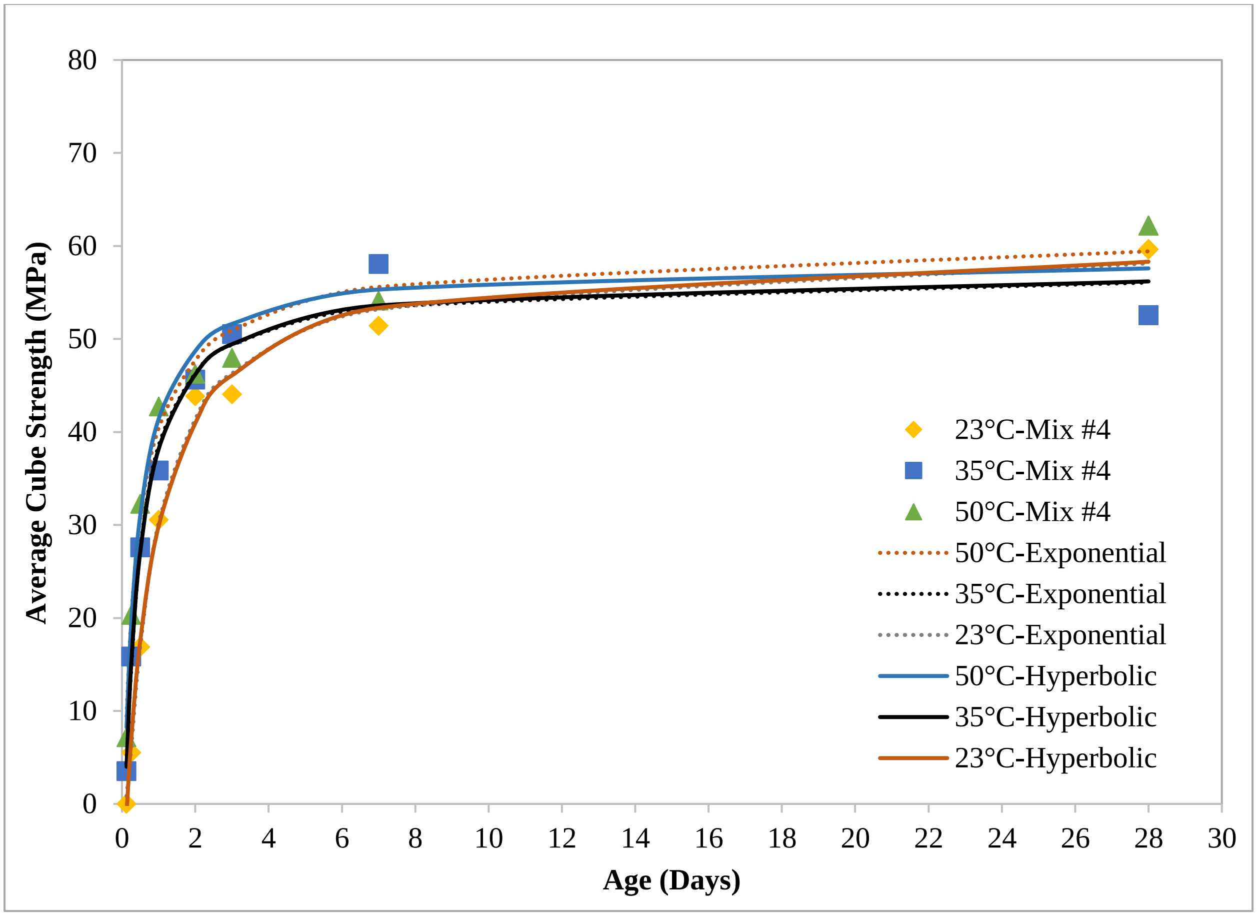

Figure 5-4: Compressive strength development for Mix #4 mixture

Strength-based E_a values calculated using the collected strength data are listed in Table 5-3. The determined activation energies are in line with the previously reported values [16]. As expected, hyperbolic and exponential functions produced different E_a values; however, the observed trend was the same in both cases. In the previous study [16], [17], the exponential function was selected over the hyperbolic, as it is better able to predict compressive strength at later ages [14].

E_a values were lowest for Mixes #1 and #4 and highest for Mixes #2 and #3. The main difference between these mixes was their cement content and presence of superplasticizer; E_a increased with reduction of cement content and addition of superplasticizer. Wirquin et al. [18] reported a slight increase in strength-based E_a with addition of superplasticizer, although the chemical composition of superplasticizer was not reported in their study. On the other hand, Riding et al. [19] reported a decrease in E_a with addition of superplasticizer, although in their study E_a was determined from calorimetry data. While the authors did not find any publications in the current literature comparing strength-based activation energies of concrete mixes with variable cement content, Han et al. [20] reported a decrease in strength-based E_a with an increase in cement replacement by fly ash, which is known to have low reactivity at early ages. A decrease in the w/c ratio and the addition of SRA resulted in a slight decrease in activation energy.

Table 5-3: Strength-based E_a calculated using the hyperbolic and exponential functions

Mix #	**Hyperbolic function**		**Exponential function**	
	E_a (J/mol)	**R^2**	**E_a (J/mol)**	**R^2**
Mix #1	36,324	0.997	28,575	0.994
Mix #2	53,825	0.978	39,410	0.921
Mix #3	44,706	1.000	35,266	0.969
Mix #4	23,706	0.863	22,495	0.878

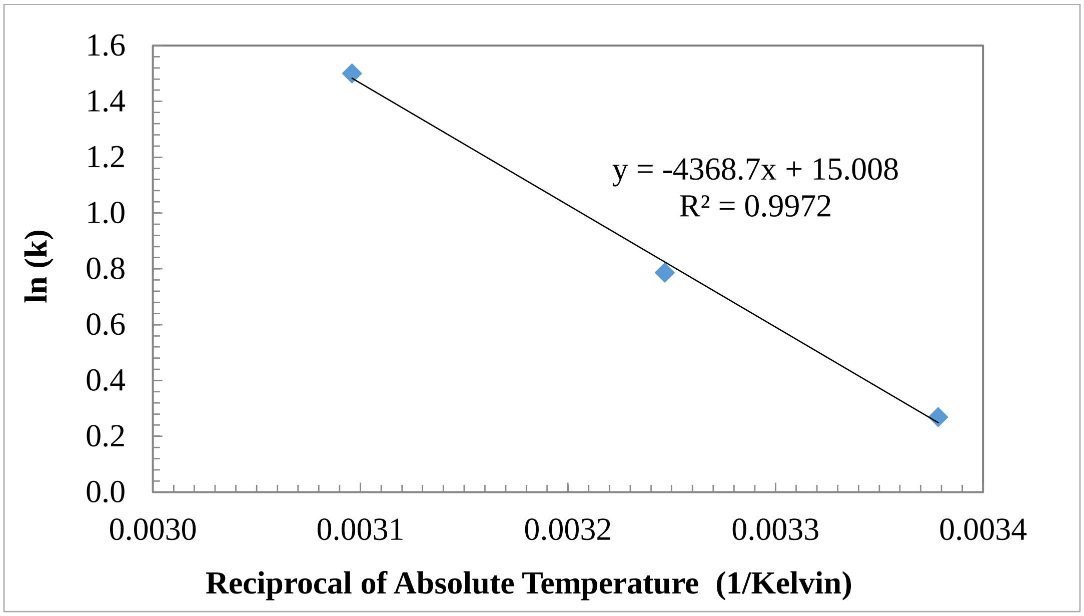

Figure 5-5: Arrhenius plot for activation energy determination using the hyperbolic function for Mix #1

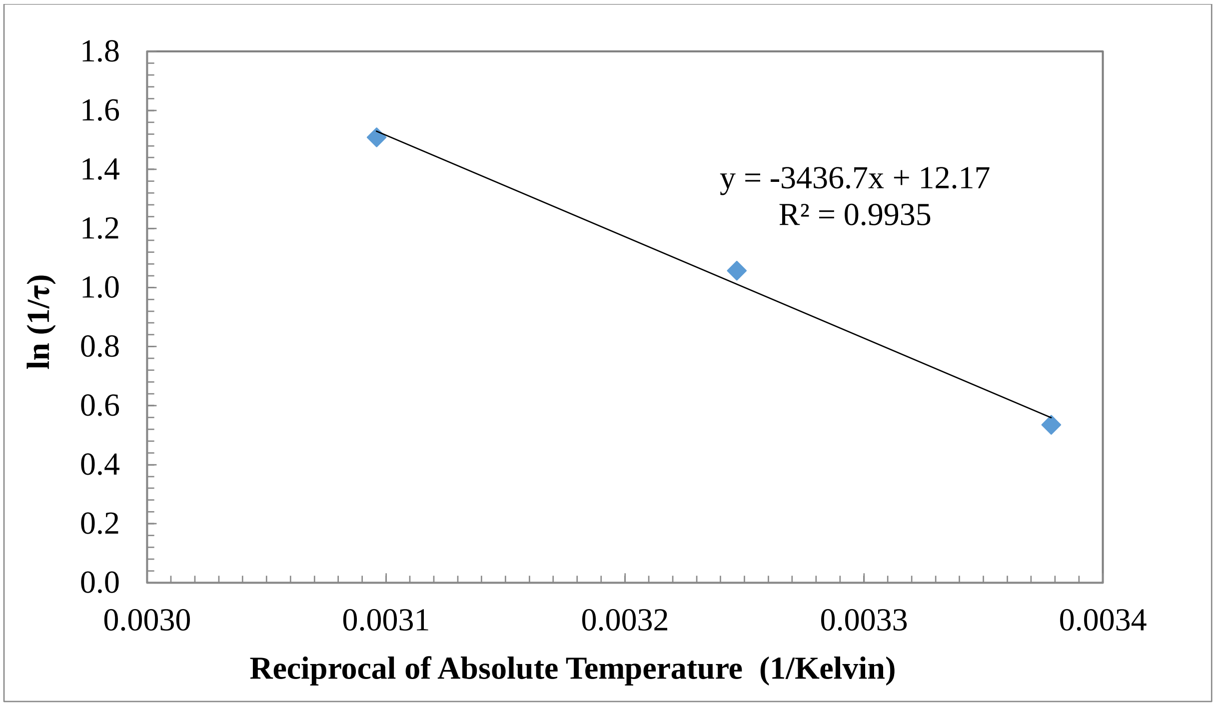

Figure 5-6: Arrhenius plot for activation energy determination using the exponential function for Mix #1

5.4 Conclusions

Strength-based activation energies were determined for Mixtures #1 through #4. A change in the w/c ratio and addition of SRA did not appear to have a significant effect on E_a values. However, a decrease in cement content, which was accompanied by the addition of superplasticizer, notably increased strength-based activation energy.

5.5 References

[1] N. J. Carino, “The Maturity Method,” in *Handbook on Nondestructive Testing of Concrete*, Boca Raton, FL: CRC Press, 1991, pp. 101–146.

[2] N. J. Carino and R. C. Tank, “Maturity Functions for Concretes Made with Various Cements and Admixtures,” *ACI Mater. J.*, vol. 89, no. 2, pp. 188–196, 1992.

[3] R. C. Pinto and A. K. Schindler, “Unified Modeling of Setting and Strength Development,” *Cem. Concr. Res.*, vol. 40, pp. 58–65, 2010.

[4] S. J. Barnett, M. N. Soutsos, S. G. Millard, and J. H. Bungey, “Strength Development of Mortars Containing Ground Granulated Blast-Furnace Slag: Effect of Curing Temperature and Determination of Apparent Activation Energies,” *Cem. Concr. Res.*, vol. 36, pp. 434–440, 2006.

[5] C. Ferraro, “Determination of Test Methods for the Prediction of the Behavior of Mass Concrete,” Ph.D. Dissertation, University of Florida, 2009.

[6] C. A. Ishee, “Evaluating the Performance of Portland Cement under Differing Hydration Conditions,” Ph.D. Dissertation, McGill University, 2011.

[7] P. Freiesleben Hansen and J. Pedersen, “Maturity Computer for Controlled Curing and Hardening of Concrete,” *Nord. Betong*, vol. 1, pp. 19–34, 1977.

[8] T. Poole, “Predicting Seven-Day Heat of Hydration of Hydraulic Cement from Standard Test Properties,” *J. ASTM Int.*, vol. 6, no. 6, pp. 1–10, 2009.

[9] A. J. Bien-Aime, “Effect of Cement Chemistry and Properties on Activation Energy,” University of South Florida, 2013.

[10] J. L. Poole, “Modeling Temperature Sensitivity and Heat Evolution of Concrete,” The University of Texas at Austin, 2007.

[11] ASTM C260/C260M-10a, “Standard Specification for Air-Entraining Admixtures for Concrete,” West Conshohocken, PA: ASTM International, 2016.

[12] ASTM C494/C494M-13, “Standard Specification for Chemical Admixtures for Concrete,” West Conshohocken, PA: ASTM International, 2013.

[13] ASTM C1074-11, “Standard Practice for Estimating Concrete Strength by the Maturity Method,” West Conshohocken, PA: ASTM International, 2011.

[14] N. J. Carino and H. S. Lew, “The Maturity Method: from Theory to Application,” in *2001 Structures Congress & Exposition*, 2001, pp. 1–19.

[15] A. K. Schindler, “Concrete Hydration, Temperature Development, and Setting at Early-Ages,” University of Texas at Austin, Austin, 2002.

[16] A. Zayed, K. Riding, C. C. Ferraro, A. Bien-aime, N. Shanahan, D. Buidens, T. Meagher, V. Tran, J. D. Henika, J. M. Paris, C. M. Tibbetts, and B. E. Watts, “Final Report Long-Life Slab Replacement Concrete FDOT Contract Number : BDV25-977-01,” University of South Florida, 2015.

[17] N. Shanahan, A. Bien-aime, D. Buidens, T. Meagher, A. Sedaghat, K. Riding, and A. Zayed, “Combined Effect of Water Reducer – Retarder and Variable Chloride-Based Accelerator Dosage on Rapid Repair Concrete Mixtures for Jointed Plain Concrete Pavement,” *J. Mater. Civ. Eng.*, pp. 1–10, 2016.

[18] E. Wirquin, M. Broda, and B. Duthoit, “Determination of the Apparent Activation Energy of One Concrete by Calorimetric and Mechanical Means: Influence of a Superplasticizer,” *Cem. Concr. Res.*, vol. 32, pp. 1207–1213, 2002.

[19] K. A. Riding, J. L. Poole, K. J. Folliard, M. C. G. Juenger, and a. K. Schindler, “New Model for Estimating Apparent Activation Energy of Cementitious Systems,” *ACI Mater. J.*, vol. 108, no. 5, pp. 550–557, 2011.

[20] S. H. Han, J. K. Kim, and Y. D. Park, “Prediction of Compressive Strength of Fly Ash Concrete by New Apparent Activation Energy Function,” *Cem. Concr. Res.*, vol. 33, no. 7, pp. 965–971, Jul. 2003.

Chapter 6 Concrete Mixture Design and Adiabatic Temperature Rise

6.1 Introduction

This project was initiated in order to identify the factors contributing to early-age cracking in concrete pavements. One of the goals of the project was to examine different concrete mixture combinations and their effect on cracking potential. Thermal and moisture-related concrete stresses have been identified as the typical causes of early-age cracking [1]. Cement hydration is an exothermic process that results in the liberation of a significant amount of heat [2]–[5]. Since concrete is a poor conductor of heat, this results in a concrete temperature rise, which under adiabatic conditions can result in a 20-50°C temperature rise [5]. Of concern, is not only the temperature rise in concrete, but also the temperature difference between the core of the structure, which is well-insulated by the surrounding concrete and will have the highest temperature, and the surface exposed to ambient temperatures. Temperature gradients between the core and the surface of a concrete element will lead to the development of thermal stresses that can contribute to early-age cracking. Moisture-related stresses are a result of the loss of moisture from concrete capillary pores due to either the hydration process (autogenous shrinkage) or external drying (drying shrinkage). This loss of moisture generates air-water menisci in the partially filled capillary pores, which results in tensile stresses [6]–[8]. Concrete pavements experience volume change from both thermal and drying shrinkage.

One of the objectives of the current study was to identify a typical mix design that is currently used by the Florida Department of Transportation (FDOT) for concrete pavement, and modify it in several ways to minimize the potential for thermal and moisture-related stresses. Therefore, the heat generated by concrete mixtures during hydration must be assessed. While under adiabatic conditions, heat loss is essentially eliminated, under semi-adiabatic conditions heat losses are minimized with the use of insulation and should be "less than 100 J/(h·K)"[9]. Measurements of heat of hydration under true adiabatic conditions is difficult experimentally and requires very expensive equipment. However, semiadiabatic calorimetry can be used instead and the heat loss from the semi-adiabatic calorimeter can be measured and used to calculate the adiabatic concrete temperature, as detailed in [10]. This approach was adopted in the current study.

6.2 Methodology

6.2.1 Concrete Mix Design

A typical high-early-strength (HES) concrete mix design used for concrete pavement construction was obtained from the FDOT and used as the control mix (Mix #1). A series of cracking mitigation strategies were implemented in Mixes #2- #6 in order to evaluate their effectiveness in minimizing the cracking potential of HES concrete pavement slabs during early ages. These strategies included the following:

1. Granular aggregate matrix: was optimized based on packing theory and gradation charts in order to reduce paste content and therefore the amount of cement per cubic yard of concrete [11] . Cement reduction decreases the heat generated from cement hydration and, consequently, the temperature rise in concrete, thus reducing thermal stresses. Reducing the excess paste content while maintaining the water-to-cementitious-materials ratio (w/cm) does not necessarily reduce the strength, but does reduce the shrinkage [12], [13]. To examine this further, two optimized mixes were prepared: Mix #2 and Mix #3. For Mix #2, the same water-to-cementitious materials ratio (w/cm) was adopted as in Mix#1. Since lower cement content at the same w/cm ratio can lead to a decrease in early-age mechanical properties [14], a lower w/cm ratio was adopted for Mix #3 in order to offset this effect. Mix #3 was also expected to show the effect of a lower w/cm ratio on autogenous shrinkage and the subsequent cracking potential.
2. Shrinkage Reducing Admixture (SRA): was used in Mix #4 in order to mitigate capillary stresses generated due to autogenous or drying shrinkage. SRAs reduce the surface tension of the pore water, thus lowering capillary stresses and reducing concrete shrinkage. Additionally, SRAs increase the relative humidity (RH) inside concrete pores [1], [15], which also reduces capillary stresses.
3. Pre-wetted lightweight aggregate (LWA): was implemented in Mix #5. Pre-wetted lightweight aggregate was used at half the dosage required to offset the paste chemical shrinkage so as to limit the effects of the lightweight aggregate on the strength development. This was expected to reduce autogenous shrinkage by providing additional internal (entrained) curing water to maintain a higher saturation level and increase the ultimate degree of hydration [6], [16]. Due to a possible increase in the degree of hydration,

an increase in ultimate strength was also expected. Additionally, because the elastic modulus of concrete incorporating LWA is lower, the expected stress relaxation would be higher at early ages [16].

4. Polypropylene fibers: were used to reduce or control cracking progression and likely increase early-age tensile strength [17][18]. This strategy was adopted for Mix#6.

6.2.2 Optimization of Granular Aggregate Matrix

Typical aggregates that are used in Florida for concrete production are #57 limestone and low fineness modulus sand. This combination of coarse and fine aggregates could inevitably lead to a gap-graded granular aggregate system as reflected in the gradation chart of Figure 6-1. Concrete incorporating gap-graded aggregates is more prone to segregation due to pumping, vibration or the lowering of yield stress brought about by on-site addition of water-reducer. Optimization of the original granular aggregate system was therefore done with the following objectives in mind:

1. Quantifying the paste-to-void volume ratio of the original base mix in order to reduce binder content not contributing to an increase in cementing efficiency (ratio of cement content to strength) but likely leading to higher temperature rise, autogenous and drying shrinkage.
2. Identify blending ratios for coarse and fine aggregates that would maximize packing density and thus further help in decreasing the paste content (and consequently binder content at the same w/cm ratio).
3. Improving segregation resistance by determining an aggregate matrix that is more stable than a conventional gap-graded system and more robust to any changes in yield stress of concrete brought about by the addition of HRWR (High-Range-Water-Reducer).

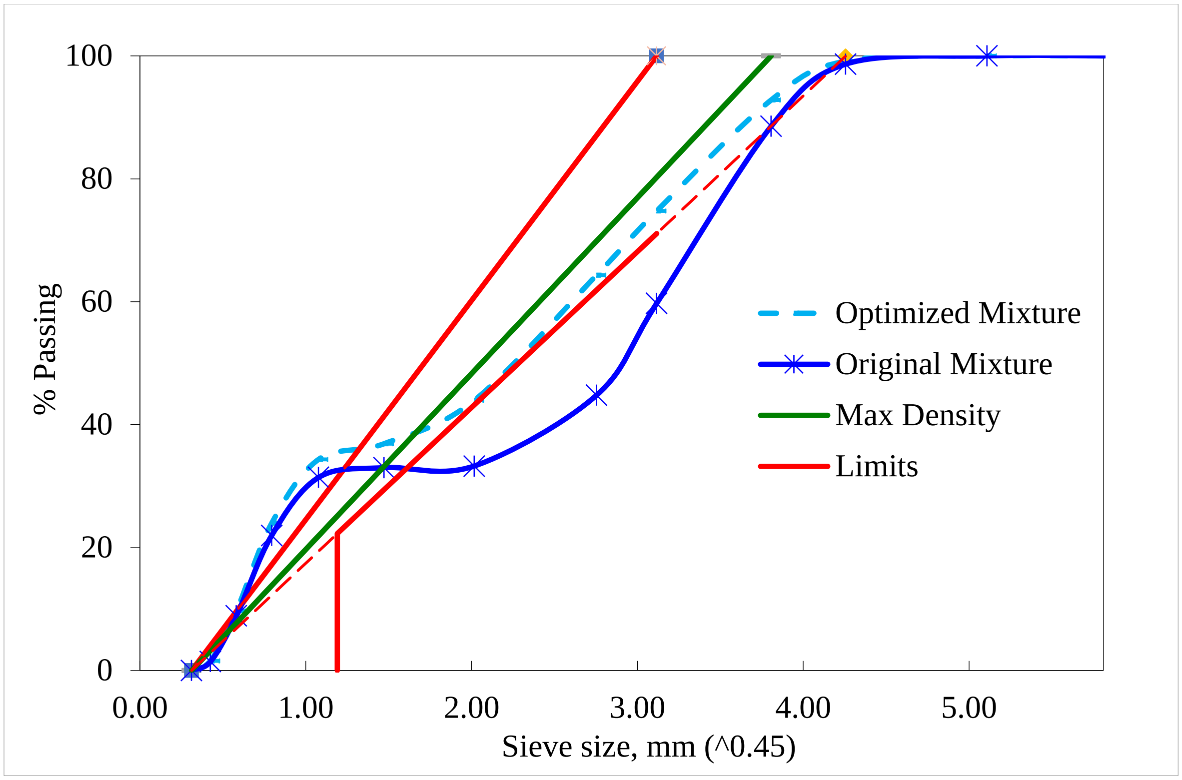

Figure 6-1: Power 45 chart comparison for original and optimized gradation (generated using spreadsheet from [19])

The void fraction or packing density of a binary aggregate system comprised of coarse and fine aggregate can be obtained from the Toufar model, which generates a packing density curve based on the fine-aggregate-to-coarse-aggregate mass ratio. For void fraction/packing density calculations, the Toufar model assumes that if the diameter ratio between a smaller and larger particle is higher than 0.22, then it cannot be situated in the interstices of the larger particles. The general packing density equation is of the form shown in Equation 6-1, [20] :

$$\phi = \frac{1}{\frac{y_1}{\phi_1} + y_2 + z \cdot \left\{ \frac{1}{\phi_2} - 1 \right\}} \qquad \text{Equation 6-1}$$

Where,

ϕ = effective packing density of the binary mix

y_1 = volume fraction of the fine particles (mm)

y_2 = volume fraction of the coarse particles (mm)

ϕ_2 = packing densities of the coarse fractions

ϕ_1 = packing densities of the fine fractions

z = correction for void space created by the volume of larger particles which are not densely packed and not distributed in a matrix of smaller particles

For multi-component systems, this computation of packing density is done stepwise with the packing density for two aggregates being calculated in each step [20], [21]. For each, a characteristic diameter (y_i) is obtained based on the sieve size distribution. For obtaining the variation of packing density with mass ratio for the various aggregate systems in this study, the aggregate gradation module from COMPASS was used [22]. Properties of aggregates used as inputs are: bulk specific gravity in oven dried condition, dry-rodded unit weights and individual systems gradation. COMPASS uses this information to generate a packing density that is a function of the proportions of the aggregates selected. For a 2-aggregate system such as the base mixture, a chart showing the variation of packing density relative to the mass blending ratios for coarse and fine aggregate is generated as shown in Figure 6-2 . As had been discussed previously, the Toufar model was used to determine the packing density of the combined aggregate system. When 3-aggregate systems are adopted, ternary charts such as the one shown in Figure 6-3 were generated. As can be seen in Figure 6-2, for the base system, changing the FA/CA (fine aggregate/coarse aggregate) ratio would be of limited consequence for improving the packing density due to the close proximity of the adopted FA/CA in the base mixture to the maxima. Including an intermediate aggregate size such as #89 was therefore implemented with the expectation of getting an improvement in the packing density (and consequently a lower cement content), and a more continuously-graded combined system to improve segregation resistance.

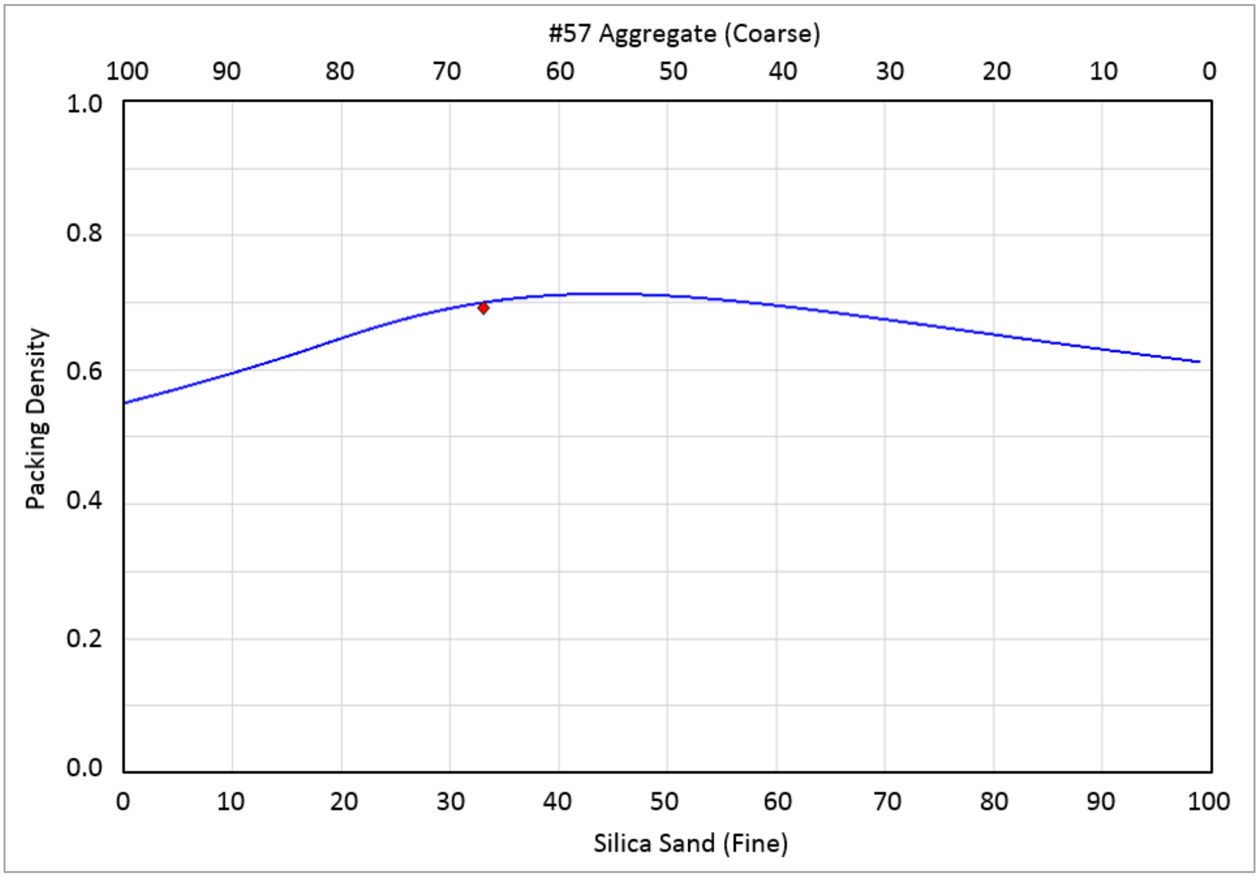

Figure 6-2: Packing density chart for original aggregate system using Toufar model based on original fine aggregate to coarse aggregate mass ratio (courtesy: Transtec Group)

In order to determine the mass blending ratios for the coarse aggregate, intermediate aggregate, and fine aggregate, the packing densities of the individual #57, #89, and fine aggregates were determined using dry-rodded unit weights according to ASTM C29 [23]. The aggregate properties for the three systems were input into the aggregate gradation module of the COMPASS software. For a three-aggregate system, such as the one used for optimized mixes in this study, a ternary chart was used for the estimation of packing density. A point in the ternary chart which lies within a region of high packing density was used, and a corresponding mass ratio was chosen. Another gradation was chosen which had a low deviation from the maximum density line in the 0.45 power chart. This deviation could be used as a measure of how continuously graded the granular matrix was, and was likely indicative of the extent of the particle lattice effect [24], which contributes to static segregation resistance of the concrete mix. For this purpose, a spreadsheet that uses a 0.45 power chart, developed by Taylor et al. [25], was adopted. The spreadsheet developed by Taylor et al. specifies a minimum particle size for its 0.45 power chart and applies a correction factor for cement content in determining the position of the combined aggregate gradation on the Shilstone chart, both of which are not implemented in the COMPASS aggregate gradation module. Mass ratios for the three-aggregate systems were then determined, based on increasing the packing density and reducing the deviation from maximum density line in the 0.45 power chart. The final combined aggregate system comprised the following mass allocations: 42% coarse (#57 stone), 22% intermediate (#89 stone) and 36% fine aggregate. The improvements are reflected in the curve for the optimized aggregate system shown in Figure 6-1 and packing densities obtained from the ternary chart in Figure 6-3. Because the theoretically-determined void content from the packing theory might be higher than the actual void fraction, the void contents of the combined aggregate system for both the base and optimized systems were calculated from the dry-rodded unit weight (DRUW) using the ASTM C29 procedure and oven-dried (OD) specific gravities listed in Table 6-1.

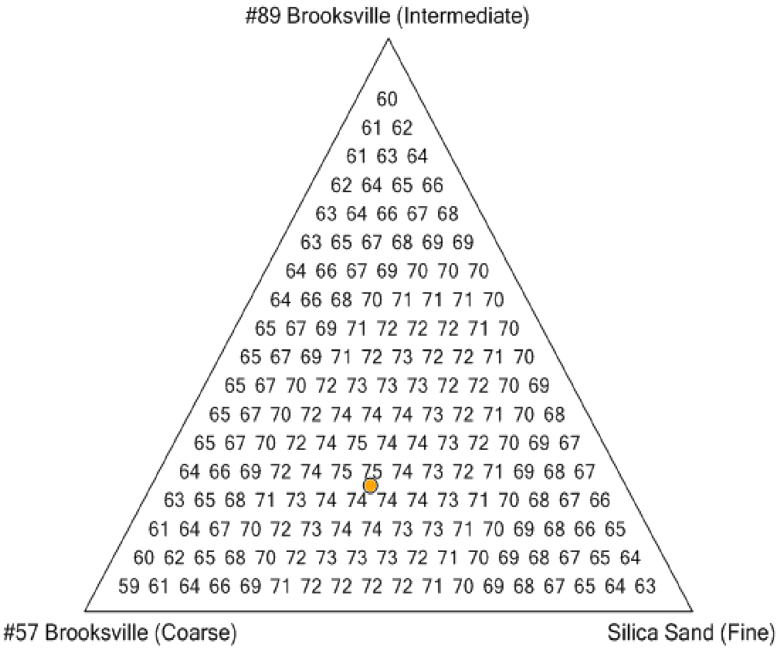

Figure 6-3: Ternary chart corresponding to packing densities obtained from COMPASS for the optimized system (courtesy: Transtec Group)

Table 6-1: Void content of the combined aggregate system

Combined Aggregate System	Mix designation	DRUW Void Content
#57/Fine Aggregate (67/33)*	Mix#1 (Control)	0.296
#57/#89/Fine Aggregate (42/22/36)*	Mix#2/#3	0.276

* Mass allocation for aggregate type as % of total aggregate mass

6.2.3 Selection of Paste Volume-to-Void Volume Ratio and W/C ratio for Mixtures

After optimizing the combined aggregate system and determining the void content of the granular matrix, the paste content can be determined by choosing an appropriate paste-to-void volume ratio. This ratio should be high enough to ensure sufficient workability and adequate early age strength development for HES mixtures. For Mix #1, the paste-to-void volume ratio was determined to be 2.15 (based on the determination of the packing density for the base FDOT mixture using ASTM C29). In the optimized system, the increase in the packing density was estimated to be about 2.5-3%. For typical pavement concrete, paste-to-void volume ratios between 1.4-1.8 are considered adequate when using high-range water-reducing admixtures (HRWRs) [13]. Lowering the paste volume results in a decrease in workability; however, workability can be improved with HRWRs. For Mix #1 and #2, where the w/c ratio was maintained at 0.384, the paste -to-void volume ratio of 1.74 was adopted, which corresponds to a cement content of 700 lb/yd^3. For Mix #3 with a lower w/c ratio (0.34), the paste-to-void volume ratio was 1.47.

6.2.4 Selection of SRA Dosage

The use of SRA has been found to retard early-age strength gain [26], [27], which was observed during the preparation of trial batches. Therefore, the low end of the manufacturer-recommended dosage range was selected for Mix #4. As recommended by the manufacturer, SRA was used as water replacement on a weight basis.

6.2.5 Lightweight Aggregate Proportioning

The use of pre-wetted saturated LWA was adopted for Mix#5 to assess the benefit of internal curing on mitigating cracking potential in concrete pavement slabs. Internal curing was selected to reduce early-age cracking potential by:

1. Providing water to the capillary pore system thus preventing the development of excessive autogenous strain and, consequently, reducing tensile stress development.
2. Replacement of a portion of sand with lightweight aggregate reduces the elastic modulus of concrete, thereby allowing greater stress relaxation and reducing early-age stress development.
3. The additional water available for hydration results in a higher degree of hydration.

Lightweight aggregate proportioning was based on Equation 6-2, which takes into account chemical shrinkage, absorption capacity of the aggregate, and cementitious material content [28], [29].

$$M_{LWA} = \frac{C_f \cdot C_s \cdot \alpha_{\max}}{S \cdot W_{LWA}} \qquad \text{Equation 6-2}$$

Where,

M_{LWA} = mass of lightweight aggregate required in oven-dry condition (lb/yd^3)

C_f = cement factor (total amount of cementitious materials, lb/yd^3)

α_{max} = maximum degree of hydration attainable based on the w/cm ratio used

C_s = chemical shrinkage (lb/lb of the cementitious material)

S = saturation level of the aggregate (between 0 and 1)

W_{LWA} = mass of water released by the LWA from pre-soaked to equilibrium mass in a 94% RH environment (lb)

A chemical shrinkage value of 0.07 lb/lb of cementitious material, as suggested in ASTM C1761 [29], was used for mixture proportioning. One-half of the LWA dosage determined from Equation 6-2 was used in the mixture proportioning in order to reduce potential strength loss [30][31]. LWA was used to replace an equivalent volume of sand as specified in ASTM C1761 [29].

Trial batches were made for all the concrete mixtures, except for Mix #1, in order to adjust the chemical admixture dosages to produce the required fresh and hardened concrete properties. All mixtures contained a fixed dosage of an air-entraining admixture (AEA), ASTM C260 [32], and a Type E chloride-based accelerator, ASTM C494 [33]. In addition, all the mixes contained a lignosulfonate-based Type D water-reducing and retarding admixture [33]. Mixes #2 and #3 also included a polyacrylate-based Type F high-range water-reducing admixture [33]. The finalized concrete mix proportions are listed in Table 6-2.

Table 6-2: Concrete mix proportions per 1 m^3 (1 yd^3)

Materials	**Mix #1**	**Mix #2**	**Mix #3**	**Mix #4**	**Mix #5**	**Mix #6**
Cement, kg (lb)	534 (900)	415 (700)	415 (700)	534 (900)	534 (900)	534 (900)
Coarse Aggregate #57 limestone (SSD), kg (lb)	997 (1680)	682 (1150)	700 (1180)	997 (1680)	997 (1680)	997 (1680)
Intermediate Aggregate #89 limestone (SSD), kg (lb)	0.0	409 (690)	421 (710)	0.0	0.0	0.0
Fine Aggregate (SSD), kg (lb)	492 (829)	610 (1028)	625 (1054)	501 (844)	326 (549)	491 (827)
Lightweight Aggregate (SSD), kg (lb)	0.0	0.0	0.0	0.0	97 (163)	0.0
Water, kg (lb)	193 (325)	150 (252)	131 (221)	189 (319)	193 (325)	193 (325)
Type F Superplasticizer, ml (fl. oz)	0.0	948 (24.5)	1354 (35.0)	0.0	0.0	0.0
Type E Accelerator, ml (fl. oz)	14853 (384)	11554 (298.7)	11554 (298.7)	14853 (384)	14853 (384)	14853 (384)
AEA, ml (fl. oz)	38 (1.0)	38 (1.0)	38 (1.0)	38 (1.0)	38 (1.0)	38 (1.0)
Type D water-reducing admixture, ml (fl. oz)	874 (22.6)	696 (18.0)	696 (18.0)	909 (23.5)	874 (22.6)	874 (22.6)
SRA, ml (gallons)	0.0	0.0	0.0	3713 (0.75)	0.0	0.0
Fiber, kg (lb)	0.0	0.0	0.0	0.0	0.0	0.297 (0.5)
w/c	0.384	0.384	0.34	0.384	0.384	0.384

6.2.6 Semi-Adiabatic Calorimetry

A description of the steps involved in the fabrication and calibration of the semi-adiabatic calorimeter, as well as a detailed testing procedure, can be found elsewhere [34]. The semi-adiabatic testing procedures were in line with those published in the literature [9], [35]. Prior to the start of the semi-adiabatic measurements, the calorimeters were calibrated with deionized-water to determine the calibration factors that characterize the insulating properties of the calorimeter, which were used to calculate heat losses during the semi-adiabatic testing. The calorimeter calibration factors are listed in Table 6-3.

Table 6-3: Semi-adiabatic calorimeter calibration factors

Calibration factors	**Calorimeter 1**	**Calorimeter 2**	**Calorimeter 3**
C f1 =	0.1429	0.0524	0.0414
C f2 =	1.6794	1.314	0.5855

Mixes #1-5 were tested using semi-adiabatic calorimetry. Since Mix#6 had an identical cementitious material content to Mix#1, it was not included in the testing matrix. Two semi-adiabatic calorimeters were used in this study, and the average values for measurements were reported here. Concrete for semi-adiabatic calorimetry was prepared in one-cubic foot batches following ASTM C192 [36]. A Type D water-reducing admixture was added to the mixing water, air-entraining agent was added to the sand, and Type F HRWRA, when used, was added after the rest period. Chloride-based accelerator was added at the end of the mixing procedure described in ASTM C192 [36], and concrete was mixed for an additional 30 sec. For each mixture, two 6- x 12-in. concrete cylinders were prepared immediately after the end of mixing and placed into the calorimeter chamber. Air content was determined in accordance with ASTM C231 [37], slump was measured per ASTM C143 [38], and unit weight was measured following ASTM C138 [39]. Fresh concrete properties are listed in Table 6-4.

Table 6-4: Fresh concrete properties

Fresh Property	**Mix #1**	**Mix #2**	**Mix #3**	**Mix #4**	**Mix #5**
Slump (in)	2.5	6.5	1.5	3.0	5.5
Air content (%)	2.7	3.3	3.0	2.8	2.9
Unit weight (lb/ft^3)	144.89	144.11	146.09	142.14	139.19

6.3 Results and Discussion

Results of semi-adiabatic concrete testing are presented in Figures 6-3 through 6-7 for both calorimeters that were used in this study. Only minor variations were observed in the between-calorimeter data generated for each mix.

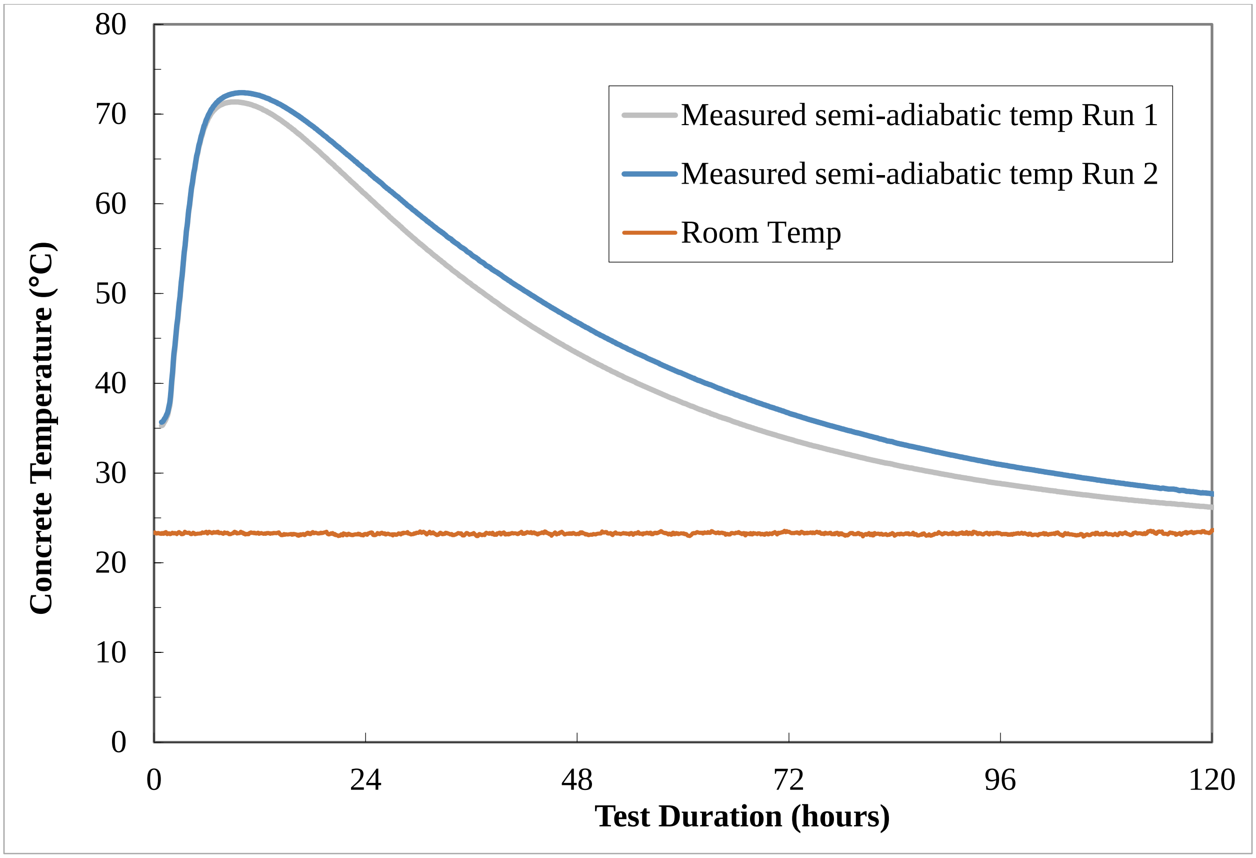

Figure 6-4: Measured semi-adiabatic temperature for Mix #1

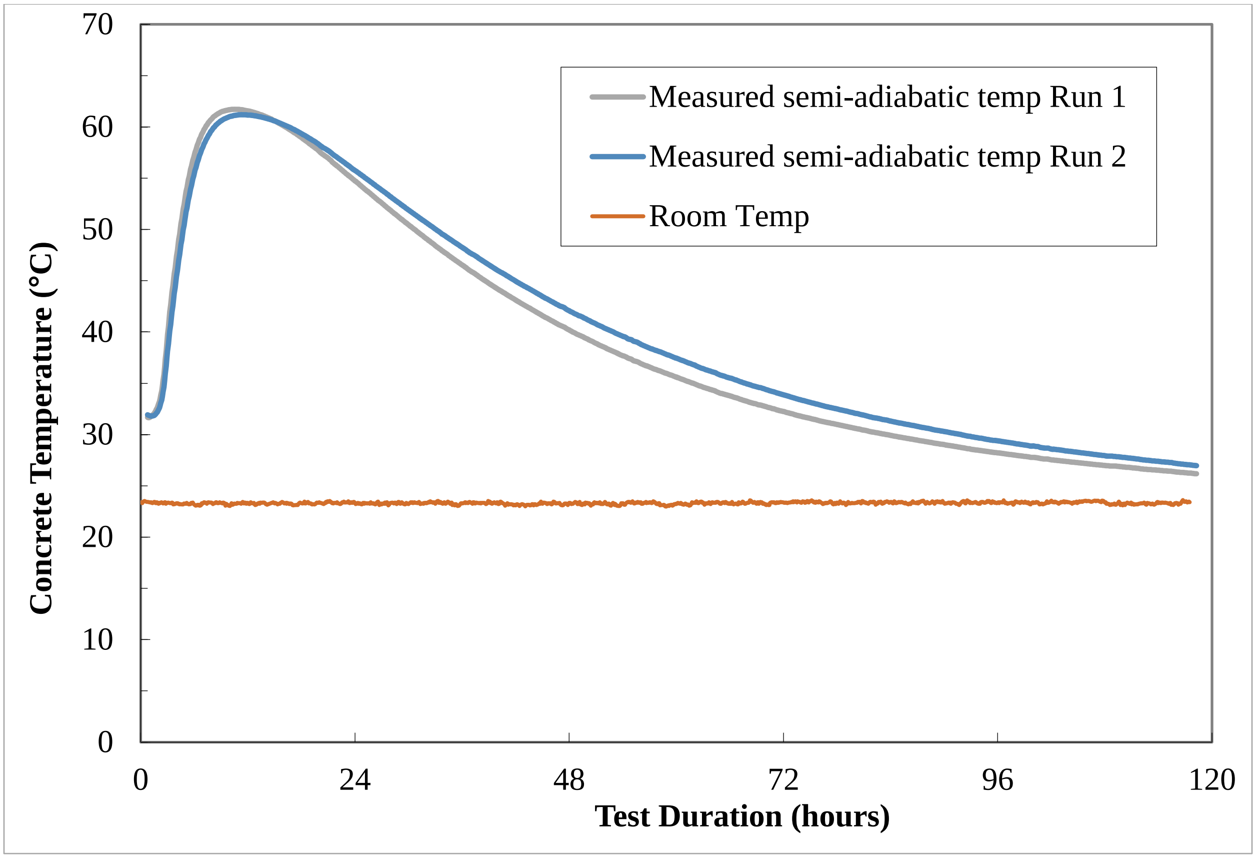

Figure 6-5: Measured semi-adiabatic temperature for Mix #2

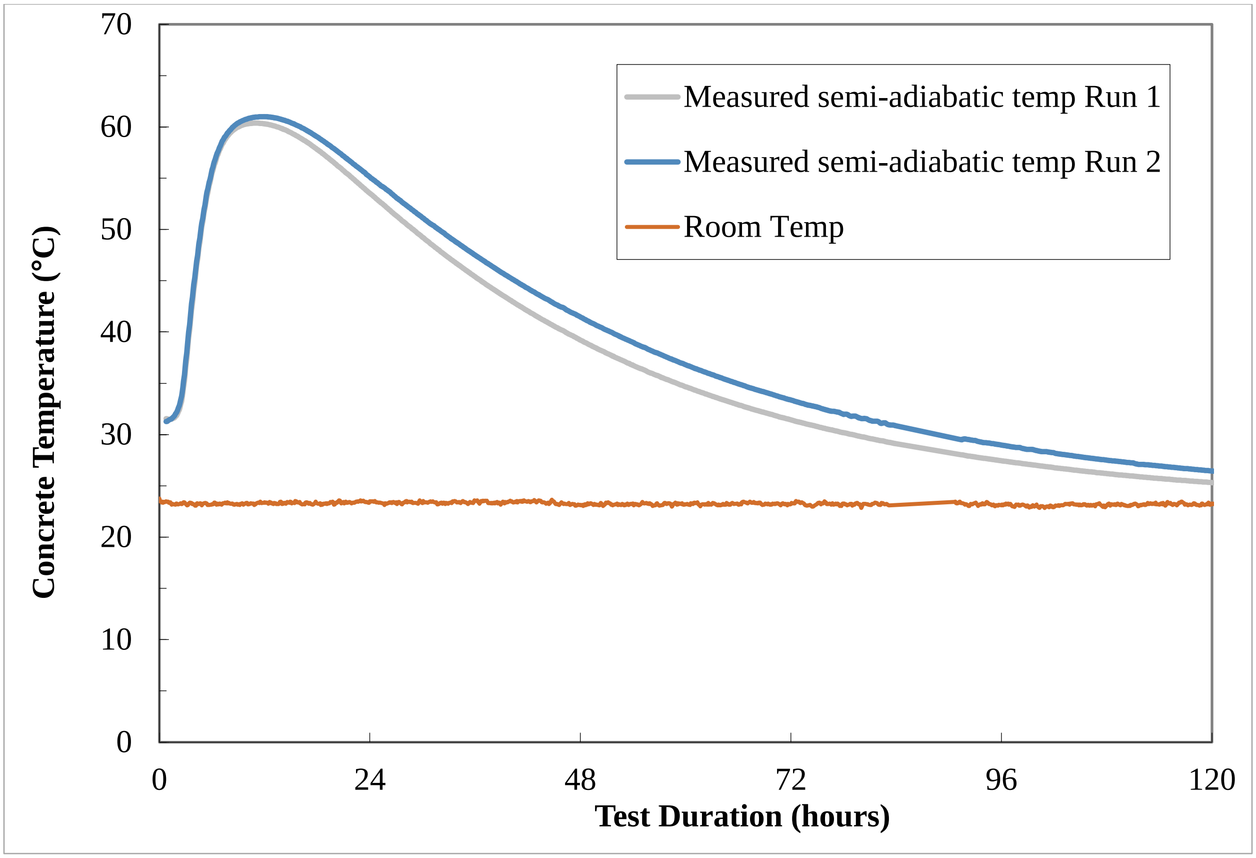

Figure 6-6: Measured semi-adiabatic temperature for Mix #3

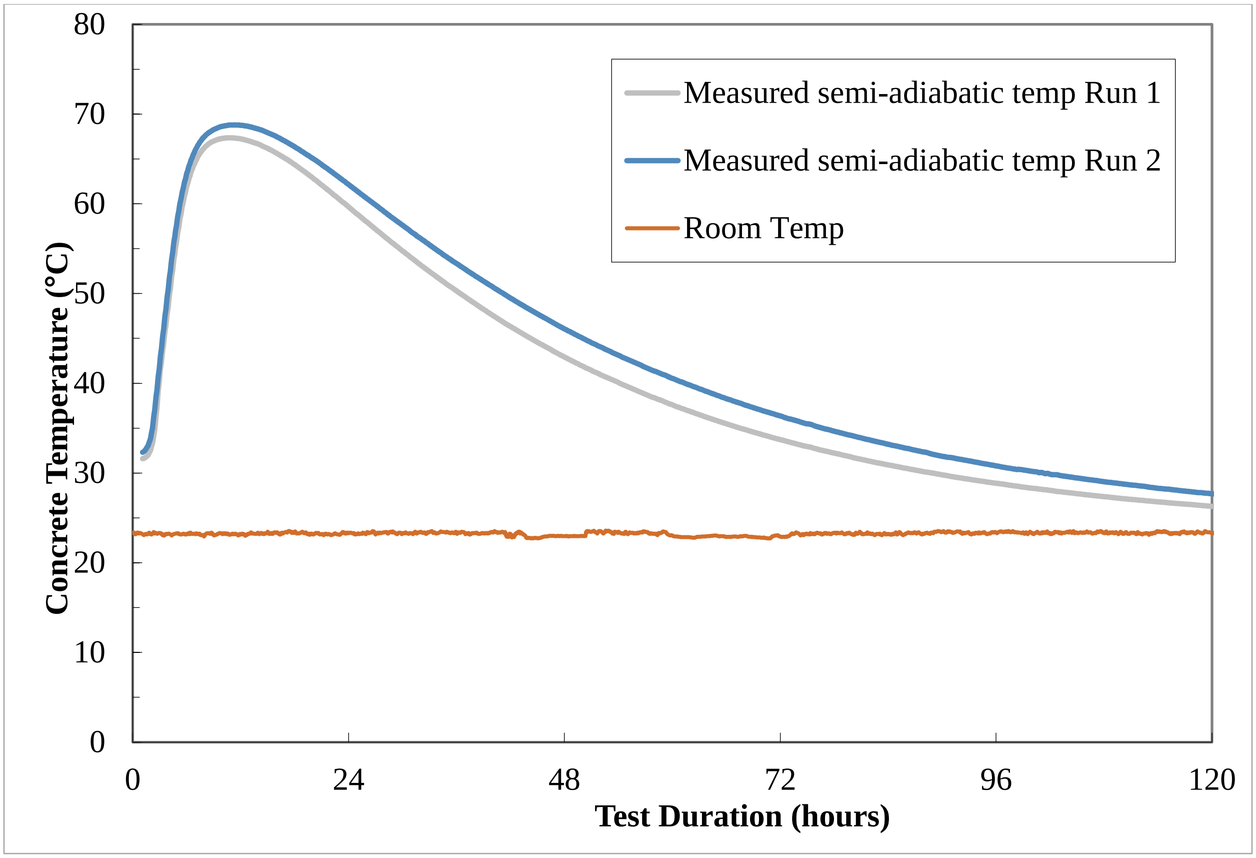

Figure 6-7: Measured semi-adiabatic temperature for Mix #4

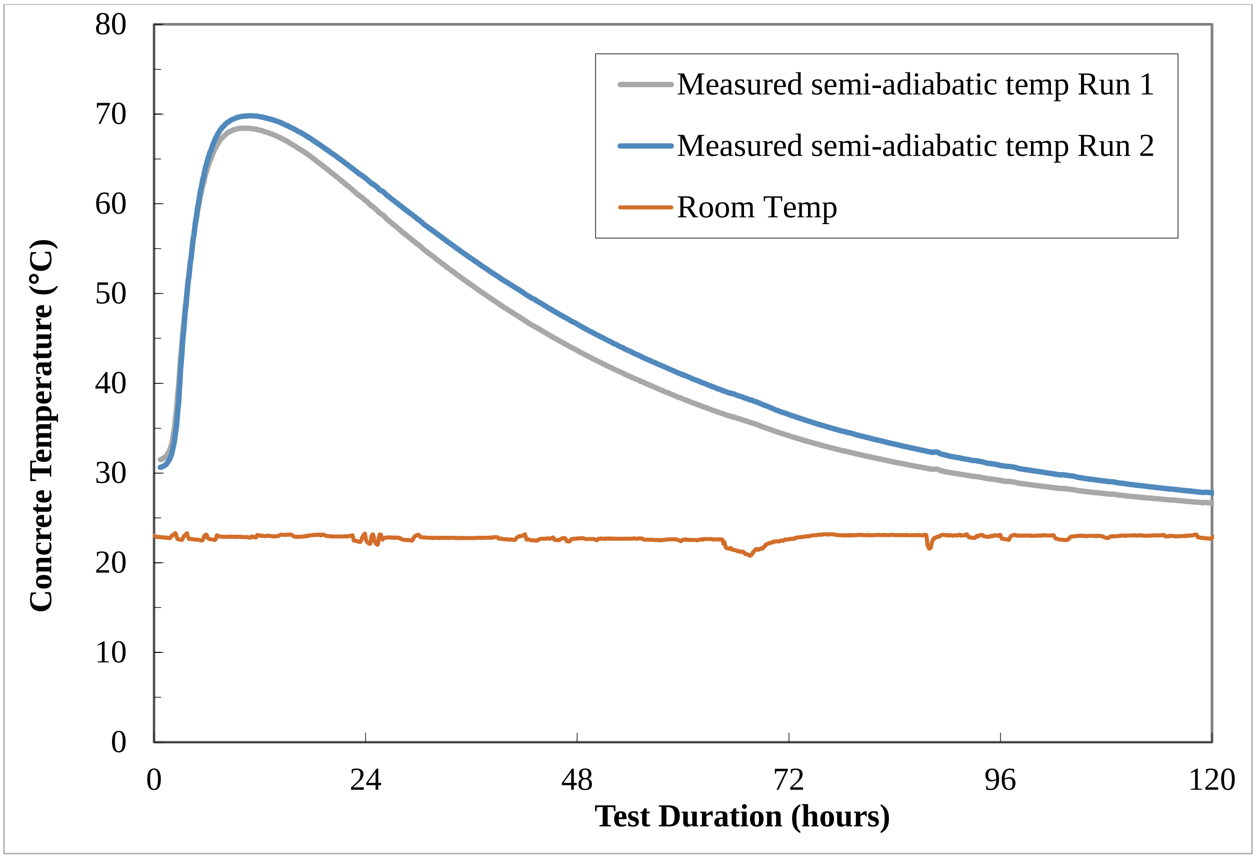

Figure 6-8: Measured semi-adiabatic temperature for Mix #5

Figure 6-9 presents a comparative plot of all the semi-adiabatic temperature profiles generated for each mix. As expected, reduction of the paste content resulted in a notable decrease in the concrete temperature rise. For Mixes #2 and 3, the maximum concrete temperature was approximately 10°C lower compared to Mix #1, which can be directly related to decreasing the cement content by 200 lb/yd^3. The decrease in the w/c ratio from 0.384 in Mix #2 to 0.34 in Mix #3 did not appear to have a significant effect on temperature rise in these two mixtures. Mix #1 had the highest maximum concrete temperature compared to the rest of the mixes; this is likely due to its higher initial concrete temperature, which was approximately 5°C higher. Taking this into account, the temperature profiles for Mixes #4 and 5 were similar to those of Mix #1. Therefore, it does not appear that addition of SRA or LWA had a significant effect on concrete temperature development. Although LWA has a lower specific heat, which would imply a higher temperature rise above the control mixture (Mix #1), the low LWA content used did not significantly affect temperature rise.

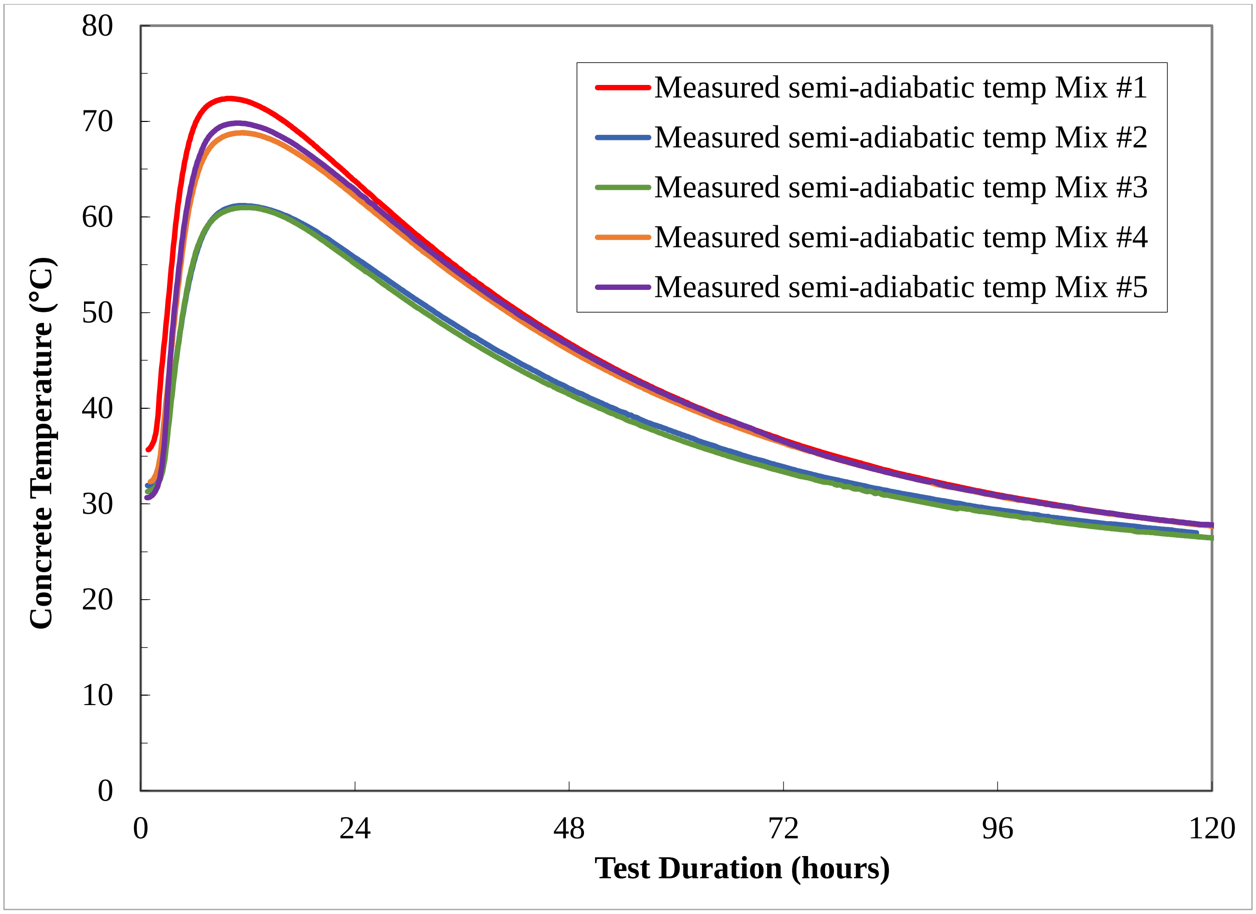

Figure 6-9: Comparative plot of all the semi-adiabatic temperature profiles

Hydration parameters α_u, (ultimate degree of hydration) β (shape parameter), and τ (time parameter), determined from the semi-adiabatic calorimetry, and the activation energy determined from isothermal calorimetry are listed in Table 6-5. The data were fitted to Equation 6-3.

$$\alpha_t = \alpha_u \cdot \exp\left(-\left(\frac{\tau}{t_e}\right)\right)^{\beta} \qquad \text{Equation 6-3}$$

Where,

α_t = degree of hydration at time ‘t’

α_u = ultimate degree of hydration

τ = time parameter

β = shape parameter

t = maturity time or time

Mixes # 2 and #3, which contained Type F HRWRA, showed a lower activation energy when compared to Mixes 1, 4 and 5 with no HRWRA.

Table 6-5: Semi-adiabatic hydration parameters

Average Semi-Adiabatic Parameters	**Mix**				
	Mix #1	**Mix #2**	**Mix #3**	**Mix #4**	**Mix #5**
Activation Energy (J/mol)	32,200	25,900	18,600	31,600	32,200
β =	0.930	1.164	1.248	0.970	0.877
τ (hr)=	8.280	7.295	6.400	8.378	8.250
α_u=	0.725	0.731	0.679	0.685	0.755

In terms of the β and τ parameters, the results presented in Table 6-5 are similar for all the 900 lb/yd^3 mixes (Mix #1, 4, and 5). The value of the shape parameter β increased for Mixes #2 and 3, which had a lower cement content; the value of τ, on the other hand, decreased for these mixes, indicating a possibly faster rate of hydration at early ages. Although the SRA used in the current study was reported to have a retarding effect, no increase in the τ parameter was noted at the dosage adopted here.

The results indicate that reducing the cement content from 900 lb/yd^3 (Mix #1) to 700 lb/yd^3 (Mix #2), without a change in w/c ratio, did not have a significant effect on α_u as expected [14]. A reduction in the w/c ratio (Mix #3) resulted in a slight reduction of α_u, as less water was available for hydration. The α_u value for Mix #4 with SRA was similar to Mix #3, despite the higher w/c ratio (0.384). Results for Mix #5 showed a slightly higher α_u value, which is consistent with results obtained by Byard et al. [16] . This increase can be due to the effects of internal curing on the degree of hydration. However, the increase was less than 5% and, therefore, may not be statistically significant. For comparison purposes between the current results and those from Byard et al [16], the following has to be clarified: 1. Entrained water for internal curing in the current study was normalized with respect to the internal curing water demand required to maintain saturation of capillary porosity as identified by Equation 6-2. In this regard, the internal curing water demand is a function of chemical shrinkage (dictated by cement content, assumed α_u =1, and the chemical composition of cement). However, in Byard et al. [16], Equation 6-4 (Mills Equation) and Equation 6-5 (Hansen Equation) were used to quantify the α_u value used in estimating LWA content. The designations ICM and ICH correspond to mixtures that were proportioned based on the expected ultimate degree of hydration values found from Equation 6-4 and Equation 6-5, respectively.

$$\alpha_u = \frac{1.031 \cdot (w/c)}{0.194 + w/c} \qquad \text{Equation 6-4}$$

$$\alpha_u = \frac{w/c}{0.36} \qquad \text{Equation 6-5}$$

Comparisons between Mix #5 and Mix 0.42-Shale, and Mix #5 and Mix 0.36-ICM (highlighted in bold in Table 6-6), suggest that for mixtures with similar internally-entrained-water-to-demand ratios, similar increases in α_u were reported [16].

Table 6-6: Comparison of increase in ultimate degree of hydration for concretes incorporating LWA from [16] and Mix 5 from current study

Mix ID	**Added IE Water/Demand**	**Increase in α_u relative to Control**	**% Difference in α_u**
0.42-Shale*	**0.51**	**0.040**	**5.13%**
0.42-Slate*	0.74	0.070	8.97%
0.42-Clay*	0.74	0.070	8.97%
0.36-ICM*	**0.64**	**0.040**	**5.56%**
0.36 ICH*	0.97	0.130	18.06%
Mix #5	**0.50**	**0.032**	**4.26%**

The hydration parameters presented in Table 6-5 were used to generate a degree of hydration plot for each mix as a function of equivalent age using Equation 6-3, as can be seen in Figure 6-10.

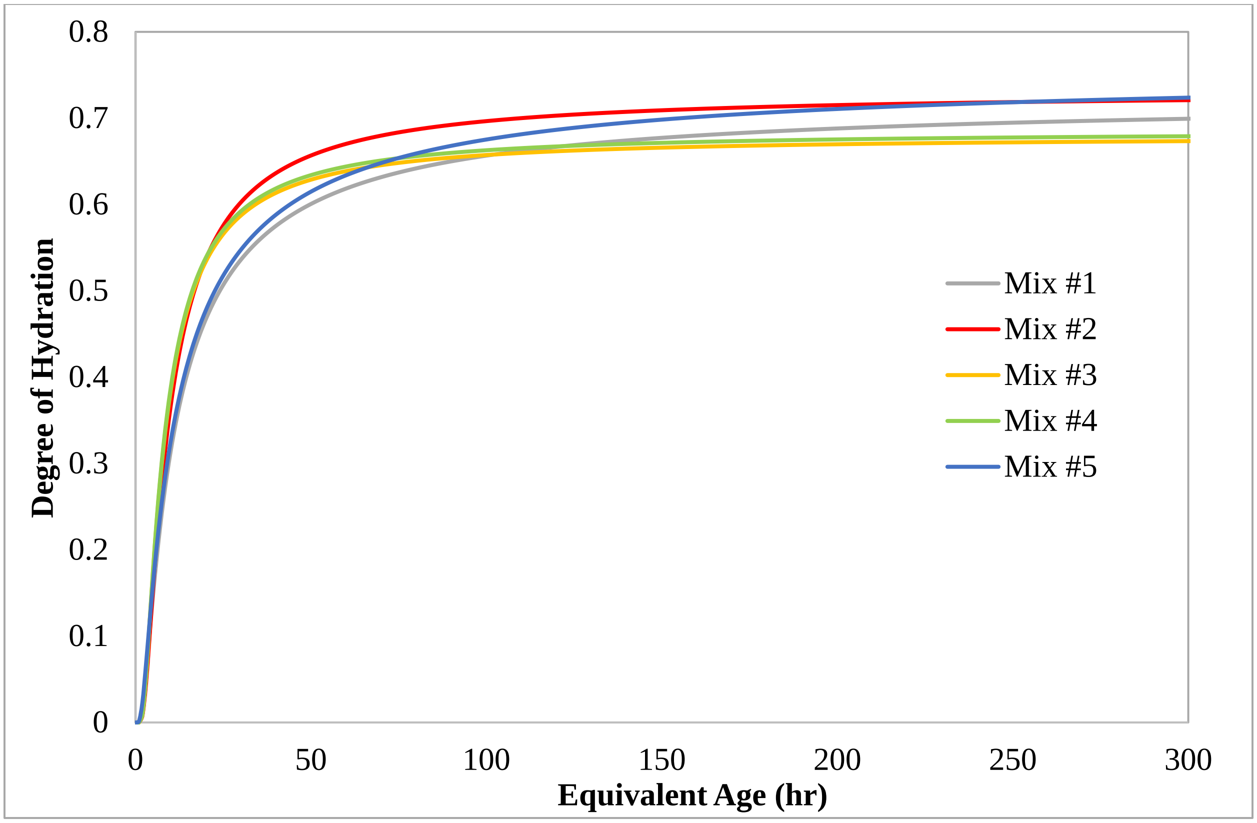

Figure 6-10: Degree of hydration vs. equivalent age

The hydration parameters were also used to determine the best-fit curves to model the experimentally-measured semi-adiabatic temperature profiles. While false adiabatic temperature accounts only for the heat loss from the calorimeter, the calculated true adiabatic temperature includes the influence of temperature on the rate of hydration. The calculated values for true adiabatic temperature, as well as the adiabatic temperature rise, are presented in Table 6-7, Figure 6-11, and Figure 6-12. As expected, Mixes #2 and 3 had the lowest adiabatic temperature and the lowest adiabatic temperature rise due to their reduced cement content. It can also be observed that not only was the adiabatic temperature lower for these mixes, the rate of temperature increase was also lower, which would be beneficial in terms of heat dissipation. The higher temperature rise of Mix #5 can be attributed to its higher α_u compared to the other mixes, including Mix #1.

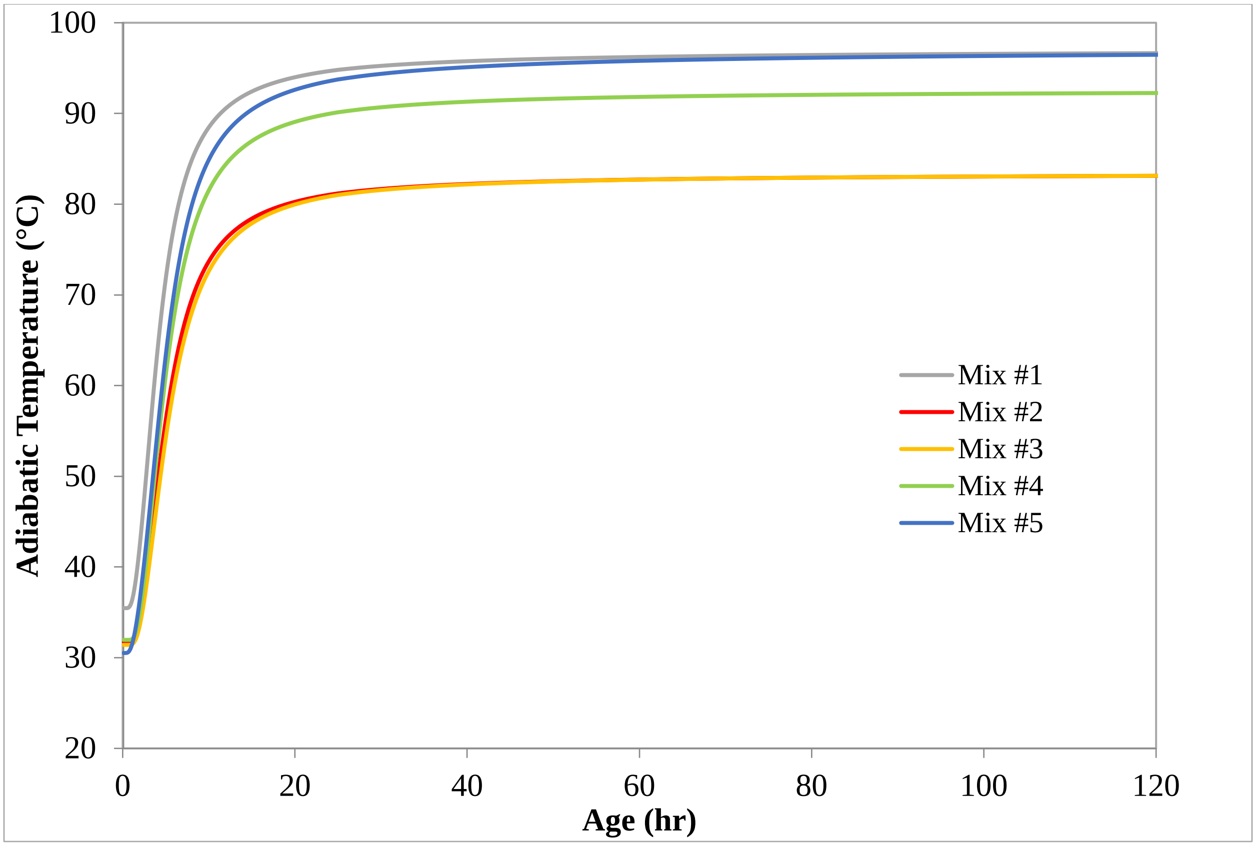

Figure 6-11: Adiabatic temperature for concrete mixtures

Table 6-7: Adiabatic temperature rise

Average Adiabatic Temperature	**Mix**				
	Mix #1	**Mix #2**	**Mix #3**	**Mix #4**	**Mix #5**
Adiabatic Temp (°C) =	98.3	84.2	83.4	94.1	97.2
Adiabatic Temp Rise (°C)=	62.8	52.4	52.0	62.1	66.7

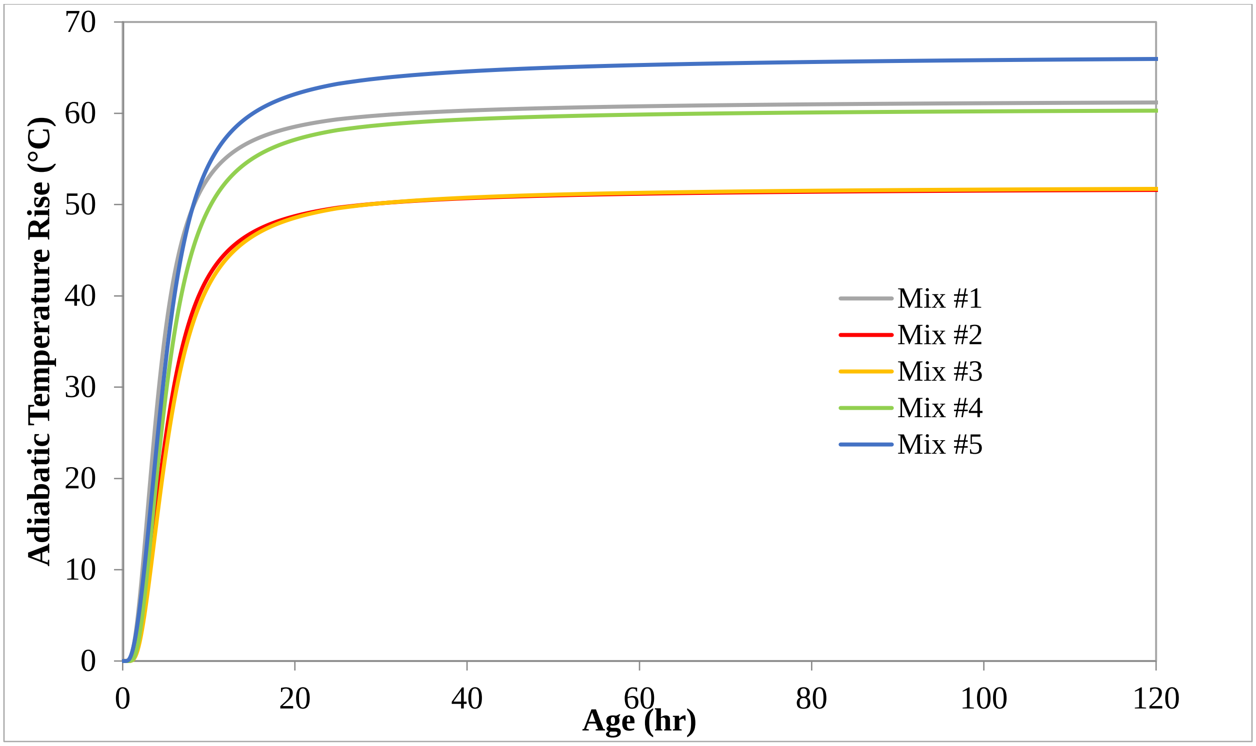

Figure 6-12: Adiabatic temperature rise for concrete mixtures

6.4 Conclusions

The analysis of the semi-adiabatic calorimetry data revealed the following:

- Decreasing cement content from 900 to 700 lb/yd^3 reduced the adiabatic temperature rise in concrete by approximately 10°C. This temperature reduction could help reduce early-age thermal stresses, and reduce temperature-related durability issues such as delayed ettringite formation (DEF).
- Incorporation of SRA at the adopted dosage did not result in significant retardation, as evidenced by a lack of an increase in the τ parameter.
- An increase in the average α_u value was observed for Mix #5 incorporating LWA, indicating a higher degree of reaction due to the extra water supplied by the LWA, which is consistent with previous semi-adiabatic work conducted within a similar experimental framework [16].

6.5 References

[1] ACI Committee 231, “ACI 231R-10: Early-Age Cracking: Causes, Measurement, and Mitigation,” American Concrete Institute, Farmington Hills, MI, 2010.

[2] S. Mindess, F. J. Young, and D. Darwin, *Concrete*. Upper Saddle River, NJ: Pearson Education, Inc., 2003.

[3] P. C. Hewlett, Ed., *Lea’s Chemistry of Cement and Concrete*, 4th ed. New York, NY: Arnold, 1998.

[4] F. De Larrard, P. Acker, and R. Le Roy, “Shrinkage Creep and Thermal Properties,” in *High Performance Concrete: Properties and Applications*, S. Shah and S. Ahmad, Eds. New York, NY: McGraw Hill, 1994, pp. 65–114.

[5] H. Gotfredsen and G. Idorn, “Curing Technology at the Faroe Bridge, Denmark,” in *Properties of Concrete at Early Ages*, J. F. Young, Ed. Detroit, MI: American Concrete Institute, 1986, pp. 17–32.

[6] “Early-Age Properties of Cement-Based Materials. I: Influence of Cement Fineness.” [Online]. Available: http://ascelibrary.org/doi/pdf/10.1061/(ASCE)0899-1561(2008)20:7(502). [Accessed: 13-Jan-2016].

[7] P. Lura, O. M. Jensen, and K. Van Breugel, “Autogenous Shrinkage in High-Performance Cement Paste : An evaluation of basic mechanisms,” *Cem. Concr. Res.*, vol. 33, pp. 223–232, 2003.

[8] C. Hua, P. Acker, and A. Ehrlacher, “Analyses and Models of the Autogenous Shrinkage of Hardening Cement Paste I. Modelling at Macroscopic Scale,” *Cem. Concr. Res.*, vol. 25, no. 7, pp. 1457–1468, 1995.

[9] RILEM Technical Committee 119-TCE, “Adiabatic and Semi-Adiabatic Calorimetry to Determine the Temperature Increase in Concrete Due to Hydration Heat of the Cement,” *Mater. Struct.*, vol. 30, no. 8, pp. 451–464, 1998.

[10] A. K. Schindler, “Concrete Hydration, Temperature Development, and Setting at Early-Ages,” University of Texas at Austin, Austin, 2002.

[11] H. J. H. Brouwers and H. J. Radix, “Self-Compacting Concrete: the Role of the Particle

Size Distribution," *First Int. Symp. on Design Performance. and Use of Self-Consolidating Concrete.*, May 26-28, 2005 in Changsha, Hunan, China, RILEM, Bagneux, France, pp. 109–118.

[12] M. S. Smit, "The Effect of Mixture Proportions on the Properties of High Strength Concrete used in Pavement," University of Pretoria, 2015.

[13] E. Yurdakul, P. C. Taylor, H. Ceylan, and F. Bektas, "Effect of Paste-to-Voids Volume Ratio on the Performance of Concrete Mixtures.," *J. Mater. Civ. Eng.*, vol. 25, no. 12, pp. 1840–1851, 2013.

[14] J. L. Poole, "Modeling Temperature Sensitivity and Heat Evolution of Concrete," The University of Texas at Austin, 2007.

[15] D. P. Bentz, M. R. Geiker, and K. K. Hansen, "Shrinkage-Reducing Admixtures and Early-Age Desiccation in Cement Pastes and Mortars," *Cem. Concr. Res.*, vol. 31, no. 7, pp. 1075–1085, 2001.

[16] B. E. Byard, A. K. Schindler, and R. W. Barnes, "Early-Age Cracking Tendency and Ultimate Degree of Hydration of Internally Cured Concrete," *J. Mater. Civ. Eng.*, vol. 24, no. 8, pp. 1025–1033, 2012.

[17] P. K. Mehta and P. J. M. Monteiro, *Concrete: Microstructure, Properties and Materials*, 3rd ed. New York, NY: McGraw-Hill, 2006.

[18] N. Buch, "Impact of Processed Cellulose Fibers on Portland Cement Concrete Properties," *Transp. Res. Rec.*, vol. 1668, no. 1, pp. 72–80, 1999.

[19] E. Yurdakul, "Proportioning for Performance-Based Concrete Pavement Mixtures," Iowa State University, 2013.

[20] L. Shen, L. Struble, and D. Lange, "Modeling Static Segregation of Self-Consolidating Concrete," *ACI Mater. J.*, vol. 106, no. 4, pp. 367–374, 2009.

[21] P. Goltermann, V. Johansen, and L. Palbøl, "Packing of Aggregates: An Alternative Tool to Determine the Optimal Aggregate Mix," *ACI Mater. J.*, vol. 94, no. 5, pp. 435–443, 1997.

[22] Transtec Group, *COMPASS User's Guide*. Federal Highway Administration, 2000.

[23] ASTM C29 / C29M-16, “Standard Test Method for Bulk Density (‘Unit Weight’) and Voids in Aggregate,” West Conshohocken, PA: ASTM International, 2016.

[24] B. Esmaeilkhanian, P. Diederich, K. H. Khayat, A. Yahia, and Ó. H. Wallevik, “Influence of Particle Lattice Effect on Stability of Suspensions: Application to Self-Consolidating Concrete,” *Mater. Struct.*, vol. 50, no. 1, p. 39, 2017.

[25] P. Taylor, E. Yurdakul, and M. Brink, “Performance-Based Proportioning: An innovative Approach and Tool for Concrete Mixtures,” *Concr. Int.*, vol. 37, no. 8, pp. 41–46, 2015.

[26] R. Rixom and N. Mailvaganam, *Chemical Admixtures for Concrete*, 3rd ed. New York, NY: Routledge, 1999.

[27] A. B. Ribeiro, A. Gonçalves, and A. Carrajola, “Effect of Shrinkage Reduction Admixtures on the Pore Structure Properties of Mortars,” *Mater. Struct.*, vol. 39, no. 2, pp. 179–187, Apr. 2006.

[28] D. P. Bentz and W. J. Weiss, “Internal Curing : A 2010 State-of-the-Art Review,” *Civ. Eng.*, 2011.

[29] ASTM C1761-15, “Standard Specification for Lightweight Aggregate for Internal Curing of Concrete,” West Conshohocken, PA: ASTM International, 2015.

[30] P. Suraneni, P. C. Bran, and R. J. Flatt, “Factors Affecting the Strength of Structural Lightweight Aggregate Concrete with and without Fibers in the 1,200 – 1,600 kg/m^3 Density Range,” *Mater. Struct.*, pp. 677–688, 2016.

[31] J. A. Bogas and A. Gomes, “Compressive Behavior and Failure Modes of Structural Lightweight Aggregate Concrete – Characterization and Strength Prediction,” *Mater. Des.*, vol. 46, pp. 832–841, 2013.

[32] ASTM C260/C260M-10a, “Standard Specification for Air-Entraining Admixtures for Concrete,” West Conshohocken, PA: ASTM International, 2010.

[33] ASTM C494/C494M-13, “Standard Specification for Chemical Admixtures for Concrete,” West Conshohocken, PA: ASTM International, 2013.

[34] A. Zayed, K. Riding, C. C. Ferraro, A. Bien-Aime, N. Shanahan, D. Buidens, T. Meagher, V. Tran, J. D. Henika, J. M. Paris, C. M. Tibbetts, and B. E. Watts, “Final Report Long-

Life Slab Replacement Concrete FDOT Contract Number : BDV25-977-01," University of South Florida, Tampa, FL, 2015

[35] J. L. Poole, K. A. Riding, K. J. Folliard, M. C. G. Juenger, and A. K. Schindler, "Hydration Study of Cementitious Materials using Semi-Adiabatic Calorimetry," *Aci*, vol. SP 241, pp. 59–76, 2007.

[36] ASTM C192/192M-07, "Standard Practice for Making and Curing Concrete Test Specimens in the Laboratory," West Conshohocken, PA: ASTM International, 2010.

[37] ASTM C231/C231M-14, "Standard Test Method for Air Content of Freshly Mixed Concrete by the Pressure Method," West Conshohocken, PA: ASTM International, 2014.

[38] ASTM C143/C143M-15a, "Standard Test Method for Slump of Hydraulic-Cement Concrete," West Conshohocken, PA: ASTM International, 2015.

[39] ASTM C138/C138M-16a, "Standard Test Method for Density (Unit Weight), Yield, and Air Content (Gravimetric)," West Conshohocken, PA: ASTM International, 2016.

Chapter 7 Effect of Concrete Constituents on Coefficient of Thermal Expansion

7.1 Introduction

Coefficient of thermal expansion (CTE) is the change in length per unit length per degree of temperature change. The concrete CTE and change in temperature determine the amount of thermally-induced volume change, which is a main contributor to thermal stress development in concrete. Hence, pavement distresses such as early-age cracking, fatigue cracking, faulting, and joint spalling are influenced by CTE [1]. Reduction of CTE could therefore result in minimizing distress in concrete. Furthermore, CTE is included as a design parameter in the Mechanistic-Empirical Pavement Design Guide (MEPDG) due to its effect on the pavement performance and service life [2] .

Concrete CTE is influenced by three main factors: CTE of aggregates, CTE of cement paste, and the mixture proportions. Cement paste has a higher CTE compared to aggregates. Table 7-1 shows the typical range of CTE of aggregates compared to cement paste.

Table 7-1: Typical range of CTE of aggregates (adapted from [3])

Material	**Thermal Expansion Coefficient (x10^{-6}/°C)**	**Thermal Expansion Coefficient(x 10^{-6}/°F)**
Granite Aggregate	7-9	4-5
Basalt Aggregate	6-8	3.3-4.4
Limestone Aggregate	6	3.3
Dolomite Aggregate	7-10	4-5.5
Sandstone Aggregate	11-12	6.1-6.7
Quartzite Aggregate	11-13	6.1-7.2
Marble Aggregate	4-7	2.2-4
Cement Paste (saturated)	18-20	10-11
Concrete	7.4-13	4.1-7.3

Aggregates compose 70 % to 80 % of concrete solid volume, and therefore aggregate characteristics such as mineralogy and chemical composition greatly affect the concrete CTE [1], [4]–[6]. Mallela et al. [1] stated that concrete made from aggregates of igneous origin exhibited lower CTE compared to those from sedimentary origin, which is contradictory to the findings by others [7], [8]. Generally, aggregate properties are determined by the aggregate chemical constituents such as sodium (Na), aluminum (Al), magnesium (Mg), silicon (Si), calcium (Ca), and iron (Fe). Primary elements which determine the CTE of aggregates are the percentages of Si and Ca in the aggregates [7]. Mccullough et al. [7] developed Equation 7-1 to predict the CTE of aggregates based on their elemental oxide composition.

$$CTE_{agg} = 2.36\,(\mathrm{Na}) - 0.757\,(\mathrm{Al}) - 0.109\,(\mathrm{Ca}) - 0.271\,(\mathrm{Fe}) + 16.017 \qquad \text{Equation 7-1}$$

Where,

Na = percent by weight of Na_2O

Al = percent by weight of Al_2O_3

Ca = percent by weight of CaO

Fe = percent by weight of Fe_2O_3

Mukhopadhyay et al. [9] developed Equation 7-2 to predict aggregate CTE, based on the CTEs of the pure minerals contained in the aggregates and their respective volume percentage in aggregates.

$$\alpha_a = x\sum_{i=1}^{n}\alpha_i V_i + (1-x)\left\{\frac{\sum_{i=1}^{n}\alpha_i V_i E_i}{\sum_{i=1}^{n} V_i E_i}\right\} \qquad \text{Equation 7-2}$$

Where,

α_a = Aggregate CTE

α_i = CTE of individual mineral

V_i = Volume fraction of each mineral in aggregate

E_i = Young’s modulus of each mineral phase

x and $(1-x)$ = relative proportions of material conforming with upper and lower bound solutions

Moreover, Mindess et al. [10] stated that CTE of mortar increases when siliceous sand volume increases, while it decreases when limestone sand volume increases. Kim [11] studied the effect of the sand type on CTE and found that increasing the aggregate siliceous content increased concrete CTE, confirming the findings by Mindess et al. [10]. However, when the CTEs of concrete with different aggregates were determined, it was found that concrete with limestone had the lowest CTE [5], [6]. Therefore, blending low-CTE aggregates with high-CTE aggregates could be considered as a method to optimize concrete CTE [12]. Hence, Siddiqui and Fowler [6] used Equation 7-3 to propose a method for CTE optimization considering three techniques: blending low-CTE coarse aggregates with high-CTE coarse aggregates, blending low-CTE fine aggregates with high-CTE fine aggregates, and reducing cement content. The model presented by Emanuel and Hulsey [4], based on the rule of mixtures to predict CTE of concrete from its constituents, was used in this study [6]. Although Emanuel and Hulsey's model was developed based on the assumption that there is only one fine aggregate and one coarse aggregate in the mixture, it was modified in this study so that the CTE of concrete with one type of cement and multiple coarse and fine aggregate types could be determined.

$$\alpha_c = \beta_p \alpha_s + \sum_{i=1}^{n} \beta_{FAi} \alpha_{FAi} + \sum_{j=1}^{n} \beta_{CAj} \alpha_{CAj} \qquad \text{Equation 7-3}$$

Where,

α_c = Concrete CTE

α_s = CTE of saturated hardened cement paste

α_{FAi} = CTE of *i*th fine aggregate

α_{CAj} = CTE of *j*th coarse aggregate

β_p = Proportion of hardened cement paste by volume

β_{FAi} = Proportion of *i*th fine aggregate by volume

β_{CAj} = Proportion of *j*th coarse aggregate by volume

Moisture content and relative humidity (RH) also affects concrete CTE [2], [4], [13], [14], According to Emanuel and Hulsey [4], the CTE of partially dry cement paste is higher than that of saturated cement paste. Peak CTE occurs at about 60 to 70% moisture content, which is about twice that of the CTE for fully saturated paste and 60% higher than for completely dry paste. Chung and Shin [13] found that the maximum CTEs for expansion and contraction of concrete were obtained at about 65 and 85% relative humidity, respectively. Jeong et al. [2] also observed maximum CTE at approximately 85% RH and the minimum CTE was close to 100% and below 50%.

There are contradictory findings on the dependency of CTE on the age of concrete [15]. It was found that CTE is a function of the moisture content of the specimen and the age of the cement paste [2], [4], [16] . An initially high CTE decreases to a constant value 8-10 hours after placement [2]. However, Won [5] studied the effect of age on CTE for three weeks after mixing and found no significant effect. Chung and Shin [13] also stated that there is no significant change in CTE due to age. Also, it is important to note that since the aggregates make the largest contribution to the concrete CTE, according to the rule of mixtures, it would take a large change in the hardened paste CTE to have a statistically significant and measurable impact on the overall concrete CTE.

CTE of cement paste is higher than that of most aggregates (Table 7-1). Therefore, concrete CTE increases with an increase in cement content [15]. Conversely, concrete CTE could be reduced by decreasing the cement content. Thus, Siddiqui and Fowler [6] studied the effect of cement content on concrete CTE. They first identified the cement content required for the concrete mix to achieve the theoretical paste volume (theoretical paste volume is equal to the void content of the dry-rodded combined aggregates). Then the paste volume was increased and decreased from the theoretical paste volume to identify the effect of cement paste volume on concrete CTE. The CTE of concrete decreased when the paste volume decreased up to the theoretical paste content as expected. On the other hand, CTE increased when the paste volume was decreased below the theoretical paste volume. This was explained by the effect of internal water pressure. When the paste content is below the theoretical paste content, the remaining voids between aggregates increase the porosity in concrete. Higher porosity leads to higher amount of liquid in saturated concrete. As the liquid phase has a higher CTE than the solid phase, concrete CTE increases. Thus, it was concluded that concrete CTE could be decreased by reducing the cement content to the theoretical paste volume [6].

Several studies were performed to identify the effect of water-cement ratio (w/c) ratio on CTE of concrete. Berwanger and Sarkar [17] studied reinforced concrete slab expansion and contraction for concrete with w/c of 0.445, 0.487, 0.577, and 0.672 and same amount of aggregates. They concluded that CTE decreased with increasing w/c ratio. However, Alungbe et al. [18] studied the CTE of concrete with w/c of 0.53, 0.45, and 0.33 and cement contents of 508 lb/yd^3, 564 lb/yd^3, and 752 lb/yd^3, respectively. They did not observe any significant effect of w/c ratio on concrete CTE confirming the findings by Mindess et al. [10].

Hence, it is evident that the concrete CTE is greatly influenced by its constituents, as it is a composite material. Therefore, it is important to assess the parameters selected here, to mitigate the early-age cracking potential, on the CTE of concrete; namely cement content, coarse and fine aggregate contents, lightweight aggregate (LWA) content, and shrinkage reducing admixtures (SRA).

7.2 Methodology

7.2.1 Materials

Five mixtures listed in Table 7-2 were selected for CTE determination. The Mix ID consists of the mixture number and the field slab number. In preparing the cylinders, the temperature profile experienced by the field slabs was imposed during cylinder curing for all mixtures. All the mixtures used the same w/c ratio of 0.384 except Slab 8-Mix 3. Slab 5-Mix 1 was the base mix and Slab 9-Mix 2 and Slab 8-Mix 3 were two optimized mixtures with a cement content of 700 lb/yd^3. The other three mixtures had a cement content of 900 lb/yd^3. Slab 4-Mix 4 and Slab 2-Mix 5 were mixtures that incorporated SRA and LWA respectively. Expanded clay aggregate was used as the LWA.

Table 7-2: Mix design per 1 m^3 (1 yd^3)

Material	**Mix ID**				
	Slab 5-Mix 1	**Slab 9-Mix 2**	**Slab 8-Mix 3**	**Slab 4-Mix 4**	**Slab 2-Mix 5**
Cement (Type I/II), kg (lb)	534 (900)	415 (700)	415 (700)	534 (900)	534 (900)
Coarse Aggregate #57 limestone (SSD), kg (lb)	997 (1680)	682 (1150)	700 (1180)	997 (1680)	997 (1680)
Intermediate Aggregate #89 limestone (SSD), kg (lb)	0.0	409 (690)	421 (710)	0.0	0.0
Fine Aggregate (SSD), kg (lb)	492 (829)	610 (1028)	625 (1054)	501 (844)	326 (549)
Lightweight Aggregate (SSD), kg (lb)	0.0	0.0	0.0	0.0	97 (163)
Water, kg (lb)	193 (325)	150 (252)	131 (221)	189 (319)	193 (325)
Type F Superplasticizer, ml (fl oz)	0.0	948 (24.5)	1354 (35.0)	0.0	0.0
Type E Accelerator, ml (fl oz)	14853 (384)	11554 (298.7)	11554 (298.7)	14853 (384)	14853 (384)
Air Entrainer, ml (fl oz)	38 (1.0)	38 (1.0)	38 (1.0)	38 (1.0)	1.0
Type D Water-reducing Admixture, ml (fl oz)	874 (22.6)	696 (18.0)	696 (18.0)	909 (23.5)	874 (22.6)
Shrinkage Reducing Admixture, ml (gal)	0.0	0.0	0.0	3713 (0.75)	0.0
w/c	0.384	0.384	0.34	0.384	0.384

Volumetric proportions of mixtures were calculated and listed as percentages in Table 7-3. These proportions were used to examine the effect of constituents on concrete CTE.

Table 7-3: Volumetric proportions of mixtures as a percentage (v/o)

Material	**Mix ID**				
	Slab 5-Mix 1	**Slab 9-Mix 2**	**Slab 8-Mix 3**	**Slab 4-Mix 4**	**Slab 2-Mix 5**
Cement	17.0	13.2	13.2	16.9	17.0
CA #57 limestone (SSD)	41.2	28.3	29.0	41.1	41.2
IA #89 limestone (SSD)	0.0	16.7	17.2	0.0	0.0
FAsand (SSD)	18.5	23.0	23.6	18.8	12.3
Lightweight Aggregate (SSD)	0.0	0.0	0.0	0.0	6.3
Water	19.3	15.0	13.2	18.9	19.3
Type F Superplasticizer	0.0	0.1	0.1	0.0	0.0
Type E Accelerator	1.5	1.2	1.2	1.5	1.5
Air Entrainer	0.0	0.0	0.0	0.0	0.0
Type D Water-reducing Admixture	0.1	0.1	0.1	0.1	0.1
Shrinkage Reducing Admixture	0.0	0.0	0.0	0.4	0.0
Air	2.4	2.4	2.4	2.4	2.4

7.2.2 Experimental Procedure

Concrete was mixed according to ASTM C192 [19]. Two 100- x 200-mm (4- x 7.5-in.) cylinders were made from each concrete mixture. The CTE was determined according to AASHTO-T 336-11 [20] and Tex-428-A [21] test procedures using the apparatus constructed at the University of South Florida. Each cylinder was subjected to one cycle of heating and cooling for testing purposes. Prior to measuring the CTE, the specimens were cured for 96 hours in a water bath programmed to simulate the temperature profile collected from the stressmeter thermistor embedded in each field slab. Afterwards, specimen end surfaces were ground flat and parallel using a concrete end surface grinder so that the length of each specimen was 7.0 ± 0.05 in. They were then immersed in saturated lime solution until completion of 7 days of curing before testing. The CTE of each specimen was measured according to AASHTO-T 336-11 [20] using the following process:

1. The specimens were placed in a rigid frame built from SS304 to measure the length change as shown in Figure 7-1. The length change was measured using a D5/200AW linear variable

differential transducer (LVDT), which has a minimum resolution of 0.00025 mm (0.00001 in.). The LVDT was connected to a DR7AC signal conditioner, which was then connected to the PICO USB TC-08 data logger to record displacement data.

Figure 7-1: Supporting frame

2. Internal controls and external connections of the signal conditioner are shown in Figure 7-2. LVDT gain calibration was carried out as follows:
    - Excitation voltage was changed to 3V to achieve a higher resolution.
    - Coarse gain was selected according to the sensitivity of the LVDT (SW1 toggles ON = 3).
    - Power was switched on and a 15-minute warm up period was allowed.
    - ZERO INPUT switch (SW2 toggle 6) was switched on and the ZERO control on the DR7AC was adjusted to 0 mV. ZERO INPUT switch was turned off after this adjustment.
    - The LVDT armature was adjusted for 0-mV output from the DR7AC. The FINE ZERO control was used to obtain an absolute zero indication if the armature adjustment was too coarse.
    - Bipolar operation
        - LVDT armature was moved by 0.01” (using a gauge block) and the FINE GAIN control was adjusted to read 70 mV.

    - LVDT armature was relocated at the center of the stroke to verify whether the output was 0 mV. FINE ZERO control was readjusted if necessary.
    - Armature was moved by 0.01” in the opposite direction and checked whether the output was -70 mV.
  - LVDT was then calibrated to determine the conversion of voltage (mV) to displacement (in/mm) using gauge blocks of 0.0015”, 0.004”, 0.007” and 0.01” thicknesses.

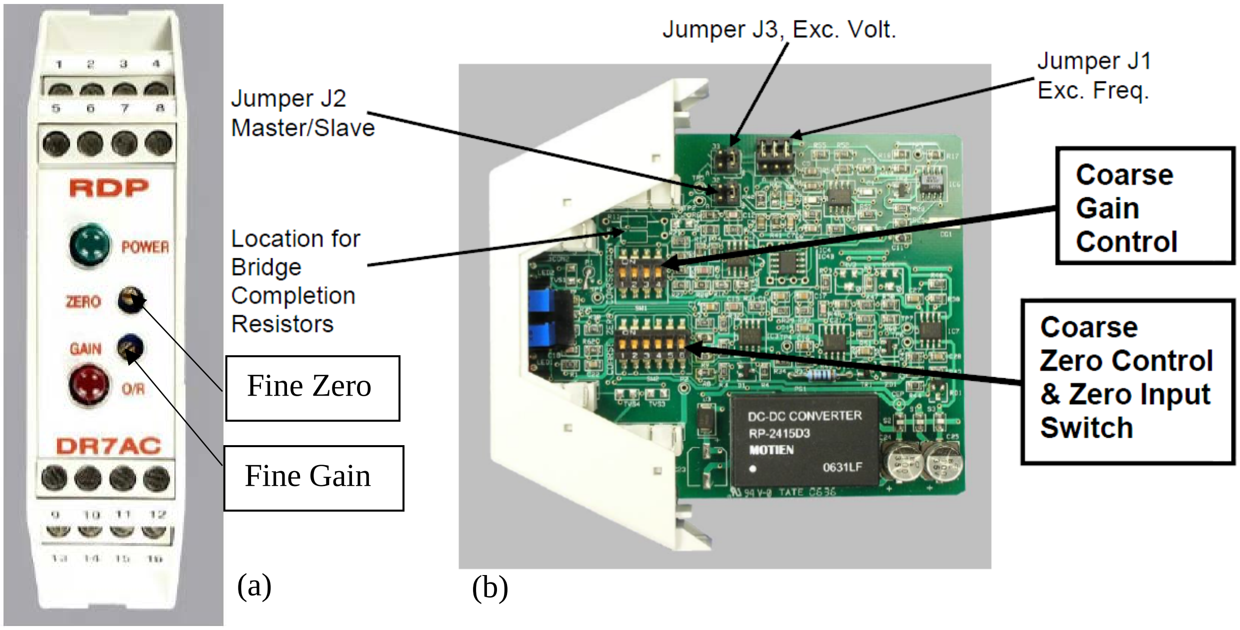

Figure 7-2: (a) External connections (b) Internal controls of DR7AC transducer amplifier

3. The testing frame with attached LVDT was placed in the water bath connected to an AD28R-30 Refrigerating/Heating Bath (Figure 7-3). It was then filled with water until the frame was fully submerged. Water from the AD28R-30 Refrigerating/Heating bath was circulated to the water bath containing the specimen to control the specimen temperature.
4. The concrete cylinder was removed from the lime solution. Its length was measured to the nearest 0.025 mm (0.001 in.) using a caliper and was placed in the CTE frame. The concrete sample was placed to sit firmly on the frame. The sample location on the frame was adjusted so that the tip of the LVDT touched the mid-point of the top surface of the cylinder.
5. The temperature of the water bath was set to 10 ± 1^{o}C (50 ± 2^{o}F) and was left for 8 hours to reach thermal equilibrium, as indicated by consistent readings of the LVDT taken every 10 minutes over a 30-minute period. The allowable difference between the readings over a 30-

minute period was 0.00025 mm (0.00001 in.). The temperature was recorded to the nearest 0.1^{o}C (0.2^{o}F) and the LVDT reading was recorded to the nearest 0.00025 mm (0.00001 in.).

6. The temperature of the water bath was set to 50 ± 1^{o}C (122 ± 2^{o}F) and left for 8 hours to reach thermal equilibrium. Similarly, the temperature and LVDT readings were recorded. The temperature of the water bath was set to 10 ± 1^{o}C (50 ± 2^{o}F) again and left for 8 hours to reach thermal equilibrium.
7. The test result was the average of the two CTE values obtained from the two test segments (heating and cooling segments), provided the two values were within 0.3 microstrain / ^{o}C (0.2 microstrain / ^{o}F) of each other. If this limit was exceeded, one or more additional test segments were completed until two successive CTE values fell within the limit.
8. The same test procedure described from steps 3-7 was used to determine the correction factor using a calibration specimen. The correction factor represents the length change of the measuring apparatus during the heating and cooling periods of the test. The calibration specimen was built from SS410 and had a CTE of 10.3 x 10^{-6} / ^{o}C within the temperature range of 10^{o}C to 50^{o}C. The CTE for SS410 cylinder was measured by PMIC Corporation conforming to ASTM E228-11 [22].
9. Two specimens, which were made from titanium and SS304, were used as verification specimens. The titanium specimen had a CTE of 8.9 x 10^{-6} / ^{o}C and the SS304 specimen had a CTE of 16.1 x 10^{-6} / ^{o}C. The CTE for each verification cylinder was measured by PMIC Corporation conforming to ASTM E228-11 [22].
10. Also, SS304 cylinders, with CTE of 16.1X10^{-6} / ^{o}C measured by PMIC Co. and 6.9” and 7.1” long, were used to verify that the specimen length did not influence the CTE measurement.
11. The CTE of a specimen for one expansion or contraction test segment was calculated using Equation 7-4 through Equation 7-6:

$$CTE = \frac{\Delta L_a}{L_0 * \Delta T}$$ Equation 7-4

$$\Delta L_a = \Delta L_m + \Delta L_f$$ Equation 7-5

$$\Delta L_f = C_f * L_0 * \Delta T$$ Equation 7-6

Where,

ΔL_a = actual length change of the specimen during temperature change

L_0 = measured length of specimen at room temperature

ΔT = measured temperature change

ΔL_m = measured length change of specimen during temperature change

ΔL_f = length change of measuring apparatus during temperature change

C_f = correction factor.

12. Average CTE of the specimen during heating and cooling segments was determined. The maximum allowable difference between the CTE for heating and cooling was 0.3 x 10^{-6} in./in./^{o}C (0.2 x 10^{-6} in./in./^{o}F).
13. The correction factor was calculated using Equation 7-7 through Equation 7-9:

$$C_f = \frac{\Delta L_f}{L_{cs} * \Delta T} \quad \text{Equation 7-7}$$

$$\Delta L_f = \Delta L_a - \Delta L_m \quad \text{Equation 7-8}$$

$$\Delta L_a = \alpha_c * L_{cs} * \Delta T \quad \text{Equation 7-9}$$

Where,

α_c = CTE of the calibration specimen

L_{cs} = measured length of calibration specimen at room temperature

Figure 7-3: Test setup

In the Tex-428-A test method, the test set up, including the testing frame, water bath, length change measuring devices, and specimen dimensions, were the same as the AASHTO T 336 method. The main difference between this method and the AASHTO method is the calculation technique, which uses measurements in heating and cooling cycles from 10 to 50^{o}C (50 to 122^{o}F). The following steps were taken to calculate CTE of each specimen according to Tex-428-A.

1. For each test specimen, a temperature vs. displacement graph was plotted using only increasing or decreasing temperature points. Separate regression analyses of the temperature vs.

displacement relationship were performed for the heating and cooling periods. The corrected CTE was calculated from Equation 7-10:

$$CTE = \frac{M}{L} + C_f \qquad \text{Equation 7-10}$$

Where,

M = slope of the best fit straight line
L = measured length of the sample at room temperature
C_f = correction factor

2. Conforming to Tex-428-A guidelines, the average CTE of the specimen during heating and cooling periods was determined. The maximum allowable difference between the CTE for heating and cooling was 0.5 x 10^{-6} in./in./ ^{o}C (0.3 x 10^{-6} in./in./ ^{o}F). The difference between the average CTEs calculated from the heating and cooling phases of two specimens, prepared from the same concrete mixture, was 0.3 x 10^{-6} in./in./ ^{o}C (0.5 x 10^{-6} in./in./ ^{o}F).
3. Performing a similar calculation for the data obtained from the calibration specimen, the correction factor was determined according to Equation 7-11 and Equation 7-12.

$$CTE_R = \frac{M}{L} \qquad \text{Equation 7-11}$$

$$C_f = K - CTE_R \qquad \text{Equation 7-12}$$

Where,

CTE_R = calculated CTE of the calibration specimen
K = known CTE of calibration specimen.

A correction factor of 16.2 x 10^{-6} in./in./ ^{o}C was obtained for the set up.

7.3 Results and Discussion

CTE was calculated for five concrete mixtures listed in Table 7-1, using both AASHTO T 336 and Tex-428-A test methods. Figure 7-4 shows the comparison of the two CTE test methods. It was evident from the results that Tex-428-A gave higher CTE values compared to the AASHTO method. The difference in calculation technique could be the main reason for this behavior.

Siddiqui and Fowler [12] attributed this to the result of internal water pressure increase due to temperature change. The difference between the CTEs of the two components of saturated concrete, the solid (hydration product and aggregates) and the liquid (gel water and capillary water), causes two types of deformation: instantaneous deformation (ID) and time-dependent deformation (TDD). ID is the deformation that occurs instantaneously with thermal changes and TDD is the deformation that occurs due to thermal changes occurring during moisture redistribution [12], [23]. When conducting the test for CTE, the temperature change followed by the isothermal period would first lead to ID, followed by TDD in both heating and cooling cycles. ID is a function of rate of temperature change, volume of interconnected porosity, and volume of internal water. TDD is a function of internal water pressure, porosity (pore volume fraction and tortuosity), and size of the concrete sample. Since the CTE of liquid is higher than the CTE of solids, the volume of water increases more than the volume of solids during the heating cycle. This results in an increase in the internal water pressure causing expansion of the sample, followed by time dependent contraction during the isothermal state at high temperature. It continues until the excess pressure in the water filled pores gradually dissipates by the flow of water to the exterior of concrete. During the cooling cycle, instantaneous contraction was followed by time-dependent contraction. However, this phenomenon led to overestimation of CTE when Tex-428-A method has been found to overestimate CTE when used, as it uses temperature increasing and decreasing points for CTE determination and does not take into account TDD.

In our experiments, the water bath temperature was recorded and used for specimen CTE calculations instead of the specimen temperature. There could be a slight difference between the specimen and water bath temperature. This was reflected in the displacement reading of the metal calibration and validation standards. It was likely that the specimen temperature lagged the water bath temperature. This effect was less with calibration specimens (Figure 7-5) than concrete specimens (Figure 7-6) due to the much lower thermal conductivity and higher specific heat of the concrete. It took some time for displacement readings with concrete specimens to reach equilibrium during the stable temperature periods. This was due to the lower thermal conductivity of concrete compared to stainless steel. Moreover, there could be effects due to the differences in temperature change between the test frame and the specimen. This effect can be further explained using displacement variation of the SS304 specimen (Figure 7-7) and Figure 7-8, which has the plots of temperature vs displacement for steel (SS410 and SS304), titanium, and concrete specimens. SS304 specimen showed a small displacement with the temperature change. This was unexpected as the test frame was also built from SS304 and therefore, the relative displacement between the test frame and the specimen should be zero. However, SS304 steel bars in the test frame had a smaller diameter compared to the SS304 verification specimen and as a result the test frame heated up or cooled down before the specimen, causing a difference in the displacement reading. Hence it is apparent that the displacement reading recorded is affected by the differences in temperature change in the water bath, test frame and the specimen. In addition, as explained by Siddiqui and Fowler [12] the effects due to change in internal water pressure of the specimen can also be reflected in the displacement reading.

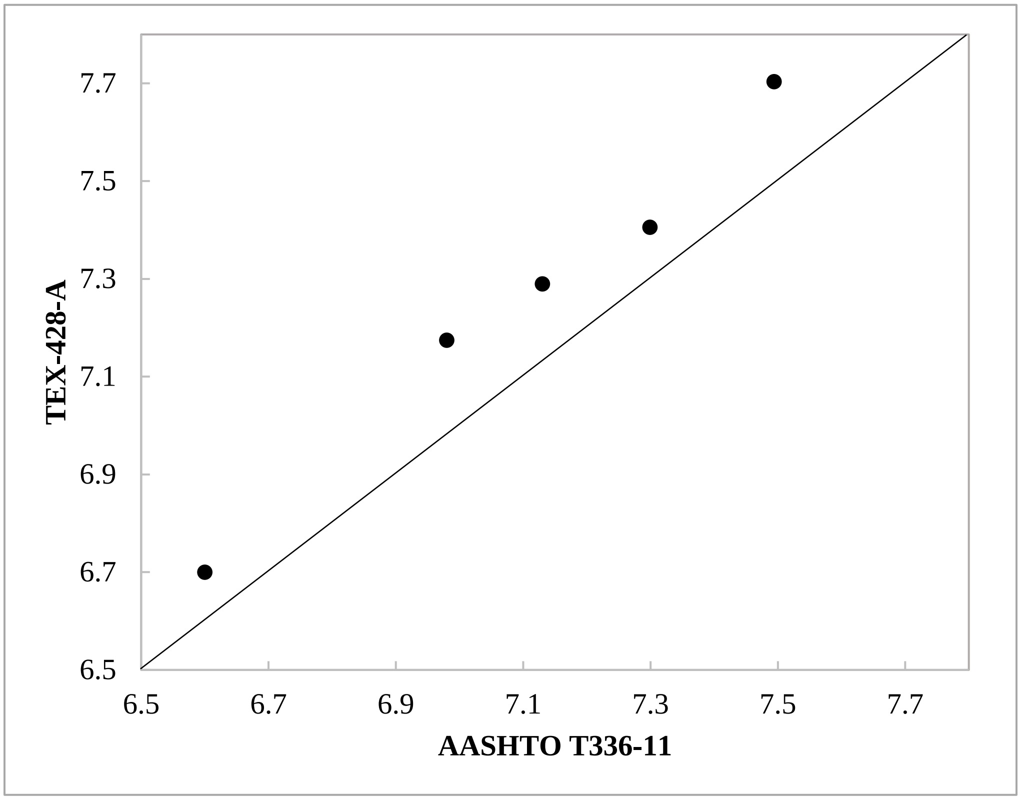

Figure 7-4: Effect of test method on CTE determination

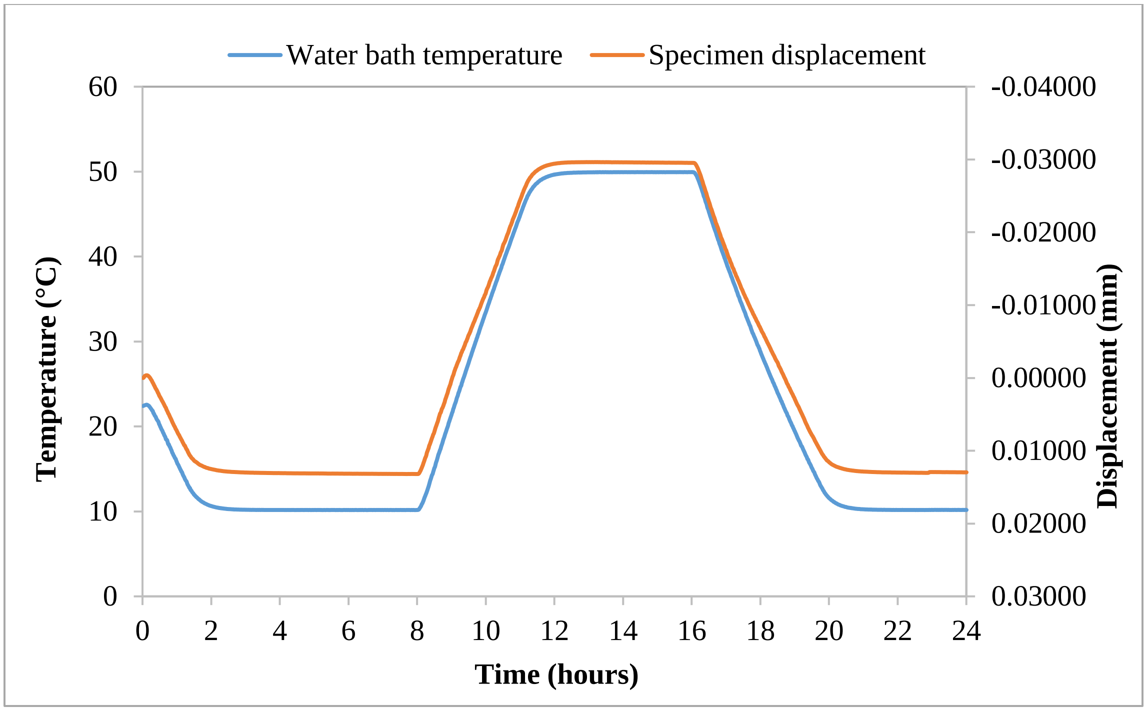

Figure 7-5: Plot of temperature and displacement versus time for SS410

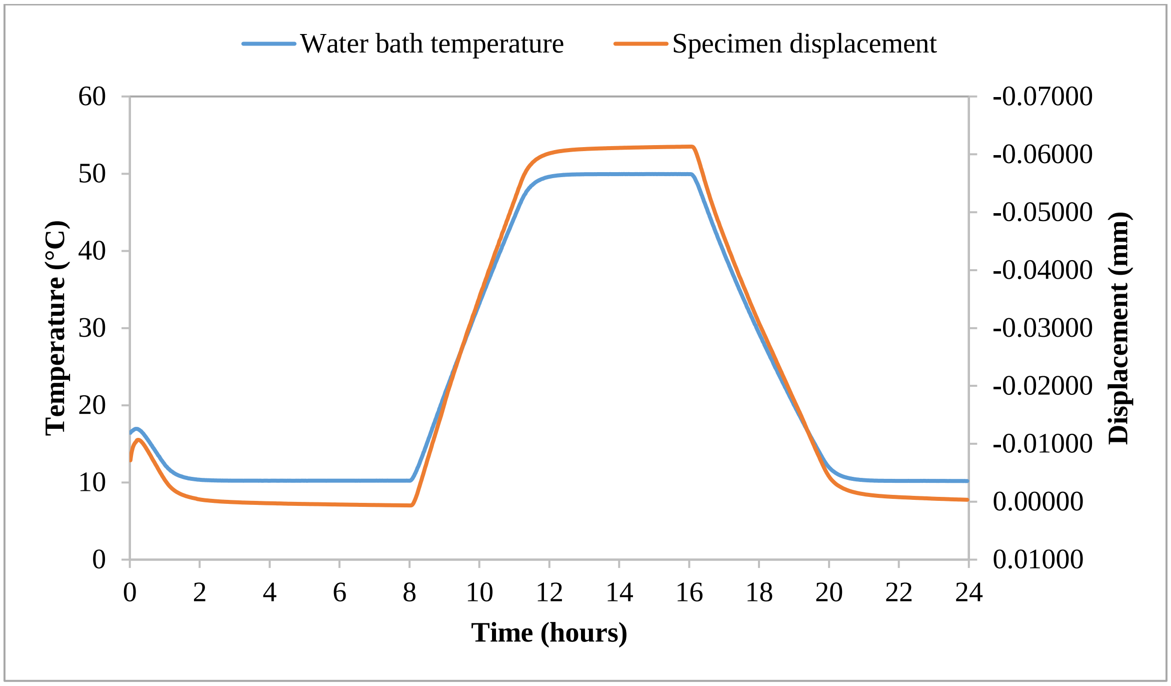

Figure 7-6: Plot of temperature and displacement versus time for concrete

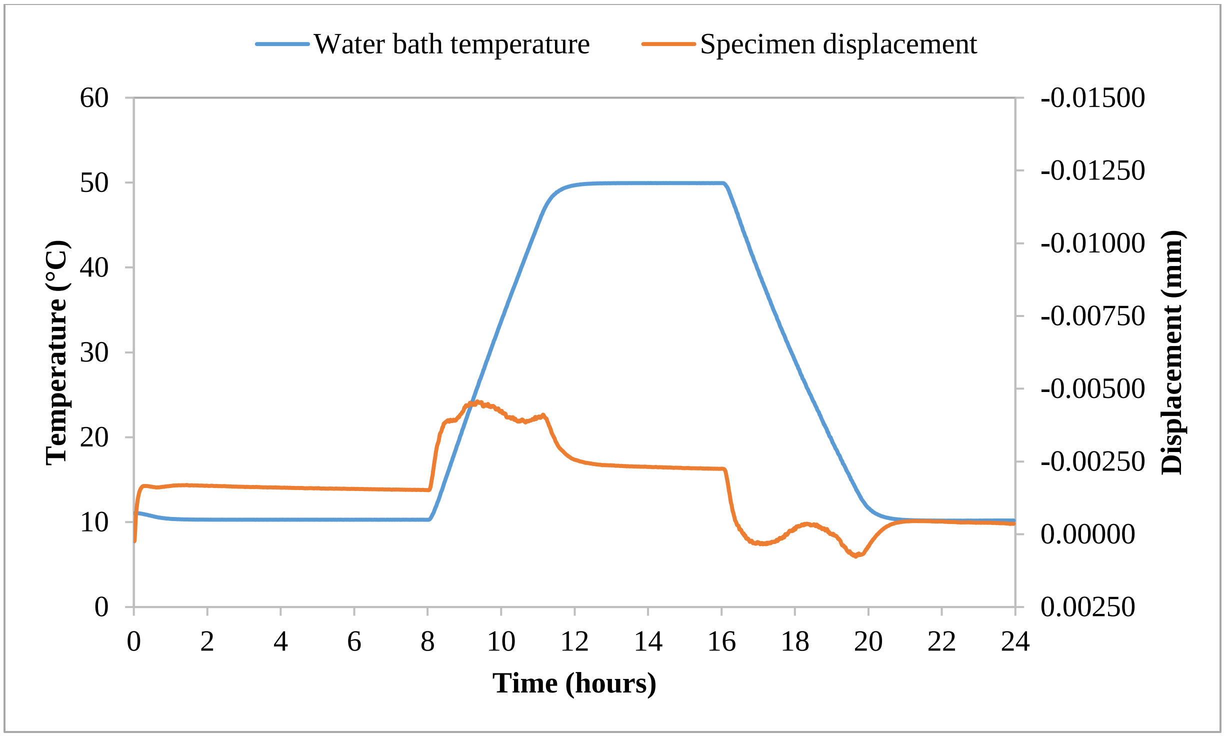

Figure 7-7: Plot of temperature and displacement versus time for SS304

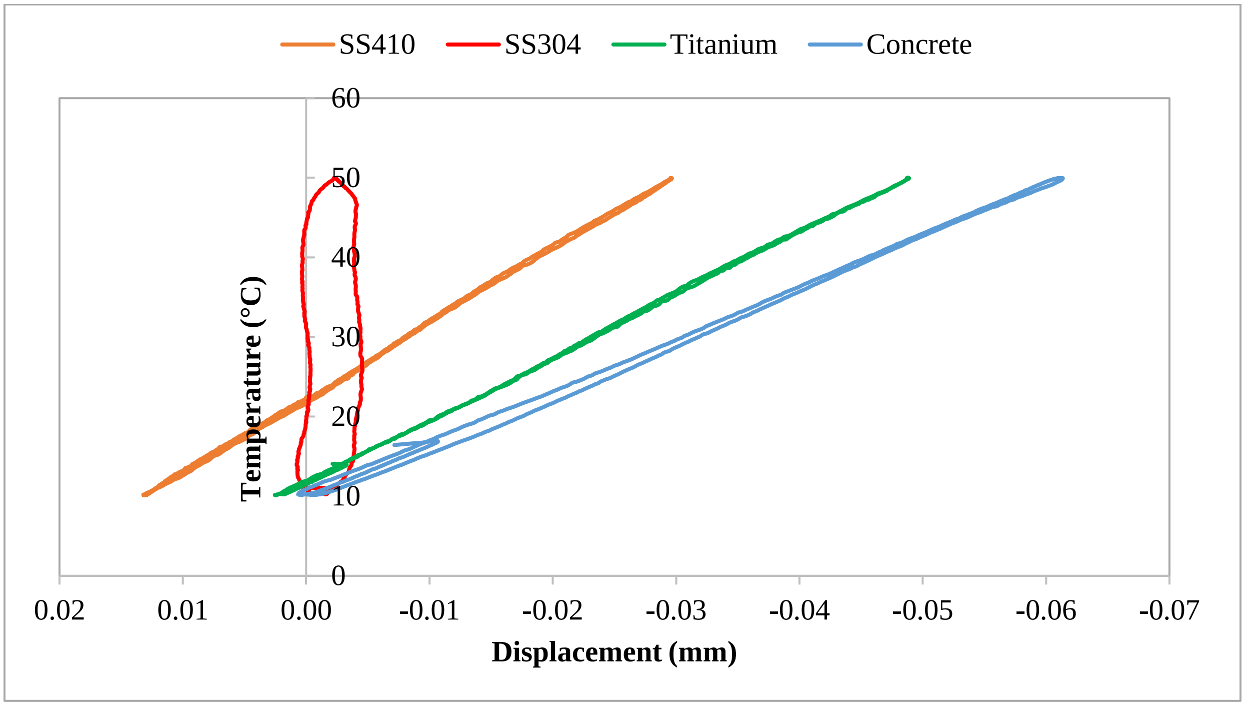

Figure 7-8: Plot of displacement vs. temperature for steel, titanium and concrete specimens

Comparison between the measured CTE of each mixture is shown in Figure 7-9. Slab 2-Mix 5, which incorporated LWA in the mix, had the lowest CTE. Slab 8-Mix 3, the optimized mix with the lower w/c ratio, had the highest CTE. Slab 5-Mix 1 and Slab 4-Mix 4 had similar aggregate contents whereas Slab 9-Mix 2 and Slab 8-Mix 3 had higher total aggregate contents since those were the optimized mixtures and their cement contents were lower than the rest (Table 7-3). Therefore, both of these mixtures had a higher limestone content and sand content. On the other hand, Slab 2-Mix 5 had a lower sand content, as it was partially replaced by LWA.

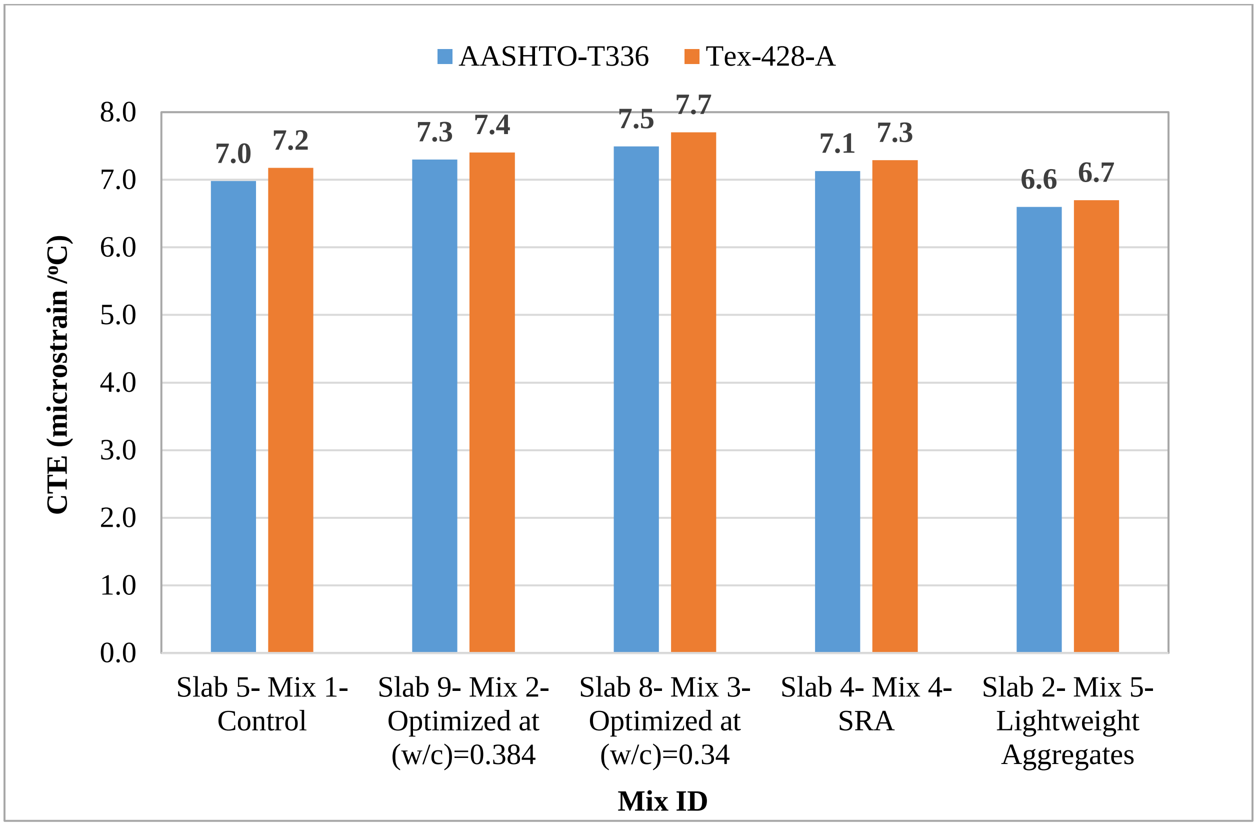

Figure 7-9: Measured CTE values for the mixtures

Analysis of variance (ANOVA) and Fisher least significance difference (LSD) methods were performed on CTE values calculated using AASHTO T 336 method and Tex-428-A method to assess if there was a statistical difference between the CTEs of the control mix (Mix 1) and mixes 2-5. The analyses were conducted at a 95% confidence interval. All statistical analyses were carried out following Montgomery [24]. The outcome of ANOVA and LSD analyses are summarized in Table 7-4.

Table 7-4: Outcome of ANOVA and LSD analyses

ANOVA Summary	Null hypothesis (Reject/Accept)	
	AASHTO-T336	Tex-428-A
	Reject	Reject
LSD Summary	Statistical difference (Yes/No)	
	AASHTO-T336	Tex-428-A
Slab 5-Mix 1 vs Slab 9-Mix 2	Yes	Yes
Slab 5-Mix 1 vs Slab 8-Mix 3	Yes	Yes
Slab 5-Mix 1 vs Slab 4-Mix 4	No	No
Slab 5-Mix 1 vs Slab 2-Mix 5	Yes	Yes

CTEs of the mixes were compared with their aggregate contents as shown in Figure 7-10. It is obvious from this comparison that the variation of CTEs and the variation of fine aggregate content (which is siliceous sand) of the mixtures follow the same trend. Although limestone is the larger volume fraction in the mixtures, sand content seems to have a greater effect on concrete CTEs due to the higher CTE of sand; however, the results are within the expected margin of error of the test.

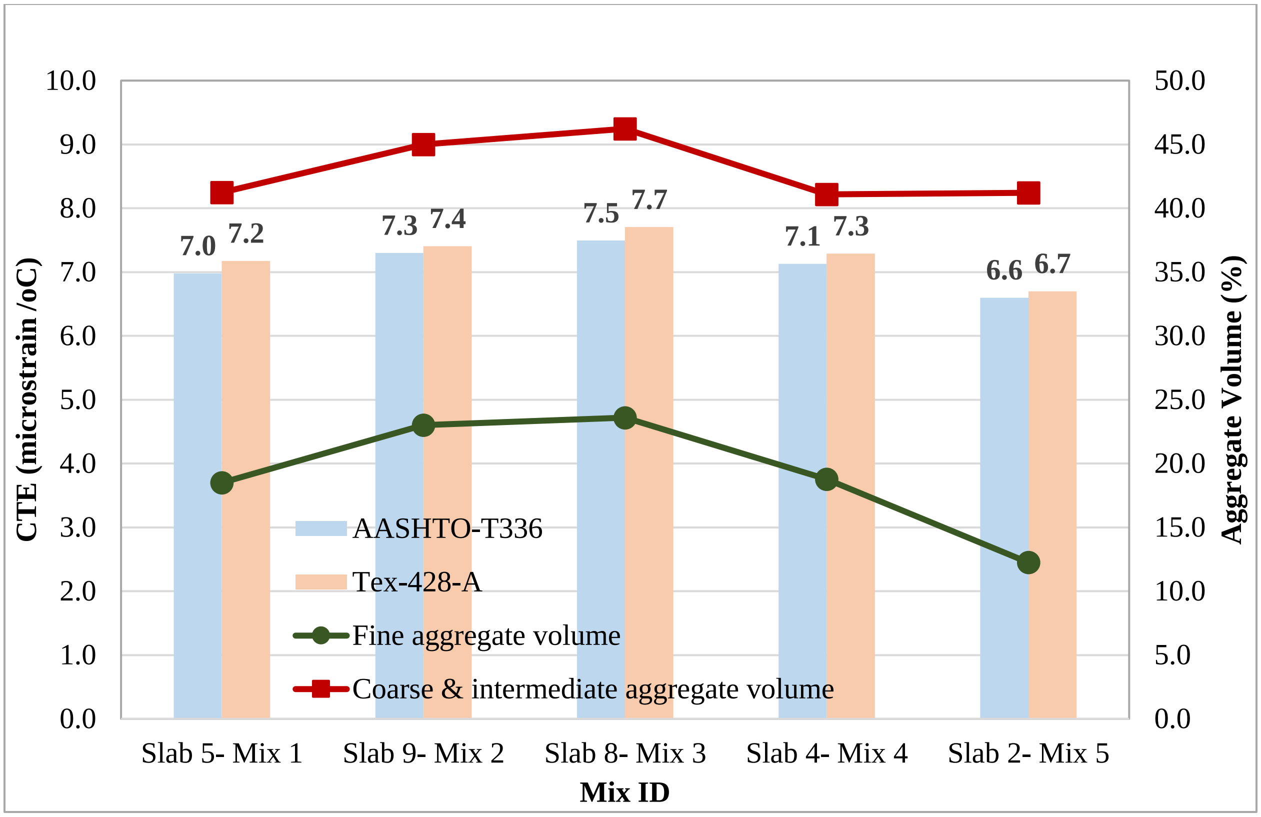

Figure 7-10: Comparison of CTE with the aggregate content in each mix

Incorporation of SRA did not make a significant difference on CTE as the values obtained for Slab 5- Mix1 and Slab 4- Mix 4 were within the expected error of the test; however, the SRA volume used was small. This was confirmed by ANOVA and LSD analyses. Moreover, Slab 2- Mix 5 had the lowest CTE, showing the effect of siliceous sand (Figure 7-10) and LWA on concrete CTE. Expanded clay is known to have lower CTE values compared to siliceous sand [8]. Byard and Schindler [25] have explained that increasing pre-wetted LWA content in concrete systematically decreased its CTE and there was a 30% reduction of CTE when compared to normal weight concrete.

On the other hand, slightly higher CTE values were observed for mixtures Slab 9-Mix 2 and Slab 8-Mix 3, although the cement content was lowered (in Mix 3), which was contrary to what was mentioned in literature [6], [15]. According to Table 7-3, these mixtures had about 5% higher fine aggregates (siliceous sand) and 4% lower cement content compared to the base mix. Therefore, the increase in fine aggregates may have had more influence on concrete CTE compared to the decrease in cement content. Mindess et al. [10] stated that the variation over the normal range of cement contents may not be as great as the effect of aggregate types on concrete CTE, although it depends on cement content. Moreover, Slab 8-Mix 3 mix had a lower w/c ratio compared to the other mixtures while it showed the highest CTE value. However, the effect of w/c ratio did not seem to be statistically significant when compared with Slab 9-Mix 2 (which had the same cement content) for the CTE values determined according to AASHTO T 336.

7.4 Summary

The CTE values of five concrete mixtures were determined using both AASHTO T 336 and Tex-428-A test methods to investigate the effect of cement content, coarse and fine aggregate content, incorporation of LWAs, and addition of SRA on concrete CTE. The following conclusions can be drawn from the experimental results:

- Incorporation of SRA did not make a statistically significant difference on concrete CTE.
- Concrete CTE increased when the volume of siliceous sand increased.
- Use of LWA reduced concrete CTE.
- Effect of cement content may not be as great as the effect of aggregate type on concrete CTE.

7.5 References

[1] J. Mallela, A. Abbas, T. Harman, C. Rao, R. Liu, and M. Darter, “Measurement and Significance of the Coefficient of Thermal Expansion of Concrete in Rigid Pavement Design,” *Transp. Res. Rec.*, vol. 1919, pp. 38–46, 2005.

[2] J. H. Jeong, D. G. Zollinger, J. S. Lim, and J. Park, “Age and Moisture Effects on Thermal Expansion of Concrete Pavement Slabs,” *J. Mater. Civ. Eng.*, vol. 24, no. 1, pp. 8–15, 2012.

[3] Federal Highway Administration Research and Technology, “Thermal Coefficient Of Portland Cement Concrete,” *Portland Cement Concrete Pavements Research*, 2016. [Online]. Available: https://www.fhwa.dot.gov/publications/research/infrastructure/pavements/pccp/thermal.cfm. [Accessed: 01-Nov-2016].

[4] J. H. Emanuel and J. L. Hulsey, “Prediction of the Thermal Coefficient of Expansion of Concrete,” *ACI J. Proc.*, vol. 74, no. 4, pp. 149–155, 1977.

[5] M. Won, “Improvements of Testing Procedures for Concrete Coefficient of Thermal Expansion,” *J. Transp. Res. Board*, vol. 1919, pp. 23–28, 2005.

[6] M. S. Siddiqui and D. W. Fowler, “A Systematic Optimization Technique for the Coefficient of Thermal Expansion of Portland Cement Concrete,” *Constr. Build. Mater.*, vol. 88, pp. 204–211, 2015.

[7] B. F. Mccullough, D. G. Zollinger, and T. Dossey, “Evaluation of the Performance of Texas Pavements Made with Different Coarse Aggregates,” Texas Department of Transportation, 2000.

[8] P. K. Mehta and P. J. M. Monteiro, *Concrete: Microstructure, Properties, And Materials*, 3rd ed. McGraw-Hill Publishing, 2006.

[9] A. Mukhopadhyay, S. Neekhra, and D. Zollinger, “Preliminary Characterization of Aggregate Coefficient of Thermal Expansion and Gradation for Paving Concrete.,” Texas Department of Transportation, 2007.

[10] S. Mindess, F. J. Young, and D. Darwin, *Concrete*. Upper Saddle River, NJ: Pearson

Education, Inc., 2003.

[11] S. H. Kim, "Determination of Coefficient of Thermal Expansion for Portland Cement Concrete Pavements for MEPDG Implementation," Southern Polytechnic State University, Marietta, GA, 2012.

[12] S. Siddiqui and D. W. Fowler, "Effect of Internal Water Pressure on the Measured Coefficient of Thermal Expansion of Concrete," *J. Mater. Civ. Eng*, vol. 27, no. 4, pp. 1–7, 2014.

[13] Y. Chung and H.-C. Shin, "Characterization of the Coefficient of Thermal Expansion and its Effect on the Performance of Portland Cement Concrete Pavements," *Can. J. Civ. Eng.*, vol. 38, no. 2, pp. 175–183, 2011.

[14] J. H. Yeon, S. Choi, and M. C. Won, "Effect of Relative Humidity on Coefficient of Thermal Expansion of Hardened Cement Paste and Concrete," *Transp. Res. Rec. J. Transp. Res. Board*, vol. 2113, pp. 83–91, 2009.

[15] M. S. Siddiqui, "Effect of Portland Cement Concrete Characteristics and Constituents on Thermal Expansion," PhD Thesis, The University of Texas at Austin, 2014.

[16] S. L. Meyers, "How Temperature and Moisture Changes may Affect the Durability of Concrete," *Rock Prod. devoted to Prod. sale rock clay Prod.*, vol. 54, pp. 153–158, 1951.

[17] C. Berwanger and S. Faruque, "Thermal Expansion of Concrete and Reinforced Concrete," *ACI J.*, no. 73, pp. 618–621, 1976.

[18] G. D. Alungbe, M. Tia, and D. G. Bloomquist, "Effects of Aggregate, Water/Cement Ratio, and Curing on the Coefficient of Linear Thermal Expansion of Concrete," *Transp. Res. Rec.* , vol. 1335, pp. 44–51, 1992.

[19] ASTM C192/C192M-14, "Standard Practice for Making and Curing Concrete Test Specimens in the Laboratory," West Conshohocken, PA: ASTM International, 2014.

[20] AASHTO T 336-11, "Standard Method of Test for Coefficient of Thermal Expansion of Hydraulic Cement Concrete Hydraulic Cement Concrete," Washington, DC: American Association of State Highway and Transportation Officials, 2013.

[21] Tex-428-A, "Test Procedure for Determining the Coefficient of Thermal Expansion of

Concrete," Austin, TX: Texas Department o, 2011.

[22] ASTM E228-11, "Standard Test Method for Linear Thermal Expansion of Solid Materials With a Push-Rod Dilatometer," West Conshohocken, PA: ASTM International, 2016.

[23] E. J. Sellevold and Ø Bjøntegaard, "Coefficient of thermal expansion of cement paste and concrete: Mechanisms of moisture interaction," *Mater. Struct.*, vol. 39, pp. 809–815, 2006.

[24] D. C. Montgomery, *Design and Analysis of Experiments*. Hoboken, NJ: Wiley, 2005.

[25] B. E. Byard and A. K. Schindler, "Cracking Tendency of Lightweight Concrete," Auburn University, Auburn, AL, 2010.

Chapter 8 Stress and Temperature Evolution in Concrete Pavement Slabs

8.1 Introduction

High-early-strength (HES) concrete used for pavement slab replacement projects has a higher susceptibility to cracking at early ages due to the addition of an accelerating admixture that accelerates hydration and enables rapid setting and strength gain that is typically sufficient to satisfy the criteria of opening to traffic in 4 to 6 hours. The use of an accelerating admixture in addition to high cement contents in FDOT HES concretes promote higher temperature rises and higher shrinkage, which lead to higher cracking potentials and associated durability issues [1]–[4]. In this project, several approaches to reduce the potential for early-age cracking were evaluated using 12 ft x 15 ft x 1 ft concrete slabs. A mock-up slab (slab 1) was first made just to test placement and instrumentation procedures. Eight instrumented concrete slabs were produced with the following characteristics:

<u>Control Mix (Slab 5)</u>: HES concrete with 900 lb/yd^3 of cement and w/c = 0.384.

<u>Internal Curing (Slab 2)</u>: Control Mix with partial replacement of fine aggregates with saturated lightweight aggregates (LWA) to provide extra water for hydration.

<u>Shrinkage-Reducing Admixture (Slab 4)</u>: Control Mix with SRA added to minimize overall shrinkage.

<u>Fiber Reinforcement (Slab 3)</u>: Control Mix with addition of polypropylene fibers to provide restraint to cracking.

<u>Paste Reduction (Slab 9)</u>: Control Mix with paste volume reduced by lowering the cement content from 900 lb to 700 lb. This was aided by improving the aggregate particle packing by replacing some of the standard coarse aggregate (#57 limestone) with an intermediate-sized aggregate (#89 limestone). The relative amounts of the two coarse aggregates were determined from particle packing optimization calculations.

<u>Paste and w/c Reduction (Slab 8)</u>: Paste Reduction mix with w/c reduced from 0.384 to 0.340.

<u>Modified Base Restraint (Slab 6)</u>: Paste and w/c Reduction mix with two layers of plastic between the base and concrete to reduce the base restraint.

Modified Base Restraint (Slab 7) Paste and w/c Reduction mix with a nonwoven geotextile between the base and concrete to reduce the base restraint.

Presoaked LWA provides an internal source of curing water that reduces autogenous shrinkage and maintains a high level of internal humidity in the concrete, which reduces the drying shrinkage. Reduction of the autogenous and drying shrinkage of the concrete significantly reduces its potential for cracking [5]–[10]. The polypropylene fiber was used to improve the cracking resistance of the early-age concrete by increasing its tensile strength. This allows the concrete to resist higher stresses, produced by differential temperatures and shrinkage, before cracking. The shrinkage-reducing admixture was used to reduce the surface tension of the pore water, which reduces the capillary pressure in the system. A reduction in the capillary pressure, which acts to pull adjacent particles closer together, results in a reduction in drying shrinkage. This also reduces the differential drying shrinkage that occurs between the exposed surface of the concrete and its interior, thereby reducing the tendency of the slab to curl [11]–[13]. The double plastic sheet and geotextile liners were used in the attempt to reduce the restraint between the concrete slab and the base. The optimized mixtures were designed to incorporate intermediate-sized aggregates in the mix to improve the aggregate gradation. This approach was used to reduce the paste-to-void content (the void content is the portion of the bulk volume that is unoccupied by the aggregate), thus reducing cement content in the mix. A reduction in cement paste content decreases the concrete temperature rise, and the drying and autogenous shrinkage, all of which lead to a reduction in the cracking tendency of the concrete.

8.2 Methodology

Eight 12 ft x 15 ft x 1 ft concrete slabs with a standard FDOT 12-inch base were constructed. The proportions for the slab mixture designs are listed in Table 8-1. An environmentally-friendly release agent was sprayed on the inside faces of the wood side forms. Type T thermocouples were mounted in the center of the slab at heights of 1, 6, and 11 inches from the surface of the base. The wires were attached to insulated pieces of reinforcing steel embedded into the subbase. The thermocouple placed in slab 5 at 6 inches malfunctioned shortly after the concrete was placed; therefore, no data was collected from this thermocouple. The rest of the thermocouples remained operational for the duration of data collection.

Geokon Model 4370 concrete stressmeters, based on vibrating-wire gauge technology, were used to monitor concrete stress development. The center of each stressmeter was mounted 8 inches from the slab bottom using rebars and tie wire. During placement of the concrete, the stressmeter tube was uncapped and filled with consolidated concrete. Once full, the stressmeter cap was placed back on the tube and the stressmeter was tied onto the rebar frame, centered and leveled. While the slab was being placed, measurements for unit weight, slump, and air content were performed, and 4-inch x 8-inch concrete cylinders were prepared for tensile splitting strength, elastic modulus, and compressive strength testing. After the concrete was finished, two coats of curing compound were applied to the surface of the concrete. For the first 48 hours, the cylinders were placed on top of their respective slabs. A thermocouple was placed into one cylinder for each slab to monitor temperature development of the cylinders, and was later used for maturity calculations. During the first 24 hours, the cylinders were covered by two layers of curing blankets, after which time the blankets were removed and the cylinders were exposed to ambient field conditions. At 48 hours, the cylinders were transferred from the site to the Construction Materials Research Laboratory at the University of South Florida and immersed in saturated lime solution maintained at an ambient temperature of 23 ± 1ºC until the time of testing. Compressive strength, splitting tensile strength and elastic modulus testing were performed using a Universal Testing Machine (UTM) manufactured by MTS Systems in accordance with ASTM C39 [14], ASTM C496 [15], and ASTM C469 [16], respectively. Cylinders were tested at the ages of 0.25, 1, 3, 7, and 28 days.

Table 8-1: Concrete mixture designs, 1 m^3 (1 yd^3)

	Mix #1	**Mix #2**	**Mix #3**	**Mix #4**	**Mix #5**	**Mix #6**
	Control	**Optimized at w/c=0.384**	**Optimized at w/c=0.34**	**SRA**	**LWA**	**Fiber**
Slab number	**Slab 5**	**Slab 9**	**Slab 6,7,8**	**Slab 4**	**Slab 2**	**Slab 3**
Cement, kg (lb)	534 (900)	415 (700)	415 (700)	534 (900)	534 (900)	534 (900)
Coarse (SSD), kg (lb)	997 (1680)	682 (1150)	700 (1180)	997 (1680)	997 (1680)	997 (1680)
Intermediate (SSD), kg (lb)	0.0	409 (690)	421 (710)	0.0	0.0	0.0
Fine (SSD), kg (lb)	492 (829)	610 (1028)	625 (1054)	501 (844)	326 (549)	491 (827)
Lightweight (SSD), kg (lb)	0.0	0.0	0.0	0.0	97 (163)	0.0
Mix Water, kg (lb)	193 (325)	150 (252)	131 (221)	189 (319)	193 (325)	193 (325)
SP1, ml (fl. oz)	0.0	948 (24.5)	1354 (35.0)	0.0	0.0	0.0
ACC, ml (fl. oz)	14853 (384)	11554 (298.7)	11554 (298.7)	14853 (384)	14853 (384)	14853 (384)
AE, ml (fl. oz)	38 (1.0)	38 (1.0)	38 (1.0)	38 (1.0)	38 (1.0)	38 (1.0)
WR, ml (fl. oz)	596 (15.4)	696 (18.0)	696 (18.0)	874 (22.6)	874 (22.6)	874 (22.6)
SRA, ml (gal)	0.0	0.0	0.0	3713 (0.75)	0.0	0.0
Fiber, kg (lb)	0.0	0.0	0.0	0.0	0.0	0.297 (0.5)
w/c	0.384	0.384	0.340	0.384	0.384	0.384

Calculations for stress and calibration factors for the concrete stressmeter were found in the accompanying stressmeter calibration reports. Equation 8-1 was used to calculate the stress development in the concrete.

$$S = G\,(R_1 - R_0) \qquad \text{Equation 8-13}$$

Where,

S = Stress

G = Linear Gauge Factor (psi/digit) from Geokon Calibration Report

R_1 = Stressmeter reading at the specified time

R_0 = Initial stressmeter reading

The initial values for time and stressmeter readings were taken as the time when the accelerating admixture was added to the concrete truck on site.

The concrete stress-to-tensile-strength ratio was calculated for each slab. This was performed by first calculating the Nurse-Saul maturity of the concrete cylinders and slabs separately, since they had slightly different temperature profiles. The maturity was calculated using the Nurse-Saul function (Equation 8-2):

$$M = \sum (T-T_0)\, \Delta t \qquad \text{Equation 8-14}$$

Where,

M = Maturity (time-°C)

Δt = Time interval (time)

T = Average temperature of concrete over time interval Δt (°C)

T_0 = Datum temperature (°C)

The tensile splitting strengths of concrete cylinders were then plotted against their maturity, and an exponential function (Equation 8-3) was used to obtain S_u, τ, and β parameters using the solver function in Microsoft Excel [17]–[20].

$$S = S_u\, e^{-(\frac{\tau}{t})^{\beta}} \qquad \text{Equation 8-15}$$

Where,

S = Average tensile strength at age t (psi)

t = Test age (days)

S_u = Limiting strength (psi)

τ = Time constant (days)

β = Curve shape parameter (dimensionless)

S_u, τ and β parameters were used to calculate the tensile strength development of the concrete slabs based on their maturity. After that, the stresses were divided by the corresponding tensile strengths to obtain the stress-to-tensile-strength ratio development for each slab.

8.3 Results

The compressive strengths shown in Table 8-2 exceeded the 1600 psi required by FDOT for opening to traffic in less than 6 hours, and were considerably higher at 28 days than the required 3000 psi [21]. Splitting tensile strength and elastic modulus values are listed in Table 8-3 and Table 8-4, respectively. Generally, mechanical properties were similar for all the slabs.

Table 8-2: Compressive strength (psi)

Slab Age (days)	Slab 2 Mix #5 LWA	Slab 3 Mix #6 Fiber	Slab 4 Mix #4 SRA	Slab 5 Mix #1 Control	Slab 6 Mix #3 Plastic	Slab 7 Mix #3 Geotextile	Slab 8 Mix #3 Optimized at w/c=0.34	Slab 9 Mix #2 Optimized at w/c=0.384
0.25	3,320	3,660	3,370	3,800	3,620	4,010	3,760	4,020
1	6,160	6,120	5,900	6,120	6,640	6,090	6,480	6,530
3	6,440	6,330	6,520	7,200	7,020	6,750	7,400	6,970
7	7,120	6,920	6,680	6,980	7,060	7,200	7,650	6,730
28	7,670	7,460	7,870	7,700	7,830	7,840	8,430	7,990

Table 8-3: Tensile splitting strength (psi)

Slab Age (days)	Slab 2 Mix #5 LWA	Slab 3 Mix #6 Fiber	Slab 4 Mix #4 SRA	Slab 5 Mix #1 Control	Slab 6 Mix #3 Plastic	Slab 7 Mix #3 Geotextile	Slab 8 Mix #3 Optimized at w/c=0.34	Slab 9 Mix #2 Optimized at w/c=0.384
0.25	365	405	440	470	465	490	440	475
1	495	525	540	535	595	525	640	535
3	545	540	570	630	655	560	595	635
7	570	610	585	585	730	640	710	655
28	625	605	605	580	745	625	745	705

Table 8-4: Elastic modulus

Slab / **Age (days)**	**Slab 2 Mix #5 LWA (10^6 psi)**	**Slab 3 Mix #6 Fiber (10^6 psi)**	**Slab 4 Mix #4 SRA (10^6 psi)**	**Slab 5 Mix #1 Control (10^6 psi)**	**Slab 6 Mix #3 Plastic (10^6 psi)**	**Slab 7 Mix #3 Geotextile (10^6 psi)**	**Slab 8 Mix #3 Optimized at w/c=0.34 (10^6 psi)**	**Slab 9 Mix #2 Optimized at w/c=0.384 (10^6 psi)**
0.25	2.88	2.90	3.13	3.13	3.55	3.08	3.45	3.53
1	3.85	4.43	4.13	4.10	4.80	4.00	4.18	3.65
3	4.10	4.15	4.40	4.55	4.91	4.35	4.65	4.68
7	3.70	4.39	4.50	4.52	5.60	4.48	5.23	4.63
28	4.35	4.38	4.94	4.95	5.34	4.91	5.18	4.69

In order to evaluate the effect of LWA, fiber, SRA, and mix optimization on stress development, the data collected for slabs 2, 3, 4 and 9 were compared to the data collected for slab 5, which was designated as the Control. Concrete stresses, when there are no external loads, can be generally associated with temperature- and moisture-related volume changes [22]. The heat of hydration contributes significantly to the temperature development during the first day. Afterwards, the concrete temperature development is mostly determined by the daily ambient temperature variation. Since the base material was not wetted prior to concrete placement, it was expected that they would absorb some of the mix water from concrete, contributing to the moisture gradients and warping between the tops and the bottoms of the slabs.

Temperature profiles at the top, middle and bottom of slabs 2 (LWA) and 5 (Control) are displayed in Figure 8-1. During the first 24 hours, the temperatures at the top and bottom of slabs 2 and 5 were very similar, while the temperature in the middle was somewhat higher for slab 2.

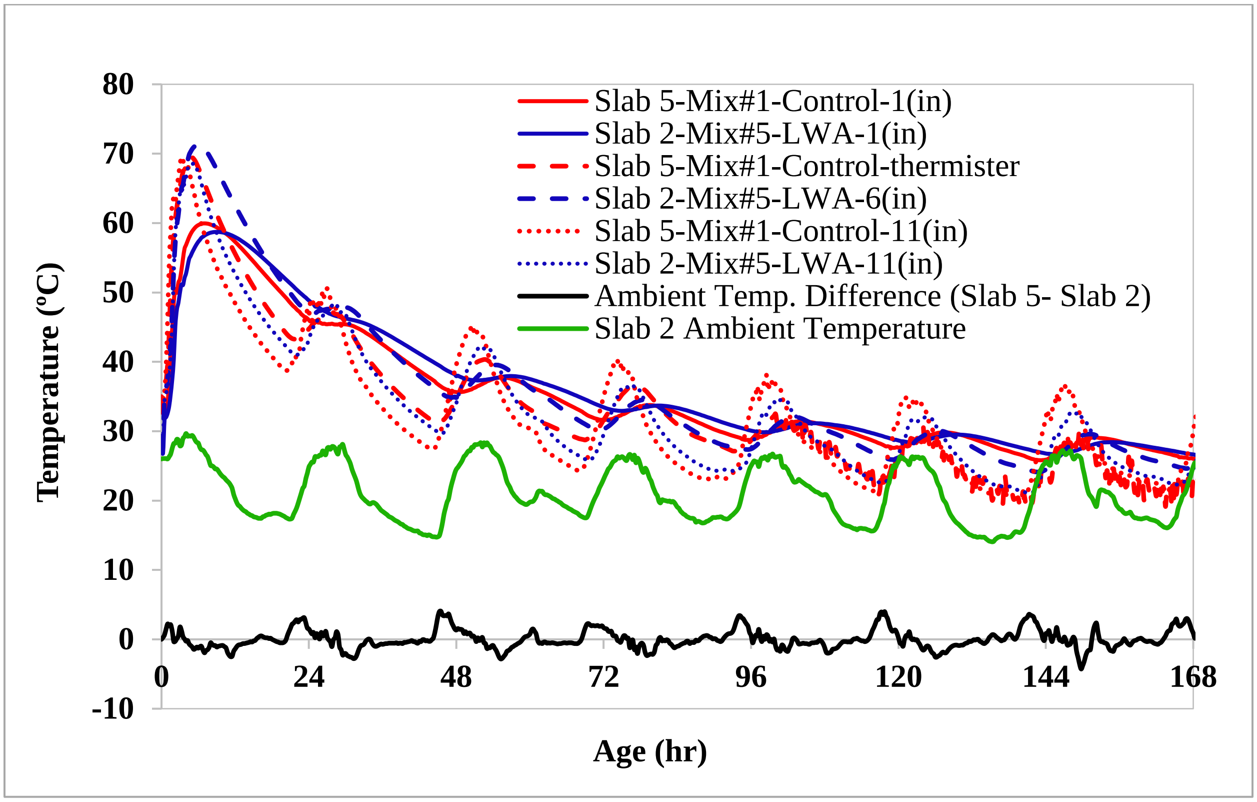

Figure 8-1: Thermocouple readings for slabs 2 and 5

Stress development in slabs 2 and 5 was very similar during the first 6 hours, as can be seen in Figure 8-2 (b). This can be attributed to similar temperature profiles of the slabs at the location of the stressmeters (Figure 8-2 (a)). Both slabs experienced high tensile stresses at approximately 2.5 hours after placement, and the magnitude of these stresses was similar for both slabs. However, after 6 hours, tensile stresses in slab 2 continued to decrease and changed from tensile to compressive, while slab 5 remained in tension during the first 24 hours. After 24 hours, the stresses in slab 2 were slightly higher compared to slab 5.

Stress development alone cannot be used as a predictor of cracking potential, as cracking is dependent on the stress-to-tensile-strength ratio. Although the initial peak stresses were similar in slabs 2 and 5, as can be seen in Figure 8-3, addition of LWA significantly reduced the corresponding stress-to-tensile-strength ratio from approximately 0.8 for slab 5 to 0.4 for slab 2.

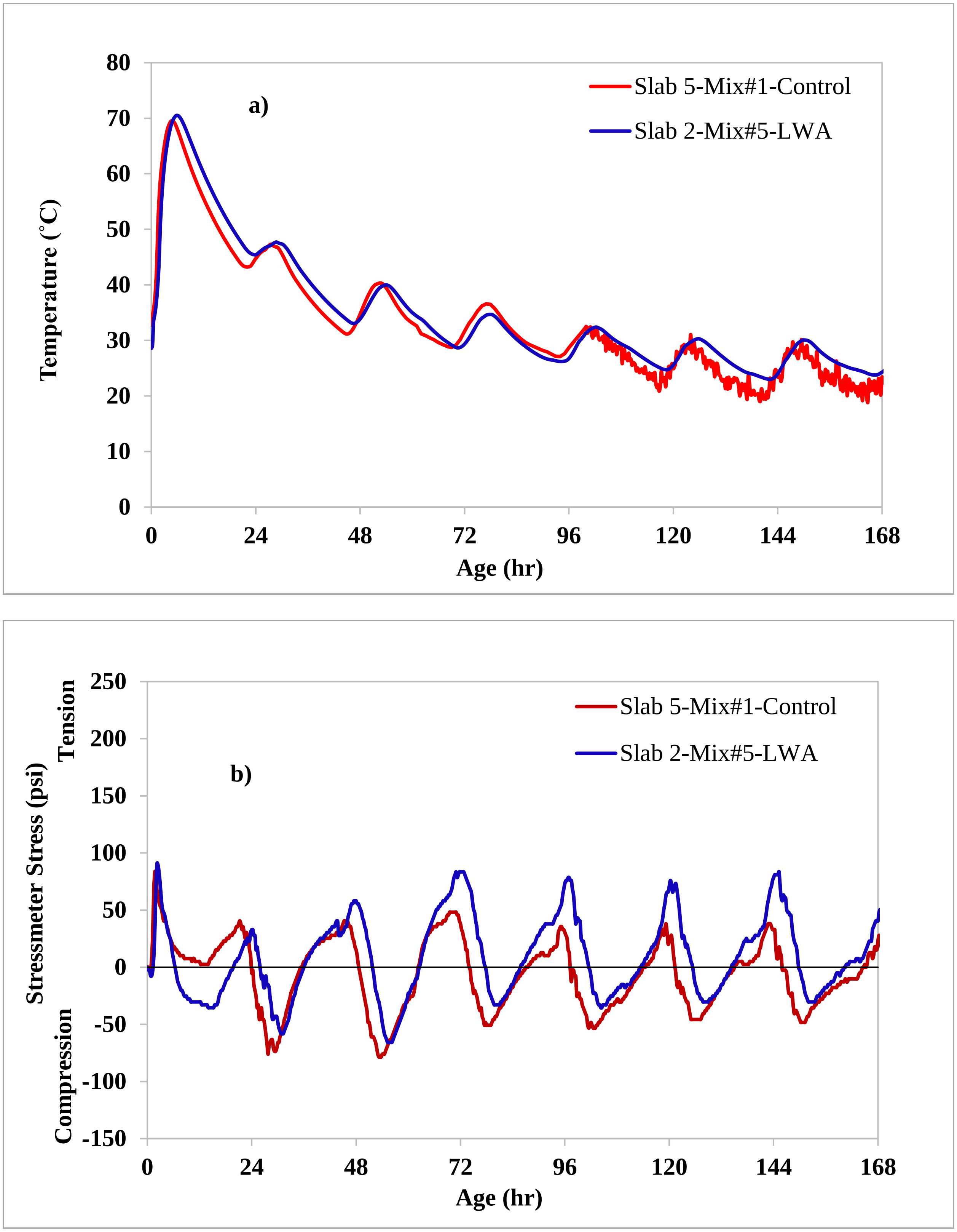

Figure 8-2: (a) Temperature and (b) stress profiles from the stressmeter for slabs 2 and 5

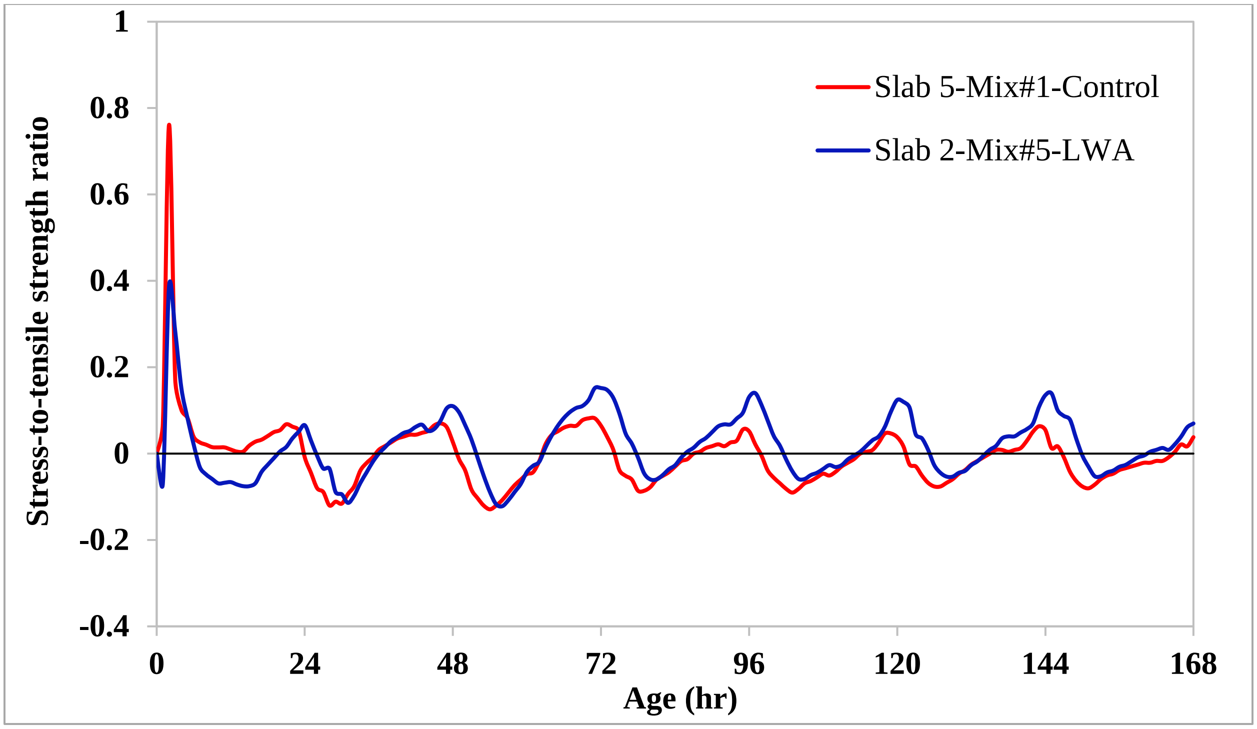

Figure 8-3: Stress-to-tensile strength ratio for slabs 2 and 5

As can be seen in Figure 8-4 and Figure 8-5(a), slabs 3 (fiber) and 5 had similar temperature profiles. After 24 hours, stress development in these slabs was also similar (Figure 8-5(b)). However, significantly lower stresses were recorded during the first 24 hours in slab 3. Addition of fibers decreased initial peak stresses from 78 to 30 psi. Figure 8-6 shows that the decrease in the corresponding the stress-to-tensile-strength ratio was even more drastic. Addition of fibers decreased the stress-to-strength ratio from approximately 0.8 for slab 5 to 0.1 for slab 3. The dramatic decrease in the stress-to-strength ratio occurred during the critical first day when early-age cracking risk is high. The lower stresses likely occurred because the fibers improved strength during the early ages, reduced water absorption by the base material [23], [24], and lowered moisture movement resulting in a uniform moisture profile. Additionally, fibers increased the tensile strength, helping resist the induced tensile stresses, thus effectively lowering the stress-to-tensile-strength ratio.

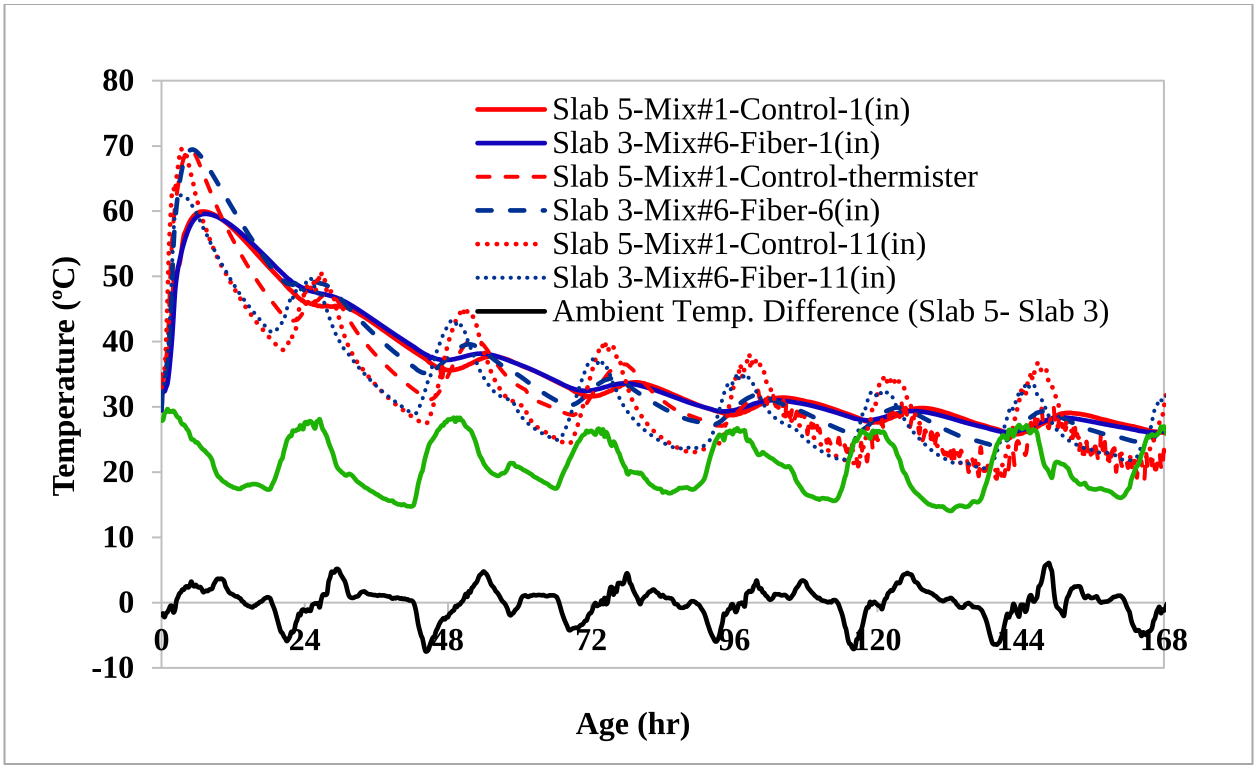

Figure 8-4: Thermocouple readings for slabs 3 and 5

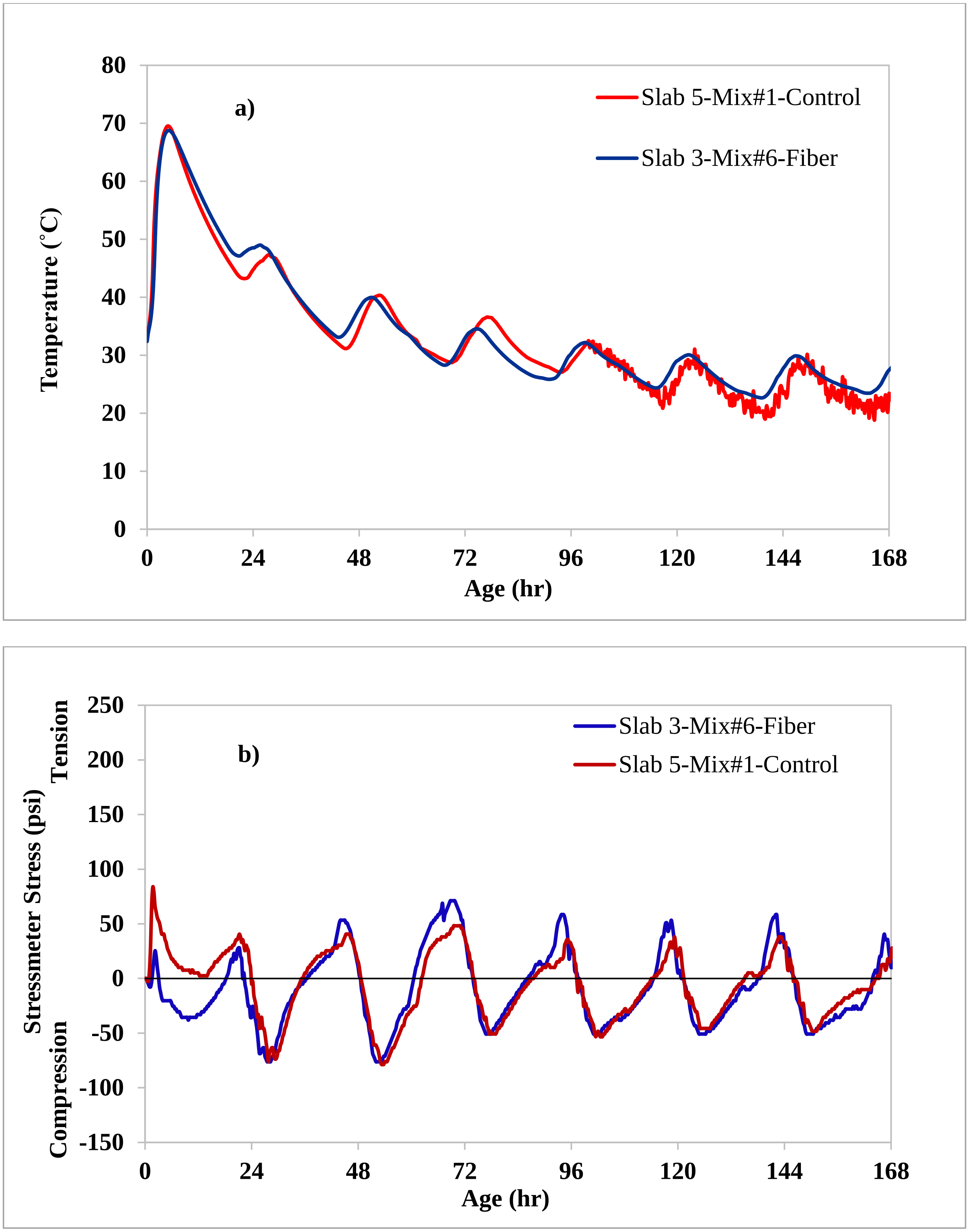

Figure 8-5: (a) Temperature and (b) stress profiles from the stressmeter for slabs 3 and 5

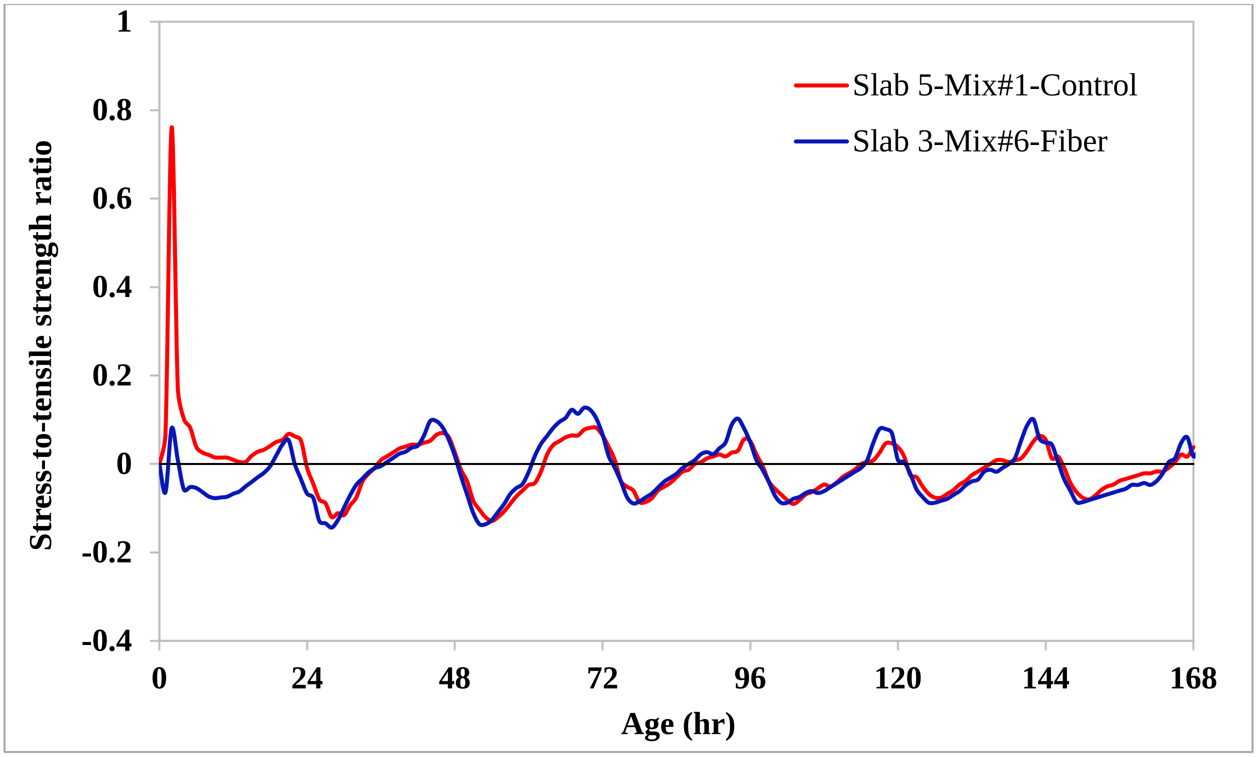

Figure 8-6: Stress-to-tensile strength ratio for slabs 3 and 5

Shrinkage-reducing admixture (SRA) has been reported to have a retarding effect on cement hydration [25], [26]; however, no significant changes in initial temperature development were observed in this study with the addition of a moderate dosage of SRA (Figure 8-7). After 24 hours, the temperature profiles for slabs 4 (SRA) and 5 were also very similar. SRA substantially reduced the tensile stresses of the concrete during the first 12 hours, as shown in Figure 8-8. This corresponded to a significant reduction in the stress-to-tensile-strength ratio (Figure 8-9). Despite the similar temperature trends at all depths up to 168 hours, the tensile stresses in slab 4 were consistently higher after the first 24 hours. Moreover, only tensile stresses were recorded for slab 4 after approximately 55 hours. However, this was not considered to be a problem since the stress-to-tensile-strength ratio seen in slab 4 remained very low.

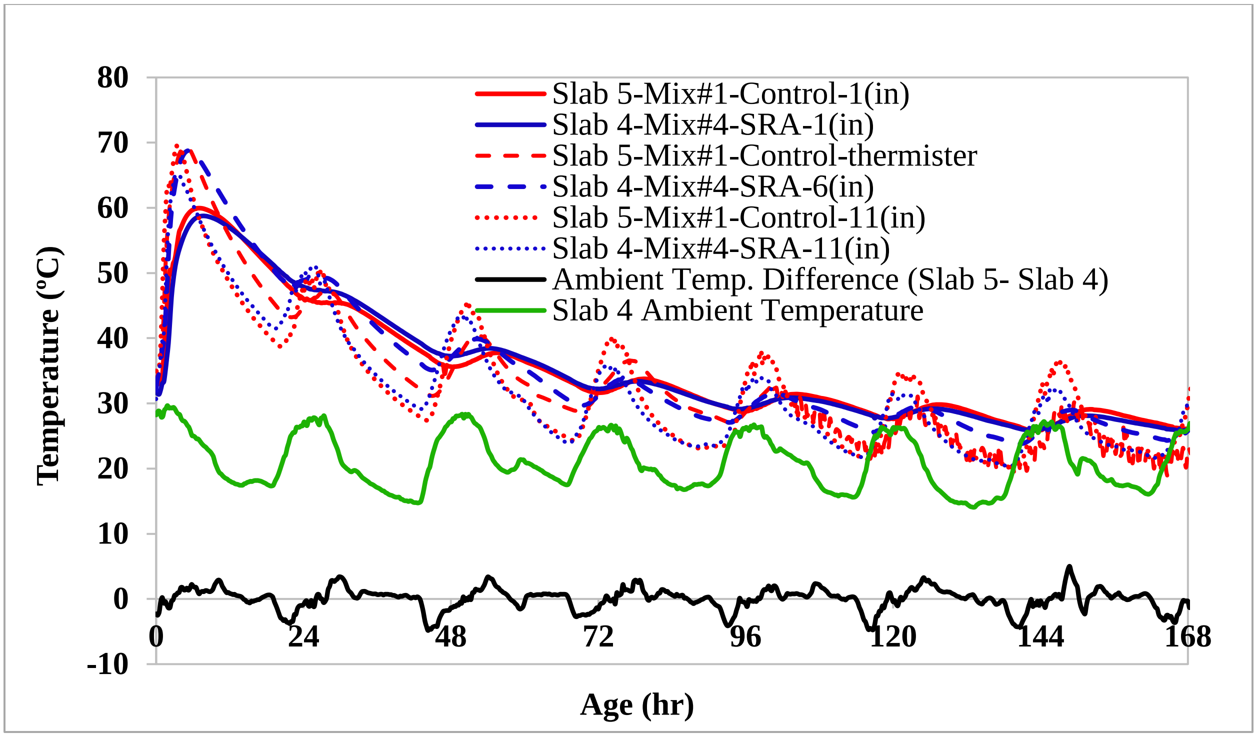

Figure 8-7: Thermocouple readings for slabs 4 and 5

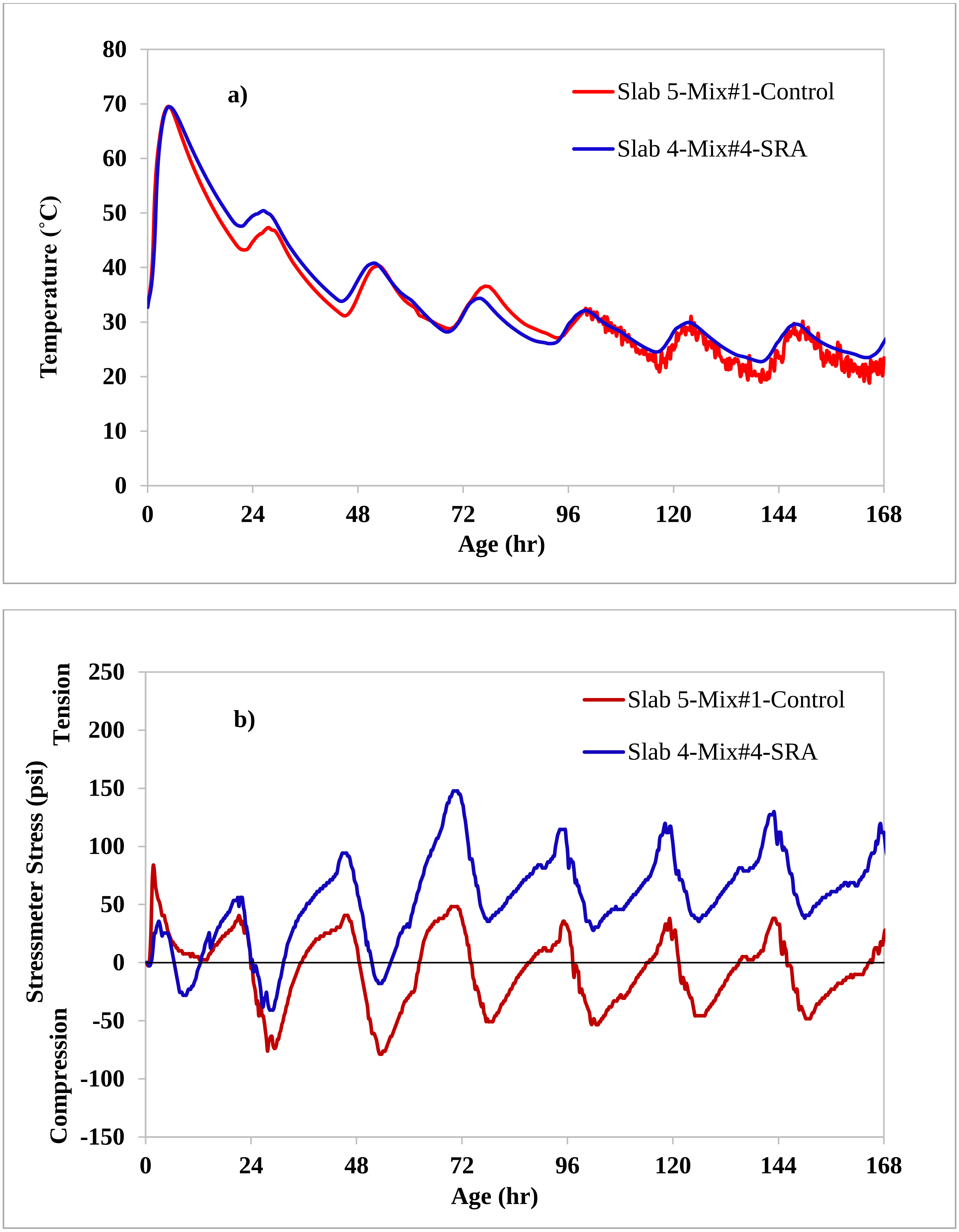

Figure 8-8: (a) Temperature and (b) stress profiles from the stressmeter for slabs 4 and 5

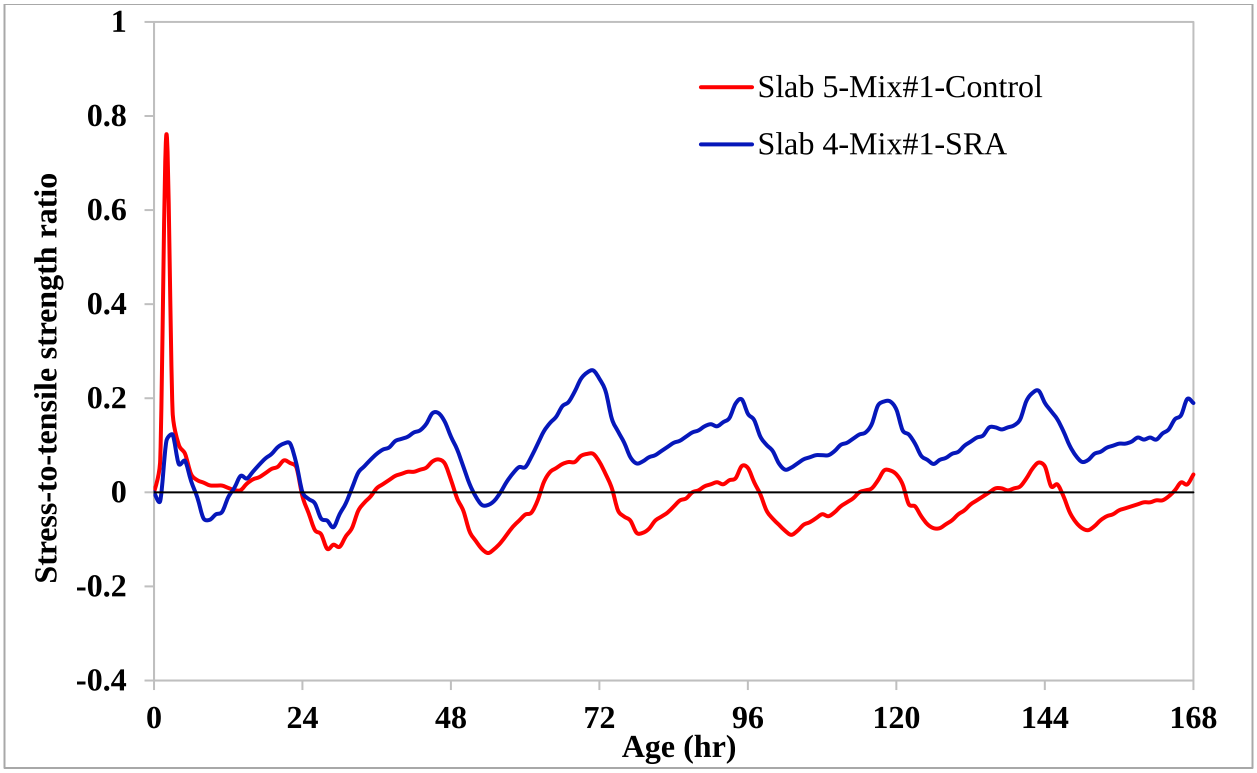

Figure 8-9: Stress-to-tensile strength ratio for slabs 4 and 5

Figure 8-10 shows the effect of paste content reduction on concrete temperature development. Slab 9, which had an optimized aggregate gradation, but the same water-to-cementitious material ratio (w/cm) as the Control, had considerably lower peak temperatures during the first 24 hours when compared to slab 5. Tensile stresses, during this time, were also significantly lower for slab 9, which remained in compression for the majority of the time (Figure 8-11). After the first 24 hours, the temperatures in both slabs were very similar. However, tensile stresses in slab 9 were consistently lower compared to slab 5 during the rest of the 168 hours with the exception of the higher peak at 96 hours. Stress-to-tensile strength ratio of slab 9 was also constantly lower over the whole measurement period, with a large reduction of the peak ratio at 2 hours from approximately 0.8 for slab 5 to 0.05 for slab 9 (Figure 8-12). An optimized mixture probably made the concrete mixture more stable and less likely to lose water to the subbase during the first two hours after placement.

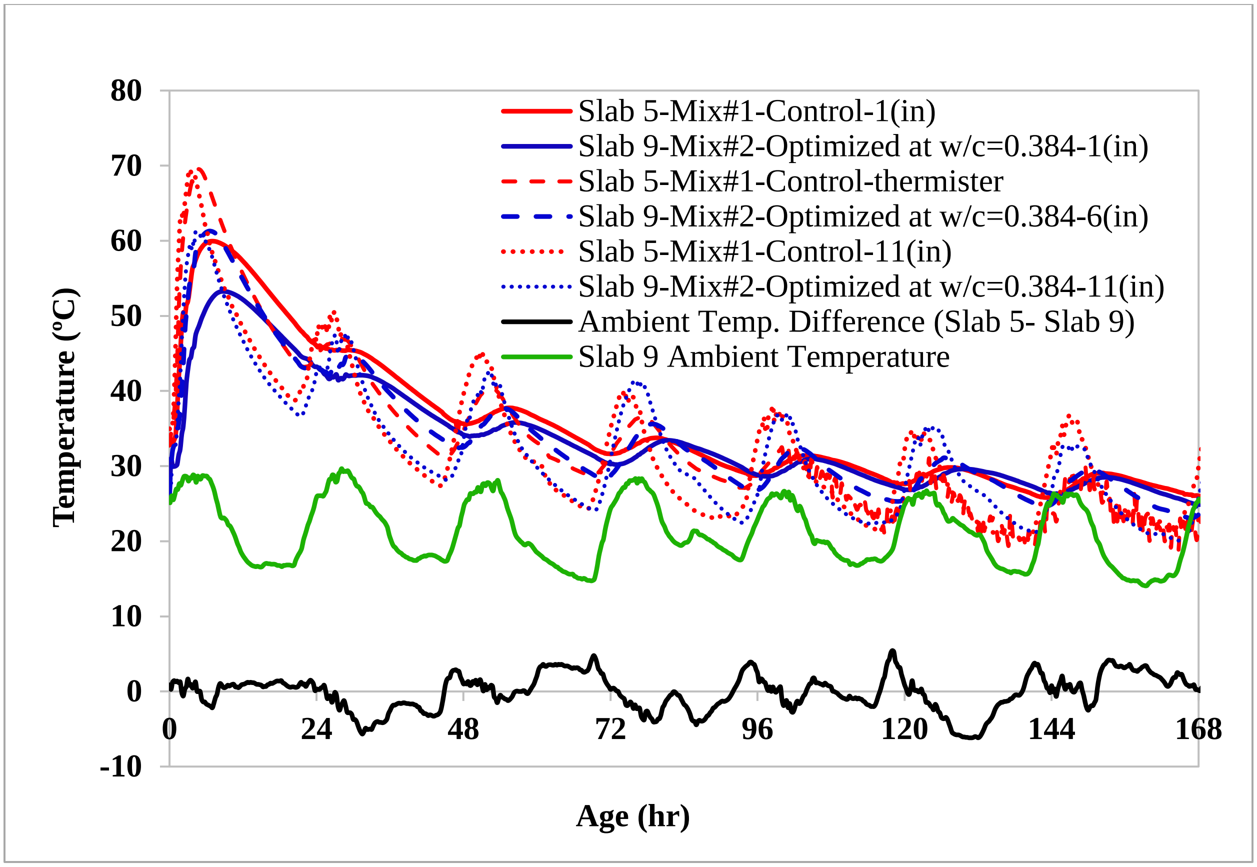

Figure 8-10: Thermocouple readings for slabs 5 and 9

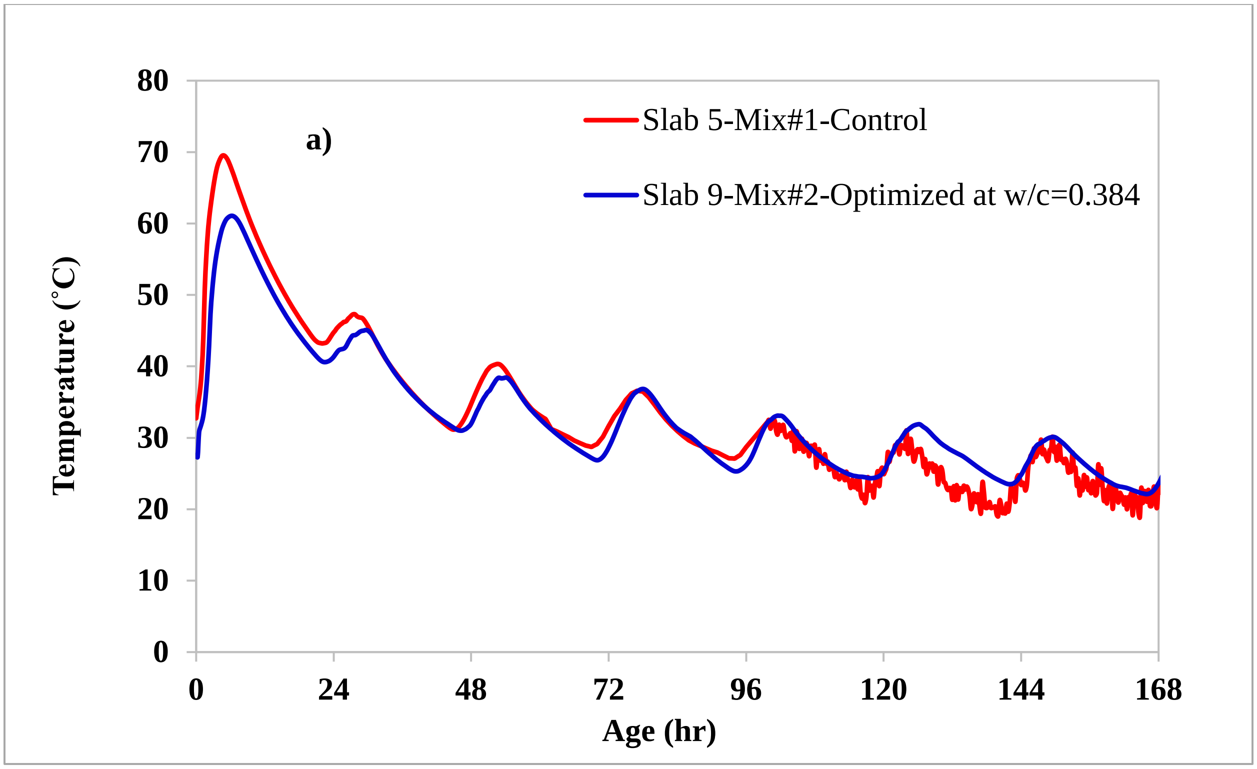

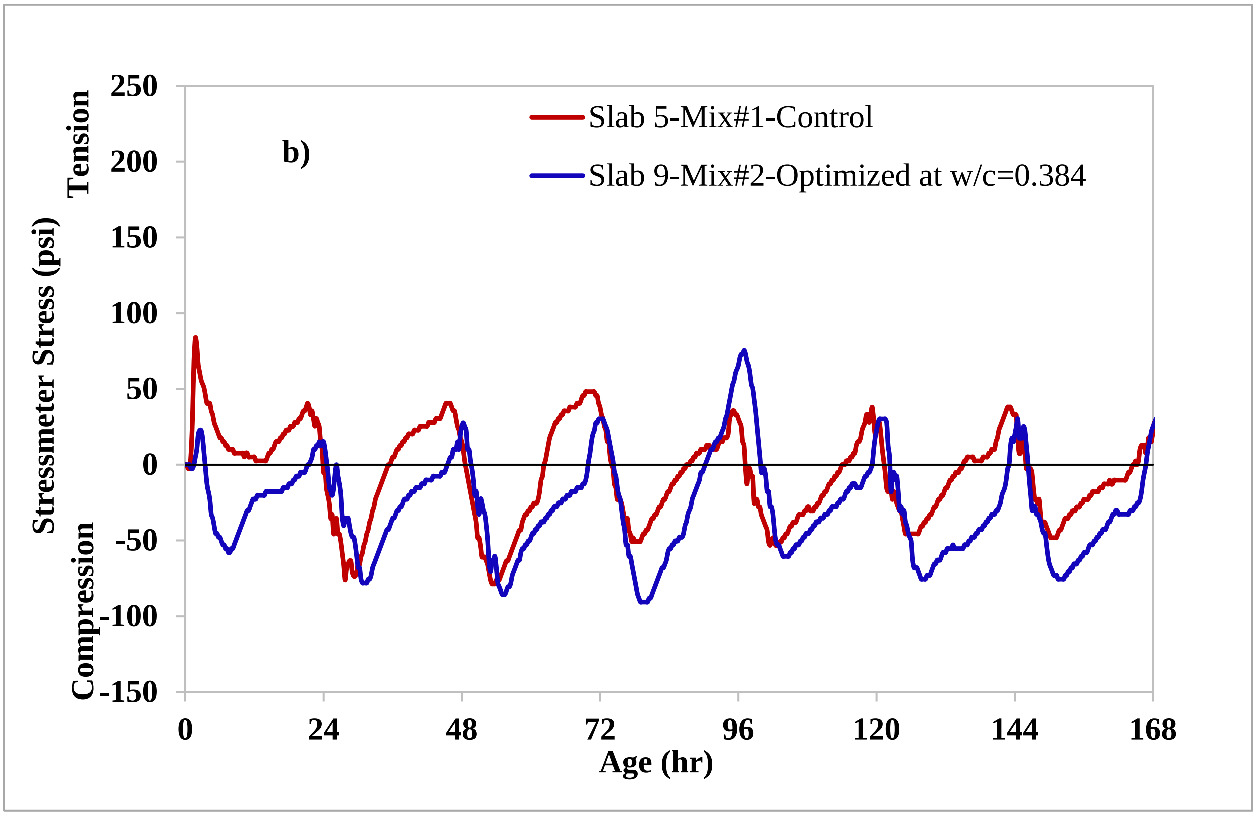

Figure 8-11: (a) Temperature and (b) stress profiles from the stressmeter for slabs 5 and 9

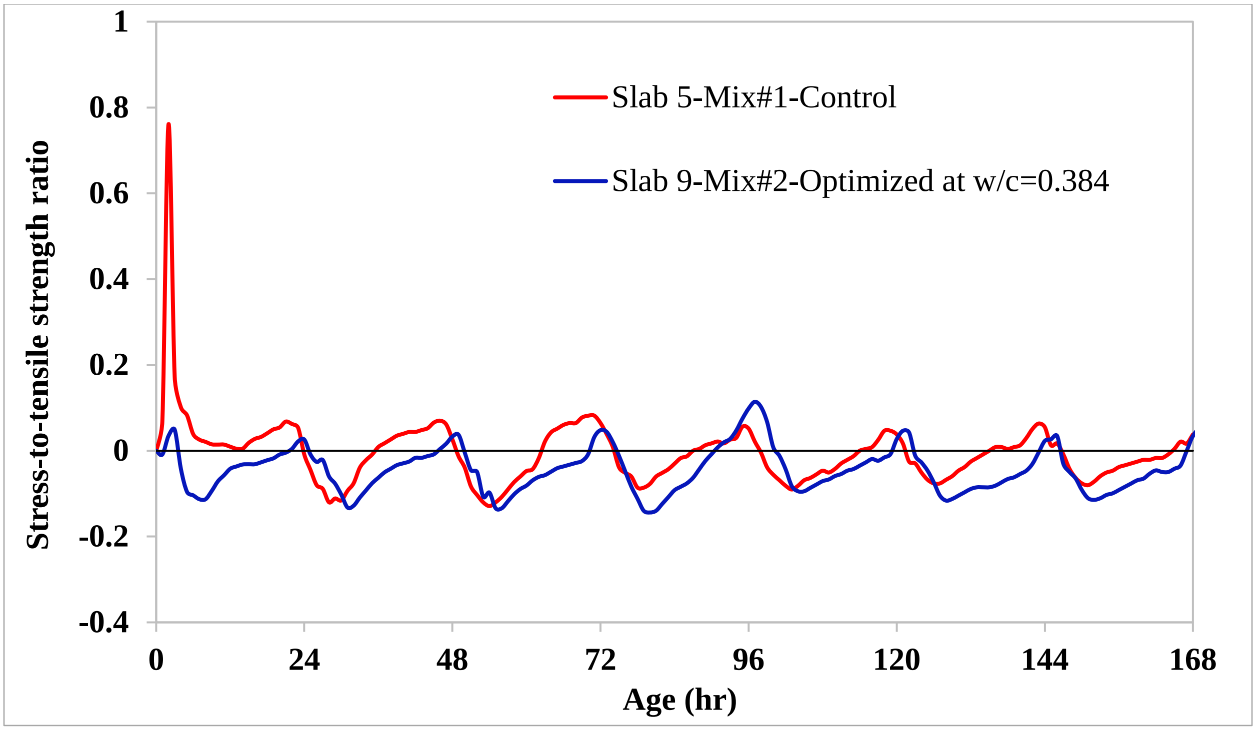

Figure 8-12: Stress-to-tensile strength ratio for slabs 5 and 9

Lowering the w/c of the optimized mix (slab 8) further reduced the peak concrete temperatures during the first 24 hours compared to slab 9 as shown in Figure 8-13. However, this did not translate to a reduction in tensile stresses, which were significantly higher for slab 8 (Figure 8-14). Although the stress-to-tensile strength ratio of slab 8 at approximately 0.4 was about half of that of slab 5, it was notably higher than that of slab 9 (Figure 8-15). After the first 24 hours, the temperature profiles of slabs 8 and 9 were similar, although the tensile stresses and the stress-to-tensile strength ratio remained higher for slab 8. The increases in tensile stresses in slab 8 may be due to an increase in autogenous shrinkage resulting from a lower w/c ratio.

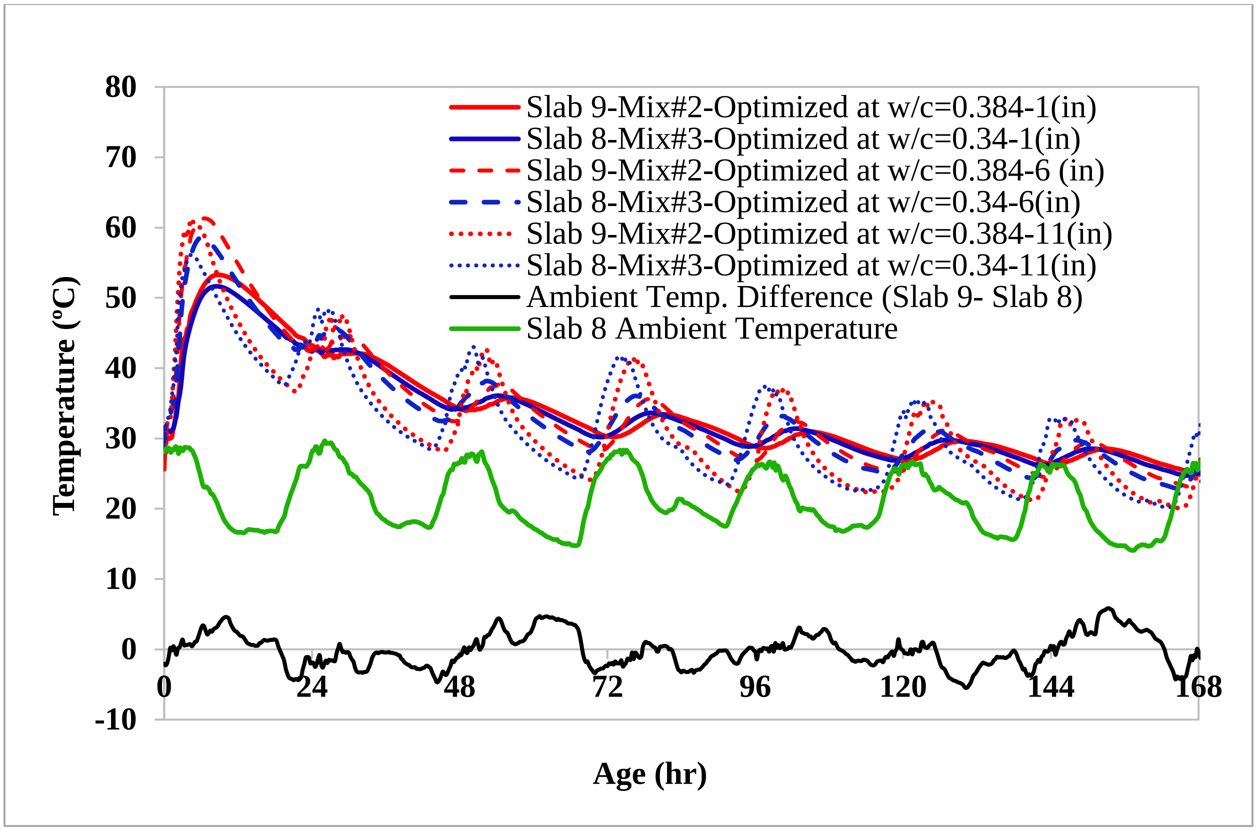

Figure 8-13: Thermocouple readings for slabs 9 and 8

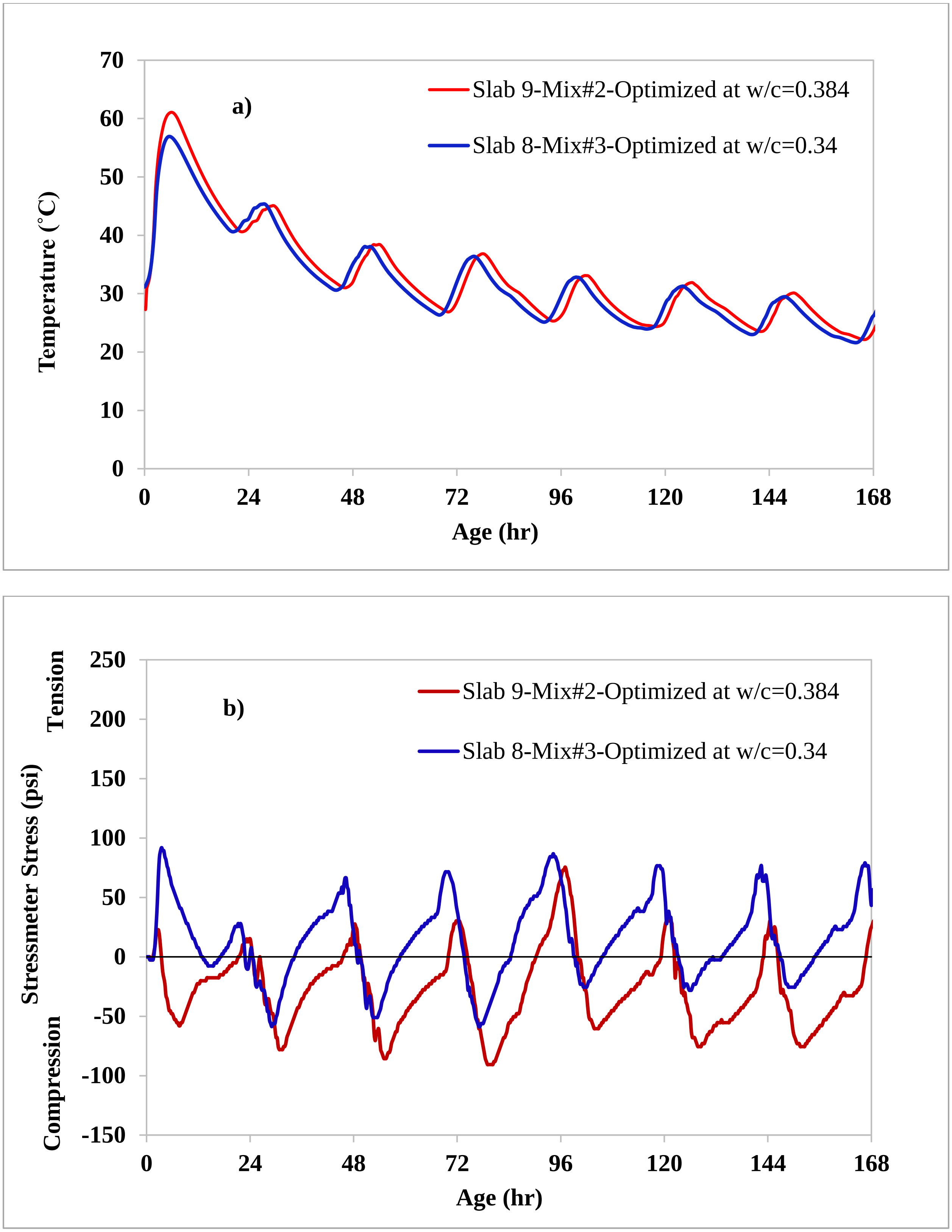

Figure 8-14: (a) Temperature and (b) stress profiles from the stressmeter for slabs 9 and 8

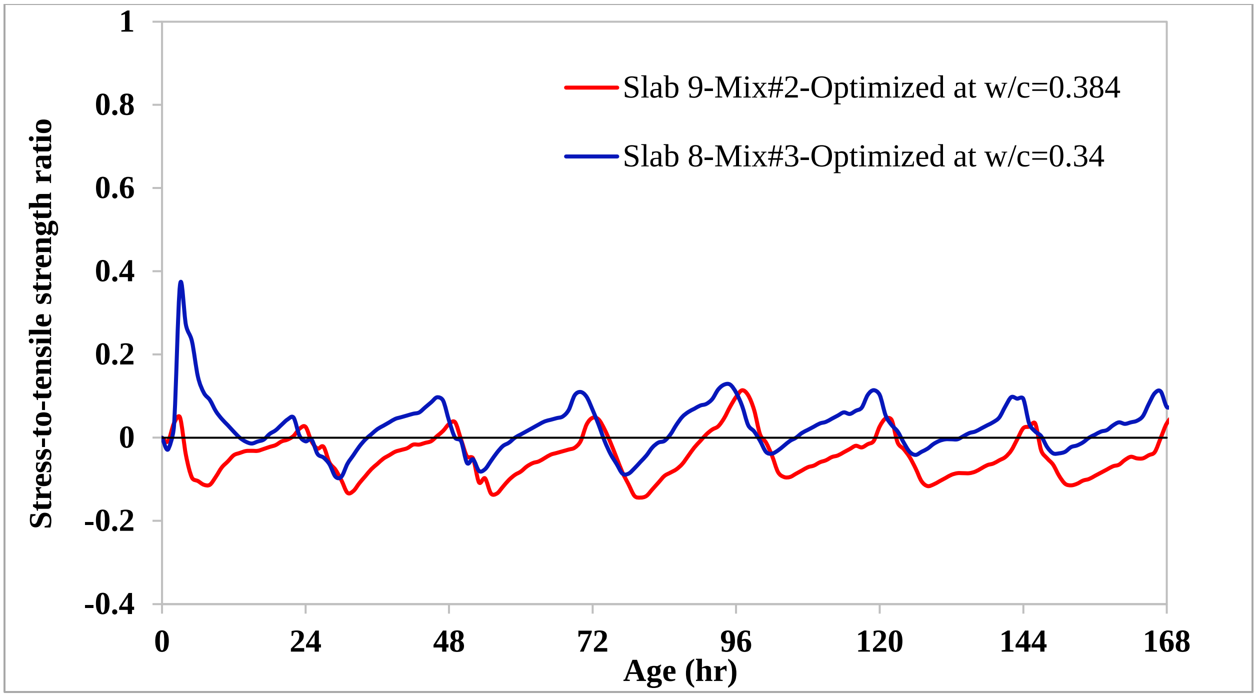

Figure 8-15: Stress-to-tensile strength ratio for slabs 8 and 9

The effect of base condition on stress development was also evaluated. Slabs with and without base-restraint modifications were placed using the optimized mixture with w/c ratio of 0.340 (Mix#3). Plastic sheeting (slab 6) or geotextile (slab 7) was used as a bond breaker. The use of plastic (slab 6) did not have a significant effect on the concrete temperature profiles (Figure 8-16). As can be seen in Figure 8-17, tensile stresses during the first 24 hours were significantly lower for slab 6, likely because the two sheets of plastic prevented the base from absorbing water from the bottom of the slab and causing shrinkage. After 24 hours, the stresses were essentially identical in both slabs. The same trend was observed with respect to stress-to-tensile strength ratio (Figure 8-18). This implies that either the bond-breaking ability of the double layer of plastic was low or that most of the stresses came from curling causing the slab to cantilever over the base and gravity causing stresses on the cantilevered slab.

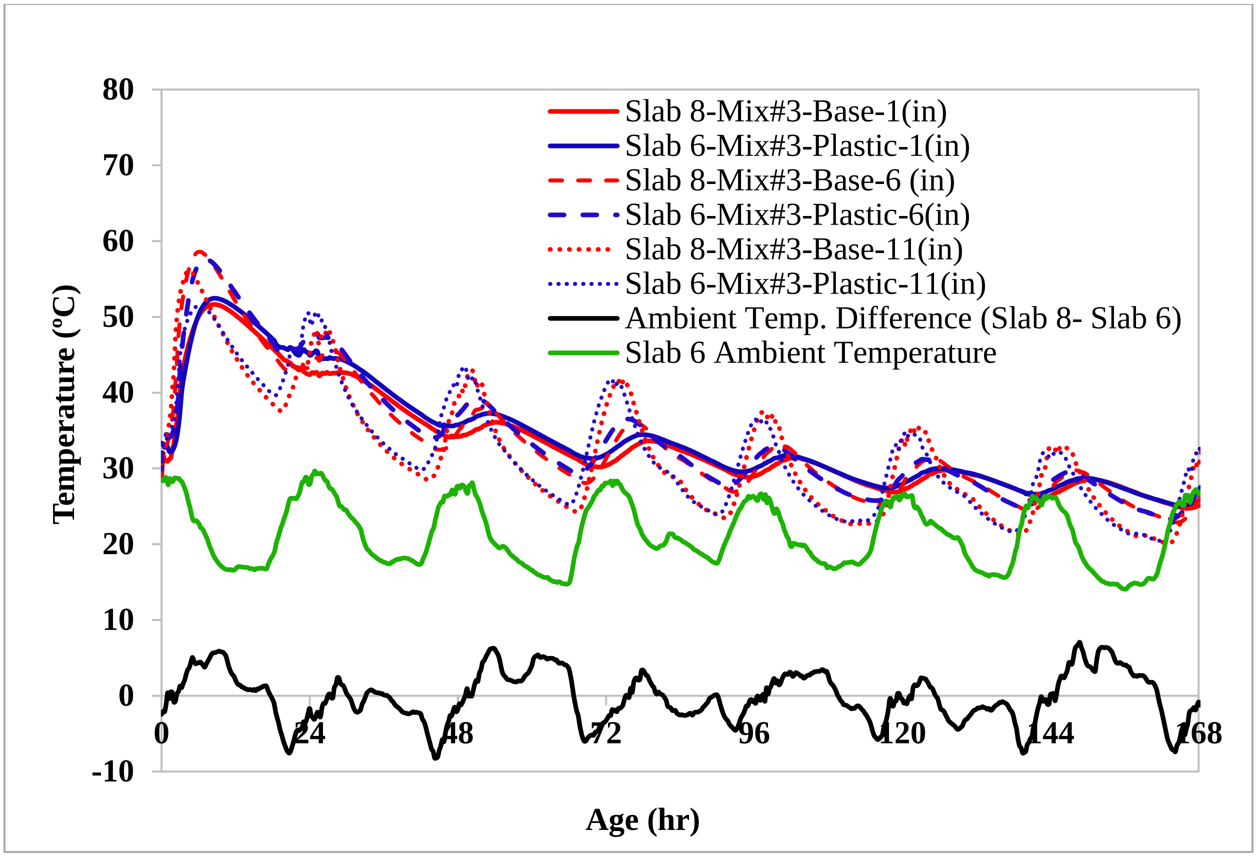

Figure 8-16: Thermocouple readings for slabs 8 and 6

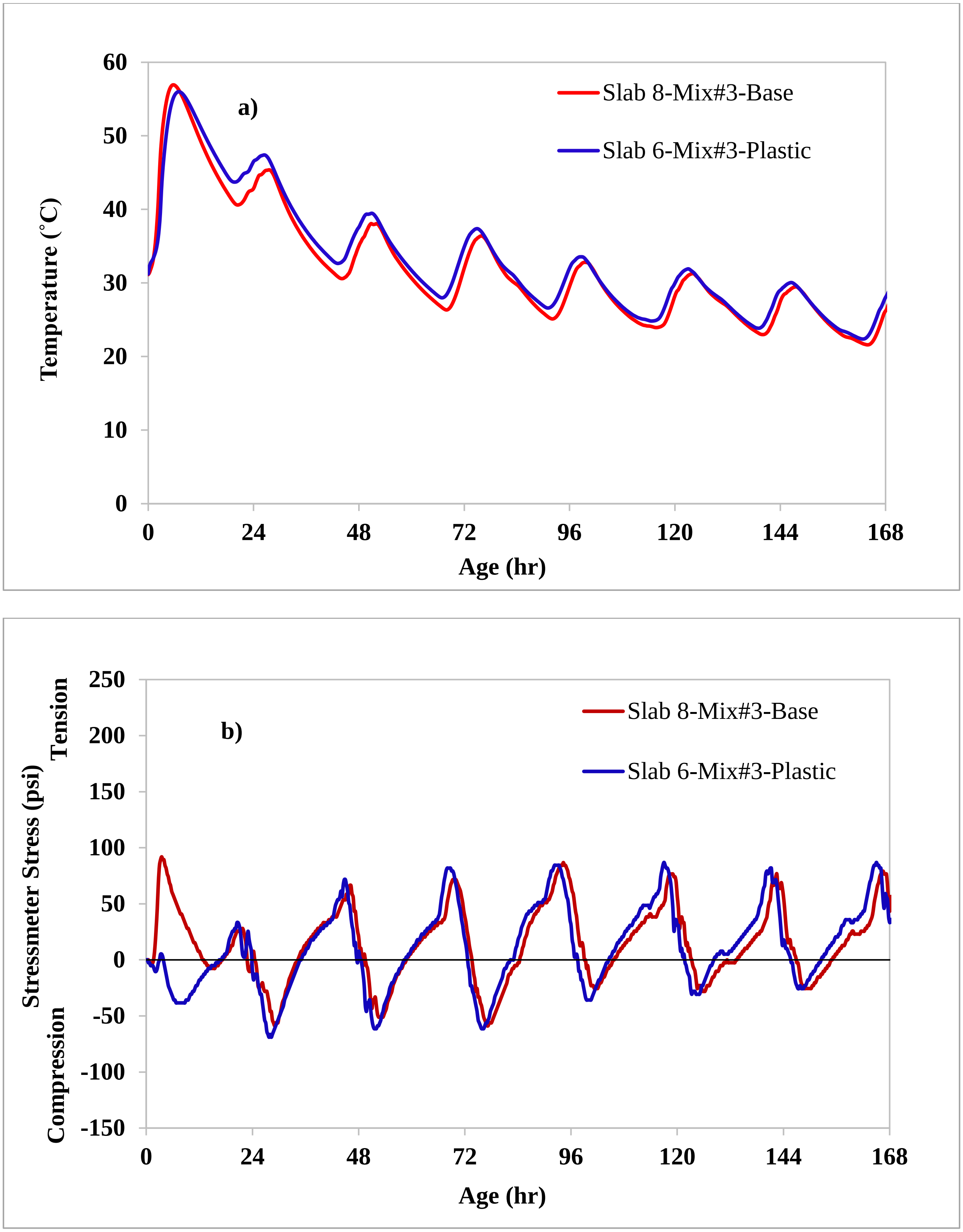

Figure 8-17: (a) Temperature and (b) stress profiles from the stressmeter for slabs 8 and 6

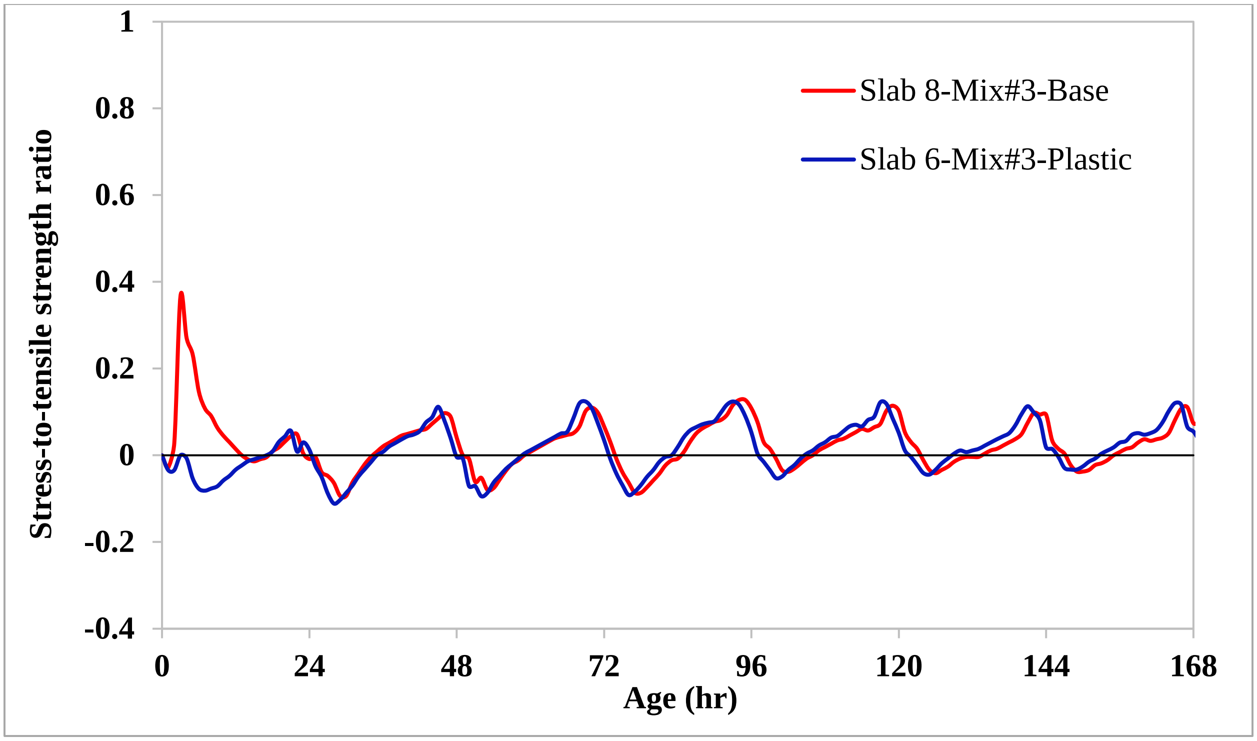

Figure 8-18: Stress-to-tensile strength ratio for slabs 6 and 8

The temperature profiles for slabs 7 and 8 were similar, except the initial peak temperature was higher for slab 7, especially at the bottom of the slab (Figure 8-19). The use of a geotextile fabric under the concrete slab caused a large tensile stress during the first 12 hours, as shown in Figure 8-20. The stress-to-tensile-strength ratio increased by 0.16 during the first 12 hours for the geotextile fabric, as shown in Figure 8-21. After that point, the use of geotextile had a small effect on reducing the tensile stress development compared to the slab without the geotextile fabric. Most likely the increase in tensile stress up to about 5 hours was caused by the geotextile fabric absorbing water from the concrete, resulting in an increase in early-age autogenous shrinkage. Afterwards, tensile stresses in slab 7 decreased below that of slab 8, possibly because the concrete started to wick up the water stored in the geotextile fabric. Prewetting the geotextile fabric could help reduce water loss from the concrete to the fabric and reduce shrinkage.

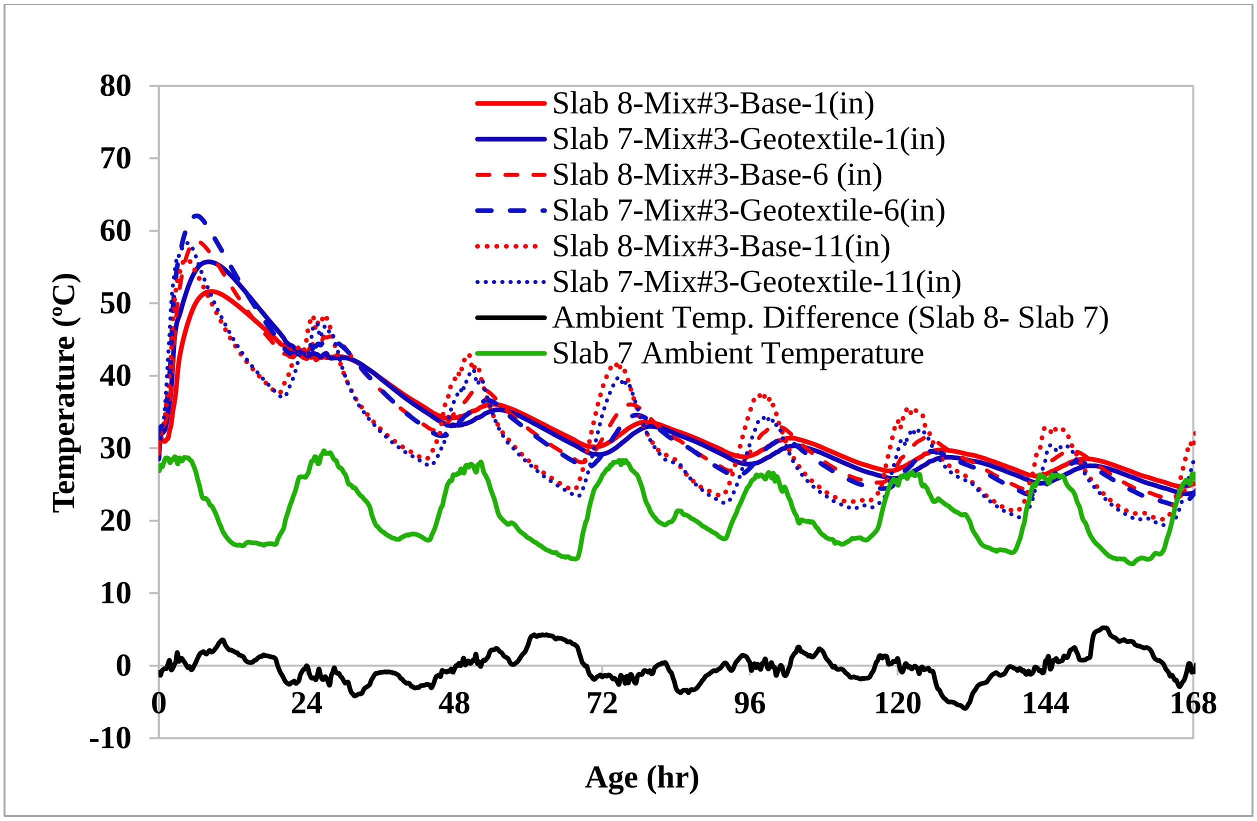

Figure 8-19: Thermocouple readings for slabs 8 and 7

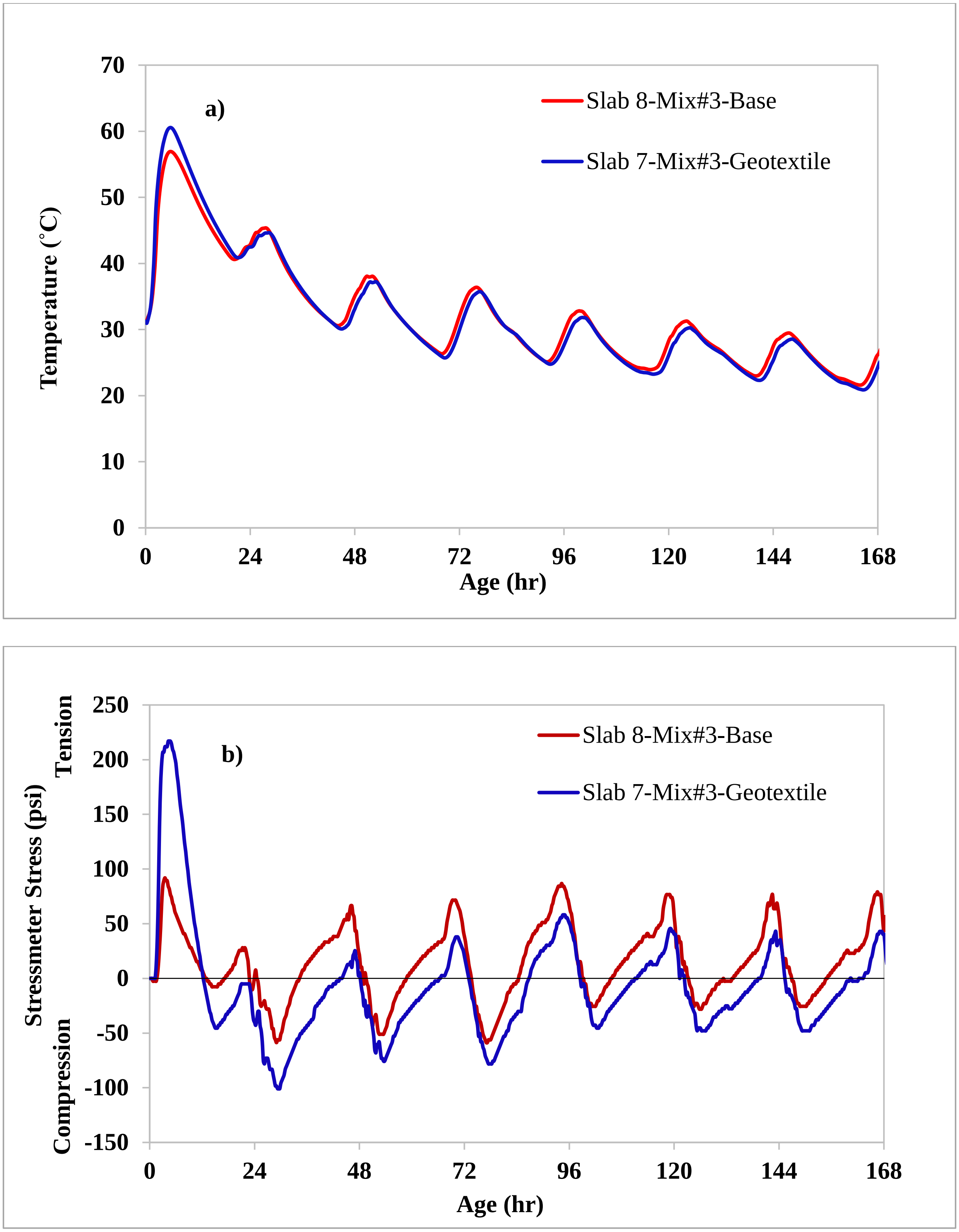

Figure 8-20: (a) Temperature and (b) stress profiles from the stressmeter for slabs 7 and 8

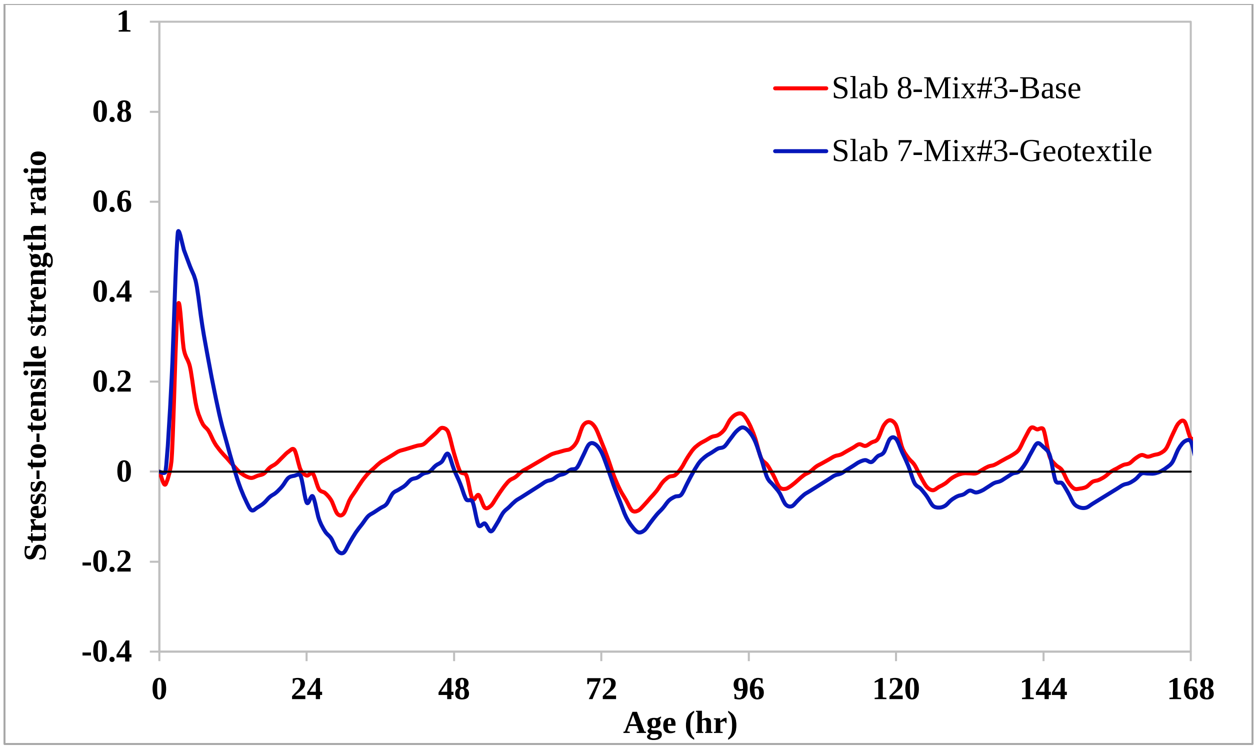

Figure 8-21: Stress-to-tensile strength ratio for slabs 7 and 8

8.4 Conclusion

In this project, several strategies to reduce concrete potential for early-age cracking were evaluated using 12 ft x 15 ft x 1 ft concrete slabs. The findings indicate that among the different strategies examined here, cement paste reduction through aggregate optimization, in concrete typically used in high-early-age-strength pavement slab replacement mixtures, resulted in the lowest stress-to-strength ratio. Cement paste reduction decreased the maximum temperature and lowered the magnitude of the induced tensile stresses in field slabs. Inclusion of shrinkage reducing admixture was effective in reducing tensile stresses during the first 12 hours. Internal curing using LWA reduced the stress-strength ratio during the first 24-44 hours. The results also indicate that the use of plastic sheeting had the primary benefit of reducing moisture loss to the base. The effects of plastic sheeting on reducing the tensile stress after 24 hours, by reducing the base friction, were less than expected.

8.5 References

[1] A. Sedaghat, “Cement Heat of Hydration and Thermal Control,” University of South Florida, 2016.

[2] K. van Breugel, “Prediction of Temperature Development in Hardening Concrete, RILEM Report 15, Prevention of Thermal Cracking in Concrete at Early Ages, Edited by R. Springenschmid, E & FN Spon, London,” 1998.

[3] A. Zayed, K. Riding, C. C. Ferraro, A. Bien-aime, N. Shanahan, D. Buidens, T. Meagher, V. Tran, J. D. Henika, J. M. Paris, C. M. Tibbetts, and B. E. Watts, “Final Report Long-Life Slab Replacement Concrete FDOT Contract Number : BDV25-977-01,” University of South Florida, 2015.

[4] K. A. Riding, “Early Age Concrete Thermal Stress Measurement and Modeling,” University of Texas, Austin, 2007.

[5] S. Zhutovsky and K. Kovler, “Effect of Internal Curing on Durability-Related Properties of High Performance Concrete,” *Cem. Concr. Res.*, vol. 42, no. 1, pp. 20–26, 2012.

[6] S. Zhutovsky, K. Kovler, and A Bentur, “Efficiency of lightweight Aggregates for Internal Curing of High Strength Concrete to Eliminate Autogenous Shrinkage,” *Mater. Struct.*, vol. 35, no. 2, pp. 97–101, 2002.

[7] D. Shen, J. Jiang, J. Shen, P. Yao, and G. Jiang, “Influence of Prewetted Lightweight Aggregates on the Behavior and Cracking Potential of Internally Cured Concrete at an Early Age,” *Constr. Build. Mater.*, vol. 99, no. 1, pp. 260–271, 2015.

[8] D. Cusson and T. Hoogeveen, “Internal Curing of High-Performance Concrete with Pre-soaked Fine Lightweight Aggregate for Prevention of Autogenous Shrinkage Cracking,” *Cem. Concr. Res.*, vol. 38, no. 6, pp. 757–765, 2008.

[9] A. Bentur, S. Igarashi, and K. Kovler, “Prevention of Autogenous Shrinkage in High-Strength Concrete by Internal Curing Using Wet Lightweight Aggregates,” *Cem. Concr. Res.*, vol. 31, no. 11, pp. 1587–1591, 2001.

[10] R. Henkensiefken, D. Bentz, T. Nantung, and J. Weiss, “Volume Change and Cracking in Internally Cured Mixtures Made with Saturated Lightweight Aggregate Under Sealed and

Unsealed Conditions," *Cem. Concr. Compos.*, vol. 31, no. 7, pp. 427–437, 2009.

[11] J. Mora-Ruacho, R. Gettu, and A. Aguado, "Influence of Shrinkage-Reducing Admixtures on the Reduction of Plastic Shrinkage Cracking in Concrete," *Cem. Concr. Res.*, vol. 39, no. 3, pp. 141–146, 2009.

[12] F. Rajabipour, G. Sant, and J. Weiss, "Interactions between Shrinkage Reducing Admixtures (SRA) and Cement Paste's Pore Solution," *Cem. Concr. Res.*, vol. 38, no. 5, pp. 606–615, May 2008.

[13] D. P. Bentz, M. R. Geiker, and K. K. Hansen, "Shrinkage-Reducing Admixtures and Early-age Desiccation in Cement Pastes and Mortars," *Cem. Concr. Res.*, vol. 31, no. 7, pp. 1075–1085, 2001.

[14] ASTM C39/39M-15a, "Standard Test Method for Compressive Strength of Cylindrical Concrete Specimens," West Conshohocken, PA: ASTM International, 2015.

[15] ASTM C496/C496M-11, "Standard Test Method for Splitting Tensile Strength of Cylindrical Concrete Specimens," West Conshohocken, PA: ASTM International, 2011.

[16] ASTM C469/C469M-14, "Standard Test Method for Static Modulus of Elasticity and Poisson's Ratio of Concrete in Compression," West Conshohocken, PA, 2014.

[17] A. J. Bien-Aime, "Effect of Cement Chemistry and Properties on Activation Energy," University of South Florida, 2013.

[18] C. A. Ishee, "Evaluating the Performance of Portland Cement under Differing Hydration Conditions," Ph.D. Dissertation, McGill University, 2011.

[19] C. Ferraro, "Determination of Test Methods for the Prediction of the Behavior of Mass Concrete," Ph.D. Dissertation, University of Florida, 2009.

[20] J. L. Poole, "Modeling Temperature Sensitivity and Heat Evolution of Concrete," Ph.D. Dissertation, The University of Texas at Austin, 2007.

[21] Florida Department of Transportation, "Standard specifications for road and bridge construction," Tallahassee, FL, 2016.

[22] ACI Committee 231, "ACI 231R-10: Early-Age Cracking: Causes, Measurement, and Mitigation," American Concrete Institute, Farmington Hills, MI, 2010.

[23] C. Qi, J. Weiss, and J. Olek, “Characterization of Plastic Shrinkage Cracking in Fiber Reinforced Concrete Using Image Analysis and a Modified Weibull Function,” *Mater. Struct.*, vol. 36, no. 6, pp. 386–395, 2003.

[24] A. Sivakumar and M. Santhanam, “A Quantitative Study on the Plastic Shrinkage Cracking in High Strength Hybrid Fibre Reinforced Concrete,” *Cem. Concr. Compos.*, vol. 29, no. 7, pp. 575–581, 2007.

[25] J. Plank, E. Sakai, C. W. Miao, C. Yu, and J. X. Hong, “Chemical Admixtures — Chemistry, Applications and their Impact on Concrete Microstructure and Durability,” *Cem. Concr. Res.*, vol. 78, pp. 81–99, Dec. 2015.

[26] R. Rixom and N. Mailvaganam, *Chemical Admixtures for Concrete*, 3rd ed. New York, NY: Routledge, 1999.

Chapter 9 Laboratory Assessment of Mixture Proportions and Cracking Potential

9.1 Introduction

In this chapter, the laboratory study conducted on the development of the mechanical properties (compressive strength, splitting tensile, and Young's modulus) for different concrete mixtures and their effectiveness in mitigating cracking tendencies are presented. Achieving high early strength is a crucial objective in design of concrete pavements since time of opening-to-traffic is a controlling factor. According to the Standard Specification for Road and Bridge Construction published by the FDOT in July 2016, cylinders associated with concrete slabs must reach a minimum compressive strength of 1600 psi before the pavement slab can be exposed to traffic and 3,000 psi at 28 days [1].

As a part of this chapter, six mixture designs, as outlined in Table 9-1, were used for the evaluation of cracking tendency using a rigid cracking frame (RCF). For each RCF experiment (corresponding to each mix design), the temperature profile, obtained from the thermistor contained in the stressmeter used for the slab field testing of each mix, was imposed on the concrete in the cracking frame during testing for the first 96 hours, followed by cooling at 1°C/h. Compressive strength, splitting tensile strength, and Young's modulus for each of the mixtures were determined by conducting experiments on the 4"x8" concrete cylinders prepared in the field for each slab. Further information is available in the experimental section.

9.2 Experimental

A rigid cracking frame, as shown in Figure 9-1, was used to evaluate the uniaxial stress development of the concrete specimens under restrained conditions. The test was originally developed in Munich, Germany [2]. Concrete experiences thermal and autogenous shrinkage due to the hydration process and undergoes temperature- and moisture-related volume changes. The cracking frame restrains the concrete against volume change and records uniaxial stresses induced by these volume changes. It is noteworthy that development of the concrete modulus of elasticity, creep, and stress relaxation affect the stress in the concrete [3]. Further information about cracking frame testing can be found in [4], [5]. Concrete for the RCF testing was prepared conforming to ASTM C192 [6]. The mix proportions for the mixtures used in this part of the study are outlined in Table 9-1. Each concrete mixture was subjected to the temperature profile, collected from its respective field slab by the thermistor in the stressmeter, for the first 96 hours after mixing. After 96 hours, cooling was induced at the rate of 1ºC/h until the age of 120 hours or when the temperature reached 3°C. Since three slabs were placed in the field with Mix #3 (one on top of the road base, one on top of plastic sheeting, and one of top of geotextile), only the temperature profile of the slab placed on road base was used in the cracking frame.

Table 9-5: Mixture design per 1 m^3 (1 yd^3)

Mix Constituents	**Mix #1 (Control)**	**Mix #2**	**Mix #3**	**Mix #4**	**Mix #5**	**Mix #6**
Cement, kg (lb)	534 (900)	415 (700)	415 (700)	534 (900)	534 (900)	534 (900)
CA #57 limestone (SSD), kg (lb)	997 (1680)	682 (1150)	700 (1180)	997 (1680)	997 (1680)	997 (1680)
IA #89 limestone (SSD), kg (lb)	0.0	409 (690)	421 (710)	0.0	0.0	0.0
FA silica sand (SSD), kg (lb)	492 (829)	610 (1028)	625 (1054)	501 (844)	326 (549)	491 (827)
LWA (SSD), kg (lb)	0.0	0.0	0.0	0.0	97 (163)	0.0
Water, kg (lb)	193 (325)	150 (252)	131 (221)	189 (319)	193 (325)	193 (325)
Type F Superplasticizer, ml (fl. oz)	0.0	948 (24.5)	1354 (35.0)	0.0	0.0	0.0
Type E Accelerator, ml (fl. oz)	14853 (384)	11554 (298.7)	11554 (298.7)	14853 (384)	14853 (384)	14853 (384)
Air Entrainer, ml (fl. oz)	38 (1.0)	38 (1.0)	38 (1.0)	38 (1.0)	38 (1.0)	38 (1.0)
Type D Water-reducing Admixture, ml (fl. oz)	874 (22.6)	696 (18.0)	696 (18.0)	874 (22.6)	874 (22.6)	874 (22.6)
Shrinkage Reducing Admixture, ml (gal)	0.0	0.0	0.0	3713 (0.75)	0.0	0.0
Fiber, kg (lb)	0.0	0.0	0.0	0.0	0.0	0.297 (0.5)
w/c	0.384	0.384	0.340	0.384	0.384	0.384

Figure 9-1: Cracking frame

To determine the mechanical properties of each mix associated with each slab, 26 cylinders (4”x8”) were prepared from the concrete delivered to the site for each field slab. Concrete cylinders were tested at the ages of 0.25, 1, 3, 7, and 28 days. One cylinder was instrumented with a thermocouple and used for determination of temperature history, and calculation of equivalent age and maturity. The cylinders were cured on top of the slabs for 48 hours. For the first 24 hours, the cylinders were covered with two layers of blankets. After 48 hours, the cylinders were transferred from the site to the laboratory at the University of South Florida, and immersed in saturated lime water solution at an ambient temperature of 23 ± 1ºC until the time of testing. The cylinders tested at 6 and 24 hours were cured under the blankets only. A Universal Testing Machine (UTM) manufactured by MTS was used to determine the compressive strength (conforming to ASTM C39 [7]), splitting tensile strength (conforming to ASTM C496 [8]), and static elastic modulus (conforming ASTM C469 [9]).

9.3 Results and Discussion

9.3.1 Mechanical Properties Testing of Field Cylinders

The compressive strength results are shown in Figure 9-2. Figure 9-3 shows the splitting tensile strength results, while Figure 9-4 shows the Young's modulus results. The compressive strengths for all the mixes exceeded 1600 psi at 6 hours and 3,000 psi at 28 days, indicating conformance with Florida specification guidelines [1].

The optimized Mix #3 showed equal or better Young's modulus, compressive strength, and tensile strength compared to Mix #1 (control). Optimization of the mix was accomplished by reducing the w/c to 0.34, partial replacement of coarse aggregate with intermediate aggregate to reduce the paste-to-void volume ratio from 2.15 to 1.74, and increasing the packing density in the concrete. The use of intermediate aggregates to reduce gradation gaps allowed for a reduction in the paste content, while maintaining workability and reducing voids [10].

Mix #4 with 0.75 gal/yd^3 of shrinkage reducing admixture (SRA) showed similar elastic modulus, tensile, and compressive strength compared to Mix #1, with only a slight reduction in compressive strength of approximately 11% at 6 hours. Shah et al. [11] reported a reduction in compressive strength with increase in the amount of SRA at all ages, while this effect was minor at later ages. Folliard and Berke [12] found that the inclusion of 1.5% SRA reduced compressive strength at all ages, and elastic modulus at 28 days for concrete samples containing both ordinary portland cement (OPC) and OPC with silica fume.

As expected, the use of lightweight aggregates (LWA) in Mix 5 showed a small decrease in Young's modulus compared to the control. The LWA mixture also had a lower splitting tensile strength during the first three days. The LWA mixture also had a slightly lower compressive strength at 6 hours compared to the control, but similar values at later ages. A reduction in compressive strength was reported by other researchers who used varying additions of LWA and moisture states of aggregates [13]. Even using the same material with different specific gravities and sizes showed lowered strength values at early ages [14]. However, during the later ages, it is common for LWA concrete to have strength equivalent to that of typical concrete [15].

Integrating fibers resulted in similar tensile strength for Mix 6 compared to the control mix at all ages. Research conducted by Bissonnette and Pigeon [16] showed that using macro-sized fibers increased the tensile strength of the concrete compared to the control at 7 and 28 days.

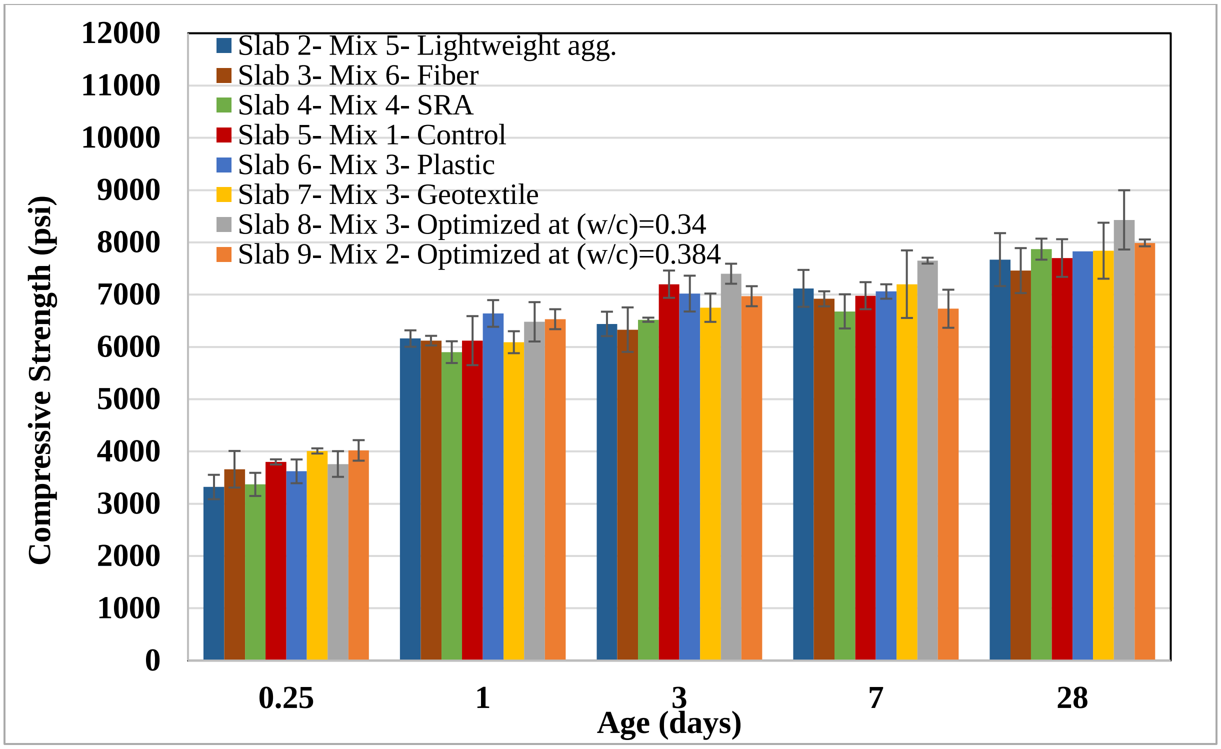

Figure 9-2: Compressive strength development for each mix

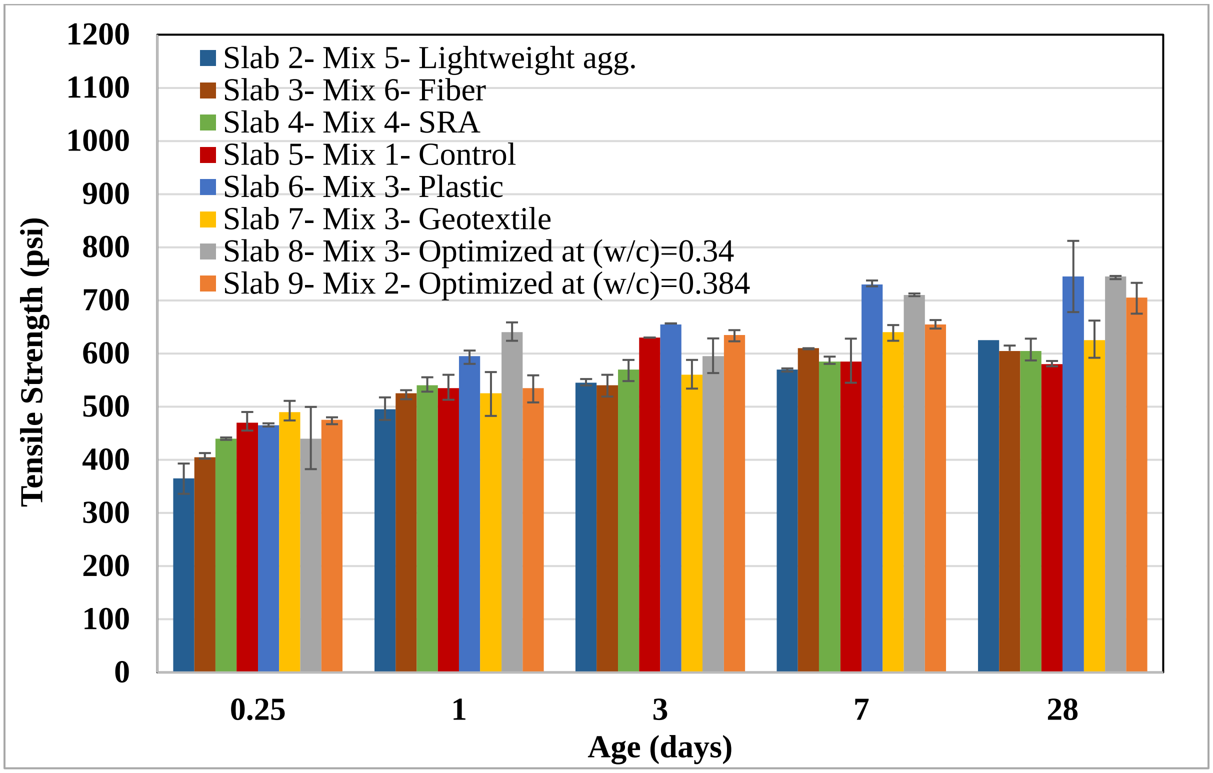

Figure 9-3: Splitting Tensile strength development for each mix

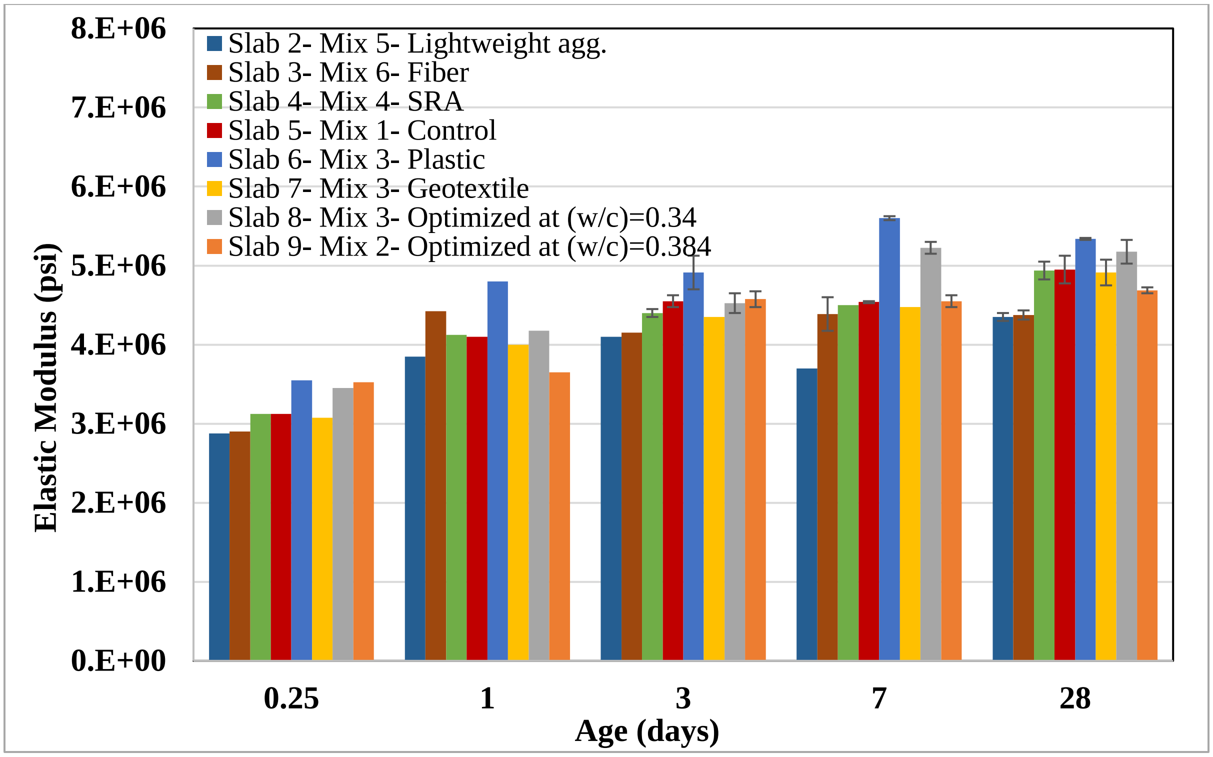

Figure 9-4: Elastic modulus development for each mix

Soroushian and Ravanbakhsh [17] attributed an increase in early-age strength to the confining effect of fibers.

9.3.2 Cracking Frame

LWA was incorporated into the mix as a means for internal curing. The internal curing concept, using prewetted, lightweight, fine aggregates in high-strength concrete, was proposed by Robert Philleo in 1991 [18]. Implementation of internal curing is considered a suitable method to ensure the continuous hydration of the cementitious system in concrete to avoid self-desiccation and reduction of self-induced internal capillary stress in the concrete. As can be seen in Figure 9-5, incorporation of LWA (Mix#5) did not seem to noticeably affect the temperature of the concrete compared to the control mix. However, Mix 5 outperformed the control mix in RCF experimental work. In the first 80 hours, the LWA mix showed continuously lower tensile stress compared to the control mix. During this period, Mix 5 experienced a maximum tensile stress of 163 psi, while the control mix experienced a 205-psi maximum tensile stress. In general, incorporation of lightweight aggregates reduced the tensile stress development at all ages until cooling was induced. These results conform to the research conducted by Byard and Schindler [19] on lightweight sand, where tensile stress decreased with increasing the levels of internal curing water. The reduction of tensile stress in the LWA mix can be attributed to the higher humidity levels provided by the lightweight aggregates, thus reducing autogenous shrinkage. Cusson and Hoogeveen [20] showed mitigation of autogenous shrinkage through the use of varying amounts of prewetted lightweight aggregates.

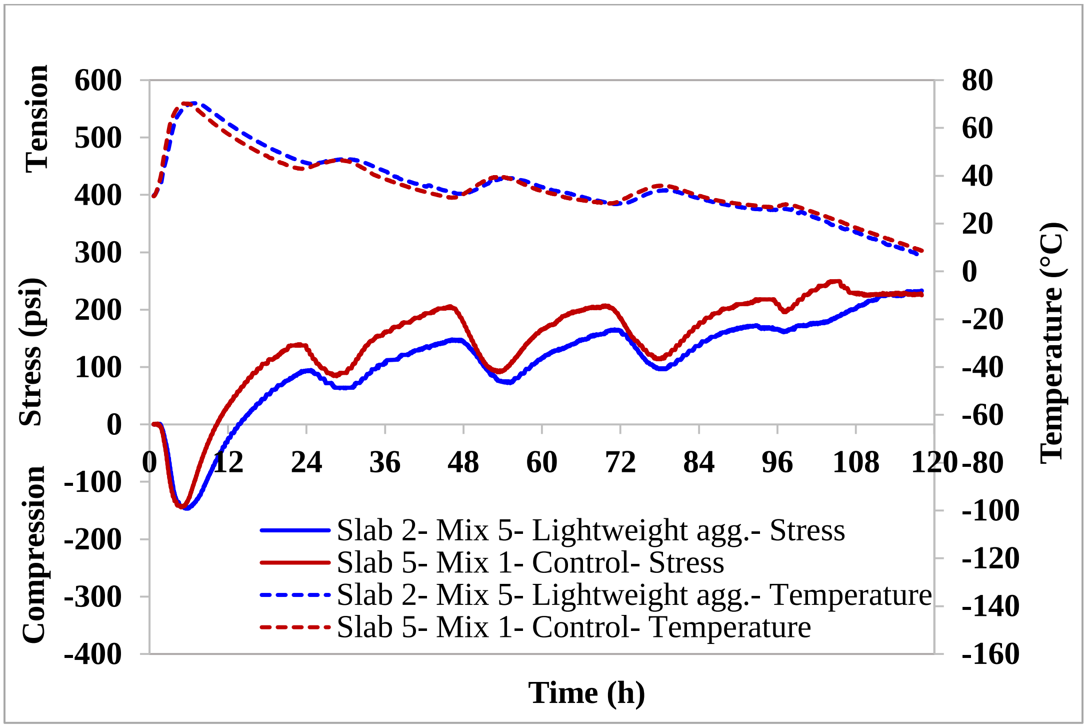

Figure 9-5: Cracking frame results for slabs 2 and 5

As shown in Figure 9-6, the inclusion of polypropylene fibers had almost no effect on the stress development. In general, polypropylene fibers are mostly used to control plastic shrinkage cracking [21], [22]. As external drying was prevented in RCF, fibers did not seem to have an effect on the stress development compared to the control.

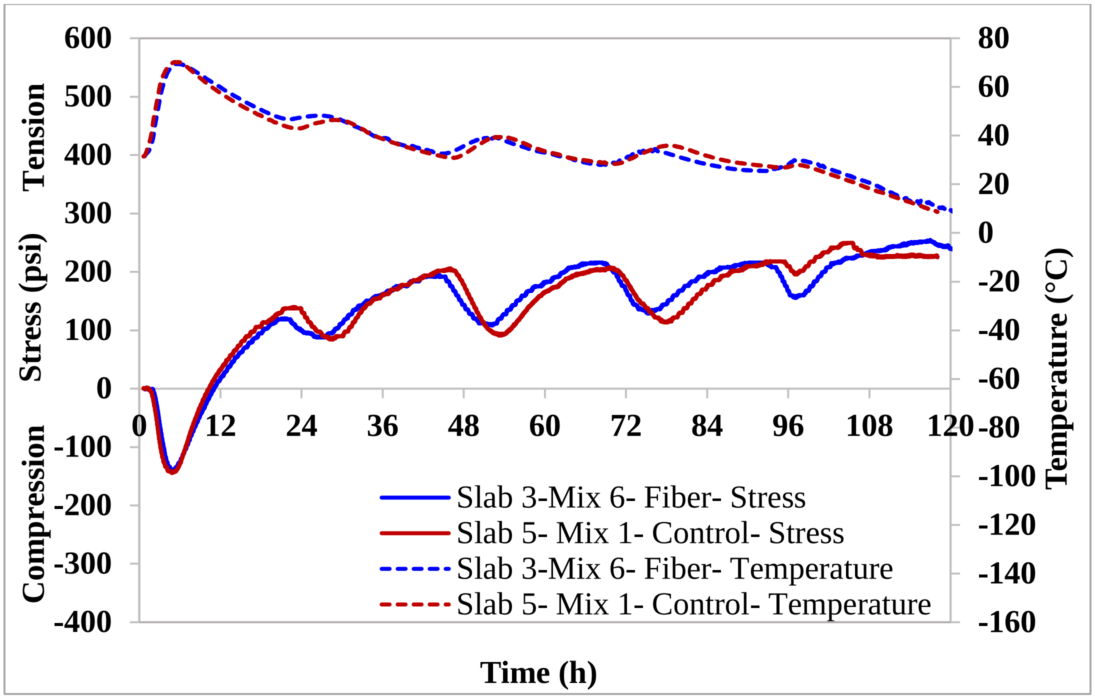

Figure 9-6: Cracking frame results for slabs 3 and 5

The incorporation of SRA did not have a significant effect on temperature development as can be seen in Figure 9-7. The minimal effect of SRA on the temperature rise of the hydrating cement systems has been reported with mortar mixes [23]. A lack of a substantial effect on temperature is appropriate considering the low dosage of the SRA used in this study.

Despite the similar temperature rise, Mix#4 with SRA experienced a higher maximum compressive stress of 170 psi, while the maximum compressive stress for the control mix was 141 psi. Higher initial pre-compression is beneficial as it may offset subsequent development of tensile stresses, similar to the mechanism used by expansive cements [24]. Although the maximum temperatures for Mix#1 and Mix#4 were very similar, temperature of the control mix decreased at a higher rate. Consequently, transition from compression to tension occurred at 10.1 hours for Mix 1 compared to 12.9 hours for the SRA mix. It appears that SRA had only a minor effect on stress development through a slight increase in precompression. Several studies have reported a decrease in autogenous shrinkage with the use of SRA [11], [25], [26]. The concrete in this study was subjected to elevated field temperature profiles. The SRA was likely less effective in reducing autogenous shrinkage at these elevated temperatures used in HES concrete than in paving applications[27]. SRA is also expected to have a beneficial effect on drying shrinkage stresses that could not be measured in this laboratory test.

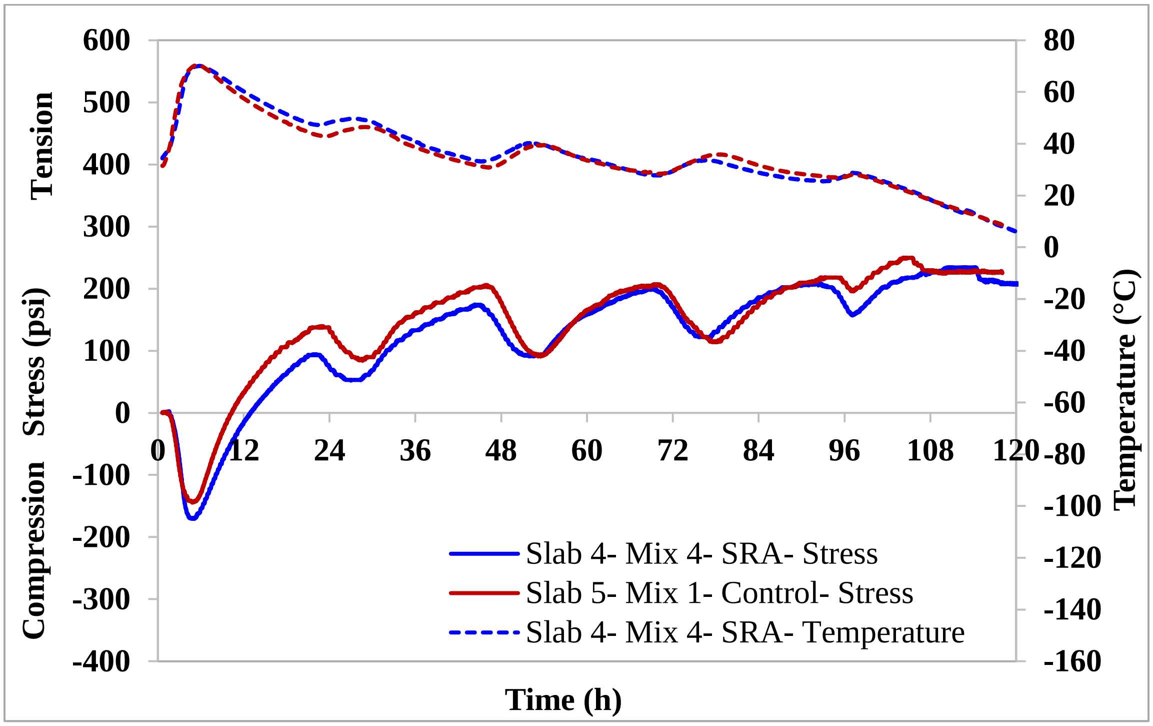

Figure 9-7: Cracking frame results for slabs 4 and 5

A decrease in the paste content (Mix#2) decreased the maximum concrete temperature rise compared to Mix#1 (Figure 9-8). Additionally, since the rate of temperature change was lower for Mix#2, tensile stresses for this mix started to develop at a later age and remained below those of Mix#1 despite the similar temperature profiles after the first 24 hours. It appears that lower cement content resulted in lower internal temperature and reduced thermal expansion. Additionally, reducing the overall paste volume is likely to have reduced the overall shrinkage [21], [28]. According to ACI [29], [30], reducing the maximum concrete temperature through mix optimization is an effective way to improve the durability of concrete elements.

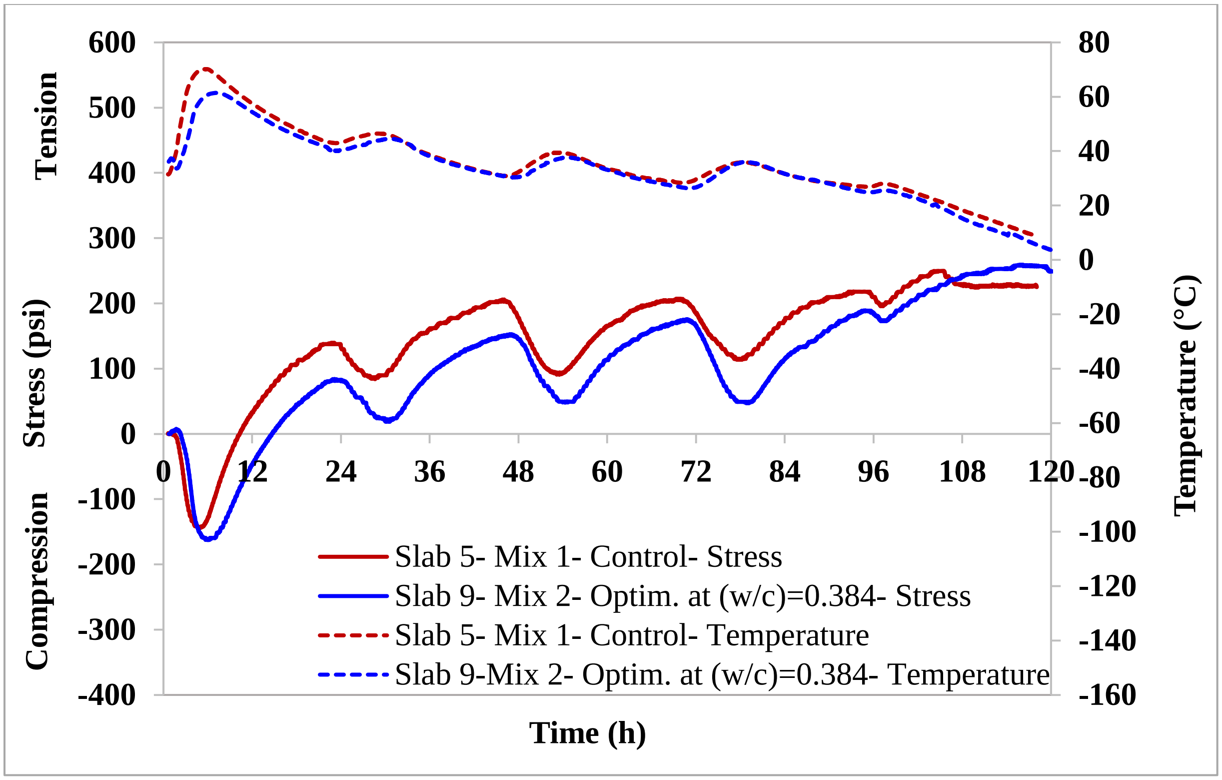

Figure 9-8: Cracking frame results for slabs 5 and 9

A reduction in the w/c ratio of the optimized mix from 0.384 (Mix#2) to 0.34 (Mix#3) did not have a significant effect on temperature and stress development as can be seen in Figure 9-9. Although an increased autogenous shrinkage with this reduction in w/c ratio was expected to increase tensile stresses for Mix#3, this was not observed from the RCF results.

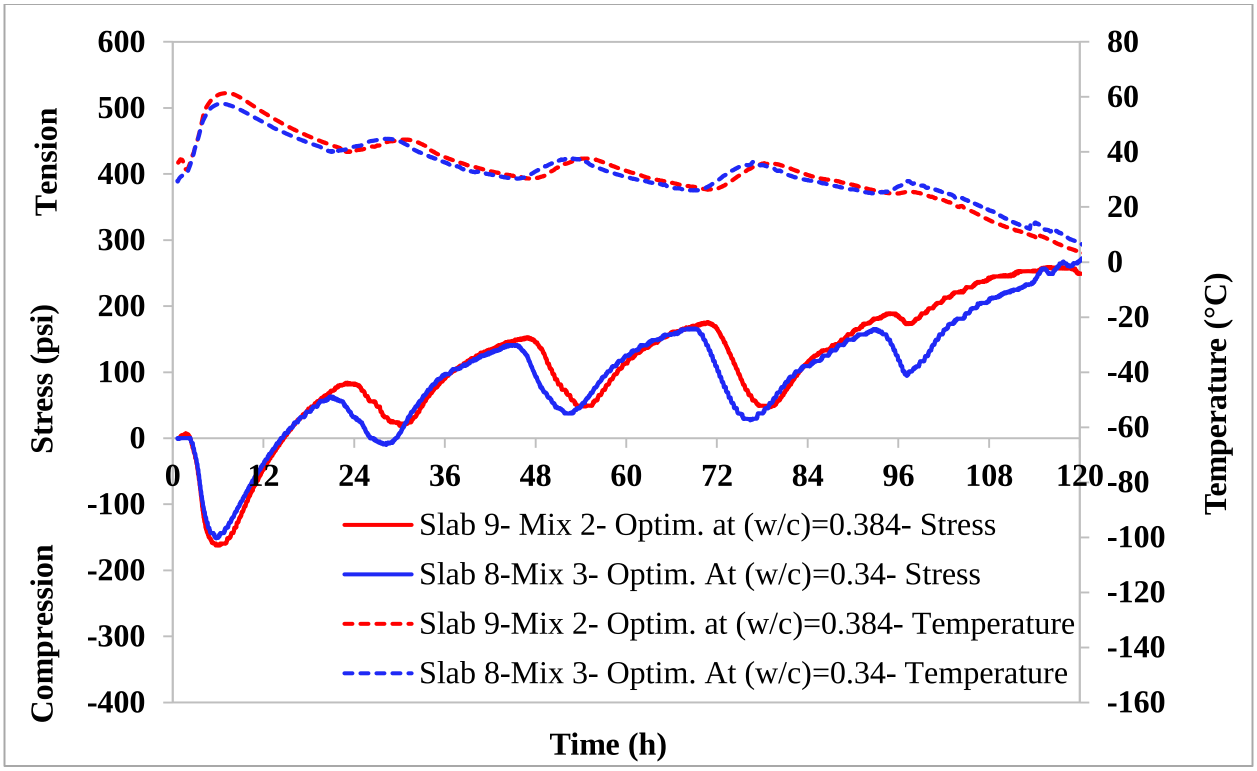

Figure 9-9: Cracking frame results for slabs 9 and 8

9.4 Conclusions

Based on the results of elastic modulus, compressive strength, and tensile strength testing, it can be concluded that the use of fibers, SRA, and mix optimization did not result in significant improvements in concrete mechanical properties. A slight reduction in strength was observed with the addition of LWA. In terms of uniaxial stress development, no significant difference was observed with the use of fibers or SRA compared to the control mix. However, using LWA and reducing the overall paste content through mix optimization resulted in a decrease in the induced tensile stresses.

9.5 References

[1] Florida Department of Transportation, “Standard Specifications for Road and Bridge Construction,” Tallahassee, FL, 2016.

[2] R. Springenschmid, R. Breitenbücher, and M. Mangold, “Development of the Cracking Frame and the Temperature-Stress Testing Machine,” in *RILEM Proceedings 25, Thermal Cracking in Concrete at Early Ages*, 1994, pp. 137–144.

[3] A. Williams, A. Markandeya, Y. Stetsko, K. Riding, and A. Zayed, “Cracking potential and temperature sensitivity of metakaolin concrete,” *Constr. Build. Mater.*, vol. 120, no. 2016, pp. 172–180, 2016.

[4] A. Zayed, K. Riding, C. C. Ferraro, A. Bien-aime, N. Shanahan, D. Buidens, T. Meagher, V. Tran, J. D. Henika, J. M. Paris, C. M. Tibbetts, and B. E. Watts, “Final Report Long-Life Slab Replacement Concrete FDOT Contract Number : BDV25-977-01,” University of South Florida, 2015.

[5] D. Buidens, “Effects of Mix Design Using Chloride-Based Accelerator on Concrete Pavement Cracking Potential,” MS Thesis, University of South Florida, 2014.

[6] ASTM C192/C192M-16a, “Standard Practice for Making and Curing Concrete Test Specimens in the Laboratory,” West Conshohocken, PA: ASTM International, 2016.

[7] ASTM C39/39M-15a, “Standard Test Method for Compressive Strength of Cylindrical Concrete Specimens,” West Conshohocken, PA: ASTM International, 2015.

[8] ASTM C496/C496M-11, “Standard Test Method for Splitting Tensile Strength of Cylindrical Concrete Specimens,” West Conshohocken, PA: ASTM International, 2011.

[9] ASTM C469/C469M-14, “Standard Test Method for Static Modulus of Elasticity and Poisson’s Ratio of Concrete in Compression,” West Conshohocken, PA: ASTM International, 2014.

[10] E. Yurdakul, P. C. Taylor, H. Ceylan, and F. Bektas, “Effect of Paste-to-Voids Volume Ratio on the Performance of Concrete Mixtures.,” *J. Mater. Civ. Eng.*, vol. 25, no. 12, pp. 1840–1851, 2013.

[11] S. P. Shah, M. E. Karaguler, and M. Sarigaphuti, “Effects of shrinkage-reducing

admixtures on restrained shrinkage cracking of concrete," *ACI Mater. J.*, vol. 89, no. 89, pp. 291–295, 1992.

[12] K. J. Folliard and N. S. Berke, "Properties of High Performance Concrete Containing Shrinkage-Reducing Admixture," *Cem. Concr. Res.*, vol. 27, no. 1, pp. 1357–1364, 1997.

[13] A. Bentur, S. Igarashi, and K. Kovler, "Prevention of Autogenous Shrinkage in High-Strength Concrete by Internal Curing Using Wet Lightweight Aggregates," *Cem. Concr. Res.*, vol. 31, no. 11, pp. 1587–1591, 2001.

[14] S. Zhutovsky, K. Kovler, and A. Bentur, "Influence of Cement Paste Matrix Properties on the Autogenous Curing of High-Performance Concrete," vol. 26, pp. 499–507, 2004.

[15] S. M. Andaleeb, "Concrete Mix Design for Lightweight Aggregates and an Overview on High Strength Concrete," 2005.

[16] B. Bissonnette and M. Pigeon, "Tensile Creep At Early Ages of Ordinary, Silica Fume and Fiber Reinforced Concretes," *Cem. Concr. Res.*, vol. 25, no. 5, pp. 1075–1085, 1995.

[17] P. Soroushian and S. Ravanbakhsh, "High-Early Strength Concrete: Mixture Proportioning with Processed Cellulose Fibers for Durability," *ACI Mater. J.*, vol. 96, no. 5, pp. 593–599, 1999.

[18] Robert Philleo, "Concrete Science and Reality," *Mater. Sci. Concr. II*, pp. 1–8, 1991.

[19] B. E. Byard and A. K. Schindler, "Cracking Tendency of Lightweight Concrete," Highway Research Center, Auburn University, 2010.

[20] D. Cusson and T. Hoogeveen, "Internal Curing of High-Performance Concrete with Pre-soaked Fine Lightweight Aggregate for Prevention of Autogenous Shrinkage Cracking," *Cem. Concr. Res.*, vol. 38, no. 6, pp. 757–765, 2008.

[21] P. C. Taylor, S. H. Kosmatka, and G. F. Voigt, "Integrated Materials and Construction Practices for Concrete Pavement: A State-of-the-Practice Manual," National Concrete Pavement Technology Center, Iowa State University, Ames, IA, 2006.

[22] P. Soroushian, F. Mirza, and A. Alhozaimy, "Plastic Shrinkage Cracking of Polypropylene Fiber Reinforced Concrete," *ACI Mater. J.*, vol. 92, no. 5, pp. 553–560, 1995.

[23] B. Pease, "The Role of Shrinkage Reducing Admixtures on Shrinkage, Stress

Development, and Cracking," Purdue University, 2005.

[24] K. A. Riding, J. L. Poole, A. K. Schindler, M. C. G. Juenger, and K. J. Folliard, "Effects of Construction Time and Coarse Aggregate on Bridge Deck Cracking," *ACI Mater. J.*, vol. 106, no. 5, pp. 448–454, 2009.

[25] K. Folliard and N. Berke, "Properties of High-Performance Concrete Containing Shrinkage-Reducing Admixture," *Cem. Concr. Res.*, vol. 27, no. 9, pp. 1357–1364, 1997.

[26] G. Sant, B. Lothenbach, P. Juilland, G. Le Saout, J. Weiss, and K. Scrivener, "The Origin of Early Age Expansions Induced in Cementitious Materials Containing Shrinkage-Reducing Admixtures," *Cem. Concr. Res.*, vol. 41, no. 3, pp. 218–229, Mar. 2011.

[27] G. Sant, "The Influence of Temperature on Autogenous Volume Changes in Cementitious Materials Containing Shrinkage Reducing Admixtures," *Cem. Concr. Compos.*, vol. 34, no. 7, pp. 855–865, Aug. 2012.

[28] E. Yurdakul, "Optimizing Concrete Mixtures with Minimum Cement Content for Performance and Sustainability," Iowa State University, 2010.

[29] ACI committee 207, "ACI 207.2R-07 Report on Thermal and Volume Change Effects on Cracking of Mass Concrete," American Concrete Institute, Farmington Hills, MI, 2007.

[30] ACI Committee 201, "ACI 201.2R - 16 Guide to Durable Concrete," American Concrete Institute, Farmington Hills, MI, 2016.

Chapter 10 Field Assessment of the Parameters Affecting Cracking Potential of Concrete Pavement Slabs

10.1 Introduction

During the first few days after concrete placement, HES pavement repair slabs can experience large amounts of autogenous and thermal shrinkage. The shrinkage of the pavement is impacted by the mix design, cement composition, ambient and internal temperatures, internal and external humidity levels, and internal and external (base) restraints. As the shrinkage of concrete pavement slabs is restrained by the friction in the slab-base interface, tensile stresses are induced. When these induced tensile stresses exceed the tensile strength of early-age concrete, which is low compared to the ultimate tensile strength, cracking occurs [1]–[4].

Different crack mitigation methods were incorporated in this project to find their effects on cracking potential. The concrete mixture designs used are listed in Table 10-1. The use of pre-wetted lightweight aggregates (LWA) provides internal curing (IC) by supplying many uniformly-distributed internal water reservoirs that delay the onset of self-desiccation, and thereby reduce autogenous shrinkage. The enhanced degree of hydration due to the increased internal humidity levels can increase the ultimate strength [5]–[7]. Polypropylene fibers (PPF) control progression of plastic-shrinkage cracks and improve the tensile strength of the concrete [8]–[10]. Incorporation of shrinkage-reducing admixtures (SRA) reduces surface tension of pore water and thereby minimizes capillary stresses leading to concrete shrinkage [11], [12]. Optimizing aggregate gradation (OAG) by including an intermediate aggregate is useful in reducing the paste-to-void ratio and thereby lowering the cement content, which reduces temperature rise and autogenous shrinkage [13]. The effects of these crack mitigation methods on early-age cracking potential were evaluated by conducting field and laboratory experiments. Seven crack mitigation strategies, which consisted of modifications to mixture design and use of base friction-reducing procedures were investigated on field-placed slabs. Rigid cracking frame (RCF) and mechanical property testing were also conducted using the same crack-mitigating strategies used in the field. The objective of this task was to compare the field results to laboratory results and assess the similarities/differences in the trends.

Stress development alone cannot be used as a method of evaluating cracking potential. Evaluation of cracking tendency of concrete pavements requires an understanding of both stress and strength development. Several methods have been proposed in the literature to evaluate the cracking tendency of concrete members [14]–[17]. Despite many indirect measures to evaluate the cracking in the member, stress-to-strength ratio can be used as a direct measure to assess the cracking tendency. This ratio is not a unique number and may change depending on loading rate (based on the degree of hydration) and formation of tertiary creep and microcracks in the member which affect the loading rate. Prediction of concrete strength is needed to determine cracking potential using stress-to-strength ratio. In general, maturity curves or strength and equivalent-age data are used in predicting concrete strength [1]

Table 10-1: Mixture design per 1 m^3 (1 yd^3)

Mix ID **Mix Constituents**	**Mix #1 (Control)**	**Mix #2**	**Mix #3**	**Mix #4**	**Mix #5**	**Mix #6**
Cement, kg (lb)	534 (900)	415 (700)	415 (700)	534 (900)	534 (900)	534 (900)
CA #57 limestone (SSD), kg (lb)	997 (1680)	682 (1150)	700 (1180)	997 (1680)	997 (1680)	997 (1680)
IA #89 limestone (SSD), kg (lb)	0.0	409 (690)	421 (710)	0.0	0.0	0.0
FA silica sand (SSD), kg (lb)	492 (829)	610 (1028)	625 (1054)	501 (844)	326 (549)	491 (827)
LWA (SSD), kg (lb)	0.0	0.0	0.0	0.0	97 (163)	0.0
Water, kg (lb)	193 (325)	150 (252)	131 (221)	189 (319)	193 (325)	193 (325)
Type F Superplasticizer, ml (fl. oz)	0.0	948 (24.5)	1354 (35.0)	0.0	0.0	0.0
Type E Accelerator, ml (fl. oz)	14853 (384)	11554 (298.7)	11554 (298.7)	14853 (384)	14853 (384)	14853 (384)
Air Entrainer, ml (fl. oz)	38 (1.0)	38 (1.0)	38 (1.0)	38 (1.0)	38 (1.0)	38 (1.0)
Type D Water-reducing Admixture, ml (fl. oz)	874 (22.6)	696 (18.0)	696 (18.0)	874 (22.6)	874 (22.6)	874 (22.6)
Shrinkage Reducing Admixture, ml (gal)	0.0	0.0	0.0	3713 (0.75)	0.0	0.0
Fiber, kg (lb)	0.0	0.0	0.0	0.0	0.0	0.297 (0.5)
w/c	0.384	0.384	0.340	0.384	0.384	0.384

10.2 Methodology

To evaluate the maturity of the mixes proposed in this project, the compressive and splitting tensile strengths of the cylinders prepared in the field were measured at 0.25, 1, 3 , 7, and 28 days, in accordance with ASTM C39 [18] and C496 [19], respectively. The temperature profile of the concrete cylinders prepared for each mix was used for calculation of maturity and temperature-time factor in accordance with Equation 10-1 [20].

$$M\,(t) = \sum (T_a - T_0)\Delta t \qquad \text{Equation 10-1}$$

Where,

$M\,(t)$ = the temperature-time factor at age t, degree-hours

Δt = a time interval, hours

T_a = average concrete temperature during time interval Δt, °C

T_0 = datum temperature, °C

The plots of maturity versus compressive and tensile strengths of the concrete cylinders were obtained. The plots were established based on fitting the nonlinear exponential function, as outlined in Equation 10-2, into the compressive and tensile strengths of the concrete cylinders at five ages of 0.25, 1, 3, 7, and 28 days.

$$S = S_u\, e^{-(\frac{\tau}{t})^{\beta}} \qquad \text{Equation 10-2}$$

Where,

S = Average compressive strength at age t (psi)

t = Test age (days)

S_u = Limiting strength (psi)

τ = Time constant (days) [1/k in the hyperbolic function]

β = Curve shape parameter (dimensionless)

In order to evaluate the experimental results further, the imposed temperature profiles associated with the rigid cracking frame (RCF) were used to calculate the time-temperature maturity according to Equation 10-1. The time-temperature maturity data was used to determine the ratio of the induced uniaxial stress (for the specimen in the cracking frame) to the tensile strength of the mix calculated using the field cylinders and implementation of maturity concept.

HIPERPAV III software [21] was used to simulate early-age tensile stress development and assess the cracking potential of each of the slabs used in this project. The tensile strength and elastic modulus of each mixture obtained from cylinder testing results and maturity data inputs were used in the analysis. Weather data collected from the field slabs for a period of 7 days was used as environmental inputs.

TNO DIANA software [22] was used to perform a three-dimensional finite element analysis and predict the stress development and cracking potential of a young concrete pavement slab. The developed model was useful in obtaining a better understanding of the stress development in field slabs. DIANA’s built-in features, such as heat of hydration modeling, equivalent-age calculation, and temperature- and time-dependent material properties, were useful in this analysis. Most of the thermal and mechanical property data inputs, such as the adiabatic temperature curve, activation energy, thermal expansion coefficient, elastic modulus, and tensile strength development, were generated from laboratory experiments. The creep/relaxation parameters for the concrete mix were obtained by a finite element modeling simulation of the concrete stress development in the rigid cracking frame. A few model inputs, such as thermal conductivity, heat capacity, and convection coefficient, were obtained from literature [23], [24]. Autogenous shrinkage input was calculated based on the model proposed by Hedlund [2], [25].

10.3 Results

Maturity curves for compressive strength and splitting tensile strength of each mix are shown in Figure 10-1 and Figure 10-2, respectively. Comparison of compressive strengths at an early age, for example at a maturity of about 700°C-h, shows strength values of about 6,150 psi for Mixes 2 (OAG, w/c = 0.384) and 3 (OAG, w/c = 0.34), 5750 psi for Mix 1 (Control, w/c = 0.384), 5,440 psi for Mixes 5 (IC-LWA, w/c = 0.384) and 6 (PPF, w/c = 0.384), and 4,950 psi for Mix 4 (SRA, w/c = 0.384). Comparison at a later age of about 8,000°C-h shows Mix 3 with a significantly higher compressive strength of about 8,400 psi, which is about 850 psi higher than the control. Mix 2, at about 550 psi lower than Mix 3, had a compressive strength of 7,850 psi, followed by Mix 1 at 7,570 psi, Mix 5 at 7,500 psi, Mix 4 at 7,420 psi, and Mix 6 at 7,310 psi.

The maturity plot for splitting tensile strength (Figure 10-2) showed interesting results. Mix 3 (OAG, w/c = 0.34), Mix 2 (OAG, w/c = 0.384), and Mix 1 (Control, w/c = 0.384) showed significant improvement of tensile strength, compared to the other mixes, up to a maturity of about 550°C-h, after which the Mix 1 tensile strength quickly leveled off to about 580 psi. The curves for Mixes 1, 4, 5, and 6 plateaued before reaching a maturity of about 4,000°C-h, and had similar splitting tensile strengths ranging from about 580 to 620 psi. Mixes 3 and 2 continued to increase in strength until becoming relatively level at about 8,000°C-h, with respective splitting tensile strengths of about 740 and 710 psi.

Mixes 2 and 3 showed significant improvements in the maturity- splitting tensile strength development at early and later ages. This is likely due to the improved aggregate interlock in the aggregate gradation with the inclusion of intermediate aggregates. The increased packing density decreased the void space and also lowered the paste requirement. Mix 3 showed more significant improvement of tensile strength compared to Mix 2 due to the lower w/c ratio in Mix 3. No significant differences in tensile strengths were seen in the rest of the mixes.

Mixtures 4, 5, and 6 were the mixtures made with SRA, LWA for internal curing, and polypropylene fiber, respectively. They showed lower compressive and tensile strengths compared to the control at early maturity levels. However, at later maturity levels, all three mixtures showed strengths similar to that of control. Although the fiber reinforcement was expected to control crack propagation and improve tensile strength of concrete, the polypropylene fibers incorporated in this study did not contribute to the tensile strength. In general, polypropylene fibers are mostly used to control plastic shrinkage cracking by reducing the quantity of surface bleed water significantly [26].

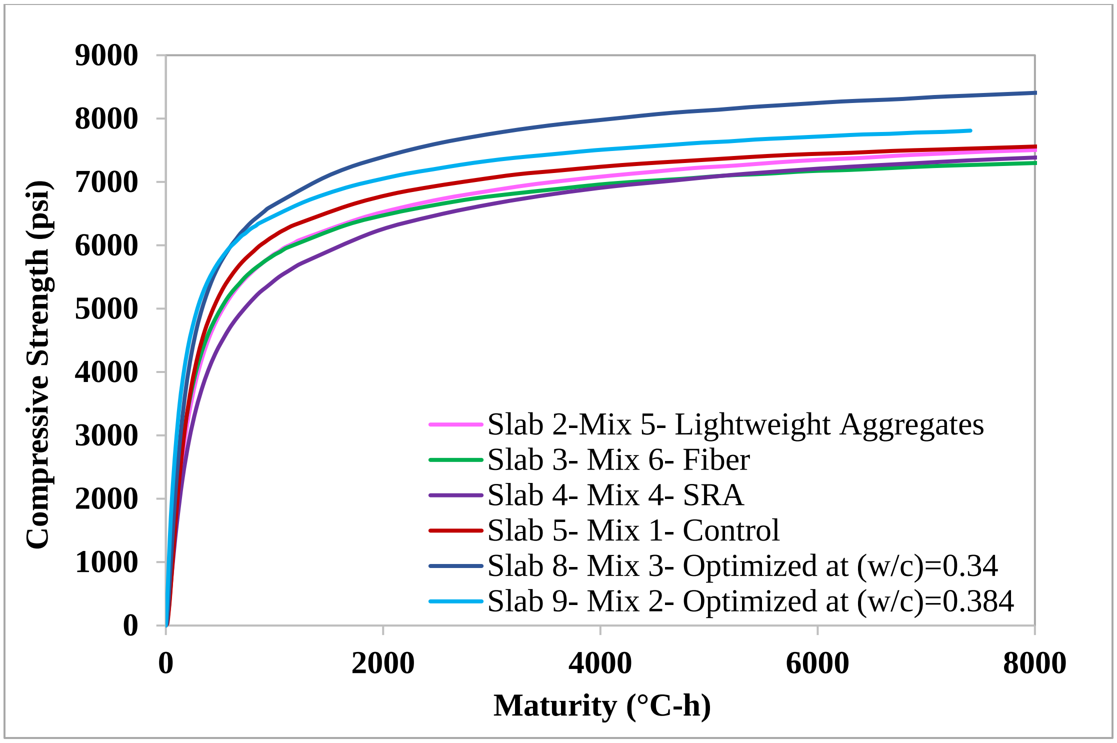

Figure 10-1: Compressive strength of cylinders versus maturity

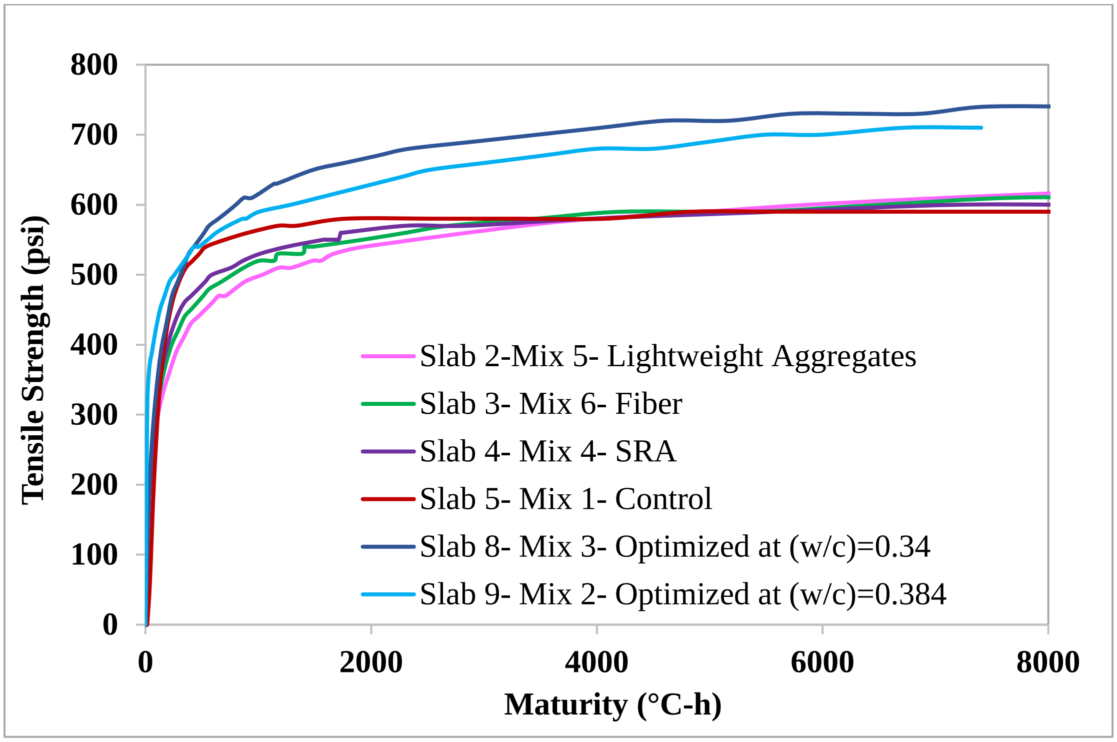

Figure 10-2: Tensile strength of cylinders versus maturity

According to the results obtained from the field experimental program, the stress development captured during the first 6 hours after placement was affected by moisture loss from concrete to the base. Thus, tensile stresses were observed in the slabs during this period due to the induced moisture gradient. However, external drying was prevented in the RCF test set up and, therefore, the stress development in RCF was only affected by temperature rise and autogenous shrinkage. Since the effect due to temperature was predominant in the RCF experiment during the first few hours, compressive stresses were monitored.

The stress-to-tensile strength ratios calculated for RCF and field slabs plotted against concrete age are shown in Figure 10-3 to Figure 10-7. As seen in Figure 10-3, addition of LWA significantly reduced the RCF stress-to-tensile strength ratio throughout the test, indicating a lower cracking potential in the LWA mix compared to the control, confirming the effectiveness of utilizing prewetted LWA as a source of internal curing. In the field slab with LWA, this behavior was only apparent during the first 24 hours and, thereafter, ratios were slightly higher compared to that of slab 5-control.

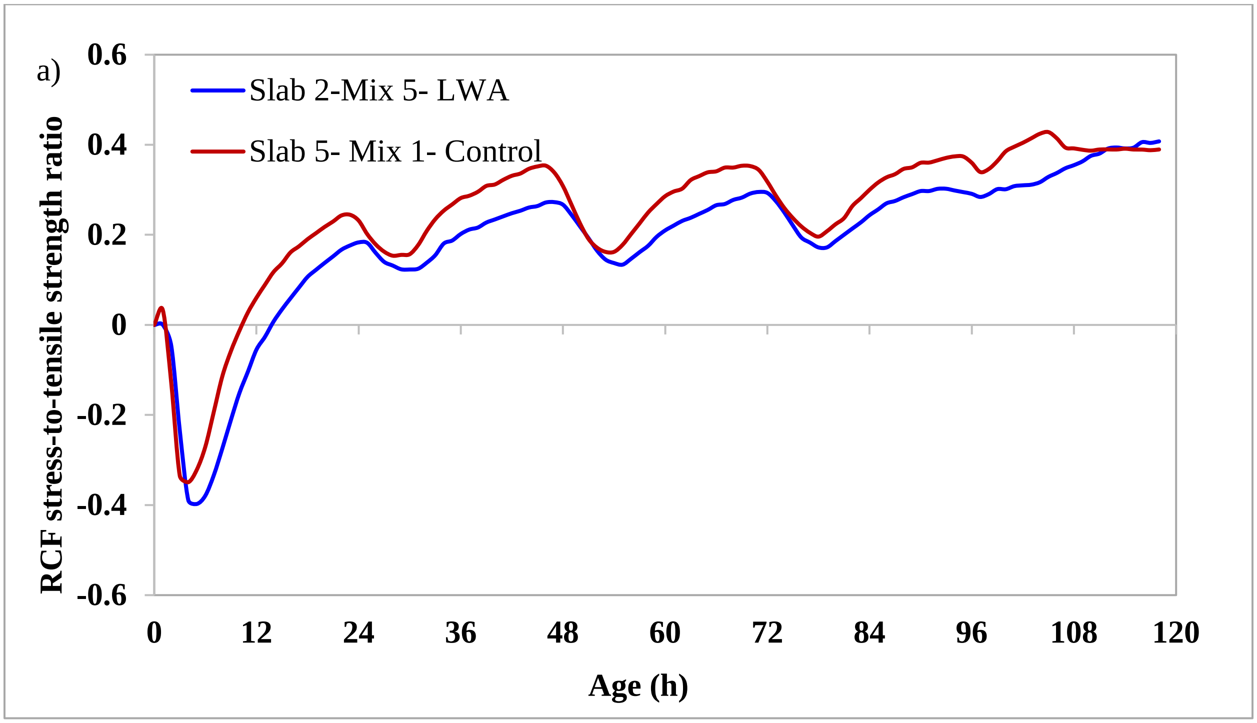

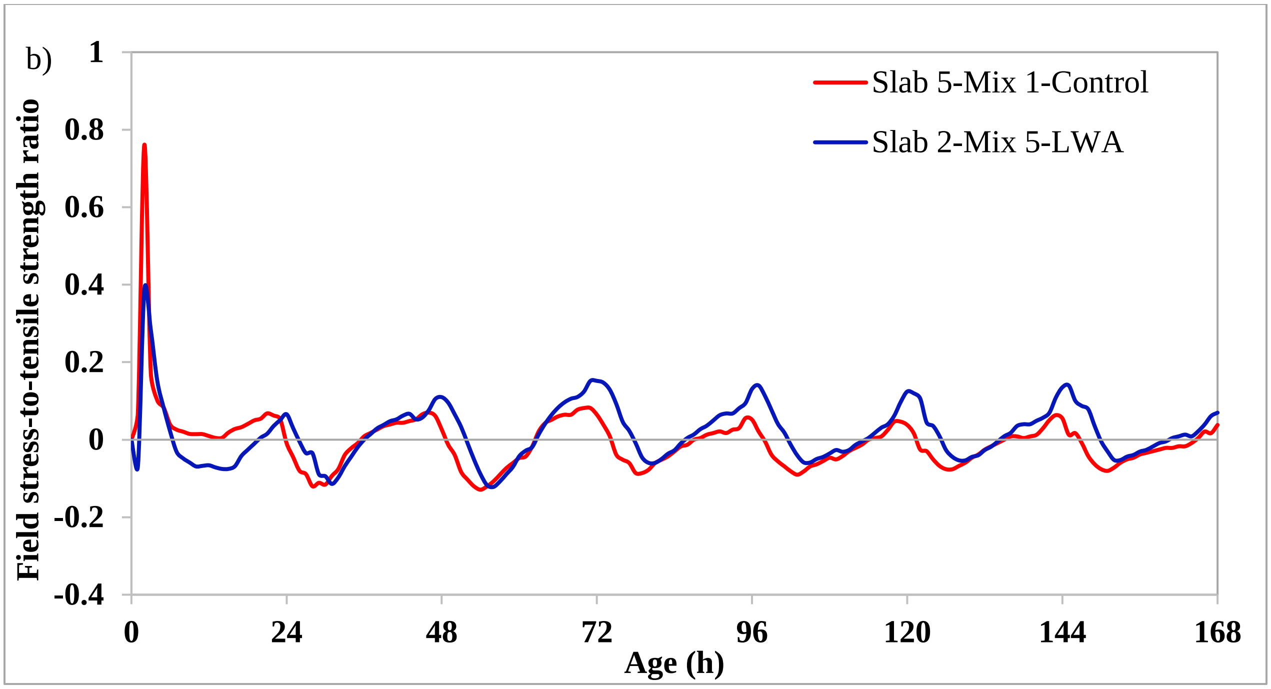

Figure 10-3: Stress-to-tensile strength ratio for slab 2 and slab 5 a) RCF b) Field slabs

Addition of fibers had almost no effect on the RCF stress-to-tensile strength ratio compared to the control, as shown in Figure 10-4. It was likely that the inclusion of fibers did not have any effect on the mechanical behavior of the concrete mix. In general, fiber reinforcement is expected to improve the tensile strength and control cracking; however, due to the lower tensile capacity of polypropylene fibers compared to other types of fibers [27] [28], they are mostly used in controlling plastic shrinkage cracking [26], [29]. Nevertheless, a drastic decrease in the stress-to-tensile strength ratio was observed during the first 24 hours in the field slab with fibers. It was likely the fibers were involved in moisture wicking and maintaining a fairly uniform moisture distribution in the slab [30], [31], minimizing tensile stress development. Moreover, it was also possible that the fibers made the mix more stable by blocking the moisture movement towards the base and thereby preventing the development of a moisture gradient, which could result in tensile stresses. The ability of polypropylene fibers to maintain a stable concrete mix without settling of the mix constituents was reported in [26], [30], [31].

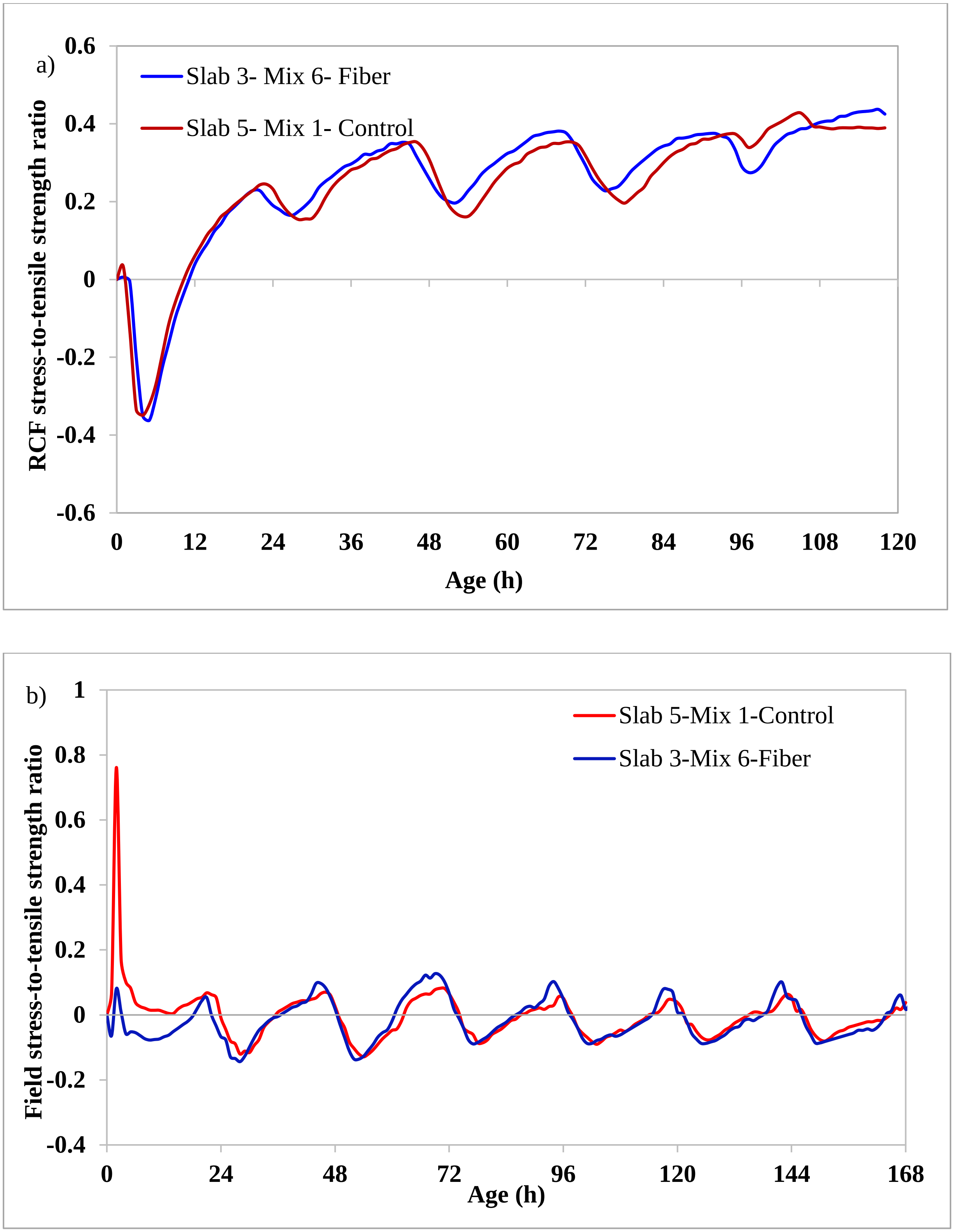

Figure 10-4: Stress-to-tensile strength ratio for slab 3 and slab 5 a) RCF b) Field slabs

According to Figure 10-5, incorporation of SRA had very little effect on the RCF stress-to-strength ratio compared to the control. Although the stress-to-tensile strength ratio of the SRA mix was slightly less in the first 48 hours, later on it was almost the same as the control. Therefore, the effect of SRA on stress development was minimal. This was likely either due to the lower autogenous effect at this w/c ratio or due to the lower SRA dosage, which may have had negligible effects on surface tension of pore water. The large reductions in tensile stresses shown during the first 12 hours in the field slab with SRA were likely due to the decrease in moisture movement that resulted from an increase in fluid viscosity with the SRA addition. The ability of SRA to lower the moisture diffusivity, by increasing the fluid viscosity and, thereby, its effect on enhancing the durability performance of concrete, was reported in [32] and [33]. However, after the first 24 hours, the SRA showed consistently higher stress-to-tensile strength ratios than the control. This was not considered an issue as these ratios remained low.

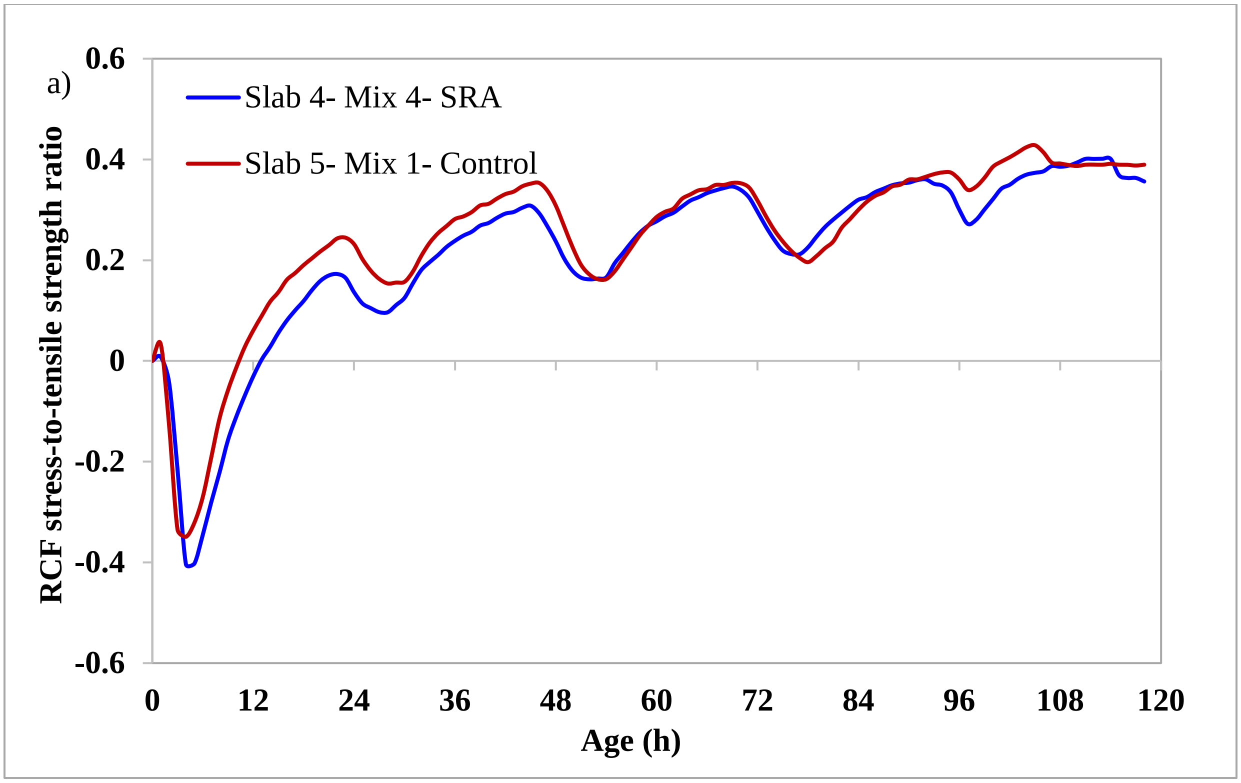

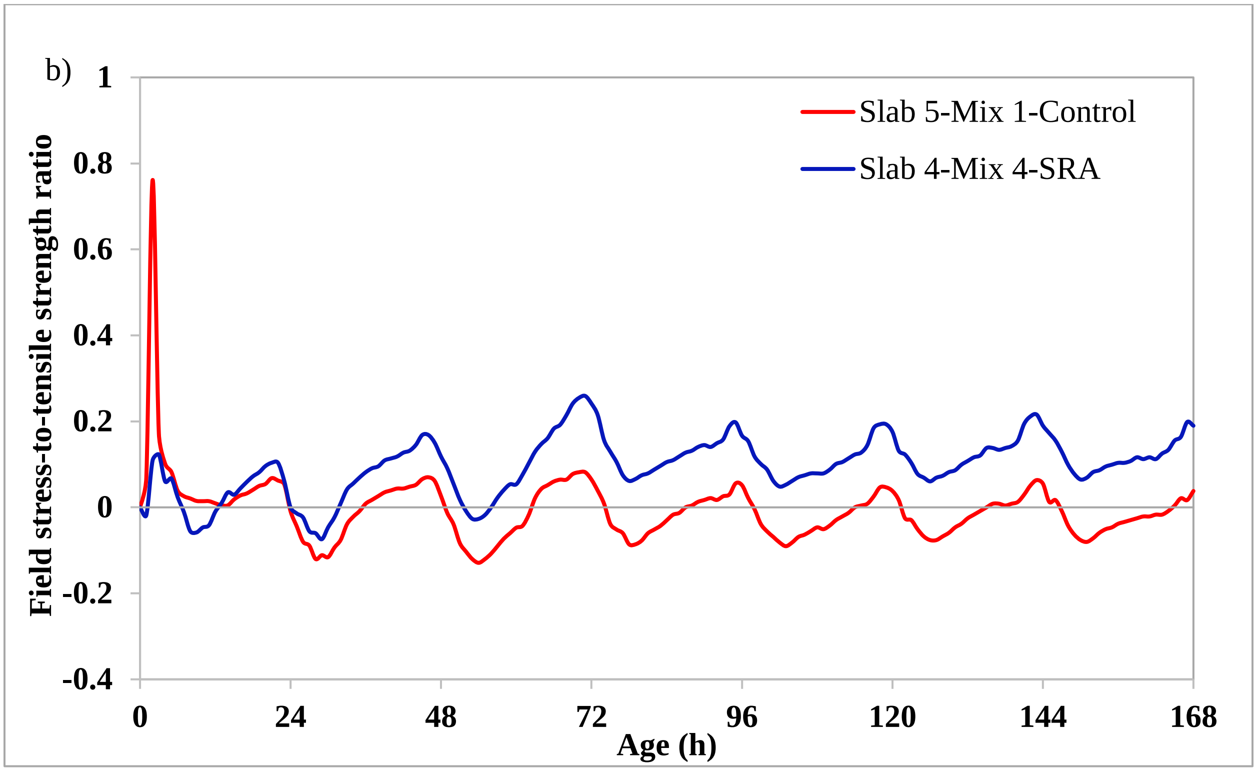

Figure 10-5: Stress-to-tensile strength ratio for slab 4 and slab 5 a) RCF b) Field slabs

Lowering the cement content from 900 lb/yd^3 to 700 lb/yd^3 and utilizing intermediate-sized aggregates significantly reduced the stress-to-tensile strength ratios as shown in Figure 10-6. Although the stress development in RCF for both optimized mixes were similar, the stress-to-tensile strength ratios of the optimized mix at w/c=0.34 showed slightly lower values compared to that of the optimized mix at w/c=0.384 after the first 24 hr. This was due to the enhanced tensile strength development of optimized mix at w/c=0.34 as shown in Figure 10-2, which was attributed to the lower w/c ratio. However, the stress-to-tensile strength ratios calculated for field slabs of optimized mixes showed results different to RCF results. Slab 8 - Mix 3 – optimized at w/c=0.34 showed significantly higher stress-to-tensile strength ratios in the first 24 hours compared to Slab 9 - Mix 2 – optimized at w/c=0.384. This increase in stress-to-tensile strength ratio of Slab 8 was due to the increased autogenous shrinkage, which was a result of reduced w/c ratio and drying shrinkage as a consequence of moisture loss to the base.

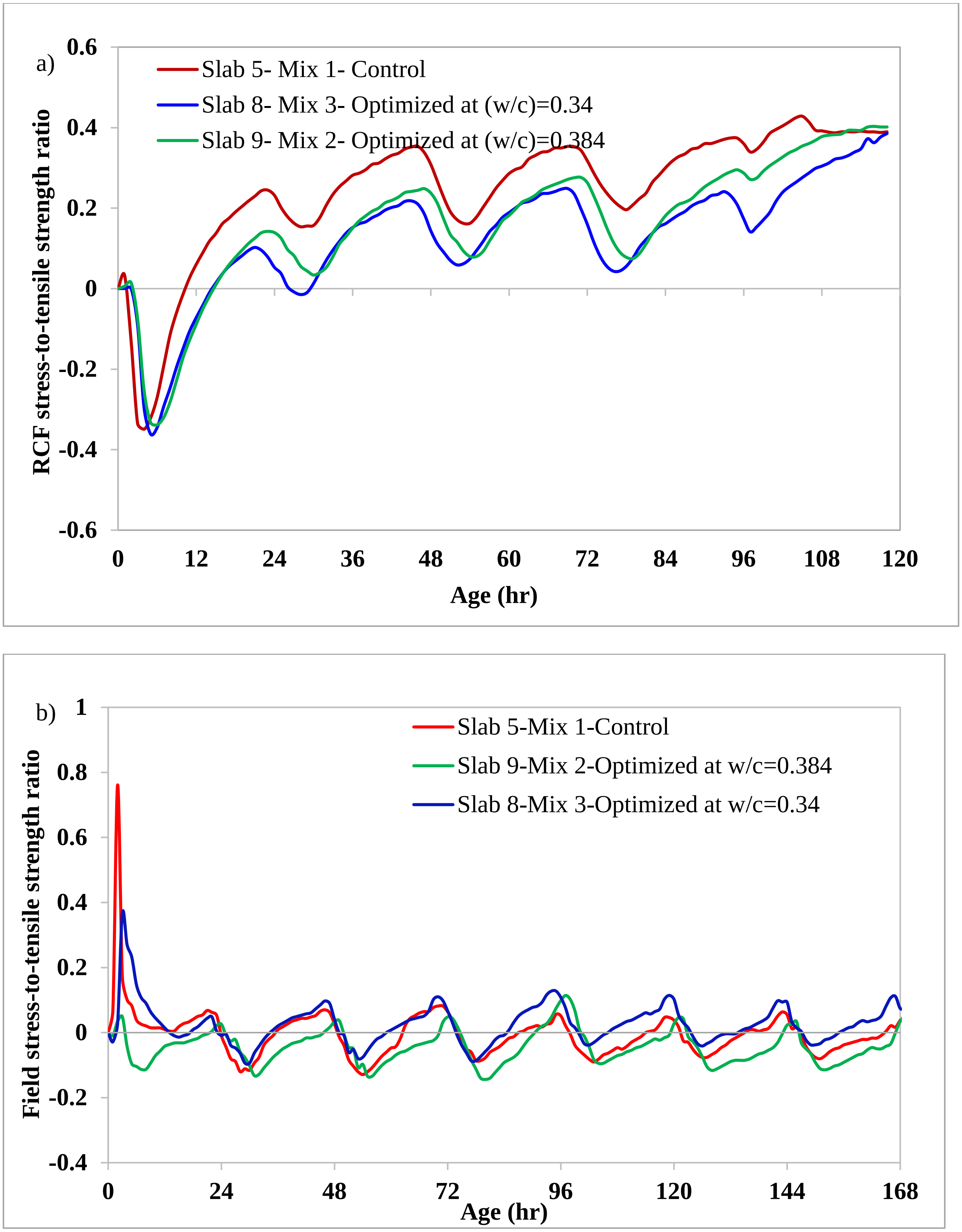

Figure 10-6: Stress-to-tensile strength ratio for slab 5, slab 8 and slab 9 a) RCF b) Field slabs

In addition to the cracking mitigation strategies related to the concrete mixture design, the effects of slab-base interface conditions were also evaluated as part of the field experimental program. The stress-to-tensile strengths obtained for the slabs with double layers of plastic sheets and non-woven geotextile as bond-breakers are shown in Figure 10-7. Two contrasting phenomena associated with moisture movement in concrete were observed with the two bond-breakers. During the first 24 hours, the two sheets of plastic possibly prevented moisture absorption by the base and reduced associated shrinkage. This resulted in significantly lower stress-to-tensile strength ratios. On the contrary, it was possible that the geotextile absorbed or wicked moisture from the concrete and increased autogenous shrinkage, causing a noticeable increase in the stress-to-tensile strength ratio during the same period.

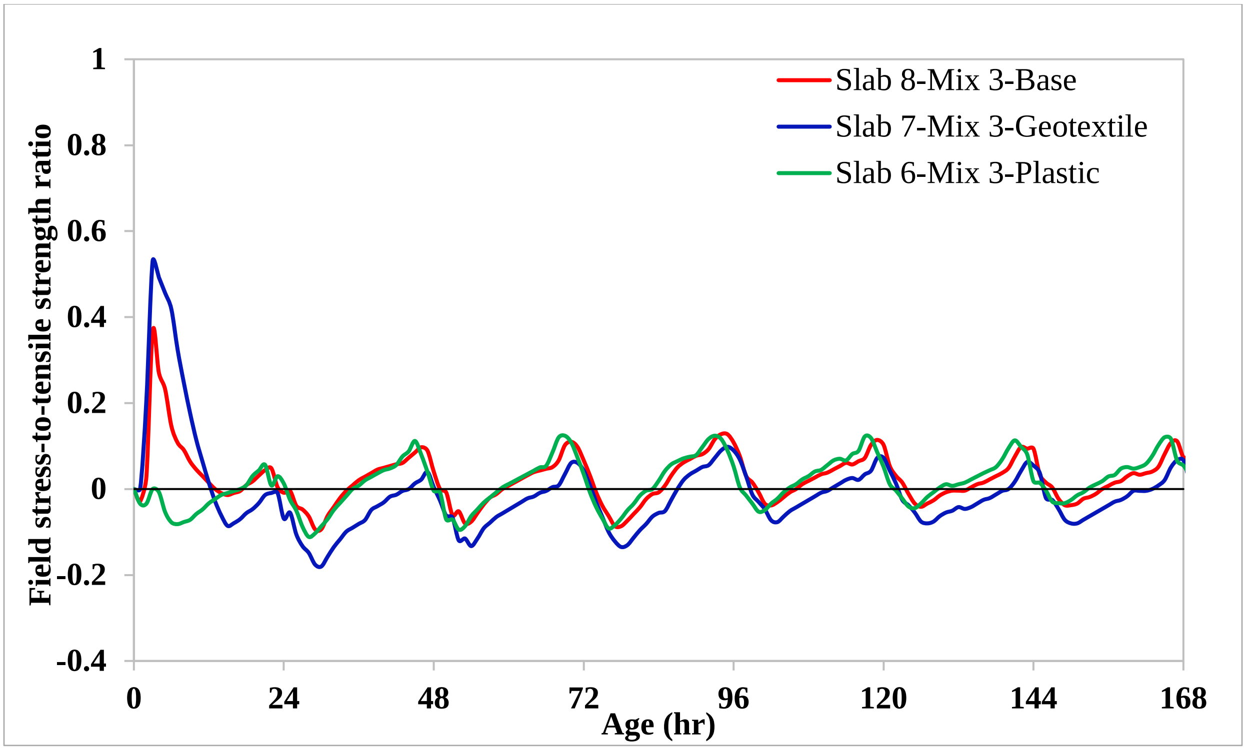

Figure 10-7: Field stress-to-tensile strength ratio for slab 6, slab 7 and slab 8

HIPERPAV analysis of the tensile strength and stress development for all slabs is presented in Figure 10-8. Typically, HIPERPAV only produces the maximum stress, which can be anywhere in the slab top and bottom. Slab 8 - Mix 3 (OAG, w/c = 0.34) showed the highest tensile strength development, while Slab 2 – Mix 5 (IC-LWA) showed the lowest tensile strength development as observed in the laboratory experimental results. Slightly lower stresses were observed in Slab 8 – Mix 3 (OAG, w/c = 0.34) and Slab 9 – Mix 2 (OAG, w/c = 0.384) during the first 24 hr. The highest initial stresses in relation to tensile strengths for all slabs were developed during the first 2-7 hours in the bottom of the slab (Figure 10-10). After 5 hours, highest stresses were predicted in top of the slab (Figure 10-9). This kind of stress distribution is generally expected for a morning placement [34]. As the peak heat evolution of these mixtures coincided with the peak daily temperatures, concrete temperature was highest in the top surface and lowest in the bottom. This would result in expansion of the slab top and, therefore, downward curling of the slab. Consequently, tensile stresses would be generated in the bottom of the slab as the weight and the restraint of the slab prevent the middle from lifting up [35]. When the temperature in the bottom of the slab increases more than the top, the slab contracts and produces upward curling, resulting in tensile stresses in the top of the slab as shown in Figure 10-9.

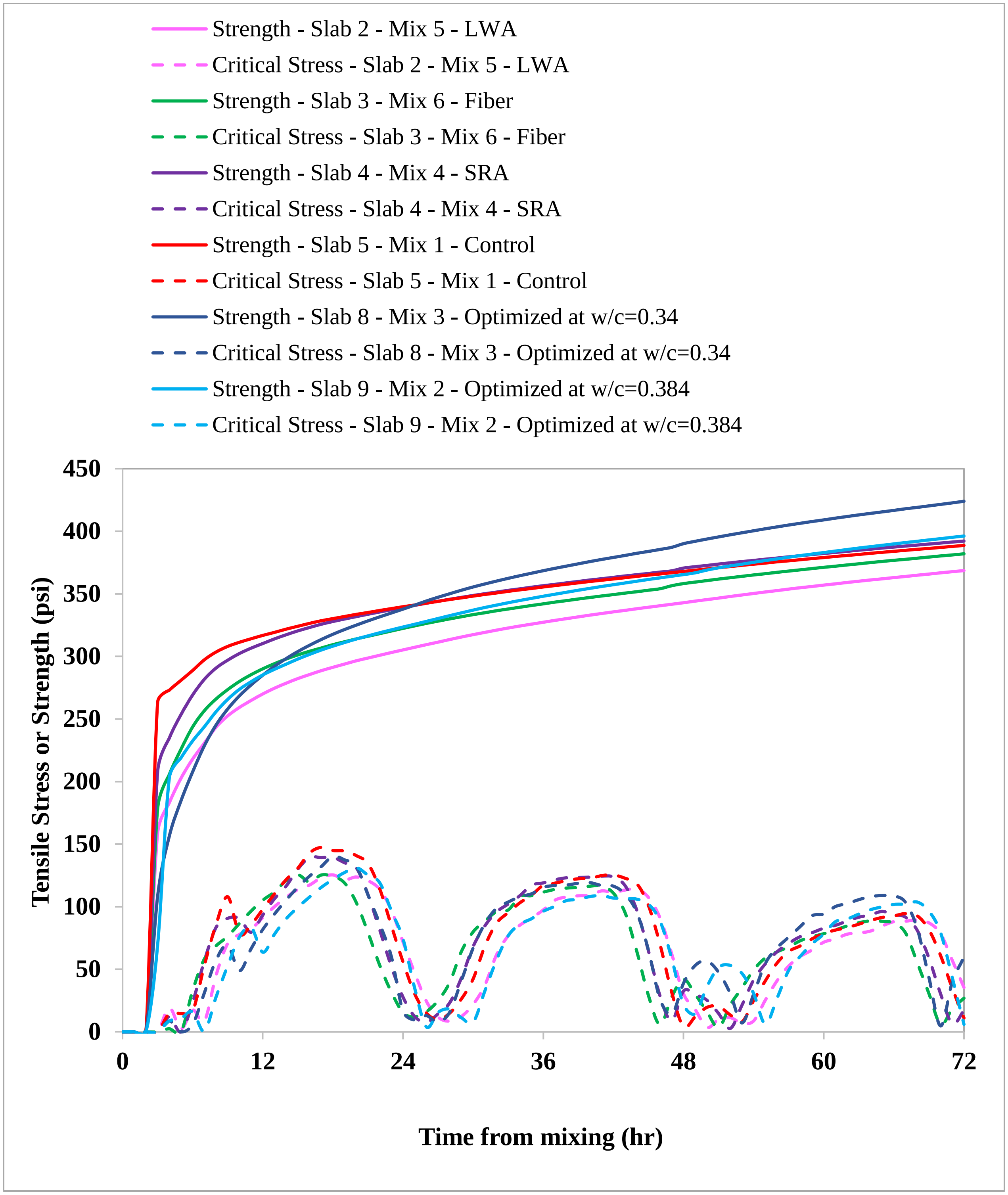

Figure 10-8: HIPERPAV predicted tensile stress and strength development of slabs

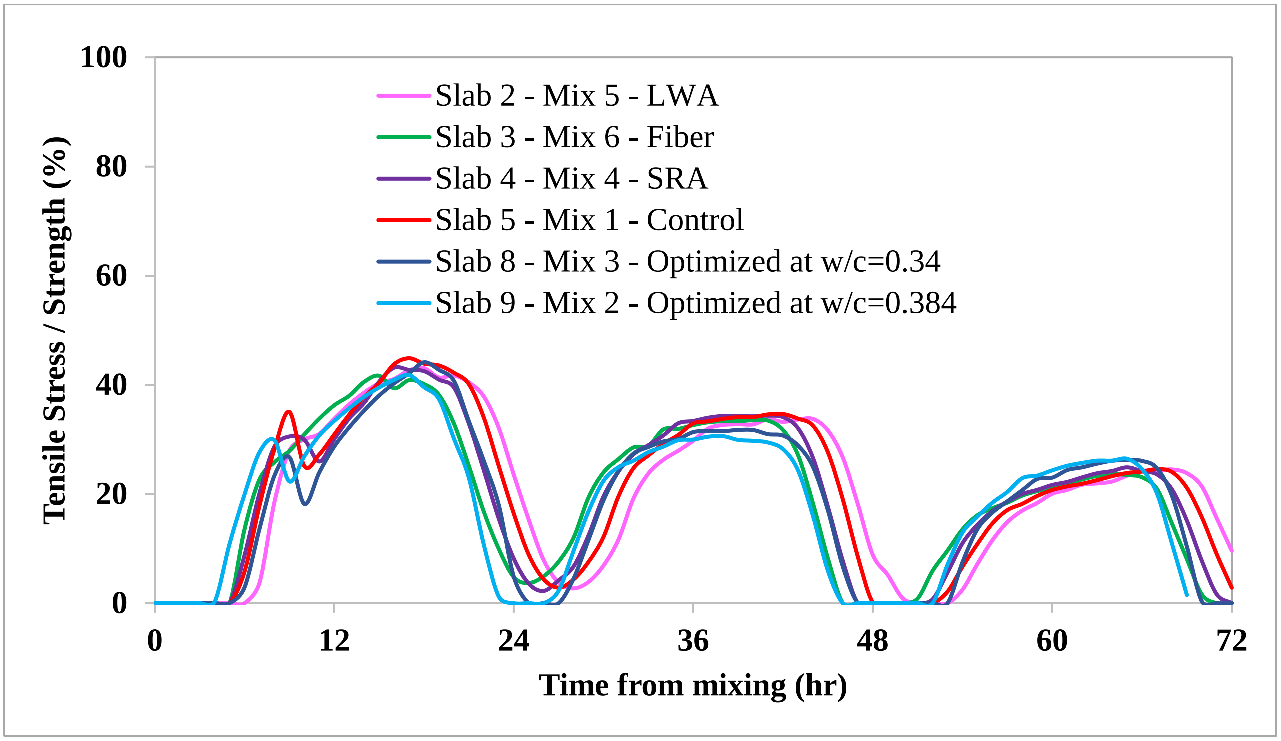

Figure 10-9: HIPERPAV analysis of tensile stress-to-tensile strength development at the top of the slabs

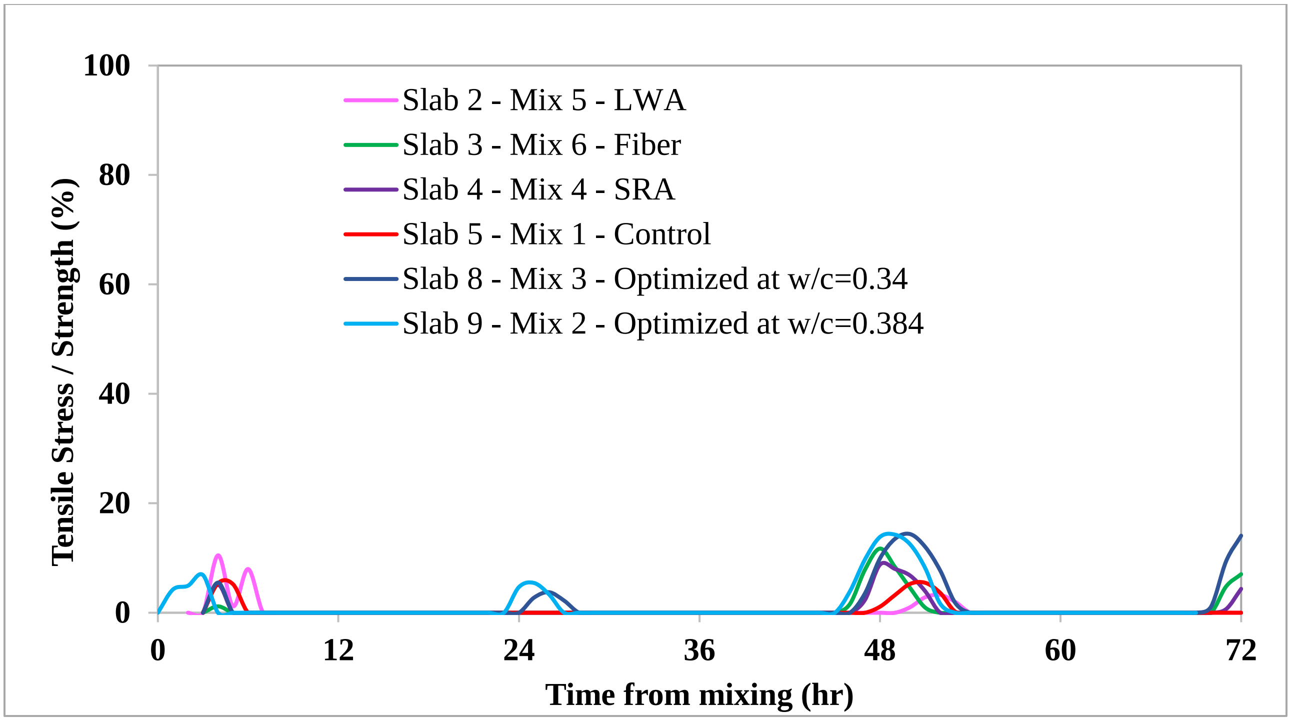

Figure 10-10: HIPERPAV analysis of tensile stress-to-tensile strength development at the bottom of the slabs

Based on the HIPERPAV analysis, none of the slabs exceeded their tensile strengths during the 72-hour period. However, night placements would be more advantageous as they allow heat of hydration and heat from environmental conditions to occur at separate times, reducing the peak concrete temperature rise and concrete tensile stresses [34], [36]. Therefore, the tensile stress development can be further reduced by considering night-time placement of slabs.

HIPERPAV analysis only presents the maximum stress developed anywhere in the slab top or bottom at a certain time. In order to study the stress development at the same location in the field slabs (8 in. from the bottom), and also to obtain a better understanding of the measured stress development of field slabs and associated phenomena, three-dimensional finite element analysis was performed using DIANA software. The predicted temperature and stress results were compared with the field stress captured for slab 5-control. As it appears in Figure 10-11, the temperature prediction obtained from DIANA analysis matched well with the field-captured temperature during the first 72 hours, and especially after 12 hours. Figure 10-12 shows the stress predicted using only the heat of hydration module without considering the creep/relaxation effects. As a result, very high compressive stresses were observed during the initial period when initial temperature rise occurred.

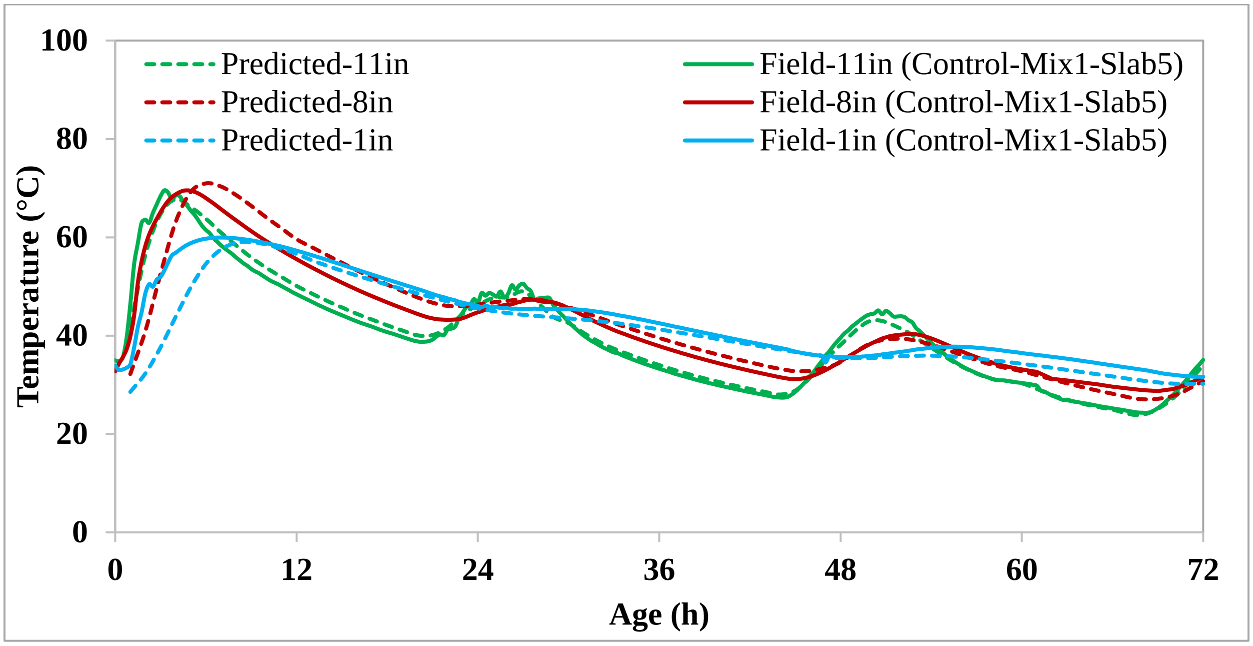

Figure 10-11: Temperature prediction obtained from DIANA for slab 5 at the same depths

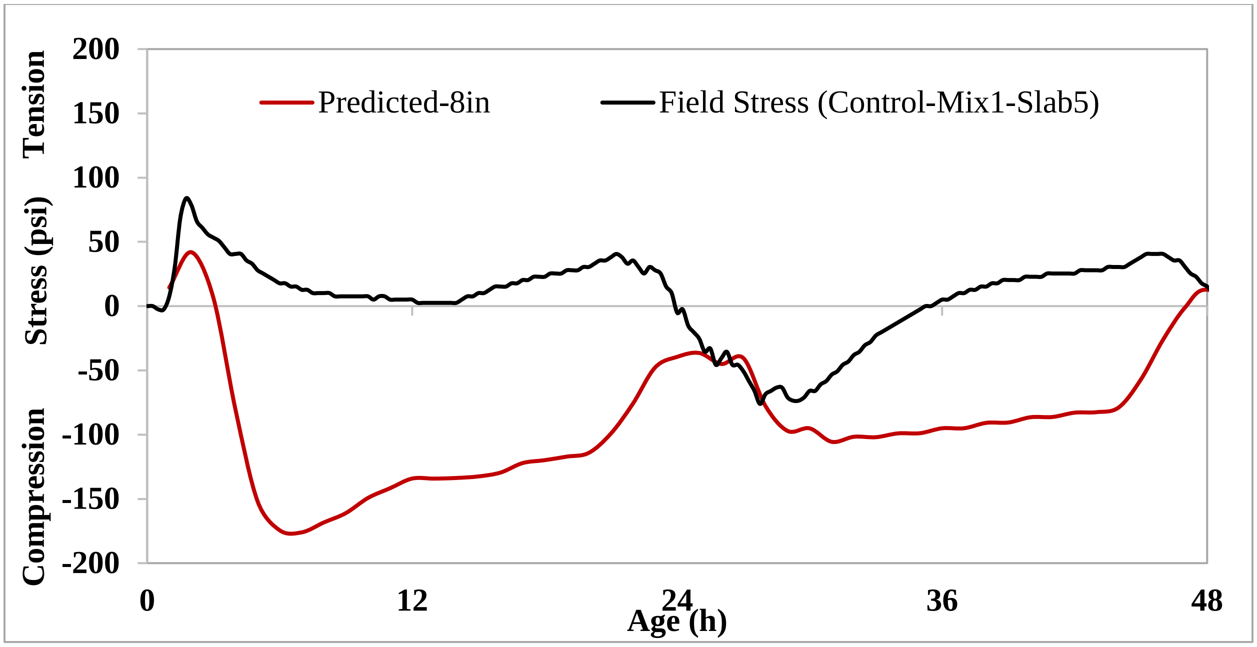

Figure 10-12: Stress prediction obtained from DIANA for slab 5 (without creep/relaxation effect)

The stress predictions obtained after incorporating creep/relaxation effects are shown in Figure 10-13. It is important to note that the initial tensile stress development observed in the field slab, which was possibly affected by the moisture migration, was not simulated in this model due to the limitations in the software. Therefore, the only early-age phenomena associated with the model output were temperature rise due to heat of hydration, autogenous shrinkage, evolution of mechanical properties, and creep/relaxation effects (viscoelastic behavior). In order to compare the qualitative stress development, field stress recorded for Slab 6 – with plastic was also plotted in the same figure. Although a different mix (Mix 3) was used in this slab, this was useful for comparison, as it showed compressive stresses during the initial period. It is likely that the plastic sheet prevented development of tensile stresses by controlling the moisture absorption by the base. As it appears in Figure 10-13, compared to Figure 10-12, the compressive stresses predicted during the first 24 hours were greatly reduced due to relaxation as expected. The double power law (DPL) model [37], [38] recommended by DIANA for early-age concrete analysis was used to simulate the creep/relaxation characteristics. The stress development shown in Figure 10-13 was predicted using DPL parameters indicated by Faria et al. [39] for early-age concrete analysis. The creep coefficient used in DPL affects the magnitude of predicted stress. Higher creep coefficients result in lower stresses and vice versa. As it can be seen in the figure, initial stress prediction shows a behavior similar to that of slab 6. However, the stress prediction after 24 hours was underestimated by the model. DPL has been criticized as it can overestimate the creep strains at later ages [38], resulting in lower stresses. Moreover, the stressmeter gives an average stress for the 3 in. of concrete included in the stressmeter. Therefore, the stress predicted at adjacent depths (10, 9, 7 and 6 in. from the bottom) are also plotted in the same figure for further clarification.

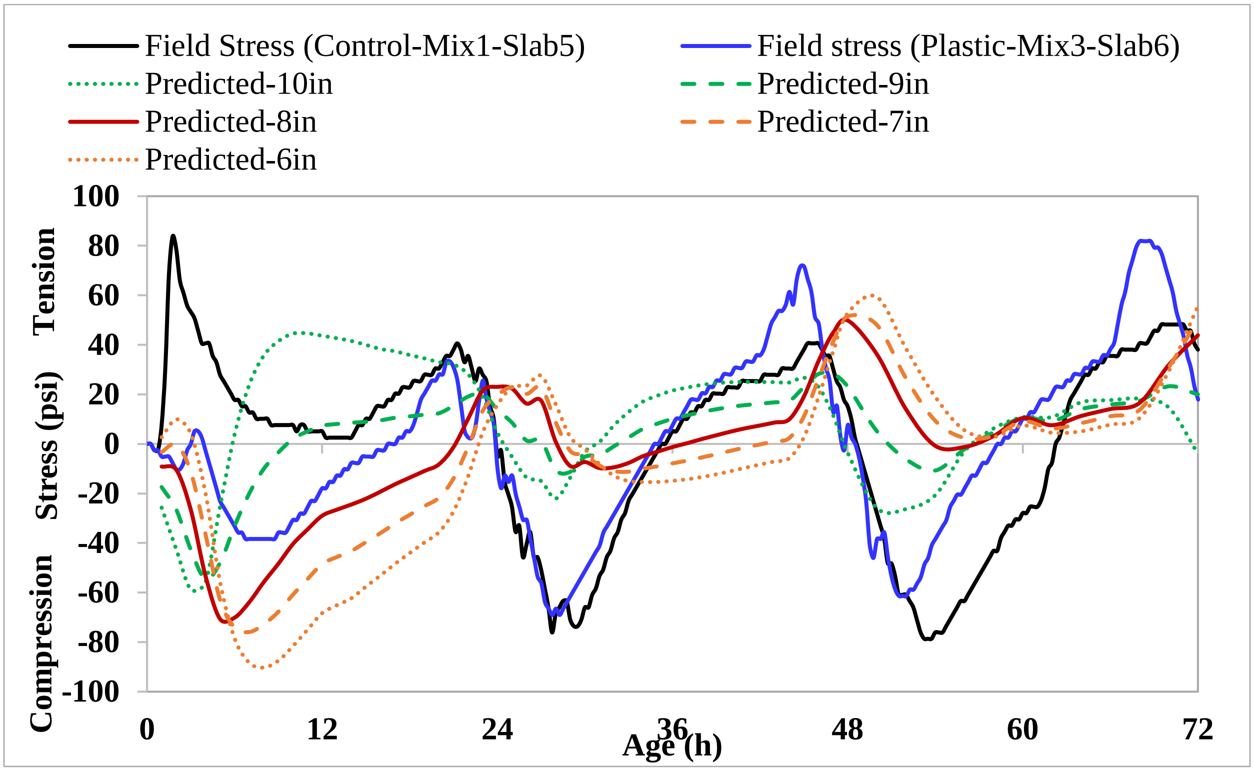

Figure 10-13: Stress prediction obtained from DIANA for slab 5 (with creep/relaxation effect)

Based on DIANA analysis results, it was apparent that the temperature gradient did not contribute to initial tensile stress development in the slab, 8 in. from the bottom. It was likely the initial tensile stresses observed in the field slabs were attributed to the moisture gradient resulting from moisture migration to the base.

10.4 Conclusions and Recommendations

The initial stress development in most of the slabs was affected by the moisture loss to the base. It is recommended that the bases be prewetted prior to concrete placement to prevent moisture migration and the resultant increase in tensile stresses.

For the five crack-mitigation strategies examined here, optimized mixtures showed improved tensile strengths and lower tensile stresses compared to other mixtures. Lower tensile stresses can be attributed to the lower cement contents of the mixes and, as a result, lower thermal and autogenous shrinkage. Therefore, a mix with an optimized aggregate gradation (denser particle packing) and reduced cement content is recommended as a potential HES mix for full depth repairs.

Although incorporation of LWA slightly reduced concrete strength at early age, Mix 5 showed a noticeable decrease in cracking tendency. Prewetted LWA is recommended in a mix as a method of internal curing to extend the hydration of cementitious system while maintaining a high level of internal humidity to reduce the drying and, as a result, autogenous shrinkage. However, inclusion of SRA and polypropylene fibers had minimal effects on reducing cracking potential compared to the control, possibly due to the lower dosage of SRA and lower volume of fiber used in this project.

Use of plastic sheeting in the slab-base interface had the primary benefit of preventing moisture loss to the base during the initial period. Afterwards, its bond breaking ability was questionable as the cracking tendency was not affected, either the plastic did not change the friction coefficient between the slab and the base, or curling lifted the slab off of the subbase slightly. On the contrary, the geotextile increased the absorption of moisture from concrete and increased cracking risks during the initial period, and thereafter the cracking tendency was greatly reduced. Therefore, prewetting of geotextiles is recommended prior to concrete placement.

10.5 References

[1] A. Zayed, K. Riding, C. C. Ferraro, A. Bien-aime, N. Shanahan, D. Buidens, T. Meagher, V. Tran, J. D. Henika, J. M. Paris, C. M. Tibbetts, and B. E. Watts, “Final Report Long-Life Slab Replacement Concrete FDOT Contract Number : BDV25-977-01,” University of South Florida, Tampa, FL, 2015.

[2] K. A. Riding, “Early Age Concrete Thermal Stress Measurement and Modeling,” University of Texas, Austin, 2007.

[3] E. E. Holt, “Early Age Autogenous Shrinkage of Concrete,” Technical Research Center of Finland, 2001.

[4] B. Klemczak and A. Knoppik-Wróbel, “Early Age Thermal and Shrinkage Cracks in Concrete Structures–Description of the Problem,” *Archit. Eng. Environ.*, 2011.

[5] A. Bentur, S. I. Igarashi, and K. Kovler, “Prevention of Autogenous Shrinkage in High-Strength Concrete by Internal Curing Using Wet Lightweight Aggregates,” *Cem. Concr. Res.*, vol. 31, no. 11, pp. 1587–1591, 2001.

[6] D. Cusson and T. Hoogeveen, “Internal Curing of High-Performance Concrete with Pre-Soaked Fine Lightweight Aggregate for Prevention of Autogenous Shrinkage Cracking,” *Cem. Concr. Res.*, vol. 38, no. 6, pp. 757–765, 2008.

[7] K. Kim, T. Subgranon, M. Tia, and M. Bergin, “Internally Cured Concrete for Use in Concrete Pavement Using Accelerated Pavement Testing and Finite-Element Analysis,” *Journal of Materials in Civil Engineering*, vol. 28, no. 6, pp. 1–8, 2016.

[8] P. K. Mehta and P. J. M. Monteiro, *Concrete: Microstructure, Properties and Materials*, 3rd ed. New York, NY: McGraw-Hill, 2006.

[9] P. Soroushian, A. Khan, and J.-W. Hsu, “Mechanical Properties of Concrete Materials Reinforced with Polypropylene or Polyethylene Fibers,” *ACI Mater. J.*, vol. 89, no. 6, pp. 535–540, 1992.

[10] N. Buch, “Impact of Processed Cellulose Fibers on Portland Cement Concrete Properties,” *Transp. Res. Rec.*, vol. 1668, no. 1, pp. 72–80, 1999.

[11] D. P. Bentz, M. R. Geiker, and K. K. Hansen, “Shrinkage-Reducing Admixtures and Early-Age Desiccation in Cement Pastes and Mortars,” *Cem. Concr. Res.*, vol. 31, no. 7, pp. 1075–1085, 2001.

[12] K. J. Folliard and N. S. Berke, “Properties of High Performance Concrete Containing

Shrinkage-Reducing Admixture," *Cem. Concr. Res.*, vol. 27, no. 1, pp. 1357–1364, 1997.

[13] E. Yurdakul, "Proportioning for Performance-based Concrete Pavement Mixtures," Iowa State University, 2013.

[14] ACI committee 207, "ACI 207.2R- Report on Thermal Volume Change Effects on Cracking of Mass Concrete," American Concrete Institute, Farmington Hills, MI, 2007.

[15] M. Emborg, "Models and Methods for Computation of Thermal Stresses," in *RILEM Report 15, Prevention of thermal cracking in concrete at early ages*, R. Springenschmid, Ed. London and New York: E & FN Spon, 1998, pp. 178–230.

[16] T. Kanda and H. Momose, "Stochastic Approach to Shrinkage Cracking Control for Reinforced Concrete Structural Elements," *J. Adv. Concr. Technol.*, vol. 6, no. 1, pp. 121–133, 2008.

[17] K. A. Riding, J. L. Poole, A. K. Schindler, M. C. G. Juenger, and K. J. Folliard, "Statistical Determination of Cracking Probability for Mass Concrete," *J. Mater. Civ. Eng.*, vol. 26, no. 9, p. 04014058, 2013.

[18] ASTM C39 /C39M-16a, "Standard Test Method for Compressive Strength of Cylindrical Concrete Specimens," West Conshohocken, PA: ASTM International, 2016.

[19] ASTM C496/C496M-11, "Standard Test Method for Splitting Tensile Strength of Cylindrical Concrete Specimens," West Conshohocken, PA: ASTM International, 2011.

[20] ASTM C1074–04, "Standard Practice for Estimating Concrete Strength by the Maturity Method," West Conshohocken, PA: ASTM International, 2004.

[21] Transtec Group, "HIPERPAV III (version 3.20.0006) [software]," 2009. [Online]. Available: www.hiperpav.com. [Accessed: 01-Dec-2016].

[22] TNO DIANA FEA, "DIANA: Displacement Analyzer 10.2." Delft, Netherlands, 2017.

[23] P. J. Robins, J. W. Bishop, and S. A. Austin, "Early-age Finite Element Modelling of Industrial Ground Floors," in *Proceedings of the Institution of Mechanical Engineers, Part L: Journal of Materials: Design and Applications*, 2003, vol. 217, no. 4, pp. 295–308.

[24] A. Lawrence, "A Finite Element Model for The Prediction of Thermal Stresses in Mass Concrete," University of Florida, 2009.

[25] H. Hedlund, "Hardening Concrete: Measurements and Evaluation Of Non-Elastic Deformation and Associated Restraint Stresses," Luleå University of Technology, 2000.

[26] P. Soroushian, F. Mirza, and A. Alhozaimy, "Plastic Shrinkage Cracking of Polypropylene

Fiber Reinforced Concrete," *ACI Mater. J.*, vol. 92, no. 5, pp. 553–560, 1995.

[27] P. S. Song, S. Hwang, and B. C. Sheu, "Strength Properties of Nylon and Polypropylene-Fiber-Reinforced Concretes," *Cem. Concr. Res.*, vol. 35, no. 8, pp. 1546–1550, 2005.

[28] A. E. Naaman, T. Wongtanakitcharoen, and G. Hauser, "Influence of Different Fibers on Plastic Shrinkage Cracking of Concrete," *ACI Mater. J.*, no. 102, pp. 49–58, 2005.

[29] N. Banthia and R. Gupta, "Influence of Polypropylene Fiber Geometry on Plastic Shrinkage Cracking in Concrete," *Cem. Concr. Res.*, vol. 36, no. 7, pp. 1263–1267, 2006.

[30] C. Qi, J. Weiss, and J. Olek, "Characterization of Plastic Shrinkage Cracking in Fiber Reinforced Concrete Using Image Analysis and a Modified Weibull Function," *Mater. Struct.*, vol. 36, no. 6, pp. 386–395, 2003.

[31] A. Sivakumar and M. Santhanam, "A Quantitative Study on the Plastic Shrinkage Cracking in High Strength Hybrid Fibre Reinforced Concrete," *Cem. Concr. Compos.*, vol. 29, no. 7, pp. 575–581, 2007.

[32] D. P. Bentz, "Influence of Shrinkage-Reducing Admixtures on Early-Age Properties of Cement Pastes," *J. Adv. Concr. Technol.*, vol. 4, no. 3, pp. 423–429, 2006.

[33] G. Sant, A. Eberhardt, D. Bentz, and J. Weiss, "Influence of Shrinkage-Reducing Admixtures on Moisture Absorption in Cementitious Materials at Early Ages," *J. Mater. Civ. Eng.*, vol. 22, no. March, pp. 277–287, 2010.

[34] N. Shanahan, A. Bien-aime, D. Buidens, T. Meagher, A. Sedaghat, K. Riding, and A. Zayed, "Combined Effect of Water Reducer – Retarder and Variable Chloride-Based Accelerator Dosage on Rapid Repair Concrete Mixtures for Jointed Plain Concrete Pavement," *J. Mater. Civ. Eng.*, pp. 1–10, 2016.

[35] E. B. Lee, V. Lamour, J. H. Pae, and J. Harvey, "Analysis of Sensitivity of Plain Jointed Concrete Pavement in California to Early-age Cracking using HIPERPAV," University of California, Pavement Research Center, Davis, CA, 2003.

[36] T. Meagher, N. Shanahan, D. Buidens, K. A. Riding, and A. Zayed, "Effects of chloride and chloride-free accelerators combined with typical admixtures on the early-age cracking risk of concrete repair slabs," *Constr. Build. Mater.*, vol. 94, pp. 270–279, 2015.

[37] TNO DIANA FEA, "Material Library," in *DIANA Finite Element Analysis - User's Manual*, Delft, Netherlands: TNO DIANA FEA, 2017.

[38] D. S. Atrushi, "Tensile and Compressive Creep of Early Age Concrete : Testing and

Modelling," The Norwegian University of Science and Technology, 2003.

[39] R. Faria, M. Azenha, and J. A. Figueiras, "Modelling of Concrete at Early Ages: Application to an Externally Restrained Slab," *Cem. Concr. Compos.*, vol. 28, no. 6, pp. 572–585, 2006.

Chapter 11 Conclusions and Recommendations

11.1 Conclusions

This study evaluated the effectiveness of several cracking mitigating strategies in reducing cracking potential in HES repair slabs. The following conclusions can be made, based on the findings from the study:

- The initial stress development in most of the field-placed slabs was affected by moisture migration into the base; tensile stresses were observed due to increased autogenous shrinkage within the slab. DIANA finite element analysis confirmed that the initial temperature gradient would not contribute to the development of tensile stresses within the slab at early ages.
- The cracking risks of HES concrete can be greatly reduced by increasing the aggregate packing density and lowering the paste content. A decrease in cement content decreased the temperature rise and overall autogenous shrinkage in concrete, and consequently its tendency to crack.
- High strengths in concrete can be achieved, even with low paste mixtures, as long as the w/cm is not increased. Differences in mechanical property results obtained for the base mix and optimized mixtures were not statistically significant.
- The cracking probability of HES concrete slabs can be minimized by incorporating LWA as a means of internal curing to extend hydration and reduce autogenous shrinkage effects.
- Lower SRA dosage and lower fiber volume utilized in this study did not show significant contributions to minimizing cracking risks after 24 hours. However, both SRA and fiber substantially reduced the initial induced tensile stresses in field-placed slabs.
- The base friction reducing mediums showed more pronounced effects on early-age stress development through base moisture absorption than by reducing friction.
    - The double layers of plastic sheeting at the slab-base interface prevented moisture loss to the base at early age. However, later on, its bond breaking ability was questionable as no significant effect on cracking potential was observed; either the plastic did not change the friction coefficient between the slab and the base, or curling lifted the slab off of the subbase slightly.

  - The geotextile augmented the absorption of moisture from concrete and increased cracking risks during early age. However, later on, the cracking tendency was greatly reduced.

11.2 Recommendations

Based on the findings of this study, the following can be recommended:

- Require that the bases be prewetted prior to concrete placement to prevent moisture migration and the resultant increase in tensile stresses.
- Require that geotextiles be prewetted prior to concrete placement.
- Use an HES mix with optimized aggregate gradation and reduced paste content to overcome thermal and shrinkage effects that result in cracking.
- Concrete mixtures with optimized aggregate gradation (denser particle packing) and reduced cement content are recommended for use for full depth repairs in HES pavement slabs.

11.3 Suggestions for Future Work

The following can be suggested for future work:

- The findings of the current study identified several strategies that if implemented can reduce the cracking potential in HES pavement replacement slabs. It would be desirable to combine several of the identified strategies in a single mixture and assess the enhancement of the crack mitigation effects when strategies are applied simultaneously.

Appendix A - Activation Energy Fit Curves and Arrhenius Plots

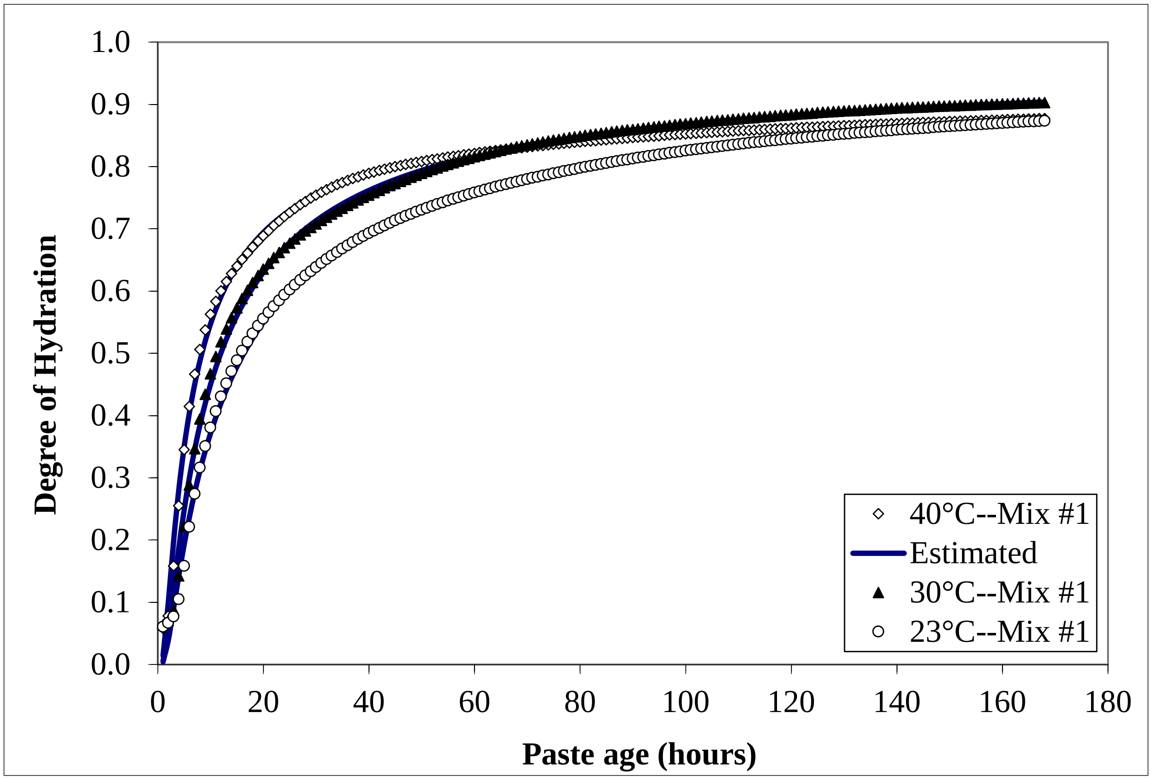

Figure A-1: Degree of hydration as a function of age for Mix#1

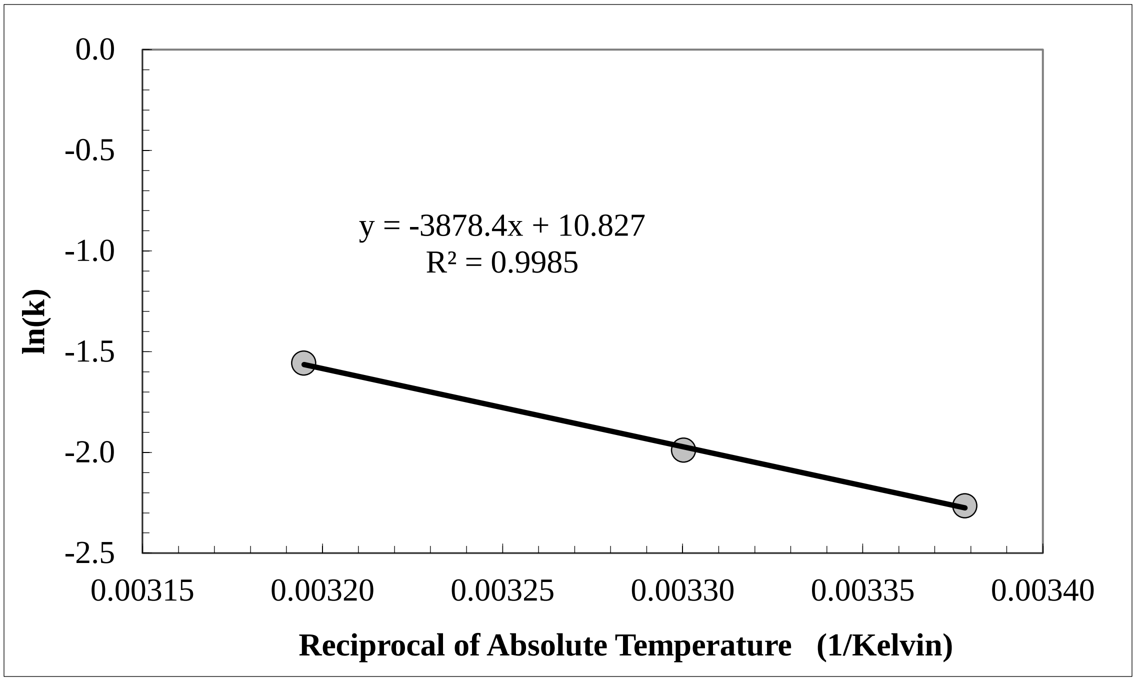

Figure A-2: Arrhenius plot for Mix#1

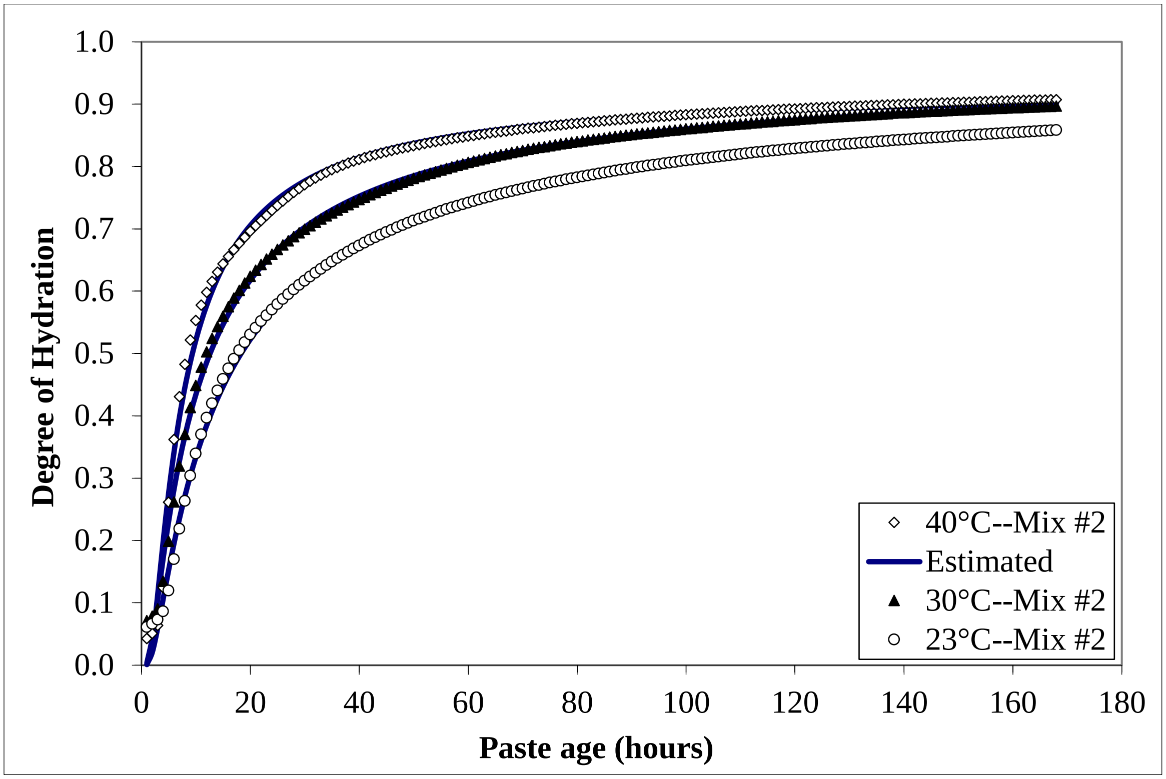

Figure A-3: Degree of hydration as a function of age for Mix#2

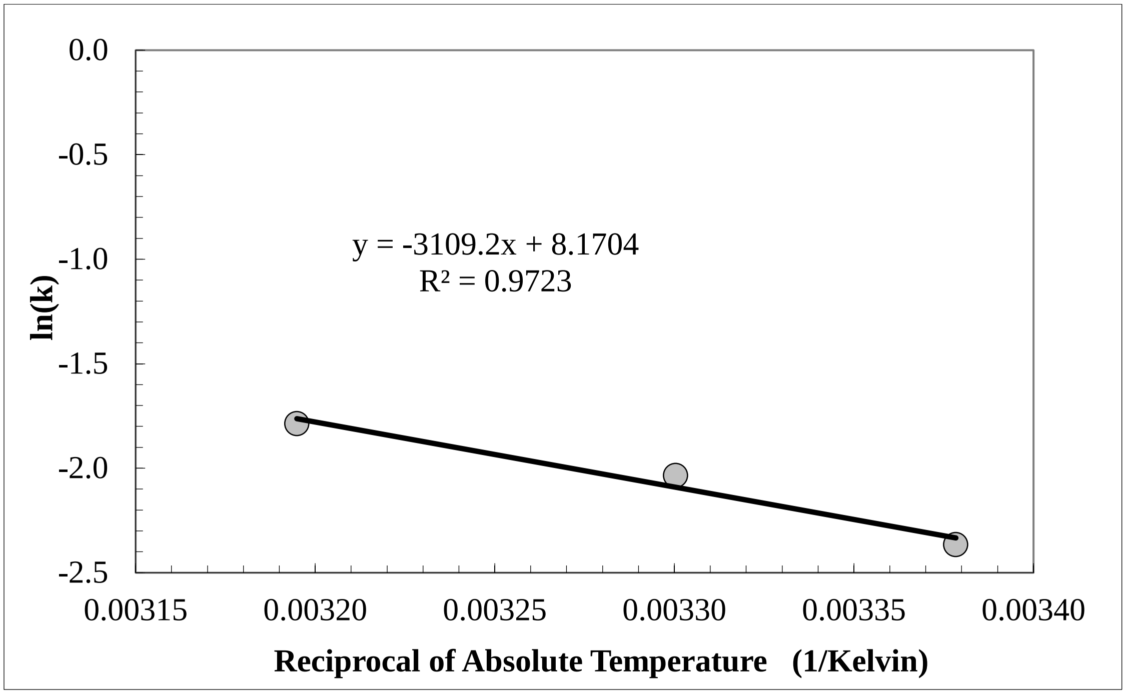

Figure A-4: Arrhenius plot for Mix#2

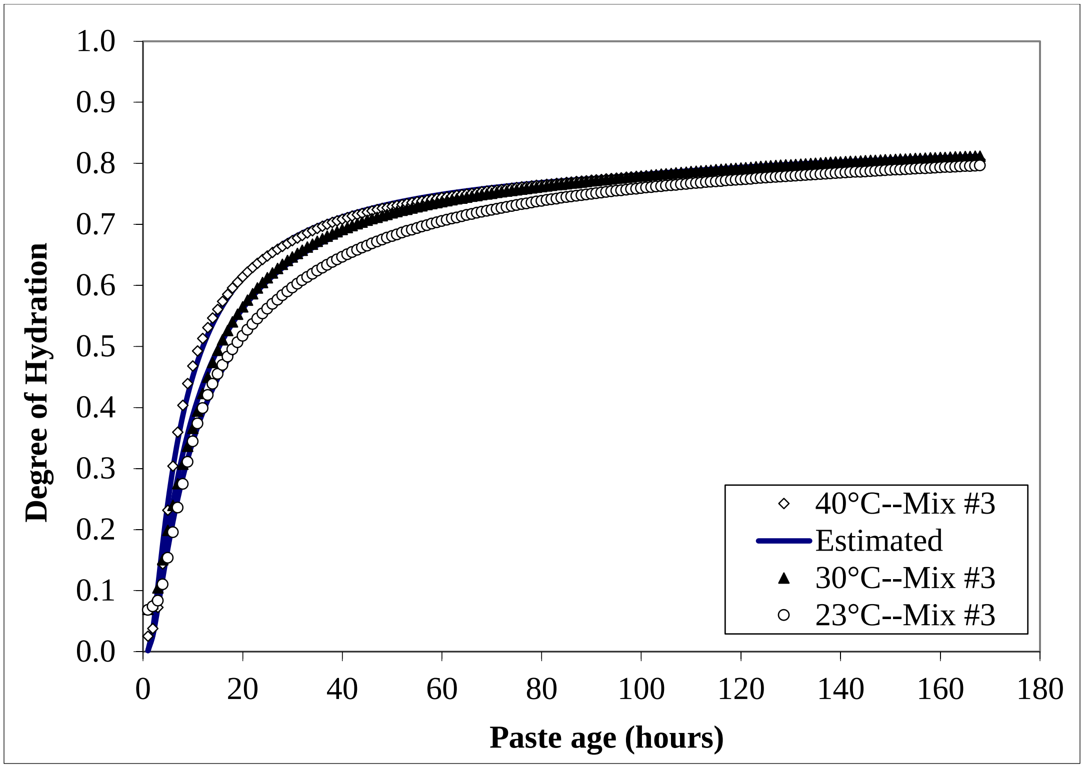

Figure A-5: Degree of hydration as a function of age for Mix#3

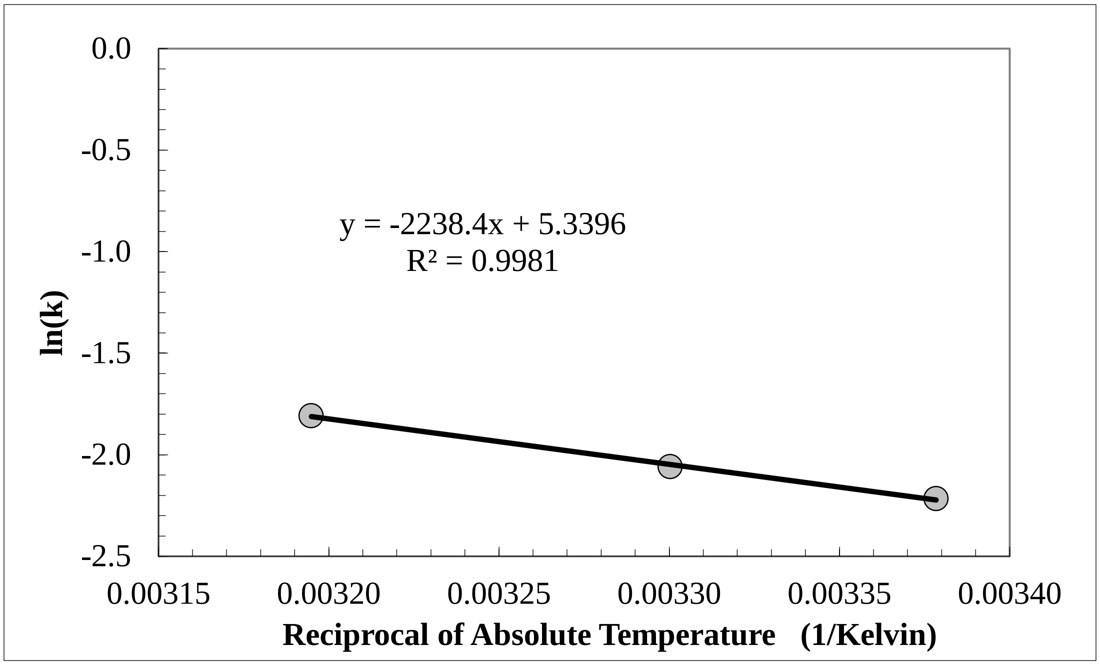

Figure A-6: Arrhenius plot for Mix#3

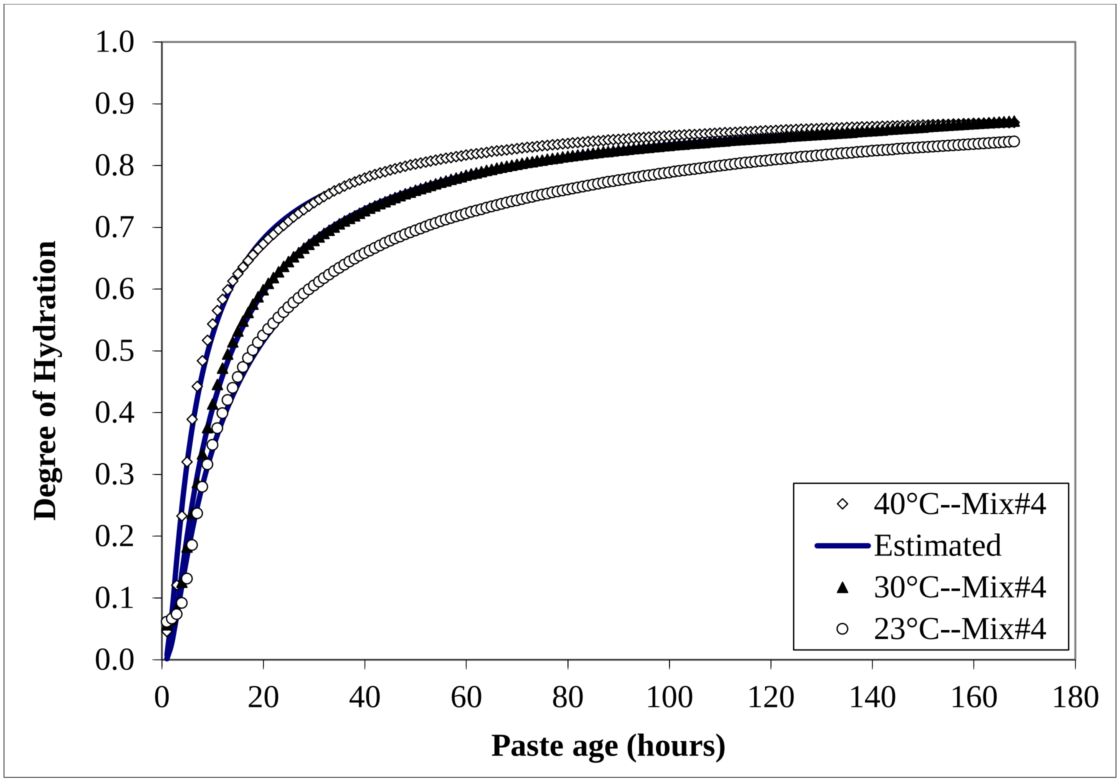

Figure A-7: Degree of hydration as a function of age for Mix#4

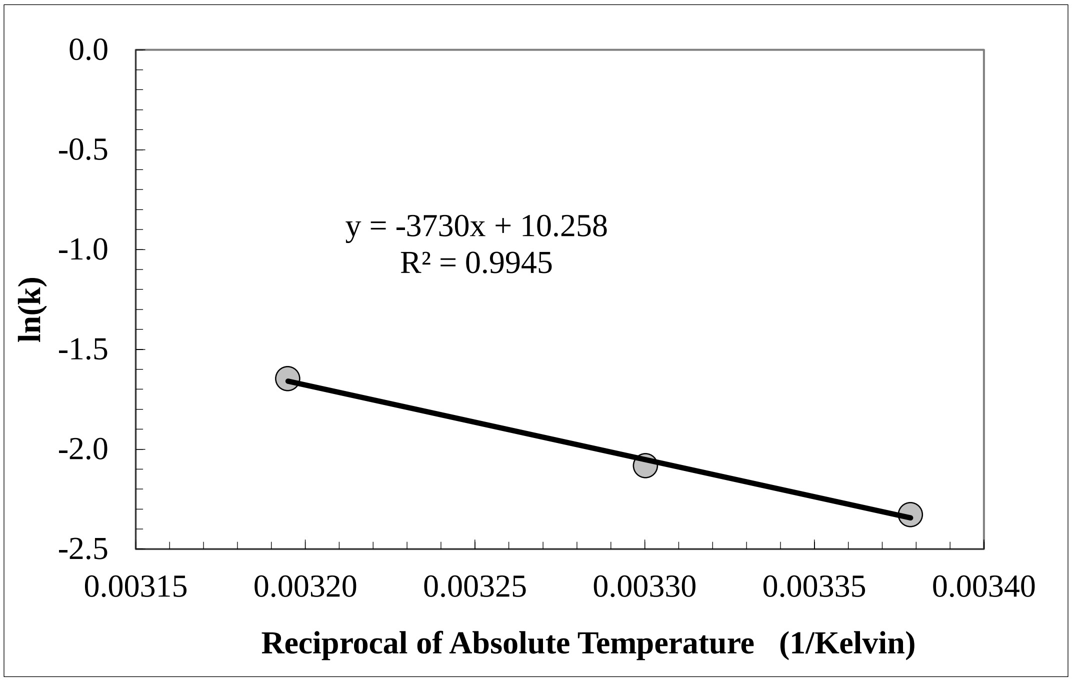

Figure A-8: Arrhenius plot for Mix#4

Appendix B - Mortar Cube Strength at Variable Temperatures

		Compressive Strength (MPa)		
Mix ID	**Age (hr)**	**23˚C**	**35˚C**	**50˚C**
Mix #1	3	N/A	4.2	7.0
	6	6.6	14.8	18.5
	12	16.5	25.1	30.2
	24	28.2	32.0	37.2
	48	34.8	41.7	38.7
	72	41.9	43.8	41.5
	168	43.7	48.3	45.4
	672	50.8	49.5	44.6
Mix #2	3	N/A	2.8	4.0
	6	4.3	12.1	15.4
	12	12.8	20.1	23.6
	24	24.5	25.2	27.3
	48	30.1	32.1	33.4
	72	36.5	33.7	30.8
	168	40.6	35.1	34.2
	672	50.9	37.9	32.7

Appendix B - Mortar Cube Strength at Variable Temperatures contd.

		Compressive Strength (MPa)		
Mix ID	**Age (hr)**	**23˚C**	**35˚C**	**50˚C**
Mix #3	3	N/A	5.0	9.5
	6	8.2	22.9	28.8
	12	21.3	36.4	37.8
	24	37.4	46.5	52.4
	48	45.9	54.4	51.6
	72	52.9	62.5	55.1
	168	64.7	66.4	62.4
	672	70.2	73.2	58.7
Mix #4	3	N/A	3.5	7.2
	6	5.5	15.9	20.3
	12	16.9	27.6	32.3
	24	30.5	35.9	42.7
	48	43.9	45.6	46.3
	72	44.1	50.5	48.0
	168	51.4	58.1	54.1
	672	59.6	52.5	62.2

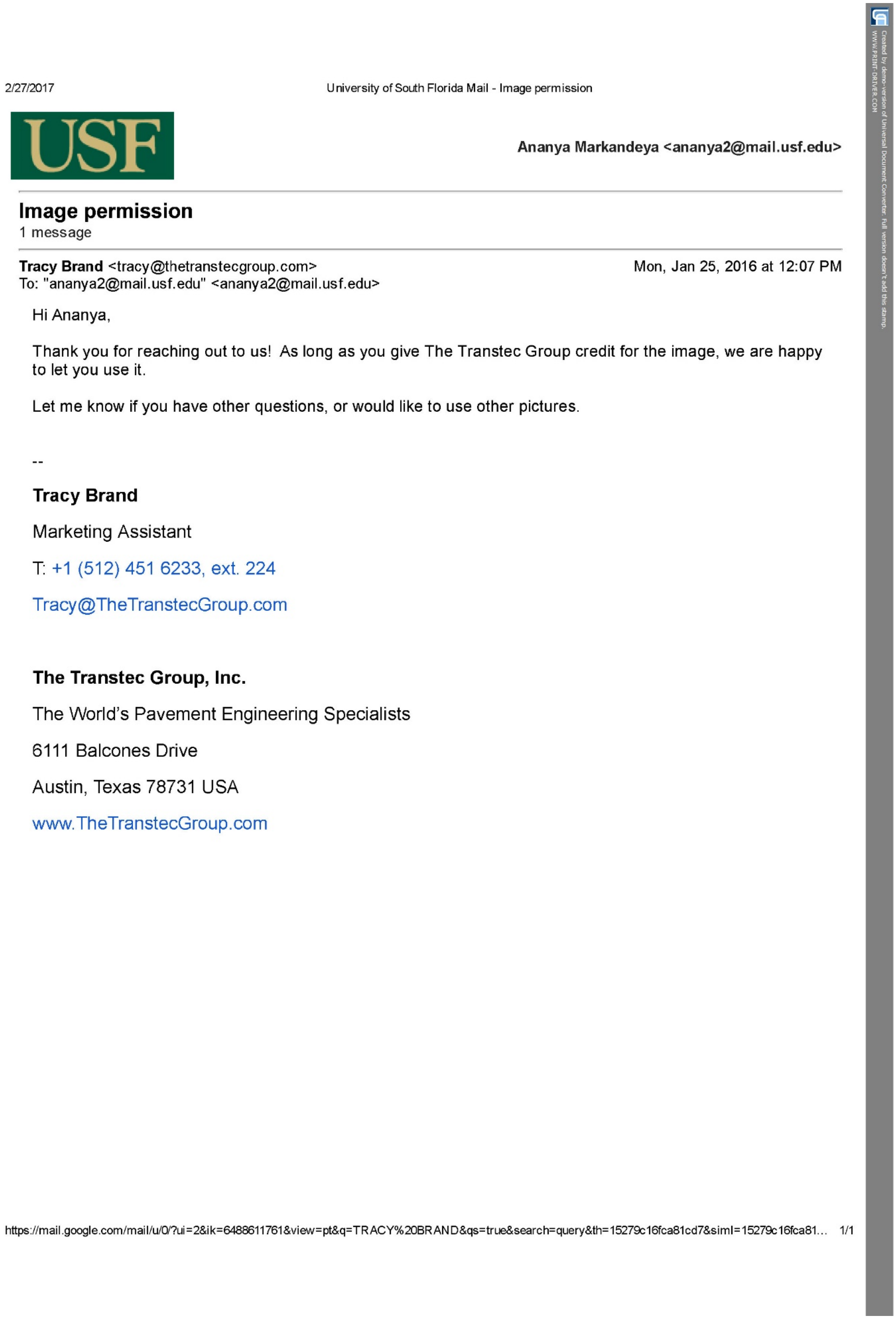

2/27/2017 University of South Florida Mail - Image permission

USF

Ananya Markandeya <ananya2@mail.usf.edu>

Image permission

1 message

Tracy Brand <tracy@thetranstecgroup.com> Mon, Jan 25, 2016 at 12:07 PM
To: "ananya2@mail.usf.edu" <ananya2@mail.usf.edu>

Hi Ananya,

Thank you for reaching out to us! As long as you give The Transtec Group credit for the image, we are happy to let you use it.

Let me know if you have other questions, or would like to use other pictures.

--

Tracy Brand

Marketing Assistant

T: +1 (512) 451 6233, ext. 224

Tracy@TheTranstecGroup.com

The Transtec Group, Inc.

The World's Pavement Engineering Specialists

6111 Balcones Drive

Austin, Texas 78731 USA

www.TheTranstecGroup.com

https://mail.google.com/mail/u/0/?ui=2&ik=6488611761&view=pt&q=TRACY%20BRAND&qs=true&search=query&th=15279c16fca81cd7&siml=15279c16fca81… 1/1

Created by demo-version of Universal Document Converter. Full version doesn't add this stamp.
WWW.PRINT-DRIVER.COM

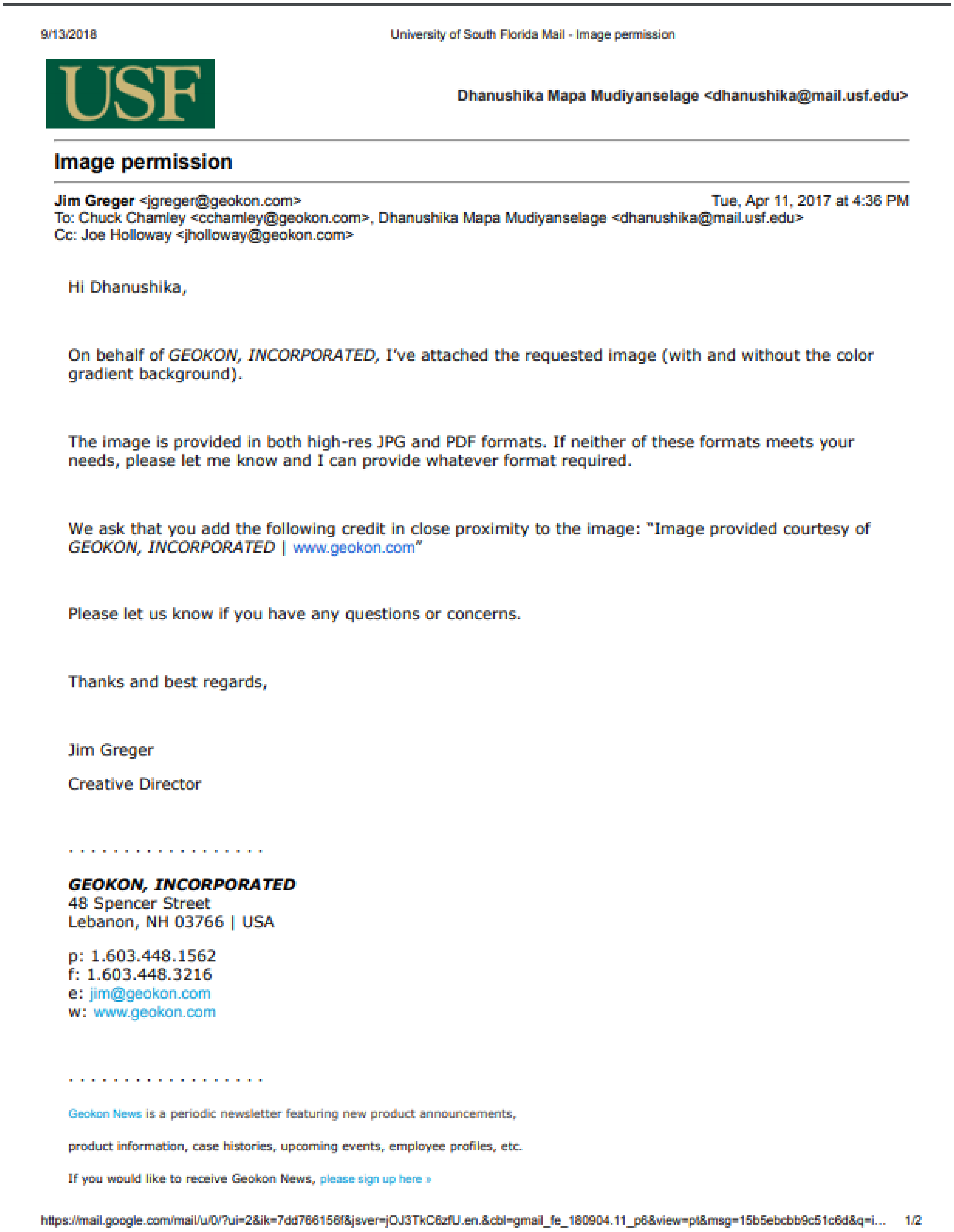

9/13/2018 University of South Florida Mail - Image permission

USF

Dhanushika Mapa Mudiyanselage <dhanushika@mail.usf.edu>

Image permission

Jim Greger <jgreger@geokon.com> Tue, Apr 11, 2017 at 4:36 PM
To: Chuck Chamley <cchamley@geokon.com>, Dhanushika Mapa Mudiyanselage <dhanushika@mail.usf.edu>
Cc: Joe Holloway <jholloway@geokon.com>

Hi Dhanushika,

On behalf of *GEOKON, INCORPORATED,* I've attached the requested image (with and without the color gradient background).

The image is provided in both high-res JPG and PDF formats. If neither of these formats meets your needs, please let me know and I can provide whatever format required.

We ask that you add the following credit in close proximity to the image: "Image provided courtesy of *GEOKON, INCORPORATED* | www.geokon.com"

Please let us know if you have any questions or concerns.

Thanks and best regards,

Jim Greger

Creative Director

. . . .

GEOKON, INCORPORATED
48 Spencer Street
Lebanon, NH 03766 | USA

p: 1.603.448.1562
f: 1.603.448.3216
e: jim@geokon.com
w: www.geokon.com

. . . .

Geokon News is a periodic newsletter featuring new product announcements,

product information, case histories, upcoming events, employee profiles, etc.

If you would like to receive Geokon News, please sign up here »

https://mail.google.com/mail/u/0/?ui=2&ik=7dd766156f&jsver=jOJ3TkC6zfU.en.&cbl=gmail_fe_180904.11_p6&view=pt&msg=15b5ebcbb9c51c6d&q=i... 1/2